THE UNIVERSITY OF HULL

INVESTIGATION OF GRAPHENE OXIDE-BASED COMPOSITE MATERIAL STRATEGIES AS POSSIBLE CANDIDATES FOR LEADING EDGE EROSION PROTECTION OF OFFSHORE WIND TURBINES

being a Thesis submitted for the Degree of Doctor of Philosophy

in the University of Hull

by

Lloyd Benjamin Lee Glanville

PGCert BSc MRSC

November 2021

Abstract

At present the current climate and energy crisis has highlighted the global need for more renewable energy generation. Offshore wind provides a reliable source of this green energy however the harsh environments these assets operate in result in frequent maintenance. The erosive force of rainfall inelastically colliding with the leading edge of the turbines causes the phenomenon, Leading Edge Erosion.

Graphene oxide an oxidised allotrope of the superlative two-dimensional material graphene could provide suitable candidates in the development of impact resistant polymer composite coatings using testing regimes such as nanoindentation and dynamic mechanical analysis. This Thesis comparatively investigates the candidacy of unmodified graphene oxide and reduced graphene oxide polyurethane composites against a bioinspired modified graphene oxide polymer composites towards impact resistance and tensile loading.

The Thesis reports the novel facile synthesis of the quadruple hydrogen bonding array, ureidopyrimidone (UPy) onto the parent graphene oxide sheet (UPyGO), taking inspiration from the hydrogen bonding exploitation of spider silk. This novel filler is extensively characterised and comparatively analysed against the parent graphene oxide and reduced graphene oxide to understand the differing properties. The reproducibility of the synthesis was tested and found a 6.20 ± 0.04% UPy functionalisation. The final chapter investigates the preparation of a complementary UPyGO-UPy-polyurethane composite and how it performs to the criterion needed for leading edge erosion protection. This work successfully reports that the addition of UPyGO into the polymer matrix and finds that the 0.033 wt.% UPyGO composite provided the best candidacy with decreases in the indentation stiffness of 77 ± 4%, and the indentation hardness decreased by 24 ± 0.4% which are key characteristics for erosion protection candidacy.

Acknowledgements

The author wishes to acknowledge the following people:

Mrs Chelsea Paige Glanville, my wife, for her unconditional support, enabling me to conduct my research tirelessly, and my energetic English Springer Spaniel, Athena, helps me wind down on weekends.

My academic supervisors Dr Tommy Horozov (Chemistry), Prof. Jim Gilbert (Aura Research & Development Lead), and Dr Lijie He (Graphitene Ltd), for their supervision. Graphitene Ltd for the gratuitous supply of graphene oxide powders and expertise in the area of graphene oxide technology as my industrial sponsor.

The Green Port Growth Programme for sponsoring my initial 18 months of research and the industrial engagement component of my programme. The University of Hull for funding my research in the final 18 months of research. A summary of industrial engagement is provided later on in the preamble.

All my undergraduate research project students and in particular, Mr Jacob Gordon and Mr Jimmy Bishop for their hard work, which has supported some of my research objectives presented in this work.

Mr Dean and Sean Moore for their support with the FTIR ATR, TGA and DSC in the Physical Chemistry teaching laboratory. Mrs Carol Kennedy for conducting the CHNS Combustion Elemental Analysis. Mr Nigel Parkin for the assistance and fabrication of all the electrical and mechanical components, and Ms Sue Taft for conducting the dynamic mechanical analysis and nanoindentation tests. Finally, Dr Michael O'Neil, for his informal support throughout my supervision transition and collaboration on the nanotechnology reproducibility crisis manuscript.

Publications and presentations

Adam J. Young, Remy Guillet-Nicolas, Ellis S. Marshall, Freddy Kleitz Alex J. Goodhand, **Lloyd B.L. Glanville**, Michael. R. Reithofer*, Jia Min Chin*, Direct write ink 3D Printing of UiO-66 polymer composites, Chem. Commun., 2019, 55, 2190-2193

Oral Presentation, Designing the next generation coatings for the offshore wind industry, ***Maryland Department of Energy Knowledge Exchange Conference***, University of Hull, January 2018

Oral Presentation, Commercial analysis of the protective coatings market, ***National Physical Laboratory Internship***, Teddington, August 2018

White Paper (Internal), The potential for graphene-related materials in the offshore wind sector, ***National Physical Laboratory Internship***, Teddington, August 2018

Conference Attendance, ***Graphene & 2D Materials: From Research to Applications***, National Physical Laboratory, Teddington, October 2018

Conference Attendance, ***Offshore Wind Connections***, Hull, May 2019

Science Outreach Oral Presentation, Graphene: The Low Carbon Paradox, ***Christ Hospital School Gaia Week***, June 2019

Oral Presentation, Graphene oxide-based materials for erosion protection, ***Aura Centre for Doctoral Training Symposium***, University of Hull, November 2019

Industrial Engagement

To satisfy the Green Port Growth Programme funding from Hull City Council and East Riding of Yorkshire Council, this PhD programme requires the participant to engage with industry actively. Therefore, the below summary satisfies this criterion.

<u>Graphitene Ltd</u>

Graphitene has supplied all my graphene oxide products and has provided expertise in the field of graphene-based products and facilitated industrial led projects.

Aura Innovation Centre (AIC)

I have contributed to the development of the materials, surfaces and coatings focus group at the 4th RDI strand meeting at Durham University, where I facilitated the discussion group for the focus area, which included industry and academics. Furthermore, I led in the specification of the centre's equipment infrastructure, which will support SMEs and Aura's funding objectives.

Photocentric3D

Visited the site and collaborated with the research and development teams on slippery liquid infused porous surfaces and incorporation of graphene oxide into their photopolymer resins. Some additional work contributed to the creation of a KTP programme supervised by Dr Chin and Prof Pamme.

Siemens Gamesa Renewable Energy

Attended a meeting at the UK headquarters in Newcastle with other academics and Aura team members, whereby I presented my research themes to the Chief Technical Officer (Future Technologies and Innovation) and the UK and German Innovation Managers.

National Physical Laboratory (NPL)

In August 2018, I had the pleasure of undertaking an internship at the National Physical Laboratory within the graphene strategy team. The experience enabled exposure to the surface analysis of metal chalcogenides, graphene metrology centre; advanced thermal analysis; electrochemistry; leading-edge erosion metrology and business development of industrial facing research. The internship culminated in an oral presentation to the leadership of the strategy team and senior scientists.This then resulted in personally, leading the proposal for a strategic partnership between the National Physical Laboratory and the University of Hull aligned along a synergistic theme of Environmental Resilience. This briefing involved effectively communicating with multiple internal departments and Senior Leadership within the University's Research and Enterprise Directorate, and NPL. The outcome resulted in the engagement of specific strategic projects, which will be on a project-by-project basis.

Postgraduate Training Scheme

During this programme, I have completed the following postgraduate training scheme modules to satisfy the Research Skills Qualification PGCert (60 credits) requirements.

05062 - The Modern Researcher	[20 credits]	Compulsory
05701 – Safety in Research in Science & Engineering	[5 credits]	Compulsory
05058 – Research Integrity & Ethics (FoSE)	[10 credits]	Compulsory
06701 – BLCS Liquid Crystal Workshop	[10 credits]	
05027 - Communication Skills (Easter School)	[10 credits]	
05039 – Negotiated Postgraduate Learning	[20 credits]	

Research Supervision

During the PhD programme, I supervised the following students during their research projects within the laboratory.

Mr Adam Bell – MChem 2017/18: Synthesis of intrinsic self-healing polymers by metal-ligand bonding

Mr Jamie Akister – MChem 2018/19: Fabrication of reduced graphene oxide-polydimethylsiloxane composites exhibiting enhanced tensile properties

Mr Dominic Rawlins – MChem 2018/19: Preparation of graphene oxide stabilised porous microcapsules for controlled release of active ingredients

Mr Sundip Sharma – MChem 2018/19: Preparation of tuneable porous materials for analytical applications

Mr Charalambos Andrea – BSc 2018/19: Preparation of porous materials by foamulsion templating

Mr Ahmodul Kabir - BSc 2018/19: Preparation of graphene oxide foams by foam templating

Mr Jimmy Bishop – BSc 2018/19: Preparation of 10 nm silica stabilised porous ceramics by foam templating

Mr Christopher Wakeham – BSc 2018/19: Preparation of 0.1µm silica stabilised porous ceramics by foam templating

Mr Jimmy Bishop – MChem 2019/20: Fabrication of reduced graphene oxide polyurethane composites

Mr Jacob Gordon – MChem 2019/20: Fabrication of complementary ureidopyrimidone functionalised polyurethane

Mr Morgan Lane – BSc 2019/20: Preparation of graphene oxide reinforced porous materials for analytical applications

Miss Rebecca Coy – BSc 2019/20: Preparation of tuneable porous materials by post functionalisation of diglycidyl methyacrylate

Miss Leah Gallagher – BSc 2019/20: Preparation of tuneable porous materials by pre functionalisation of diglycidyl methyacrylate

Miss Klaudia Nguyen - BSc 2019/20: Preparation of novel filters using high internal phase emulsion templating

Contents

List of abbreviations

ADAD	Acceptor-donor-acceptor-donor hydrogen bonding array
ANOVA	Analysis of variance testing
b.p.	Boiling point
DDAA	Donor-donor-acceptor-acceptor hydrogen bonding array
DMC	Dimethyl carbonate
DMF	*N,N*-dimethylformamide
DMTA	Dynamic mechanical thermal analysis
DSC	Differential scanning calorimetry
E	Young's Modulus
E'	Storage Modulus
E"	Loss Modulus
Eco-GO	Electrochemically exfoliated graphene oxide
EDS	Energy dispersive spectroscopy
EF120	Easyflo 120 Polyurethane
FTIR ATR	Fourier transform attenuated total internal reflectance infrared spectroscopy
GBMs	Graphene-based materials
GO	Graphene oxide
GOBMs	Graphene oxide-based materials
LEE	Leading-edge erosion
m.p.	Melting point
OSW	Offshore wind industry
PDMS	Polydimethylsiloxane
PTFE	Polytetrafluoroethylene
PU	Polyurethane
PXRD	Powder x-ray diffraction
rGO	Reduced graphene oxide
SEM	Scanning electron microscopy
STP	Standard temperature and pressure (273.15 K and 100 kPa)

tanδ	Tan Delta
T_g	Glass transition temperature
TGA	Thermogravimetric analysis
UPy	Ureidopyrimidone
UPyGO	Ureidopyrimidone functionalised graphene oxide
UPyNCO	1,6-isocyanatohexane functionalised ureidopyrimidone
UPyPU	Ureidopyrimidone functionalised polyurethane

1. Introduction

Erosion is synonymous with secondary school geography lessons that outline the natural processes that form new habitats and geological forms. Through repetitive surface processes, the fluid nature of water (all states of matter) and air interact with solid interfaces to remove this interface's constituents over time. These natural processes contribute towards the challenges of achieving global ambitions to deliver low-cost clean energy to begin meeting the 2015 Paris Agreement's targets.

This introductory chapter provides the necessary theories surrounding liquid impingement and associated mechanical properties, to provide a foundation that enables effective material design. Supported by the literature a materials specification brief can therefore be determined which provides the blueprint to investigate possible candidates that align with these studies. Due to the variability of graphene-based materials a literature review is presented specifically on graphene oxide-based materials to explain their nomenclature, structure, and effect in polyurethane composites so that correct comparisons can be drawn from the literature as early papers in the two-dimensional materials field sometimes misnamed graphite oxide as graphene oxide which makes reproducibility and comparative studies challenging. The literature then broadens into the challenges and strategies to avoid filler-matrix phase separation which are critical to developing robust materials. The literature review progresses beyond unmodified surface interactions and looks to nature for bioinspired solutions that could advance the filler-matrix adhesion properties compared to unmodified fillers by investigating a bioinspired quadruple hydrogen bonding functionalisation approach to determine whether this approach provides a favourable enhancement over unmodified graphene oxide-based materials towards erosive protection applications.

1.1 Liquid Impingement of solid surfaces

A frequently overlooked occurrence is the erosive damage that rain droplets have on solid materials. Because of the inelastic collision that occurs when the water droplet contacts the solid surface, energy changes result in the droplet surface tension being overcome, causing the observed splash. Multiple acoustic vibrations propagate in the surfaces structure (see Figure 1.1). The water hammer effect model describes this observed behaviour.

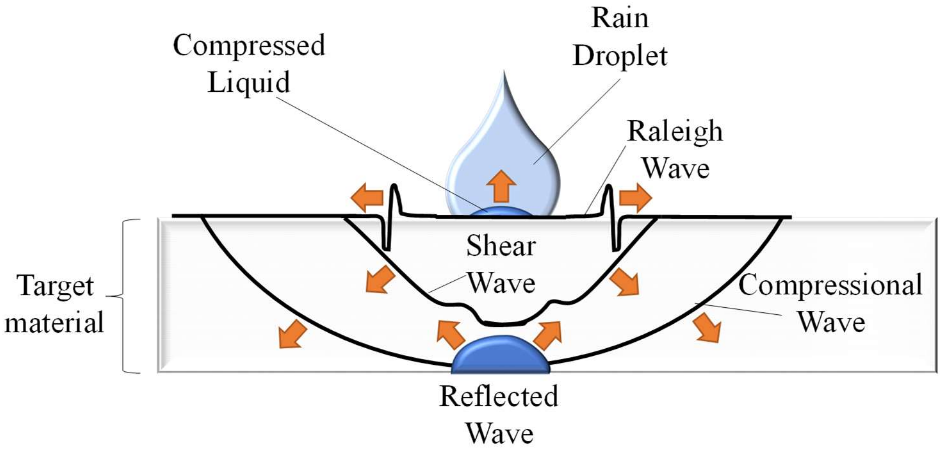

Figure 1.1. The vibrational interactions show the shock wave behaviour induced when a rain droplet impacts a solid surface target (adapted from ref. 1).

In the water hammer effect, a rain droplet impacts the surface, and it generates a compressional wave, followed by a shear wave and finally a Rayleigh wave, in addition to the wavefront created by the droplet. Therefore, because of these multiple waves, it leads to stresses at the molecular level, which can initiate plastic deformations if the material cannot dissipate the energy effectively.

One example of rain droplet erosion is within the energy industry in applications such as steam-powered turbines and offshore wind.[1] Leading-edge erosion was first described in steam-powered turbines in the early 20th century,[2] is a phenomenon that occurs at the foremost edge of a turbine blade, the leading edge. As a result of the velocity of the leading edge when it collides with rain droplets, it intensifies the shock wave behaviour in comparison to if it was a stationary surface. As such droplets act like 'liquid bullets' fired a solid surface leading to pitting of the surface, and if left unaddressed, it can begin to show the balsa wood interior resulting in decommissioning. This constant maintenance or premature decommissioning cycles results in inflated energy production expenditure, causing an obstacle to achieving Cleaner Growth.

Therefore, for a material to resist impacts like leading-edge erosion, is determined by how the material can dissipate the inelastic mechanical energy without compromising its structural integrity. Recently O'Carroll *et al.* [3] reported the experimental parameters that would result in the ideal coating for leading-edge erosion applications using techniques such as whirling arm rigs, nanoindentation and dynamic mechanical analysis. Their work enables the following design brief summarised in Figure 1.2 to be constructed.

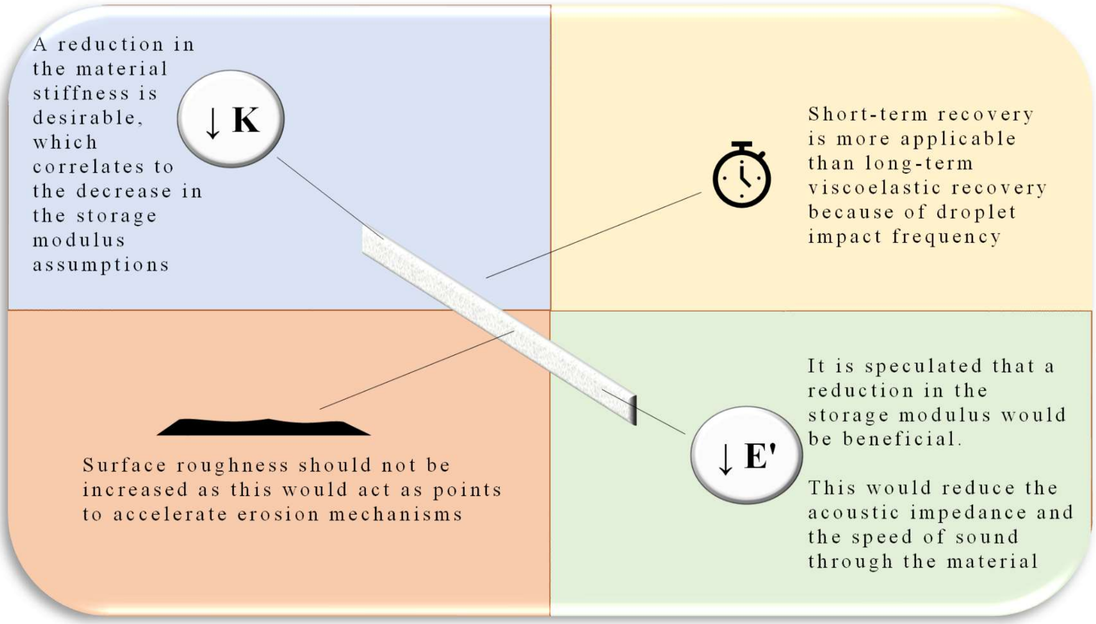

Figure 1.2. The ideal material properties for enhancing the liquid impingement properties of solid surfaces, which was investigated and summarised by O'Caroll *et al.*[3]

Intrinsically within materials science, elastic modulus parameters, viscoelasticity, and stiffness can provide some of the comparable benchmarks for applications testing.

1.2 Axial mechanics

Axial forces act along the central axis of a body. These forces can be tensile, compressive, shear, or torsional (see Figure 1.3). Tensile forces act when a sample is subjected to a stretching force that at a macro level plastically deforms with the observation of material necking. At a micro level, molecules are stretched beyond their bond strengths and yield into smaller mechanically cleaved chains.

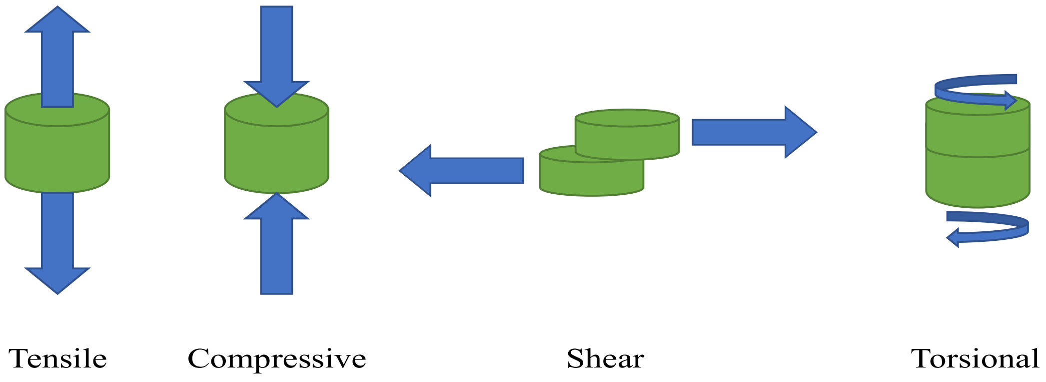

Figure 1.3. The four main types of axial mechanical forces illustrating the different directions the applied load (blue arrows) act on a body (green cylinder).

Compressive forces in contrast act when a sample is subjected to an inward pushing force that leads to macro-observations of plastic deformation from pitting or crumbling. At the micro level, the three-dimensional structure of atoms within the molecular structure are compacted onto one another leading again to the bond strengths been overcome.. Nanoindentation is a type of test that imparts compressive forces onto a sample.

Torsional forces occur when a body is subjected to a load that is applied through torque. A transmission drive shaft in cars is an example of torsional force. Shear forces are when a force is applied perpendicularly to a surface that is in opposition to the offset force acting in the opposite direction. Cutting is an example of shear force. However, for the research scope of this Thesis, tensile and compressive forces are evaluated only.

1.2.1 Tensile properties

For an ideal solid, a material is defined as possessing purely elastic behaviour. Therefore, during applied force, the material deforms elastically until the applied force exceeds the elastic limit. Once the elastic limit is reached the material plastically deforms with additional application of force until fracture. This is not the case for very brittle materials which fail without demonstrating plastic deformations.

The ability to resist elastic deformation is defined as Young's modulus (E), which is the tensile stress ratio to tensile strain and given by eq. (1.1.

$$E = \frac{\sigma_{tensile}}{\varepsilon_{tensile}} = \frac{\left(F/_A\right)}{\left(\Delta L/_{L_0}\right)} \tag{1.1}$$

where $\sigma_{tensile}$ is the tensile stress given as the force (F) ratio to the cross-sectional area (A), $\varepsilon_{tensile} = (L - L_0)/L_0 = \Delta L/L_0$ is the tensile strain which is the difference between the length of the loaded sample (L) and the original length (L_0). Experimentally, this can be calculated from the gradient of the curve (see Figure 1.4) within the elastic limit or between specified values defined by standards such as ISO-527-1.[4]

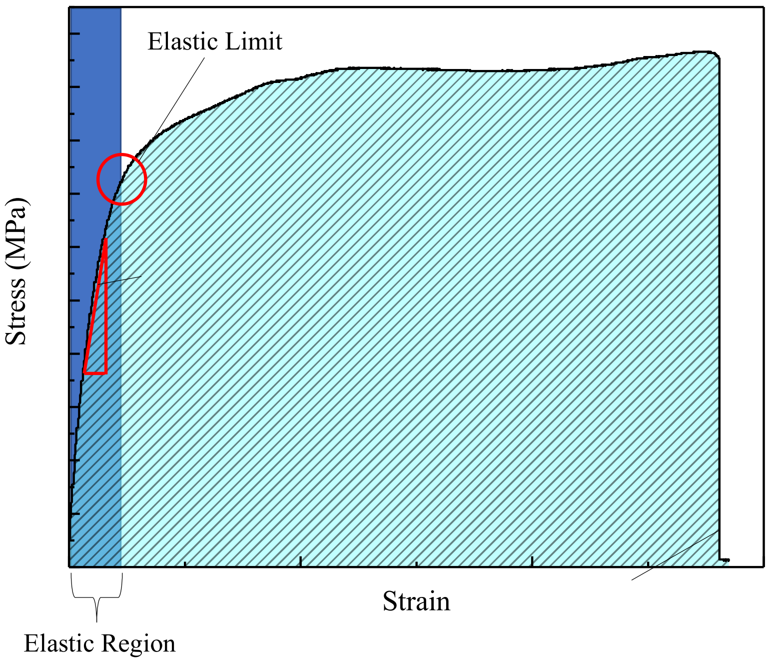

Figure 1.4. Typical stress-strain curve of a commercial polyurethane showing Young's modulus (E), and Toughness which is represented by the shaded area under the stress-strain curve

Another critical property to measure is toughness. Defined as the ability to absorb energy and plastically deform without fracturing, toughness is calculated by integrating the area under the stress-strain curve (eq. 1.2) until failure (see Figure 1.4).

$$\boldsymbol{Toughness = \int_{0}^{\varepsilon_f} \sigma d\varepsilon} \qquad (1.2)$$

Conversely to strength, which indicates the force a material can support, toughness indicates how much energy a material can withstand before failure. The units for toughness are Joules per cubic metre (J m^{-3}).

1.2.2 Dynamic mechanical thermal analysis - storage and loss moduli (E' and E")

In contrast to the solid elastic component measured only by tensile elastic modulus testing, the dynamic moduli of storage and loss modulus is a measure of the elastic and viscous part. For an ideal fluid when a force is applied a purely viscous behaviour occurs whereby the fluid is displaced, and the energy dissipated as heat. However, polymers possess a combination of both elastic and viscous behaviours and defined as viscoelastic. The degree of viscoelasticity varies and is dependent on parameters such as cross-link density, polymer processing, and additives or fillers.

Dynamic mechanical thermal analysis (DMTA) is employed to measure the viscoelasticity in materials. This technique can determine the inelastic, viscous component through varying the oscillation of a fixed frequency. DMTA enables the ability to investigate the impact dissipation of materials through measuring the storage modulus and the loss modulus. The storage modulus focuses on the elastic component and measures the stored energy as a function of the temperature or frequency. Therefore, the loss modulus represents the viscous component, which is the material's ability to dissipate energy as heat, like an ideal fluid through molecular motion. Through the combination of these two measurements, the viscoelastic behaviour can be determined by calculating the tangent of the phase difference (tanδ) enables the quantification of the impact dissipation performance of a material.

DMTA is also more advantageous than standard tensile testing because it operates within the linear viscoelastic region measuring viscoelasticity rather than just elasticity. This enables it to be more sensitive to the material structure while determining impact dissipation performance.[5]

1.2.3 Glass transition temperature (T_g)

The glass transition temperature (T_g) is defined as the point at which a polymer's structure migrates from a glassy to an amorphous system.[6] This transition within the polymer above the T_g makes the network softer and more pliable, therefore improving properties such as impact dissipation performance. Because of its kinetic nature, the T_g is sensitive to heating/cooling rates and frequency. This means that the intended end-use applications should be considered when designing materials to ensure suitability. Also, the glass transition temperature can be determined by using DMTA or differential scanning calorimetry (DSC) which is detailed further in Chapter 2.

1.2.4 Material Stiffness

Stiffness is an extensive property that represents the extent at which a body resists deformation. Evaluation of stiffness therefore does not assist in understanding changes in the constituent material but instead the sample preparation. However, with uniform sample preparation the relation between axial stiffness (k) and intensive properties such as elastic modulus (E) can provide further understanding (see equation1.3) .

$$k = E \times \left(\frac{A}{L}\right) \tag{1.3}$$

where A is the cross-sectional area and L is the length of the body. Because of the relationships stiffness has with intensive properties, O'Carroll *et al*., reported that an ideal coating candidate for leading edge erosion protection should seek to reduce the stiffness which would be related to the implications on the storage modulus and the acoustic impedance through the sample.[3] Stiffness can be measured using tensile testing techniques and also through compressive testing using instruments such as nanoindentation.

1.2.5 Material Hardness

Hardness is an intensive property that represents a materials' resistance to localised plastic deformation. Been an intensive property, hardness generally characterises the strength of the intermolecular bonding structure. Hardness measurements can be determined through scratch, indentation, and rebound measurements. Scratch testing is well known through its application to the Mohs scale which qualitatively grades minerals on a scale of 1 to 10. Rebound testing in contrast measures the height of the rebounded hammer and is related to elasticity. Indentation testing which is conducting using instruments such as nanoindentation can provide a quantitative and highly localised compressive force to the sample. Traditional instrumented indentation hardness (H_{IT}) is the measure of the resistance to plastic deformation and is given by

$$H_{IT} = \frac{F_{max}}{A_p} \tag{1.4}$$

where F_{max} is the peak load and A_p is the projected area. There are two opposing discourses within the literature with regards to the materials design of impact dissipation. Several design strategies employ that an increase in material hardness is beneficial for energy dissipation with many adding fillers to polymer composites to enhance the virgin polymer's hardness. This strategy is effective through the assumption of the intensive nature of hardness to resist large, applied loads through the creation of very strong intermolecular bonds. However, limitations are present with this strategy when repetitive applied loads are present. Due to the correlation between hardness and stiffness generally a hard polymeric material possesses a three-dimensional architecture of covalent bonds which during an applied force can be amplified at structural defects which arose in fabrication or previous impacts. Therefore, a compromise in material hardness to maintain a higher degree of material elasticity could be more desirable when designing impact dissipation materials.

1.2.6 Creep

Creep is a material property that defines how readily a material will undergo plastic deformation under constant mechanical stress. There are many mechanisms when studying creep, with each dominating under different activation conditions (stress, temperature). Creep is a time-dependant characteristic rather than activated instantly upon an applied load.

1.3 Polymer matrix composites

Composites are defined as two or more constituents which possess different chemical, and or physical phases. Distinctly different from a blend, the constituents within a composite remain recognisable while when observing blends, it does not.[7] Composites consist of a filler as the discontinuous phase and a matrix that is the continuous phase.

The ability to achieve new, and enhanced material properties through the preparation of composites, which would otherwise not be obtained from the individual constituents enables composites to dominate the current materials science landscape. Through the diversity of constituent combinations that can be achieved, composites are generically classified into three main categories (see Figure 1.5); structural, fibre, and particulate reinforced polymer composites.

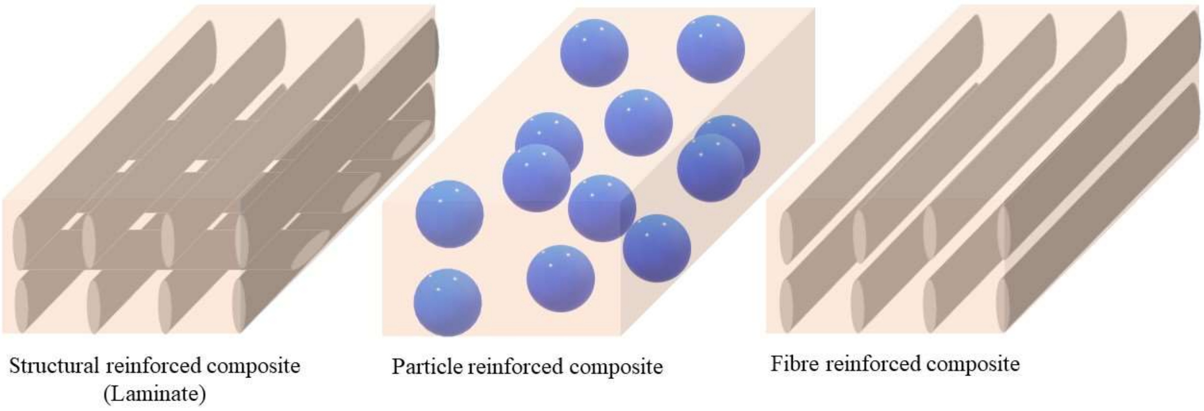

Figure 1.5. Generic examples for the three main types of polymer composite showing the stacking of fibres parallel to each other to create a laminate structure, blue spheres representing particles in a matrix and an example of a fibre reinforced polymer unidirectional reinforcement.

Structural reinforced composites are defined by how the constituent materials are arranged structurally within the composite. Examples such as laminates and sandwich composites are extensively used within the automotive sector,[8] and in the fabrication offshore wind blades.[9]

Whereas fibre reinforced composites are fibrous and can possess either long-range order as shown in Figure 1.5 or short-range order such as chopped fibres which give multiaxial enhancement compared to long-range systems limited by the fibre's orientation. Examples of fibre reinforced composites include steel-reinforced concrete.

Particulate reinforced composites by default form the broadest group of composites due to the diversity of particle fillers available. In this category, fillers are sub-divided based on size into large particles (> 30µm), reinforcing fillers, and nanofillers (< 100 nm).[10]

Examples of particle reinforced composites include silica and graphene reinforced composites.[11,12] For the purposes of this thesis particulate fillers will be focused on.

1.4 Graphene-based materials as a filler

Graphene-based materials (GBMs) are two-dimensional carbonaceous-based materials which have risen to prominence over the last two decades.[13] A constituent of graphite, a natural mineral occurring in metamorphic rocks, graphene is defined as a monolayer of characteristic sp^2 hexagonally arranged 'chicken wire' illustrated in Figure 1.6.[14]

First isolated in 2004 by Geim, and Novoselov at the University of Manchester using Scotch™ Tape to micromechanically cleave a piece of high-purity crystalline graphite.[15] Through their contributions and their resultant 2010 Nobel prize; graphene and other 2-D variants have come to dominate the field of materials chemistry.[16,17]

Determined by graphene's superlative properties it has been reported to exhibit enhanced mechanical,[18–21] electrical,[22,23] and thermal properties,[24–26] which has enabled its monopolisation into many applications such as lightweight composites,[27] devices, and fire retardancy.[28]

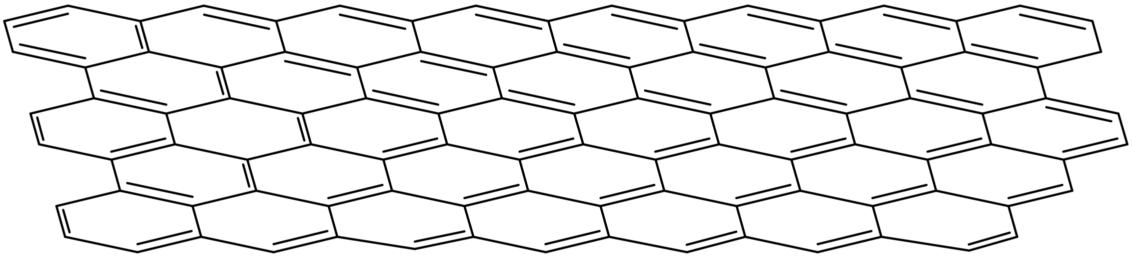

Figure 1.6. Chemical structure of graphene showing the connecting aromatic carbon rings, with no reactive functional groups present, results in an sp^2 hybridised planar structure providing the truly two-dimensional material.

Summarised in the Nobel prize lecture, graphene, "is so strong that a 1 m^2 hammock, no heavier than a cat's whisker, could bear the weight of an average-sized cat without breaking." [29] These properties exhibited by graphene make it an ideal candidate to formulate mechanical energy dissipation composites. Extensive studies have concluded an intrinsic tensile strength of 130.5 GPa and Young's modulus of approximately 1 TPa declaring graphene the strongest material ever tested.[30]

Graphene, which is prepared on larger scales using techniques such as chemical vapour deposition to produce defect-free flakes,[31,32] has enabled it to dominate the field of electronics through its zero band-gap properties. However, due to the absence of functional groups in graphene, it is prone to phase separation from the matrix by stacking to produce graphite, reducing the enhancements mentioned above. Therefore, the functionalisation and or incorporation of graphene derivative structures such as graphene oxide or other graphene oxide-based materials (GOBMs) as a reinforcement filler in polymers are of great interest.[33,34]

1.4.1 Graphene oxide

Graphene oxide is an oxidised variant of graphene which possesses oxygenated epoxide and hydroxyl moieties on the basal plane and carboxyl groups along the sheet edges as illustrated in Figure 1.7.[35,36]

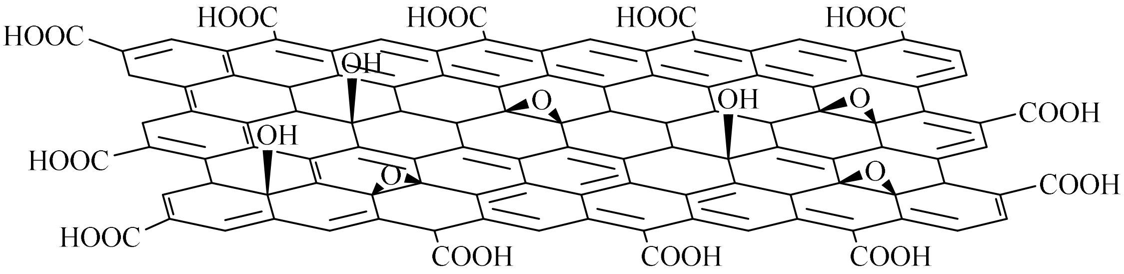

Figure 1.7. Graphene oxide structure based on the Lerf-Klinowski model

The origin of graphene oxide's functional groups is from when high purity crystalline graphite undergoes oxidation and exfoliation steps to produce it. As a result of graphite's geological nature, graphene oxide does not possess a standardised empirical formula, meaning it is classified as a berthollide.[37] Through the oxygenated moieties, it enables chemists to functionalise through different routes such as electrostatic adsorption,[38,39] covalent functionalisation with amines,[40,41] and isocyanates.[20,42,43] The production of graphene oxide used in this Thesis is through a proprietary modified Hummer's chemical exfoliation method by Graphitene Ltd.

The Hummer's method takes its namesake from the chemists W. M. Hummers Jr. and R. E. Offeman, who developed the preparation back in 1958.[44] The method is a chemical exfoliation process whereby the potent oxidising agents; potassium permanganate ($KMnO_4$), sodium nitrate ($NaNO_3$) and concentrated sulfuric acid (H_2SO_4) are added to a solution of natural graphite as Figure 1.8 illustrates. The oxidising agents lead to graphite oxide production, the stacked GO structure, which is then exfoliated to form few-layered graphene oxide. This undergoes further exfoliation methods to yield the desired monolayer graphene oxide. This method's ease and feasibility are adopted by industry, with many proprietary adapted methodologies developed using the Hummer's method as their basis.

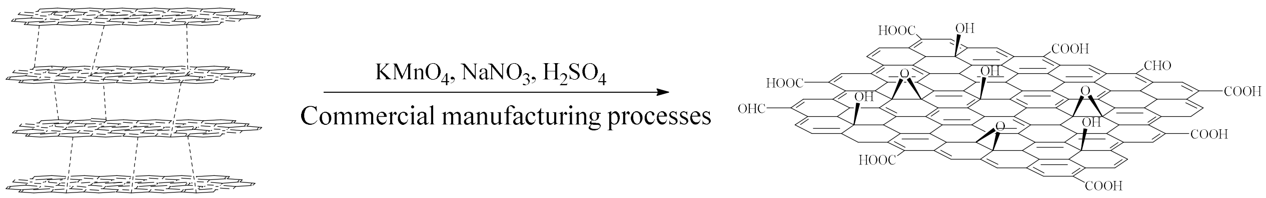

Figure 1.8. Summary of the Hummer's method, whereby the 4-layers of graphene intermolecularly hydrogen-bonded are used to illustrate graphite for clarity purposes. Industrial manufacturing processes is the collective given to company-specific methods used to produce their target products.

However, a disadvantage to this method it can result in trace impurities such as manganese complexes (MnO_2), which are sometimes not identified due to them being below the limit of detection in specific characterisation methods. In generality, these trace impurities perform in a spectator capacity. Although, such contaminants have recently been realised as the foundation of the superior catalytic properties of the oxidative reduction reaction rather than the reduced graphene oxide.[45] Therefore, such conditions must be considered before the assumption of the reported superlative features described. This method does not produce a monodisperse sheet size due to the non-selective reactions between the oxidising agents and the graphite leading to a lateral flake size distribution.

1.4.2 Reduced graphene oxide

Reduced graphene oxide (rGO) is another variant of graphene oxide-based materials defined as having a lower carbon to oxygen ratio (C:O) than graphene oxide.[46] Structurally rGO follows the same Lerf-Klinowski model as with GO (see Figure 1.7), with the only variation being a significantly lower degree of oxygenated moieties, as shown in Figure 1.9.

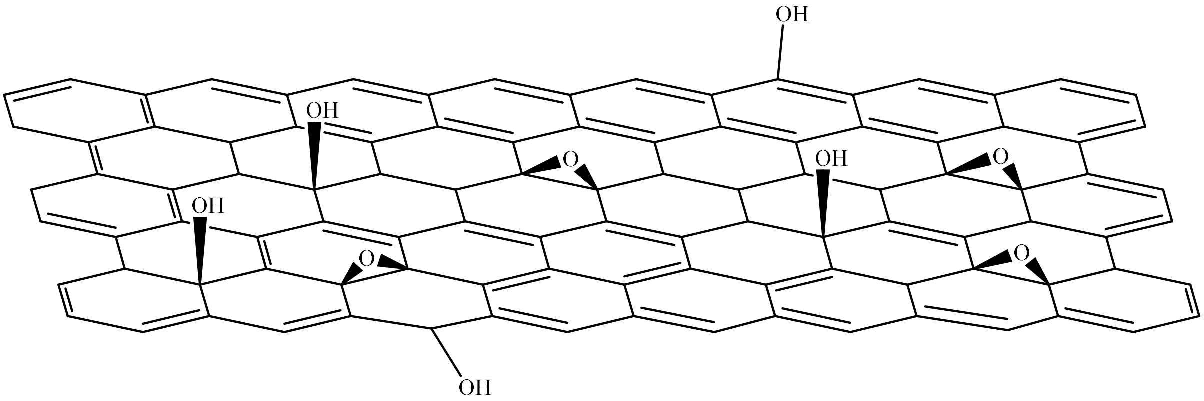

Figure 1.9. Chemical formulae for reduced graphene oxide show reduced oxygenated moieties than graphene oxide in Figure 1.7. The sheet edges are the first functionalities to reduce with the basal plane moieties being more stable to reduction.

Commonly used as an intermediate route from functionalised graphene oxide to functionalised graphene, rGO can be reduced from GO by thermal,[47–49] electrochemical,[50] and chemical reductions using hydrazine.[50–52] Through the reductive transformation from GO to rGO specific properties are restored such as thermal and electrical conductivity,[51,53,54] and hydrophobicity,[55,56] resulting from the increasing restoration of sp^2 carbon character which explains graphene's superlative properties.

The production of reduced graphene oxide used in this Thesis is again through a proprietary thermal reduction process. The general thermal reduction of graphene oxide to produce reduced graphene oxide is conducted at elevated temperatures (c. 325 °C), at atmospheric pressure for a defined time.[48,54] The effect of heat leads to thermal expansion of the sheets with the sheet edges reducing before the basal plane functionalities. An advantage of thermal reduction enables a more controllable reduction process in comparison to other techniques leading to improved purity.[57]

1.4.3 Diversity of graphene oxide-based fillers

There are numerous methods to produce graphene oxide, which results in differing degrees of oxidation and functional groups being present.[58–61] Also, just like graphene oxide, the processing of reduced graphene oxide infers different C:O ratios which therefore causes different product variants and resultant properties.[62] Therefore, to overcome the diversity of graphene oxide-based materials, reporting the physical properties is paramount to ensure reproducibility when combined with a polymeric matrix.

1.5 Polyurethanes as a matrix

Market analysis shows that polyurethane coatings are the preferred protective coating for LEE in offshore wind. A long-standing polymer since its discovery by Bayer in 1937, the polymerisation of polyurethane (PU) traditionally takes place between the reaction of a diol and diisocyanate as Figure 1.10 illustrates. By definition due to no small-molecule expulsion, this reaction is a form of addition polymerisation, despite it following a step-growth mechanism.[63]

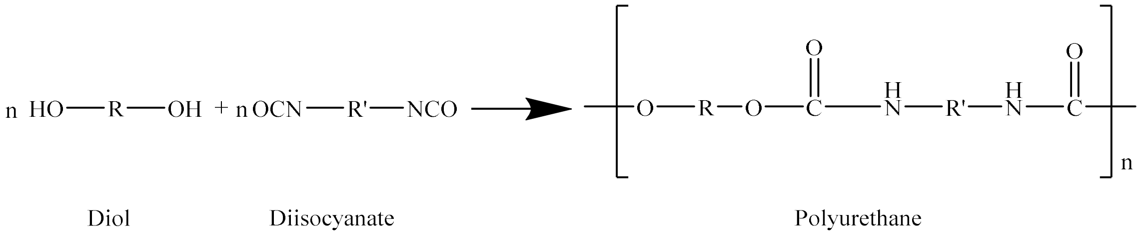

Figure 1.10. The general equation for polyurethane synthesis

Polyurethanes exist in all three forms of polymer architecture, and can be tuned by varying the diol constituent. The use of a linear diol, as shown in Figure 1.10 would result in a thermoplastic PU forming because of intramolecular hydrogen bonding being the architectural driver to create a dynamic network upon heating. Furthermore, the use of polyfunctional alcohols predicts the formation of a thermoset due to the covalently bound 3D network, which does not possess any dynamic character. Finally, an elastomeric PU can be achieved by manipulating the degree of the 3D network, with sub-ambient glass transition temperatures (T_g) observed. This capability for constructing differing architectures allows PU to be incorporated into a broad range of different applications from fire retardancy foams to impact resistance.[64]

Most commercial PU are incorporated as a copolymer, enhancing the material properties of the other copolymer. The use of polymeric alcohols (polyols) are common and can be tailored to the desired physical properties required. For example, the use of a polyether, which is hydrophilic, allows the PU to become more susceptible to moisture absorbance than polyester as the large aliphatic chains present can create a hydrophobic environment. The copolymer structure is observed through characterisation techniques such as scanning electron microscopy and differential scanning calorimetry that phase separations occur along the polymer backbone.

Due to the ability to form arrays of intramolecular hydrogen bonding and the urethane functionality through the carbonyl and amine hydrogen, the extended aliphatic chains render hydrogen bonding negligible. Therefore, the urethane region is described as hard and the polyol being the soft region. These terms also demonstrate chain mobility in the soft region and rigidity in the hard region. In particular, increasing the hard region length has led to tensile improvements in GOPU composites.[65] To further enhance the mechanical properties of a polymer, many factors need to be addressed; however, in generality, the following conclusions can be drawn: (i) Shorter chain lengths have a lower glass transition temperature (T_g); (ii) In-plane hydrogen bonding and at right angles create a hard and strong material. Therefore, polyurethane architectures' versatility can enable the fabrication of effective polymer matrix composites if the filler and matrix can impart some of their properties onto the other constituent.

As a result of this interest in incorporating graphene within polymeric materials for applications such as weather erosion prevention, Nuraje *et al.* reported the effect graphene dispersions on PU coatings' weathering.[66] The work investigated the effect of UV, water, and oxygen on coating degradation with and without the addition of graphene.

The work demonstrated by thermo-mechanical measurements that the polymer phase was stiffened with the introduction of GO and rGO.[54] Furthermore, the stiffening of the matrix, within the elastic region, was quantified by higher storage moduli and lower tanδ. Additionally, the PU rich phases shift to lower T_g temperatures and the PES rich phase increases in temperature. This was explained by the subtle differences in polymer architecture, whereby the PES is more mobile and lacks the intermolecular bonding, which is present in PU. Conversely, Nguyen *et al.* investigated the physical properties of thermoplastic PUs reinforced with functionalised graphene sheets (FGS).[67] The results showed that the "*dynamic force is enhanced at T_g in the presence of FGS*" [67]. This was postulated to be due to reduced crystallinity within the soft segments.

1.6 Factors affecting polymer matrix composite properties

As previously mentioned, the ability to design and fabricate an effective composite relies on the filler's capability and the matrix to transfer energy to one another. One of the simplest methods to describe the reinforcement achieved from a high modulus filler into a low modulus matrix is through the rule of mixtures equation (1.5).

$$\boldsymbol{E_c = E_f V_f + E_m(1 - V_f)} \tag{1.5}$$

where E_c is the theoretical elastic modulus of the composite, E_f is the elastic modulus of the filler, E_m is the elastic modulus of the matrix, and V_f is the volume fraction of the filler. The model assumes a uniform distribution of the filler and perfect bonding between the filler and the matrix. Furthermore, it is also assumed that the matrix is free of voids.[68]

The rule of mixtures should always be considered an approximation due to the assumptions made, but suitable predictions can be made at low-loadings. Therefore to get the most significant enhancements in composite reinforcement, the GOBM fillers ideally need to be aligned in the direction of strain.[69]

As the rule of mixtures assumptions suggest a matrix that is void-free to deliver such reinforcements. The introduction of voids into the polymeric matrix is commonly observed by air bubbles or phase separations in the composite. Air bubbles can be introduced into polyurethanes by adding blowing agents or poor mixing techniques. The use of blowing agents within polyurethanes is used by the introduction of moisture within the monomeric mixture to make foams. During polymerisation, the moisture competitively reacts with the isocyanate functionality to produce a carbamic acid intermediate that decarboxylates, resulting in carbon dioxide evolution.[70,71] The evolved carbon dioxide trapped within the mixture results in air bubbles (voids) in the final polymer. To overcome this requires careful storage and mixing of all the monomers to prevent moisture ingress into the polymerisation is critical.

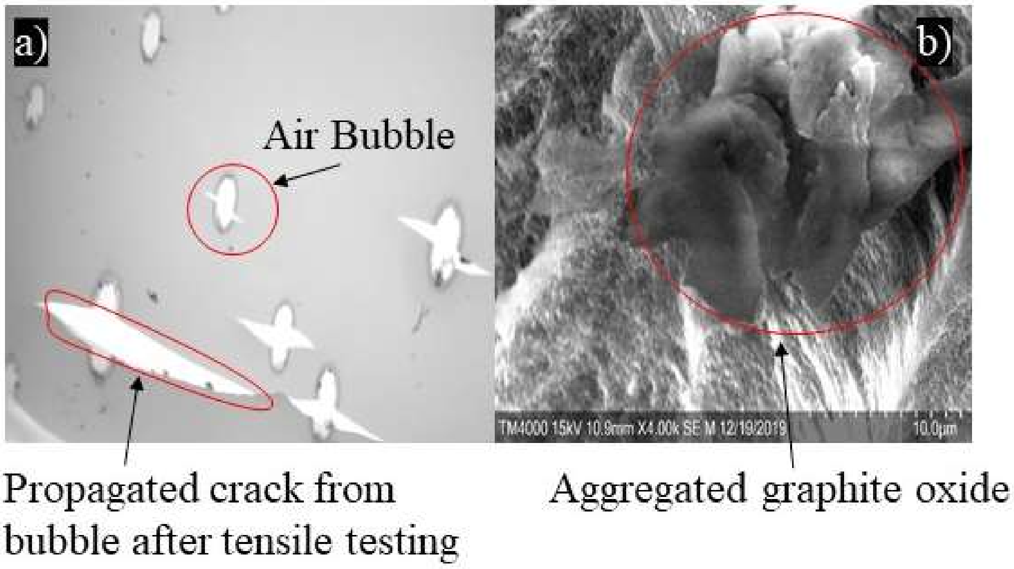

Figure 1.11. Defect polymers and composites which would have led to poor mechanical performance. a) The effect of air bubbles after tensile testing shows that they act as nucleation sites for crack propagation. b) The effect of ineffective filler matrix adhesion and dispersion has led to the GO filler stacking into one microphase and the matrix into another causing filler-matrix separation.

Furthermore the presence of air bubbles within the polymer acts as nucleation sites for fracture propagation to occur while under load, as shown by Figure 1.11a, which leads to premature failure of the material.

Another aspect that can lead to poor matrix performance is the monomers' inhomogeneity during polymerisation (see Figure 1.11b). As aforementioned in the section above, polyurethanes possess hard and soft regions which dictate their mechanical performance. Therefore, microphase separations because of inhomogeneity by poor mixing or incorrect stoichiometry can completely alter the final polyurethane. Also, due to polyurethanes following a polyaddition mechanism stoichiometry is critical to ensure reproducibility between batches.

The final and most crucial aspect of the composite design is suitable filler-matrix interfacial adhesion. For successful interfacial adhesion, the surface characteristics must be compatible to provide enough energy (W_a) to overcome the individual constituent interfaces' energy requirements as **(1.6)** illustrates for two different material bodies in a vacuum

$$\boldsymbol{W_a = \sigma_Y + \sigma_Z - \sigma_{YZ}} \tag{1.6}$$

where σ is the interfacial energy and subscript Y and subscript Z refers to the material Y and material Z respectively.

Ensuring the filler's proper dispersion within the matrix and suitable adhesion minimises filler-matrix separation, resulting in filler aggregation, as shown in Figure 1.11b. In particular, due to the large specific surface area of GOBMs destabilisation, aggregating into stacked graphite oxide structures leads to a decrease in mechanical performance.[20,72,73] Whereas on the other hand, the wrinkled morphology of the GO, due to the resultant sp^3 hybridisation, further facilitates the dispersion of GO within the PU matrix through strong adhesive forces.[74]

Therefore, the interfacial adhesion between the filler and the matrix must be as intimate as possible to ensure that the constituent properties' compounding effect remains. Any regions of imperfect wetting lead to the same responses observed by air bubbles. Therefore, these zero strength zones must be mitigated by adopting a suitable strategy to optimise the filler matrix adhesion.

1.7 Strategies to overcome filler-matrix adhesion problems

Many different strategies have developed to effectively disperse the filler throughout the matrix and overcome phase separations (see Figure 1.12).

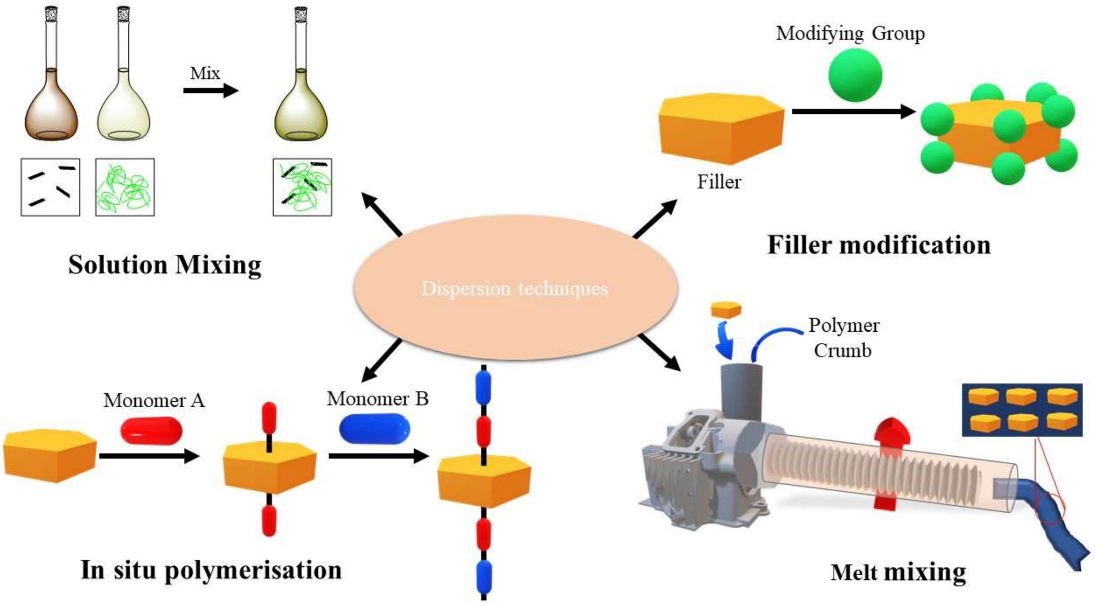

Figure 1.12. Overview of the different techniques used to disperse fillers in polymer matrices to make polymer matrix composites.

1.7.1 Solvent Mixing

Solvent mixing is the most facile technique whereby the filler along with a compatible solvent are combined to make a suspension before they are mixed with the polymer marix.

As expected, the addition of solvent reduces the system's viscosity, enabling the solvated polymer composite to be mixed effectively. The resultant composite suspension is then concentrated down by evaporation of the solvent, usually within a mould until the final polymer composite results. This technique owes itself to its simplicity and lack of specialist equipment, however, a significant drawback is ensuring that a compatible solvent can be found for the filler and the matrix and successful evaporation of the solvent to avoid plasticity.

This methodology is seen widely through the literature as its ease of filler incorporation by diluting the polymer to ease chain mobility and enable the introduction of fillers such as GO into the matrix easily. Solvent mixing can also be utilised to exfoliate GOBMs using methods such as ultrasonic dispersion[20,75,76] or charge stabilised aqueous dispersions.[54]

Because of the necessity to exfoliate GOBMs using solvents, many studies have investigated the stability of GOBMs in different solvents. Figure 1.13, showed that polar solvents are favoured for good dispersion.[77]

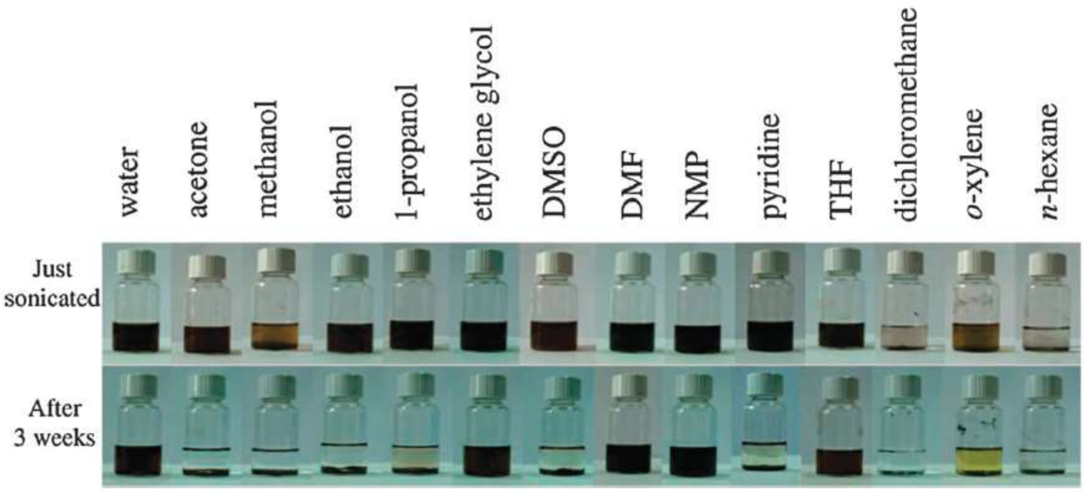

Figure 1.13. Dispersion of GO in 13 organic solvents by sonication and the extent of sedimentation after 3 weeks.[77] (The original journal notes that the yellow colour of the o-xylene after 3 weeks is due to the solvent itself)

Because of the large surface area and functionalities on GOBMs, bulk force interactions like Van Der Waals lead to attractive forces that result in sheet stacking. Therefore, it is critical to find compatible solvents that can interact at these functionalities to prevent Van Der Waals stacking forces to give a stable exfoliation which is paramount to maintaining 'graphene' characteristics rather than graphitic structures.

1.7.1.1 DVLO Theory

The dispersion of graphene oxide-based materials into a solvent or polymer matrix results in a colloidal system formation. Colloids are micro-heterogenous systems that possess a continuous phase and a discontinuous phase whereby the discontinuous phase retains some of its bulk properties. These systems generally range between 5 nm and 5 µm with particles larger than 5 µm defined as coarse particles.

The Derjaguin, Landau, Verwey and Overbeek (DVLO) theory, developed by these four scientists provides the two main fundamental concepts in colloid science. The theory is applicable when systems are in the presence of polar solvents in order to form an electric double layer which is an electroneutral surface charge originating from counter ions adsorbing at the surface The theory describes those interactions occur between macroscopic particles' surfaces and that they possess both Van Der Waal's and electrostatic contributions. The total interaction energy (U) can, therefore, be defined as the sum of the attractive Van Der Waal's energy (U_{vw}) and the repulsive electrostatic energy (U_{el}). Each component is also determined as a function of the particle distance (D), see eq. 1.6.

$$\boldsymbol{U(D) = U_{el}(D) + U_{vw}(D)} \qquad \textbf{\textit{(1.7)}}$$

The oxygenated moieties on graphene oxide-based materials result in dissociative behaviour of these surface groups in an aqueous medium to charge-stabilise the sheets. This behaviour is what demonstrates GO's superior stability in purified water systems.[77–80] This can also be achieved by using ionic surfactants which are widely used to support dispersion, particularly during the exfoliation preparations of graphite.[81–83]

On the other hand, charge-stabilised systems can be destabilised by adding electrolytes, using an electrolyte of higher valency, or neutralising the surface charge. Therefore, the cationic impurities sometimes present from preparatory techniques can impact the system's stability and consequent material properties.[45,84]

Whereas the Van Der Waal's forces are always present when surfaces are in close contact and cannot be tuned like electrostatic interactions.

Whilst the classic DVLO theory can be applied to many colloidal systems, they can be deviations which extend the theory into non-DVLO surface forces. These extensions to the classical theory are related to steric and solvent association forces. In some circumstances, these non-DVLO forces dominate the stability of the investigated system.

Steric stabilisation forces occur when larger chains such as polymers are grafted or adsorbed to the particle surface. This technique is of particular industrial importance and stabilises the system through maintaining a sufficient inter-particle distance so that Van Der Waal's attraction is negligible. The system can be improved by either increasing the inter-particle distance by increasing the chain length or increasing the grafting or adsorption density.

Comparison of charge and steric stabilised systems demonstrates that steric-stabilised designed systems are more versatile due to their insensitivity to electrolyte concentration, effectiveness in both aqueous and non-aqueous environments, and useful over an extensive volume fraction range. Whereas charge stabilised systems are sensitive to ionic strength and effective only for relatively dilute colloid systems.

1.7.2 Melt Mixing

Conversely, melt mixing requires a heated polymer extruder where the filler and polymer crumbs are combined and mixed using a threaded central rod. The viscous composite mixture then travels down the extruder where it is extruded into a filament for applications such as 3D printing. One major disadvantage of this system is that it requires thermoplastic polymer materials and relies on properly mixing the filler and matrix within the threaded chamber. Furthermore, it is expected that these systems do not undergo chemical reactions during processing, so the filler-matrix adhesion is solely reliant on short-range non-covalent interactions such as Van Der Waals.

Therefore, filler modification and in situ polymerisation present the best opportunities to create polymer composites with more significant enhancements. Therefore, this Thesis focuses on filler modification and in situ polymerisation in more detail rather than melt mixing and solution mixing.

1.7.3 In situ polymerisation

In situ polymerisation appears to be the most favourable strategy for enhancing mechanical properties, with the high levels of functionalisation on the GO surface enabling significant interactions between the GO and the urethane groups during polymerisation.[23] Furthermore, these interactions reduce polymer chain mobility, thus increasing the moduli of the nanocomposites.[33,42,85]

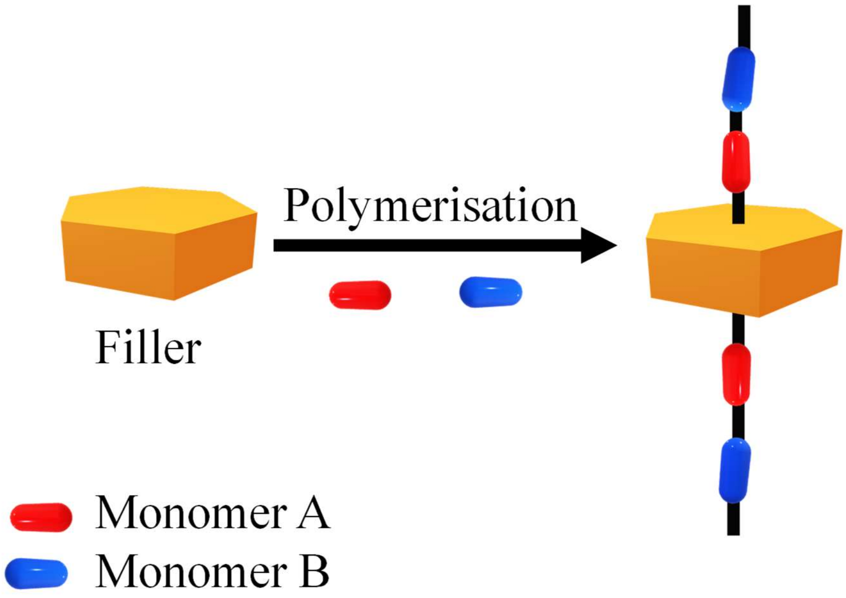

Figure 1.14. Cartoon schematic to illustrate the principles around in situ polymerisation of graphene oxide.

To overcome the interfacial interactions between the matrix and the filler, the prospect of *in-situ* polymerisation, whereby GO is chemically functionalised with monomers and polymerisation occurs outwards from the GO's basal planes to produce the polymer composite. Theoretically, this method should produce a homogeneously disperse polymer composite due to the polymer chains sterically stabilising the GO sheets, preventing aggregation. As a result of this, homogeneity and stabilisation, the mechanical properties compared to melt blending and solvent mixing methodologies are further improved.[25]

One example of this is seen by Li *et al.* with the *in-situ* polymerisation of a PU/GO/EP nanocomposite, as shown in Figure 1.15. which demonstrated enhanced thermal and mechanical properties.[25] The graphene oxide was reacted with the diisocyanate prepolymer, which functionalises through the hydroxyl moieties on the basal planes. The resultant isocyanate active GO was then polymerised with a poly(tetramethylene glycol) $\bar{M}_n = 2000$ gmol^{-1} to yield the PU/GO polymer before adding the epoxy resin and curing agent.

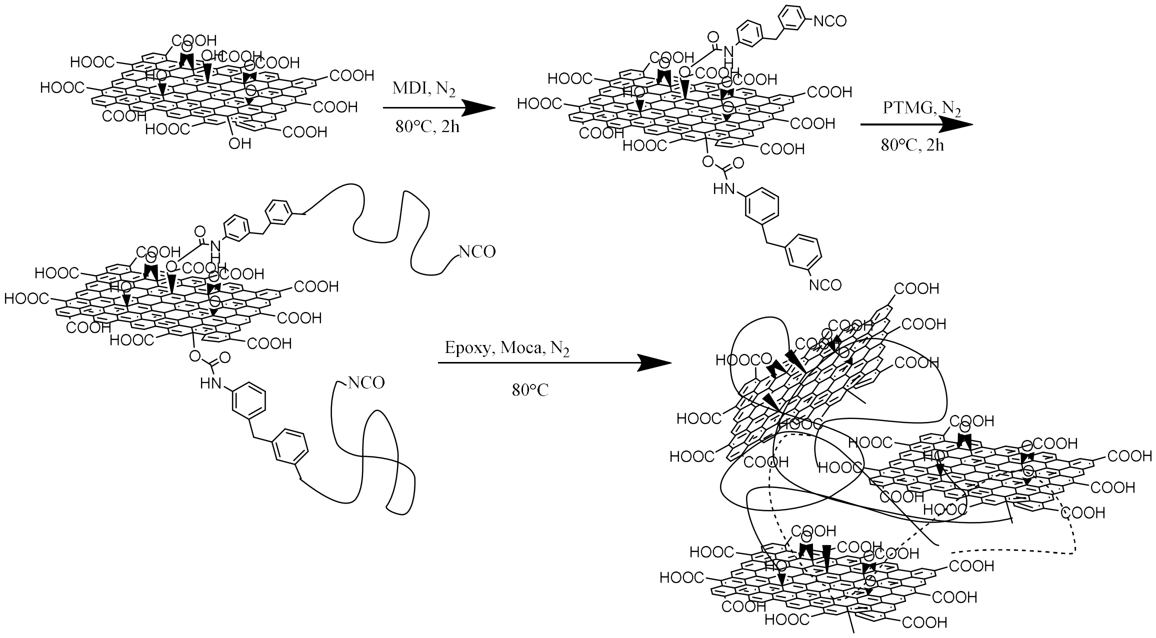

Figure 1.15. Scheme 1 from Li's work,[25] showing the in situ polymerisation of graphene oxide into a polyurethane/epoxy resin.

Ren *et al.* also adapted the in-situ polymerisation of GO with cyanoesters and investigated their mechanical properties as a function of GO incorporation.[20] The work again reported that the introduction of GO into the a polyurethane matrix improved the mechanical properties with 0.7 wt.% GO producing a flexural strength of 128.1 MPa and an impact strength of 11.5 kJ m^{-2}. Additionally, it was noted that over 0.7 wt.% the mechanical properties decreased due to the overloading of GO resulting in aggregation. As discussed, the surface's regularity reduces and becomes more irregular, which is advantageous for crack propagation reduction due to the open regions. However, the work notes that the higher loads of GO can introduce areas that could become stress concentrators.[20]

Conversely, Shamsi *et al.* reported that the addition of GO enhanced the hardness and low resistance to abrasion,[23] which are also observed in traditional silica nanocomposites.[86]

However, one limitation to this method is the absence of reaction control, which could lead to monomers not reacting on both sides of the basal plane in GO or multiple monomers reacting on one side. This lack of control can affect the filler matrix adhesion and the final composite product. To overcome another method is to modify the filler with a functionalisation that is complementary to the polymer matrix.[87] One possible method to overcome this is hyperbranched polyurethane systems, which have shown a 5-fold increase in Young's modulus, attributed to the branching within the matrix, preventing GO aggregation.[21] However, this can lead to thermoset and brittle properties if not refined.

1.7.4 Filler modification

The desire to exploit the superlative properties of pristine graphene reported within the literature,[68,88] has motivated extensive research into many functionalisation methodologies. In particular, graphene oxide with epoxides and hydroxyls in the basal plane and carboxyl groups residing along the sheet edges,[35,36] offers various reaction pathways.[37] Because of this, a myriad of strategies ranging from electrostatic interactions,[89] polydopamine grafting,[90,91] and covalent functionalisations are achievable.[92] Prevalent amongst the literature, the covalent functionalisation of graphene oxide utilises reactive amine groups to afford anti-corrosion properties.[93–95].

On the other hand, graphene oxide reactions with isocyanates are also another popular reaction protocol reported in the literature. The reactivity of the hydroxyl groups and the isocyanate functionality enables researchers to tune the filler-polymer matrix compatibility,[87,96–98] and dispersibility.[43] Through this reactivity pre-functionalisation of the other terminus of a diisocyanate offers the possibility of intermediate units for either bridging other functionalities onto them, [99] or using them for directed self-assembly.[91]

1.7.5 Ureidopyrimidone

The ureidopyrimidone motif (see Figure 1.16), was first reported by the Meijer group in 1998,[100] and has extensively been investigated in many supramolecular designs.[101,102] The ability to form a donor-donor-acceptor-acceptor (DDAA) hydrogen bond dimer, owing to a stable dimerisation constant $(3.6 \times 10^7 \mathrm{M}^{-1})$,[100,103] has enabled smarter supramolecular polymeric systems, exhibiting properties such as self-healing,[104–107] pre-emptive stress and adhesion,[108–110] and directed self-assembly.[111,112]

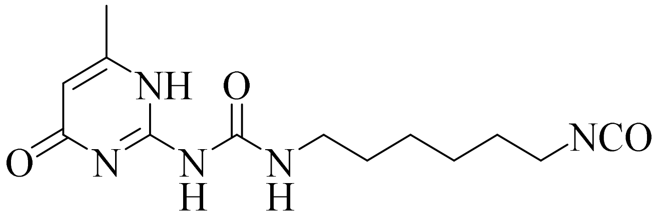

Figure 1.16. The ureidopyrimidone motif (UPyNCO) is used to synthesise self-assembly and self-healing supramolecular polymer systems by exploiting the reactivity of the terminal isocyanate group.

The last two decades have seen work undertaken to utilise UPy into polymers to enable structural supramolecular systems and more recently self-healing. At present, within the literature, the incorporation of UPy into polymeric systems is achieved by two different strategies: as a telechelic unit or by side group attachment on the polymer backbone.[113]

Examples of work such as that undertaken by Sontens *et al.,* whereby thermoplastic elastomers modified with UPy moieties were incorporated into the hard segment by functionalisation with diisocyanates.[114] The work concluded that the enhancement of mechanical properties was achieved owing to the nanocrystalline structures within the hard segment microphase resulting from UPy dimerisation.[114] This successful incorporation of UPy into the backbone enables the ability to produce enhanced mechanical properties as the mechanical energy can be dissipated through the matrix because of the flexible interphase, created by the dimerisation.

Furthermore, in 2009, Wietor *et al.* published results on the incorporation of UPy into polyurethane-polyester (PUR-PE) matrices and measured material strength and toughness properties as a function of UPy percentage concentration as shown in Table 1.1.[109]

Table 1.1. Mechanical properties of the incorporation of UPy into PU/PE matrix

UPy content (%)	DMA T_g (°C)	Storage modulus, E' (MPa)	Cross-link density, ν_e ($\times 10^{-6}$ mol cm^{-3})
0	44	7.19	739
10	48	4.24	604
20	50	2.96	299
30	54	2.24	224
40	53	0.74	74

The work found that the presence of UPy at high concentrations resulted in brittle properties, which prevented DMA data from being obtained, hence omittance of mechanical data for 47, 53 and 100% UPy concentration. Furthermore, it was observed that the addition of UPy, relaxed the stresses occurred during the preparation of coatings such as film shrinkage during curing. This led them to conclude that the addition of UPy, provides an autonomous pre-emptive healing approach for coating applications.

Separately, Faghihnejad *et al.* demonstrated that the presence of UPy within a matrix could "*dramatically enhance the polymer adhesion*".[108] This was claimed to be the result of the quadruple hydrogen bonding formed at the contact interface, which consequently led to enhanced chain interpenetration and dimer formation across the interface, thus assisting in the dissipation of energy between interfaces.

Nevertheless, the UPy group's success within supramolecular chemistry suggests that utilisation of this group within GOBM composites design could enable enhanced composites.[115] By adding complementary UPy groups on the GOBM filler and in the matrix, it provides a design strategy whereby the positioning of the filler in the matrix could be specified by exploiting a dynamic cross-linking self-assembly mechanism between the filler and matrix.

One article by Wang *et al.* reports a pristine UPyGO nacre assembly with the complementary UPy groups of neighbouring functionalised graphene oxide sheets dimerising to form the supramolecular system. Although the nacre system exhibited a tensile strength and toughness of 325.6 MPa and 11.1 MJ m^{-3} respectively, the graphene oxide's preparation with polydopamine presents limitations. The addition of a polymer grafted onto the graphene oxide basal plane leads to increased complexity resulting in additional interfaces where stress actuators could occur at the interfaces. By removal of this other interface by covalently functionalising the basal plane with an isocyanate through the hydroxyl groups of the GO which has been previously reported,[92] it presents the possibility of enhancing the mechanical properties of the filler further. By simplifying the number of interfaces in the filler and adding a complementary functionalised polyurethane matrix, the effect of these novel polymer matrix composites could enhance current impact dissipative materials.

1.8 Thesis aims and objectives

This thesis investigates the potential of reinforcing commercial polyurethane matrices by comparing functionalised and unmodified graphene oxide-based material fillers, which can effectively dissipate impact energies such as rain droplet impingement.

Because of the diverse scope of graphene oxide-based materials which has historically led to misnaming, [116,117] this thesis will characterise the commercial graphene oxide and reduced graphene oxide. This characterised data will be used to compare the UPy modified graphene oxide against the parent graphene oxide and reduced graphene oxide to investigate the physical effects of UPy modification on graphene oxide which are not reported within the literature.

The research presented in this thesis will determine the effect of unmodified graphene oxide and reduced graphene oxide composites by developing a control method and subjecting the fabricated composites to erosion candidacy tests such as nanoindentation and dynamic mechanical thermal analysis with reference to the desirable properties outlined by O'Carroll et al.[3]

The research presented aims to extend its investigation to the incorporation of UPyGO into a polyurethane matrix to produce a UPyGO-UPy polyurethane composite which is also not reported in the literature. These composites will be subjected to the same candidacy tests as the unmodified graphene oxide based composites and comparisons drawn with reference to O'Carroll et al.[3]

1.9 Thesis outline

Chapter 2 presents the materials used and protocols described for all the fabricated systems used throughout this Thesis. The principal characterisation and analysis techniques are briefly explained, and the instrument conditions used, described.

Chapter 3 initially begins with developing the polyurethane matrix to develop a fast-curing system that still possesses enough plasticity for impact dissipation applications. Once a reproducible protocol is developed unmodified graphene oxide and reduced graphene oxide are loaded through an in-situ polymerisation into the polyurethane matrix at low loadings (0.033, 0.066 and 0.1 wt.%) to investigate the effect of graphene oxide-based filler loadings on the impact dissipation properties.

Chapter 4 looks into further improving graphene oxide's mechanical performance by the reproducible covalent functionalisation of graphene oxide with the quadruple hydrogen bonding array motif, ureidopyrimidone. This chapter discusses the successful functionalisation of this novel filler, which is extensively characterised too. The physical properties such as dispersibility and zeta potential compared against the parent graphene oxide and reduced graphene oxide are also reported for the first time.

Chapter 5 demonstrates the successful functionalisation of ureidopyrimidone onto the selected polyurethane matrix to facilitate the ureidopyrimidone functionalised graphene oxide into the matrix via self-assembly. The complementary dimerised graphene oxide polyurethane composite exhibits intrinsic self-healing and enhanced mechanical properties.

Chapter 6 consolidates the comparative investigation throughout this thesis on whether functionalising the graphene oxide with ureidopyrimidone can impart greater impact energy dissipation properties by the hypothesised improved filler-matrix adhesion.

References

1 M. H. Keegan, D. H. Nash and M. M. Stack, *J. Phys. D. Appl. Phys.*, 2013, **46**, 383001.

2 F. J. Heymann, *J. Appl. Phys.*, 1969, **40**, 5113–5122.

3 A. O. Carroll, M. Hardiman, E. F. Tobin and T. M. Young, *Wear*, 2018, **412–413**, 38–48.

4 International Organisation for Standardisation, *ISO 527-1 Tensile testing Plastics*, 1996.

5 TA Instruments, *Q800 Dynamic Mechanical Analysis*, Delaware.

6 S. Ebnesajjad, in *Chemical Resistance of Commodity Thermoplastics*, eds. E. Baur, K. Ruhrberg and W. Woishnis, Elsevier Inc., 2016, pp. 8–25.

7 J. P. Jose, S. K. Malhotra, S. Thomas, K. Joseph, K. Goda and M. S. Sreekala, in *Polymer Composites*, eds. S. Thomas, K. Joseph, S. K. Malhotra, G. Koichi and M. S. Sreekala, Wiley-VCH, Singapore, 1st edn., 2012, p. 3.

8 J. Zhang, K. Chaisombat, S. He and C. H. Wang, *Mater. Des.*, 2012, **36**, 75–80.

9 L. Mishnaevsky, K. Branner, H. N. Petersen, J. Beauson, M. McGugan and B. F. Sørensen, *Materials (Basel).*, 2017, **10**, 1–24.

10 R. A. Pethrick, in *Polymer Science and Technology for Engineers and Scientists*, Whittles Publishing, Dunbeath, 2010, pp. 147–151.

11 S. G. Prolongo, A. Jimenez-Suarez, R. Moriche and A. Ureña, *Compos. Sci. Technol.*, 2013, **86**, 185–191.

12 D. K. Chattopadhyay and D. C. Webster, *Prog. Polym. Sci.*, 2009.

13 P. Article, *Nat. Mater.*, 2007, **6**, 183–191.

14 P. L. De Andres, R. Ramírez and J. A. Vergés, 2008, 1–5.

15 K. S. Novoselov, A. K. Geim, S. V. Morozov, Y. Z. D. Jiang, S. V. Dubonos, I. V. Grigorieva and A. A. Firsov, *Science (80-.).*, 2004, **306**, 666–669.

16 S. Das, J. A. Robinson, M. Dubey, H. Terrones and M. Terrones, , DOI:10.1146/annurev-matsci-070214-021034.

17 A. C. Ferrari, M. Katsnelson, L. Vandersypen, A. Loiseau, V. Morandi, A. Tredicucci, G. M. Williams and H. Hong, *Nanoscale*, 2015, **7**, 4587–5062.

18 M. Kumar, J. S. Chung, B.-S. S. Kong, E. J. Kim and S. H. Hur, *Mater. Lett.*, 2013, **106**, 319–321.

19 X. Xiao, T. Xie and Y.-T. Cheng, *J. Mater. Chem.*, 2010, **20**, 3508.

20 F. Ren, G. Zhu, P. Ren, Y. Wang and X. Cui, *Appl. Surf. Sci.*, 2014, **316**, 549–557.

21 S. T. S.K. Yadav, A. Suri, M.O. Ansari, *Polym. Compos.*, 2017, 1–6.

22 S. Stankovich, D. A. Dikin, R. D. Piner, K. A. Kohlhaas, A. Kleinhammes, Y. Jia, Y. Wu, S. B. T. Nguyen and R. S. Ruoff, *Carbon N. Y.*, 2007, **45**, 1558–1565.

23 R. Shamsi, M. Koosha and M. Mahyari, *J. Polym. Res.*, 2016, **23**, 262.

24 S. C. Shiu and J. L. Tsai, *Compos. Part B Eng.*, 2014, **56**, 691–697.

25 Y. Li, D. Pan, S. Chen, Q. Wang, G. Pan and T. Wang, *Mater. Des.*, 2013, **47**, 850–856.

26 S. Xia, Y. Liu, F. Pei, L. Zhang, Q. Gao, W. Zou, J. Peng and S. Cao, *Polym. (United Kingdom)*, 2015, **64**, 62–68.

27 Sue Keighley, Haydale Supplies Graphene for World's First Graphene Skinned Plane, https://www.haydale.com/2018/08/01/haydale-supplies-graphene-for-worlds-first-graphene-skinned-plane/, (accessed 5 August 2018).

28 European Patent Office, EP 3208300 A1, 2017.

29 Nobelprize.org, The Nobel Prize in Physics 2010 - Illustrated Information, http://www.nobelprize.org/nobel_prizes/physics/laureates/2010/illpres.html, (accessed 29 September 2017).

30 J. H. Lee, P. E. Loya, J. Lou and E. L. Thomas, *Science (80-.).*, 2014, **346**, 1092–1096.

31 H. Shin and S. Yoon, , DOI:10.1021/acsnano.8b00015.

32 N. Lisi, T. Dikonimos, F. Buonocore, M. Pittori, R. Mazzaro, R. Rizzoli, S. Marras and A. Capasso, *Sci. Rep.*, 2017, 1–11.

33 T. Kuilla, S. Bhadra, D. Yao, N. H. Kim, S. Bose and J. H. Lee, *Prog. Polym. Sci.*, 2010, **35**, 1350–1375.

34 M. J. Nine, M. A. Cole, D. N. H. Tran and D. Losic, *J. Mater. Chem. A*, 2015, **3**, 12580–12602.

35 A. Lerf, H. He, M. Forster and J. Klinowski, *J. Phys. Chem. B*, 1998, **102**, 4477–4482.

36 H. He, J. Klinowski, M. Forster and A. Lerf, *Chem. Phys. Lett.*, 1998, **287**, 98–101.

37 D. R. Dreyer, S. Park, C. W. Bielawski and S. Ruoff, Rodney, *Chem. Soc. Rev.*, 2010, **39**, 228–240.

38 H. Li, S. Pang, S. Wu, X. Feng, K. Müllen and C. Bubeck, *J. Am. Chem. Soc.*, 2011, **133**, 9423–9429.

39 C. N. Yeh, K. Raidongia, J. Shao, Q. H. Yang and J. Huang, *Nat. Chem.*, 2015, **7**, 166–170.

40 F. V. Ferreira, F. S. Brito, W. Franceschi, E. A. N. Simonetti, L. S. Cividanes, M. Chipara and K. Lozano, *Surfaces and Interfaces*, , DOI:10.1016/j.surfin.2017.12.004.

41 F. Zhou, H. N. Tien, Q. Dong, W. L. Xu, H. Li, S. Li and M. Yu, *J. Memb. Sci.*, , DOI:10.1016/j.memsci.2018.11.080.

42 X. Qian, L. Song, Q. Tai, Y. Hu and R. K. K. Yuen, *Compos. Sci. Technol.*, 2013, **74**, 228–234.

43 S. Stankovich, R. D. Piner, S. T. Nguyen and R. S. Ruoff, 2006, **44**, 3342–3347.

44 W. S. Hummers and R. E. Offeman, *J. Am. Chem. Soc.*, 1958, **80**, 1339.

45 R. Ye, J. Dong, L. Wang, R. Mendoza-Cruz, Y. Li, P. F. An, M. J. Yacamán, B. I. Yakobson, D. Chen and J. M. Tour, *Carbon N. Y.*, 2018, **132**, 623–631.

46 A. Bianco, H. M. Cheng, T. Enoki, Y. Gogotsi, R. H. Hurt, T. Kyotani, M. Monthioux, C. R. Park, J. M. D. Tascon and J. Zhang, *Carbon N. Y.*, 2013, **65**, 1–6.

47 W. Chen, L. Yan and P. R. Bangal, *Carbon N. Y.*, 2009, **48**, 1146–1152.

48 A. V Dolbin, M. V Khlistyuck, V. B. Esel, V. G. Gavrilko, N. A. Vinnikov, R. M. Basnukaeva, I. Maluenda, W. K. Maser and A. M. Benito, *Appl. Surf. Sci.*, 2016, **361**, 213–220.

49 Y. Qiu, F. Guo, R. Hurt and I. Ku, , DOI:10.1016/j.carbon.2014.02.005.

50 S. Pei and H. Cheng, *Carbon N. Y.*, 2011, **50**, 3210–3228.

51 S. Park, J. An, I. Jung, R. D. Piner, S. J. An, X. Li, A. Velamakanni and R. S. Ruoff, *Nano Lett.*, 2009, **9**, 1593–1597.

52 J. Mao, Z. Bao, R. M. Stoltenberg, Z. Liu, H. A. Becerril and Y. Chen, *ACS Nano*, 2008, **2**, 463–470.

53 D. Zheng, G. Tang, H. Zhang, Z. Yu, F. Yavari, N. Koratkar, S. Lim and M. Lee, *Compos. Sci. Technol.*, 2012, **72**, 284–289.

54 D. Schmelter and H. Hintze-Bruening, *ACS Appl. Mater. Interfaces*, 2016, **8**, 16328–16338.

55 S. Wang, Y. Zhang, N. Abidi and L. Cabrales, *Langmuir*, 2009, **25**, 11078–11081.

56 R. Raj, S. C. Maroo and E. N. Wang, *Nano Lett.*, 2013, **13**, 1509–1515.

57 I. Sengupta, S. Chakraborty and M. Talukdar, *J. Mater. Res.*, , DOI:10.1557/jmr.2018.338.

58 J. Guerrero-Contreras and F. Caballero-Briones, *Mater. Chem. Phys.*, 2015, **153**, 209–220.

59 E. M. Deemer, P. K. Paul, F. S. Manciu, C. E. Botez, D. R. Hodges, Z. Landis, T. Akter, E. Castro and R. R. Chianelli, *Mater. Sci. Eng. B Solid-State Mater. Adv. Technol.*, 2017, **224**, 150–157.

60 C. Botas, P. Álvarez, P. Blanco, M. Granda, C. Blanco, R. Santamaría, L. J. Romasanta, R. Verdejo, M. A. López-Manchado and R. Menéndez, *Carbon N. Y.*, 2013, **65**, 156–164.

61 K. Josepovits, Y. Sanakis, D. Petridis and I. De, 2006, 2740–2749.

62 O. C. Compton, B. Jain, D. A. Dikin, A. Abouimrane and K. Amine, *ACS Nano*, 2011, 4380–4391.

63 D. Walton and P. Lorimer, in *Oxford Chemistry Primers:Polymers*, ed. R. C. Compton, Oxford University Press, Oxford, 2nd edn., 2005, pp. 105–106.

64 M. Syzcher, in *Syzcher's Handbook of Polyurethanes*, CRC Press, 2nd edn., 2012,

p. 4.

65 P. Pokharel, S. Choi and D. S. Lee, *Compos. Part A Appl. Sci. Manuf.*, , DOI:10.1016/j.compositesa.2014.11.010.

66 N. Nuraje, S. I. Khan, H. Misak and R. Asmatulu, *ISRN Polym. Sci.*, 2013, **2013**, 1–8.

67 D. A. Nguyen, Y. R. Lee, A. V. Raghu, H. M. Jeong, C. M. Shin and B. K. Kim, *Polym. Int.*, 2009, **58**, 412–417.

68 D. G. Papageorgiou, I. A. Kinloch and R. J. Young, *Prog. Mater. Sci.*, 2017, **90**, 75–127.

69 Z. Li, R. J. Young, I. A. Kinloch, N. R. Wilson, A. J. Marsden, A. Prakash and A. Raju, *Carbon N. Y.*, 2015, **88**, 215–224.

70 K. H. Choe, D. L. Soo, W. J. Seo and W. N. Kim, *Polym. J.*, 2004, **36**, 368–373.

71 Y. Long, J. An and X. Xie, *Arab. J. Chem.*, 2020, **13**, 3226–3235.

72 X. J. Shen, X. Q. Pei, Y. Liu and S. Y. Fu, *Compos. Part B Eng.*, 2014, **57**, 120–125.

73 S. K. Yadav and J. W. Cho, *Appl. Surf. Sci.*, , DOI:10.1016/j.apsusc.2012.12.028.

74 P. Pokharel and D. S. Lee, *Chem. Eng. J.*, 2014, **253**, 356–365.

75 L. M. Viculis, J. J. Mack, O. M. Mayer, H. T. Hahn and R. B. Kaner, *J. Mater. Chem.*, 2005, **15**, 974.

76 S. Stankovich, D. A. Dikin, G. H. B. Dommett, K. M. Kohlhaas, E. J. Zimney, E. A. Stach, R. D. Piner, S. T. Nguyen and R. S. Ruoff, *Nature*, 2006, **442**, 282–286.

77 J. I. Paredes, A. Marti, J. M. D. Tasco and A. Martı, *Langmuir*, 2008, **24**, 10560–10564.

78 D. Konios, M. M. Stylianakis, E. Stratakis and E. Kymakis, *J. Colloid Interface Sci.*, 2014, **430**, 108–112.

79 C. Vallés, R. J. Young, D. J. Lomax and I. A. Kinloch, *J. Mater. Sci.*, 2014, **49**, 6311–6320.

80 J. J. Huang and Y. J. Yuan, *Phys. Chem. Chem. Phys.*, 2016, **18**, 12312–12322.

81 G. Zhang, F. Wang, J. Dai and Z. Huang, *Materials (Basel).*, , DOI:10.3390/ma9020092.

82 S. Stankovich, R. D. Piner, X. Chen, N. Wu, S. T. Nguyen and R. S. Ruoff, *J. Mater. Chem.*, 2006, **16**, 155–158.

83 H. Ahmad, M. Fan and D. Hui, *Compos. Part B*, 2018, **145**, 270–280.

84 D. Zhong, Q. Yang, L. Guo, S. Dou, L. Jiang and K. Liu, *Nanoscale*, 2013, **5**, 5758–5764.

85 Z. Li, R. J. Young, R. Wang, F. Yang, L. Hao, W. Jiao and W. Liu, *Polymer (Guildf).*, 2013, **54**, 5821–5829.

86 S. Sprenger, *J. Appl. Polym. Sci.*, 2013, **130**, 1421–1428.

87 Y. Zhang and U. R. Cho, *Polym. Compos.*, 2019, **40**, E1103–E1110.

88 C. Lee, X. Wei, J. W. Kysar and J. Hone, *Science (80-.).*, 2008, **321**, 385–388.

89 V. H. Pham, T. T. Dang, S. H. Hur, E. J. Kim and J. S. Chung, *ACS Appl. Mater. Interfaces*, 2012, **4**, 2630–2636.

90 M. Cui, S. Ren, H. Zhao, Q. Xue and L. Wang, *Chem. Eng. J.*, 2018, **335**, 255–266.

91 Y. Wang, T. Li, S. Zhang, H. Zhang, M. Du, Y. Xie, M. Chen, W. Dong and W. Ming, *ACS Nano*, 2018, **12**, 6228–6235.

92 S. Stankovich, R. D. Piner, S. B. T. Nguyen and R. S. Ruoff, *Carbon N. Y.*, 2006, **44**, 3342–3347.

93 N. Parhizkar, T. Shahrabi and B. Ramezanzadeh, *Corros. Sci.*, 2017, **123**, 55–75.

94 S. Pourhashem, A. Rashidi, M. R. Vaezi and M. R. Bagherzadeh, *Surf. Coatings Technol.*, 2017, **317**, 1–9.

95 B. Ramezanzadeh, S. Niroumandrad, A. Ahmadi, M. Mahdavian and M. H. Mohamadzadeh Moghadam, *Corros. Sci.*, 2016, **103**, 283–304.

96 F. Zheng, X. Yang, P. Bi, M. Niu, C. Lv and L. Feng, 2017, 17633–17639.

97 S. H. Yoon, J. H. Park, E. Y. Kim and B. K. Kim, 2011, 1809–1814.

98 P. Haghdadeh, M. Gha, B. Ramezanzadeh and G. Bahlakeh, , DOI:10.1016/j.porgcoat.2019.105243.

99 R. L. D. Whitby, A. Korobeinyk, S. V Mikhalovsky and T. Fukuda, , DOI:10.1007/s11051-011-0459-z.

100 F. H. Beijer, R. P. Sijbesma, H. Kooijman, A. L. Spek and E. W. Meijer, *J. Am. Chem. Soc.*, 1998, **120**, 6761–6769.

101 Y. Yang and M. W. Urban, *Chem. Soc. Rev.*, 2013, **42**, 7446.

102 E. Schlangen and C. Joseph, *Self-Healing Materials: Fundamentals, Design Strategies, and Applications*, Wiley-VCH, Weinheim, 2009.

103 J. Sartorius and H. J. Schneider, *Chem. - A Eur. J.*, 1996, **2**, 1446–1452.

104 M. Wei, M. Zhan, D. Yu, H. Xie, M. He, K. Yang and Y. Wang, *ACS Appl. Mater. Interfaces*, 2015, **7**, 2585–2596.

105 Y. Lin and G. Li, *J. Mater. Chem. B*, 2014, **2**, 6878–6885.

106 S. J. Garcia, *Eur. Polym. J.*, 2014, **53**, 118–125.

107 M. Nosonovsky and P. K. Rohatgi, *Biomimetics in Materials Science*, Springer-Verlag, New York, 2012.

108 A. Faghihnejad, K. E. Feldman, J. Yu, M. V. Tirrell, J. N. Israelachvili, C. J. Hawker, E. J. Kramer and H. Zeng, *Adv. Funct. Mater.*, 2014, **24**, 2322–2333.

109 J. L. Wietor, A. Dimopoulos, L. E. Govaert, R. A. T. M. Van Benthem, G. De With and R. P. Sijbesma, *Macromolecules*, 2009, **42**, 6640–6646.

110 G. E. Fantner, T. Hassenkam, J. H. Kindt, J. C. Weaver, H. Birkedal, L. Pechenik, J. A. Cutroni, G. A. G. Cidade, G. D. Stucky, D. E. Morse and P. K. Hansma, *Nat. Mater.*, 2005, **4**, 612–616.

111 M. L. Ślęczkowski, E. W. Meijer and A. R. A. Palmans, *Macromol. Rapid Commun.*, 2017, **38**, 1–5.

112 Y. Chen and Z. Guan, *Chem. Commun.*, 2014, **50**, 10868.

113 R. F. M. Lange, M. Van Gurp and E. W. Meijer, *J. Polym. Sci. Part A Polym. Chem.*, 1999, **37**, 3657–3670.

114 S. H. M. Söntjens, R. A. E. Renken, G. M. L. Van Gemert, T. A. P. Engels, A. W. Bosman, H. M. Janssen, L. E. Govaert and F. P. T. Baaijens, *Macromolecules*, 2008, **41**, 5703–5708.

115 A. Micoli, M. Nieuwenhuizen, M. Koenigs, M. Quintana, R. Sijbesma and M. Prato, *Chem. - A Eur. J.*, 2015, **21**, 14179–14185.

116 VAMAS, *Chemical composition of G/GO flakes: Elemental analysis and Oxygen content using X-ray photoelectron spectroscopy (XPS)*, 2017.

117 A. J. Pollard, K. R. Paton, C. A. Clifford, E. Legge, A. Oikonomou, S. Haigh, C. Casiraghi, L. Nguyen and D. Kelly, *Characterisation of the Structure of Graphene*, 2017.

2. Experimental

This chapter describes the preparation protocols and the principles of characterisation and analysis techniques used through this Thesis.

2.1 Materials

The glass used for the spacers were microscope slides (ISO8307/1) supplied by Thermo Scientific. Silverline 634006 Sanding Mesh Roll (80 Grit) used to support the Mark-10 tensile testing clamps was supplied by Silverline. Methylcellulose filter papers (0.42 µm) were supplied by Fisher Scientific. 25 mL polypropylene cups were purchased from Tesco Plc. Silicone Oil (-50 °C to +200 °C grade) for heating reactions was supplied by Sigma Aldrich. Huber supplied the Silicone Oil (M40.165.10) used to achieve sub-ambient temperatures on the differential scanning calorimeter.

Carbon SEM adhesive stubs and freshly cleaved ruby muscovite mica (25 mm x 25 mm x 0.15 mm) were supplied by Agar Scientific. Alumina TGA crucibles and DSC aluminium pans and lids were supplied by Perkin Elmer.

2.1.1 Reagents and analysis solutions

2-amino-4-hydroxy-6-methylpyrimidine (98%) and 1,6-diisocyanatohexane (98+%), hydrochloric acid (37%) and sodium hydroxide pellets (Lab reagent grade) were all supplied by Alfa Aesar. Sigma Aldrich supplied the dichlorodimethylsilane (≥ 99.5%). The 3-point calibration (4, 7 and 10) pH buffers Chemenvelopes (pH ± 0.02) were supplied by Hydrion.

2.1.2 Solvents

Deionised water was collected using a reverse osmosis purification system supplied by Veolia to give a resistivity of 18.2 MΩ. Acetone (99.8%), methanol (puriss, ≥ 99.7%), ethanol absolute (99.8%), isopropanol (puriss, ≥ 99.5%), methyl ethyl ketone (puriss, ≥

99.5%), chloroform (99.8%), and tetrahydrofuran (HPLC Grade, ≥ 99.9%) were all supplied by Honeywell. Dichloromethane (99.8%), *n*-hexane (GPR less than < 0.01% Water) and *n*-pentane (99.8%) were supplied by Fisher Scientific. *N*, *N*-dimethylformamide (99%) and deuterated chloroform (99.8% D) were supplied by Alfa Aesar. Dimethyl carbonate anhydrous (≥ 99.9%) was supplied Sigma Aldrich.

2.1.3 Commercial polymer resins

Moldstar 16 and Moldstar 30 silicone rubbers were purchased from Bentley Advanced Materials. Easyflo 120 polyurethane was purchased from MBK Fibreglass, and Easyflo 60 and 95 were purchased from Mouldcraft UK. The formulation for Easyflo remains proprietary; however, the general constituents and monomers are detailed in the material safety data sheet,[1,2] which Figure 2.1 outlines the chemical formulae and constituent content.

Part A formulation

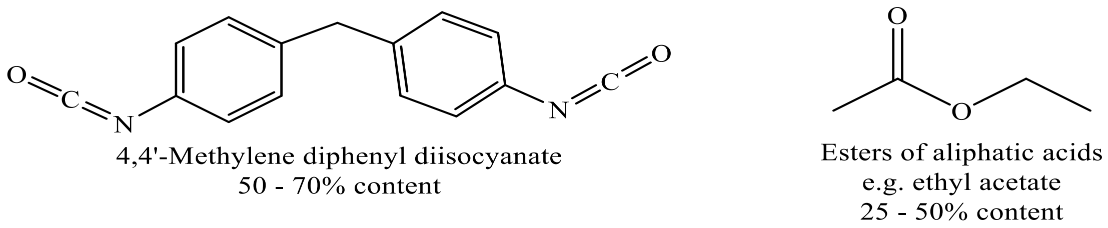

Part B formulation

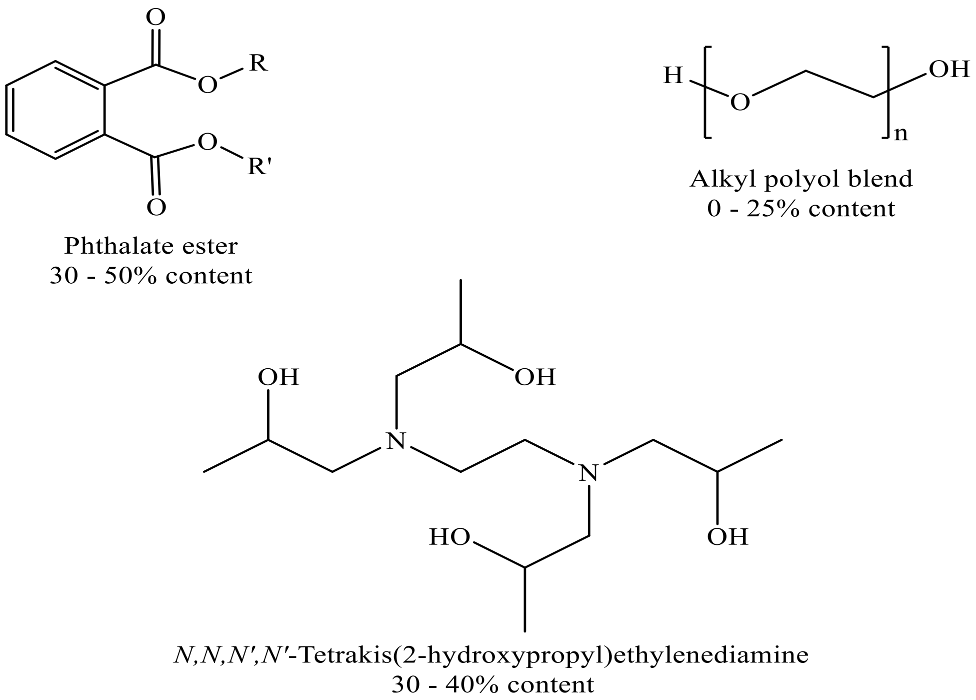

Figure 2.1. Chemical formulae of the components listed in the proprietary formulation of Easyflo 120, separated into Part A and Part B composition, respectively.

2.1.4 Graphene oxide-based materials

Graphene oxide, reduced graphene oxide and eco-GO were all supplied gratuitously from Graphitene Ltd. The following data in Table 2.1 and Table 2.2 is taken from the provided Graphitene Ltd product datasheet,[3,4] this information is crucial for in determining reproducible composites. This is because these berthollides are sensitive to the graphite starting material used and chemical oxidation processes which would alter the enhancement of any material properties reported if the same batch is not used. Due to Eco-GO been a new product under development at Graphitene Ltd, no data sheet was available.

Table 2.1. Graphitene product data sheet for graphene oxide powder (batch pc92p)

Characteristic	Value
Appearance	Brown powder
Dispersibility	Excellent in water
Carbon content (%)	~ 45
Oxygen content (XPS) (%)	~ 52
Oxygen content (SQX) (%)	37.2
Density (g cm^{-3})	0.5 – 0.8
Flake thickness	1 – 3 layers
Flake size (µm)	0.5 - 20
Conductivity	None
pH (4 mg mL^{-1} aqueous)	2.0 – 4.0

Table 2.2. Graphitene product data sheet for reduced graphene oxide

Characteristic	Value
Appearance	Black powder
Carbon content (%)	> 95
Oxygen content (%)	< 5.0
Other element (%)	< 0.5
Density (g cm^{-3})	0.001 – 0.01
Surface Area (m^2 g^{-1})	500
Flake thickness	< 3 layers
Flake size (µm)	0.5 – 5
Electrical conductivity (S m^{-1})	> 10^3

2.2 Preparation of drop-casting moulds for in situ polymerisation fabrication

To construct the final moulds used for the drop-casting of the polymer composites, a master template was constructed. A square 285 cm^3 polystyrene Petri dish was used, and two pieces of 3 mm glass taped together using Scotch™ tape and the internal area increased with the addition of 1mm thick PTFE were placed in the centre.

2.2.1 Preparation of commercial polydimethylsiloxane elastomers for mould container

Part A and Part B were weighed out in a 1:1 w/w ratio to a total volume of 150 g which was determined by volume calculations and mixed using a metal spatula for 4 minutes until a homogenous blue resin was achieved. The blue resin was poured onto the pre-constructed mould outlined in **2.2.** and covered with a glass plate treated with a quick-release wax spray. The polymerisation was left for 1 hour at room temperature for MoldStar 16 or overnight for MoldStar 30 before demoulding occurred.

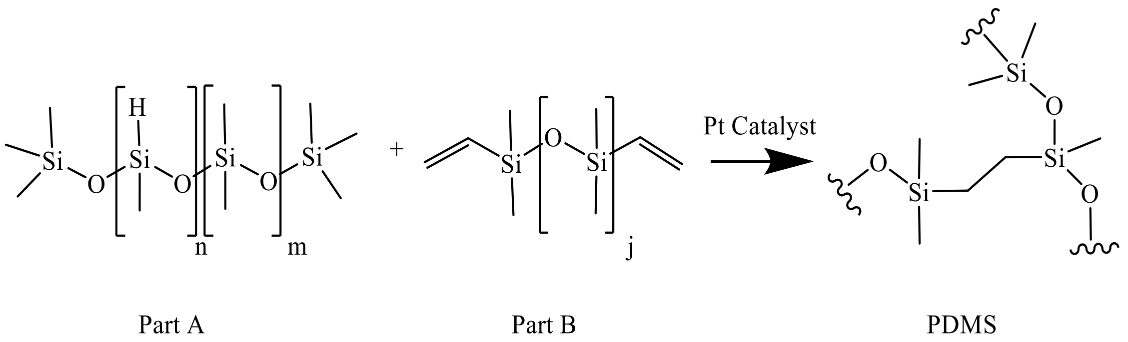

Scheme 2.1. Generalised platinum catalysed polyaddition polymerisation of commercial silicone rubbers such as Moldstar 15 and 30 used to make the drop cast moulds.

2.2.2 Vapour phase hydrophobisation of glass surfaces using dichlorodimethylsilane

Acetone cleaned, and dried glass was placed into a polypropylene container ensuring the two main glass surfaces were exposed to vapours. Into a polymeric sample vial lid placed within the polypropylene container, 500 µL of dichlorodimethylsilane was added and the cover replaced. The closed system was left to hydrophobise for 30 minutes. The surfaces were wiped to remove excess dichlorodimethylsilane before a water droplet test, showed a 'beaded' water droplet suggesting a contact angle of greater than 90 ° and successful hydrophobisation.

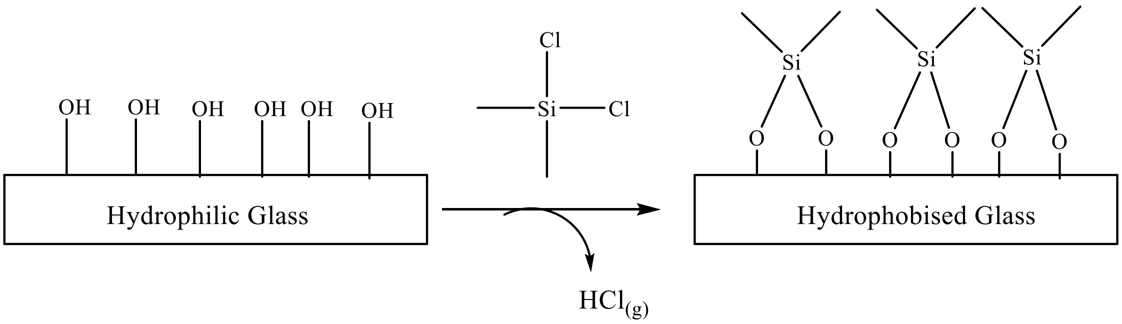

Scheme 2.2. Vapour phase hydrophobisation of glass surfaces whereby the dichlorodimethylsilane bridges the hydroxyl groups with the evolution of gaseous hydrochloric acid.

2.2.3 Mould assembly

The mould for the fabrication of polyurethanes was designed as per

Figure 2.2 and used for all experiments.

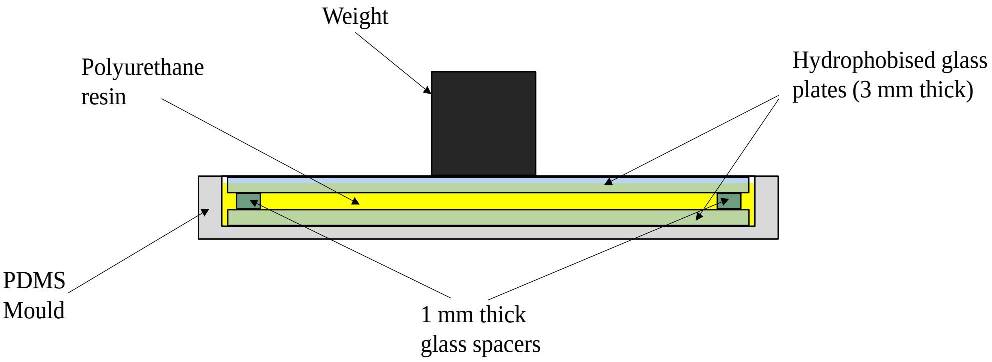

Figure 2.2. Mould design for the fabrication of polyurethanes and polyurethane composites.

The mould design was deemed successful through the ability to cast 1 mm thick polyurethane samples and through the hydrophobisation of the glass surfaces, in addition to the 3 mm thick glass, demoulding could be achieved successfully removing the vacuum created during polymerisation.

2.3 Preparation of commercial polyurethanes by room temperature casting

The final protocol for the preparation of Easyflo 120 polyurethane matrices was as follows. Easyflo 120 Part A (8.5g) and Part B (7.7 g) were measured separately by weight to a 1A:0.9B w/w formulation into polypropylene cups. Part B was poured into Part A and mixed for 90 seconds by hand with a metal spatula, ensuring constant contact with the base of the cup. The mixed resin was poured into a prepared mould outlined in the previous section and left to cure at ambient conditions for 1 hour. The cured sample was removed from the mould after 1 hour and placed into a preheated oven at 25 °C and left to post-cure for 7 days at 25 °C before cutting into test specimens for differential scanning calorimetry, dynamic mechanical thermal analysis, tensile testing, and nanoindentation.

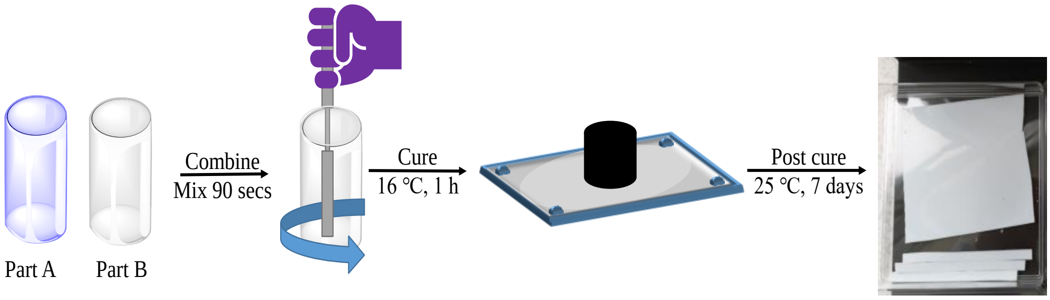

Figure 2.3. Illustrative representation for the preparation of polyurethanes and GOBM polyurethane composites made in this Thesis

2.3.1 *Investigating the effect of a post-cure temperature*

To determine whether a post-cure step was necessary for the preparation of the Easyflo polyurethanes, Easyflo 120 was prepared as per the defined protocol summarised in section 2.3. After the resins had polymerised to produce a white solid (Room temperature for 1 hour) the 100 cm^2 polyurethane solid were cut in half using a sharp Stanley blade.

One half of the sample was placed in a square polystyrene petri dish and left in the fume cupboard for 7 days with conditions reported on the hygrometer of between 15.2 and 18.1 °C with 40% humidity. The other half was placed between two glass plates (for 45 °C), or PTFE plates (for 75 °C) and post cured in a preheated Memmert Laboratory Oven for 16 hours at either 45 °C or 75 °C with a 20% flap and 20% fan setting. The samples were cut into test specimens for differential scanning calorimetry and tensile testing.

2.4 Effect of sonication time on the dispersibility and stability of graphene oxide and reduced graphene oxide Easyflo 120 suspensions

2.4.1 Graphene oxide suspensions

Stock suspensions of 10 mg mL^{-1} were made by combining graphene oxide in either Easyflo 120 Part A or B and dispersing using a Fisherbrand® FB15048 ultrasonic bath at 30kHz and ambient temperature for 5 minutes, 15 minutes and 30 minutes. The dispersibility and stability of the suspensions were observed and compared against a control sample (no sonication) over a period of 1 month. Photographs were taken immediately after sonication, 5, 10, 15, 30 minutes, 1 hour, 2 hours, 4 hours, 24 hours, 1 week, 2 weeks and 1 month.

2.4.2 Reduced graphene oxide suspensions

1 mg mL^{-1}, 5 mg mL^{-1} and 10 mg mL^{-1} suspensions were prepared by combining reduced graphene oxide in either Easyflo 120 Part A or B. The suspensions were dispersed using a Fisherbrand® FB15048 ultrasonic bath at 30kHz and ambient temperature for 5 minutes, 15 minutes and 30 minutes. The dispersibility and stability of the suspensions were observed and compared against a control sample (no sonication) over a period of 1 month. As a result of the high absorbance of reduced graphene oxide, viewing cells were prepared by sandwiching 1 mm thick PDMS silicone between two fresh microscope slides. The samples were all backlit by a white LED lamp so that the suspension could be observed. Photographs were taken immediately after sonication, 5, 10, 15, 30 minutes, 1 hour, 2 hours, 4 hours, 24 hours, 1 week, 2 weeks and 1 month.

2.5 Fabrication of graphene oxide polyurethane composites by in situ polymerisation

A suspension of 10 mg mL^{-1} stock suspension of graphene oxide in either Easyflo120 Part A or Easyflo120 Part B was prepared and dispersed for 30 minutes at 30 kHz using a Fisherbrand® FB15048 ultrasonic bath at ambient temperature. Post sonication calculated volumes (see Table 2.3) of the stock was taken volumetrically and placed into the polypropylene cup and made up to the specified weight for the resin, which was performing as the solvent for the stock. The complementary resin component was weighed out in a separate polypropylene cup before the two cups, one containing the filler and stock resin, and the other the neat component resin were combined. The resin was mixed by hand using a metal spatula for 90 seconds before being decanted into the prepared moulds detailed in 2.2.3 consecutively and left to cure at ambient conditions for 1 hour. The prepared composites were placed in a preheated laboratory oven at 25 ℃ and left to post-cure for 7 days. The samples were removed from the oven and prepared for differential scanning calorimetry, dynamic mechanical thermal analysis, nanoindentation, and tensile testing.

Table 2.3. The formulations used to fabricate graphene oxide loaded polyurethanes from 10 mg mL^{-1} stock suspensions of graphene oxide in either Part A or Part B resin

GO Loading (wt.%)	Volume of GO resin stock used (mL)
0	0
0.033	0.5
0.066	1.0
0.1	1.6

2.6 Fabrication of reduced graphene oxide polyurethane composites by in situ polymerisation

A suspension of 5 mg mL^{-1} stock suspension of reduced graphene oxide in either Easyflo120 Part A or Easyflo120 Part B was prepared and dispersed for 30 minutes at 30 kHz using a Fisherbrand® FB15048 ultrasonic bath at ambient temperature. Post sonication calculated volumes (see Table 2.4) of the stock was taken volumetrically and placed into the polypropylene cup and made up to the specified weight for the resin, which was performing as the solvent for the stock. The complementary resin component was weighed out in a separate polypropylene cup before the two cups, one containing the filler and stock resin, and the other the neat component resin were combined. The resin was mixed by hand using a metal spatula for 90 seconds before being decanted into the prepared moulds detailed in 2.2.3 consecutively and left to cure at ambient conditions for 1 hour. The prepared composites were placed in a preheated laboratory oven at 25 ℃ and left to post-cure for 7 days. The samples were removed from the oven and prepared for differential scanning calorimetry, dynamic mechanical thermal analysis, nanoindentation, and tensile testing.

Table 2.4. The formulations used to fabricate reduced graphene oxide loaded polyurethanes from 5 mg mL^{-1} reduced graphene oxide in either Part A or Part B resin

rGO Loading (wt.%)	Volume of rGO resin stock used (mL)
0	0
0.033	1.0
0.066	2.0
0.1	3.2

2.7 Synthesis of isocyanatohexane-terminated ureidopyrimidone motif

To a nitrogen purged flask, 2-amino-4-hydroxy-6-methylpyrimidine (0.8776 g, 7.01 mmol, 1 molar equivalent) and 1,6-diisocyanatohexane (7.7 mL, 1.04 gmL^{-1}, 47.6 mmol 6.8 molar equivalents) are added together with magnetic stirring under a static nitrogen atmosphere. The reaction is heated to 100 °C for 16 h to afford a white suspension. The reaction mixture was allowed to cool to room temperature, with no changes observed. The crude mixture was precipitated out in n-pentane (25 mL) and filtered *in vacuo*. The filtered product is washed further with n-pentane (3 x 10 mL) and left to dry for 15 mins. The air-dried product is dried at 50 °C for 2h to afford a pure white powder, which agreed with the literature characterisation.[5–7] (1.79 g, 87.3 %, m.p. 180 – 183 °C). ^1H NMR (400 MHz, $CDCl_3$) 13.1 (s, 1H; CH_3CNH), 11.85 (s, 1H, $CH_2NH(C=O)NH$), 10.17 (s, 1H; CH2NH(C=O)NH), 5.81 (s, 1H; $CH=CCH_3$), 3.27 (m, 4H, $NH(C=O)NHCH_2$), 2.22 (s, 3H, $CH_3C=CH$), 1.60 (m, 4H, NCH_2CH_2), 1.38 (m, 4H, $CH_2CH_2CH_2CH_2CH_2$); IR (Diamond ATR) 2^o ν_{N-H} 3200 cm^{-1}, ν_{NCO} 2285 cm^{-1}, 2^o δ_{N-H} 1700 cm^{-1}

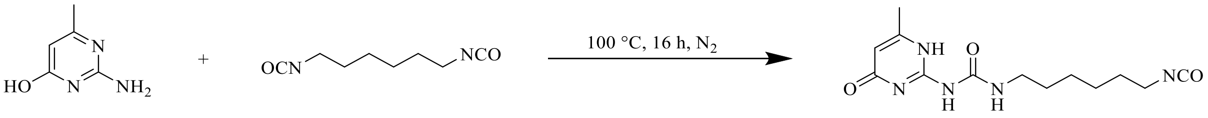

Scheme 2.3. Nucleophilic addition of 2-amino-4-hydroxy-6-methylpyrimidine and 1,6-diisocyanatohexane to produce the ureidopyrimidone motif.

2.8 Functionalisation of graphene oxide with an isocyanatohexane-terminated ureidopyrimidone motif

The white UPyNCO powder was combined with the exfoliated graphene oxide and *N, N*-dimethylformamide and sonicated further for 10 minutes to ensure efficient dispersion of the UPyNCO motif within the brown suspension. The synthesis was maintained at 80 °C for 2 hours before being allowed to cool. Dichloromethane was then added to precipitate out any unreacted UPyNCO and to dilute the higher boiling point *N*, *N*-dimethylformamide (b.p. 153 °C STP), easing the drying process. The cooled suspension was destabilised by ultracentrifugation with any unreacted UPyNCO removed in the supernatant. The washed material was then dried *in vacuo* for 2 days to remove any residual dichloromethane.

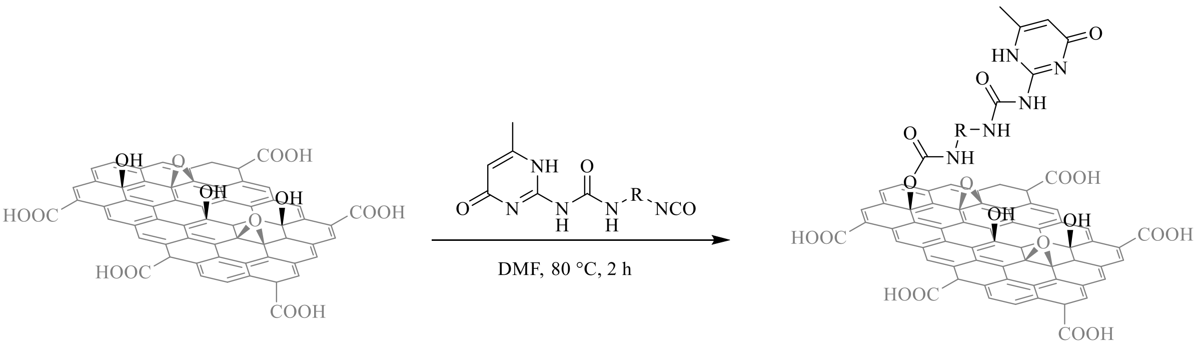

R = Hexyl chain

* Only one urethanisation has been illustrated in the product and the main graphene oxide strucutre has being faded out to aid the readers clarity, this reaction is not site specfic to a particular hydroxyl group.

Scheme 2.4. Nucleophilic addition of the ureidopyrimidone motif reacting with the hydroxyl groups on graphene oxide to produce a novel ureidopyrimidone-functionalised graphene oxide filler

2.9 Calculating the basal carbon-oxygen bond length to determine the origin of the 1041 cm^{-1} to 1093 cm^{-1} infrared transmittance shift

A pyrene ring was constructed using the ChemDraw window by fusing 4 benzene rings to produce the peri-condensed polyaromatic hydrocarbon. To produce the tertiary hydroxyl motif found on the graphene oxide basal plane a hydroxyl group was placed onto the central C_1 carbon as circled in Figure 2.4

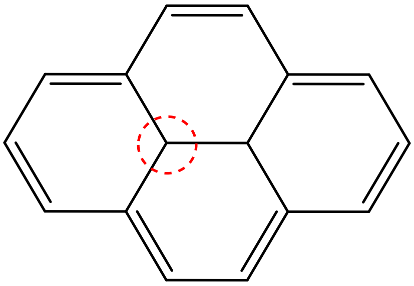

Figure 2.4. The skeletal structure of pyrene with a dotted red circle to indicate the central C_1 carbon used to add the hydroxyl and urethane functionalities to simulate the graphene oxide addressable sites and determine if any significant bond length change had occurred during transurethanisation.

The hydroxylated pyrene molecule was geometry optimised using the molecular dynamics MM2 minimisation calculations. The calculations were run under the constraints of the ChemOffice 3D software with no alterations inputted.[8] The calculation was deemed successful by the hydroxylation changing the planar structure to a 'wrinkled' system due to the hybridisation change of the central C_1 carbon from sp^2 to sp^3 which is also observed in graphene oxide.[9] The bond lengths were generated and tabulated by assigned atomic labels.

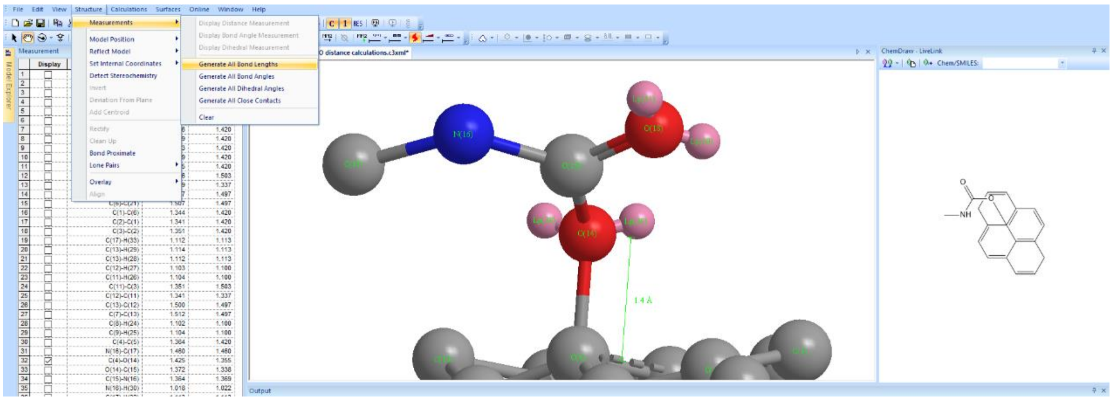

	Display			
7	☐			1.420
8	☐			1.420
9	☐			1.420
10	☐			1.420
11	☐			1.420
12	☐			1.503
13	☐			1.337
14	☐			1.497
15	☐	C(6)-C(21)	1.507	1.497
16	☐	C(1)-C(6)	1.344	1.420
17	☐	C(2)-C(1)	1.341	1.420
18	☐	C(3)-C(2)	1.351	1.420
19	☐	C(17)-H(33)	1.112	1.113
20	☐	C(13)-H(29)	1.114	1.113
21	☐	C(13)-H(28)	1.112	1.113
22	☐	C(12)-H(27)	1.103	1.100
23	☐	C(11)-H(26)	1.104	1.100
24	☐	C(11)-C(3)	1.351	1.503
25	☐	C(12)-C(11)	1.341	1.337
26	☐	C(13)-C(12)	1.500	1.497
27	☐	C(7)-C(13)	1.512	1.497
28	☐	C(8)-H(24)	1.102	1.100
29	☐	C(9)-H(25)	1.104	1.100
30	☐	C(4)-C(5)	1.364	1.420
31	☐	N(16)-C(17)	1.460	1.460
32	☑	C(4)-O(14)	1.425	1.355
33	☐	O(14)-C(15)	1.372	1.338
34	☐	C(15)-N(16)	1.364	1.369
35	☐	N(16)-H(30)	1.018	1.022

For presentation, the hydrogen atoms were hidden to aid clarity and the atomic labels and numbers displayed on each atom. The basal plane carbon-oxygen bond was then selected for comparison.

To produce the expected urethane functionality on the basal plane the same processed was repeated however instead of hydroxylation of the C_1 carbon a methyl carbamate molecule was added due to it being the simplest urethane possible and possessing the necessary structure to provide a reliable result.

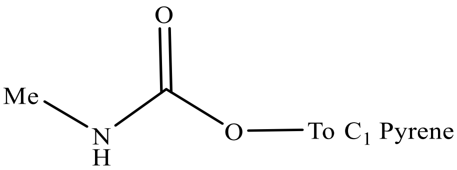

Figure 2.5. The skeletal structure of the methyl carbamate functionality used to simulate the transurethanisation between the isocyanato hexane terminated ureidopyrimidone and the graphene oxide

2.10 Determination of extent of functionalisation using carbon, hydrogen, nitrogen elemental combustion analysis

Elemental combustion analysis was used to show the successful functionalisation of graphene oxide species bearing a nitrogenated constituent. A Fisons Instruments EA 1108 CHNS elemental analyser was used which contains a gas chromatographic component fitted with a flame ionisation detector. The powdered samples were first dried in a laboratory oven at 110 °C to remove any adsorbed moisture for 3 hours before been cooled to room temperature in a desiccated environment.

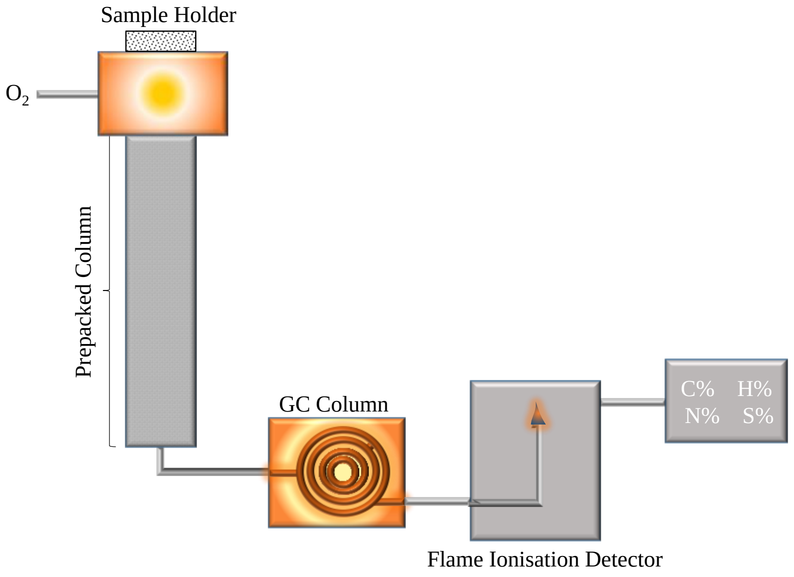

Figure 2.6. Instrumental arrangement for carbon, hydrogen, nitrogen, and sulphur elemental combustion analyser

Three repeats of 3 mg samples were analysed and averaged to determine the concentration of nitrogen present within the samples. Additionally, the degree of functionalisation ($f_\circ$) can be calculated by (2.1).

$$\boldsymbol{f_\circ} = \left(\frac{[\boldsymbol{N}]_{\boldsymbol{UPy}}}{[\boldsymbol{C}]_{\boldsymbol{GO}}}\right) \times \mathbf{100} \tag{2.1}$$

Where $[N]_{UPy}$ is the number of ureidopyrimidine groups (UPy), which is determined by the nitrogen percentage composition and $[C]_{GO}$ is the number of carbon atoms in graphene oxide which is determined by carbon percentage composition analysis of the graphene oxide powder.

2.11 Determination of the flake size distribution of graphene oxide-based materials

100 mL aqueous stock suspensions of 0.1 mg mL^{-1} were prepared and sonicated for 1 hour at 30 kHz using a Fisherbrand® FB15048 ultrasonic bath at ambient temperature to produce a light brown (GO), black (rGO) and a pale grey (UPyGO) suspension. 10 µL aliquots were taken from these volumetric flasks and drop cast onto freshly cleaved mica preheated to 100 ℃ to allow the water to evaporate. The drop cast samples were then quality checked using brightfield microscopy at 20 x magnification before scanning electron microscopy observations.

2.11.1 Flake size analysis using ImageJ

For the flake size distribution analysis, 200 flakes were used and analysed as per the Good Practice Guide No. 145.[10] The image processing was conducted using ImageJ software with each lateral flake size measured down its length and the width is taken perpendicular to the length measurement as Figure 2.7 shows. All the flakes analysed were selected based on their entire circumference being visible. Any stacked or partially overlaid flakes were rejected from the analysis. A histogram was then created with 20 bins based on the 200 measurements taken.

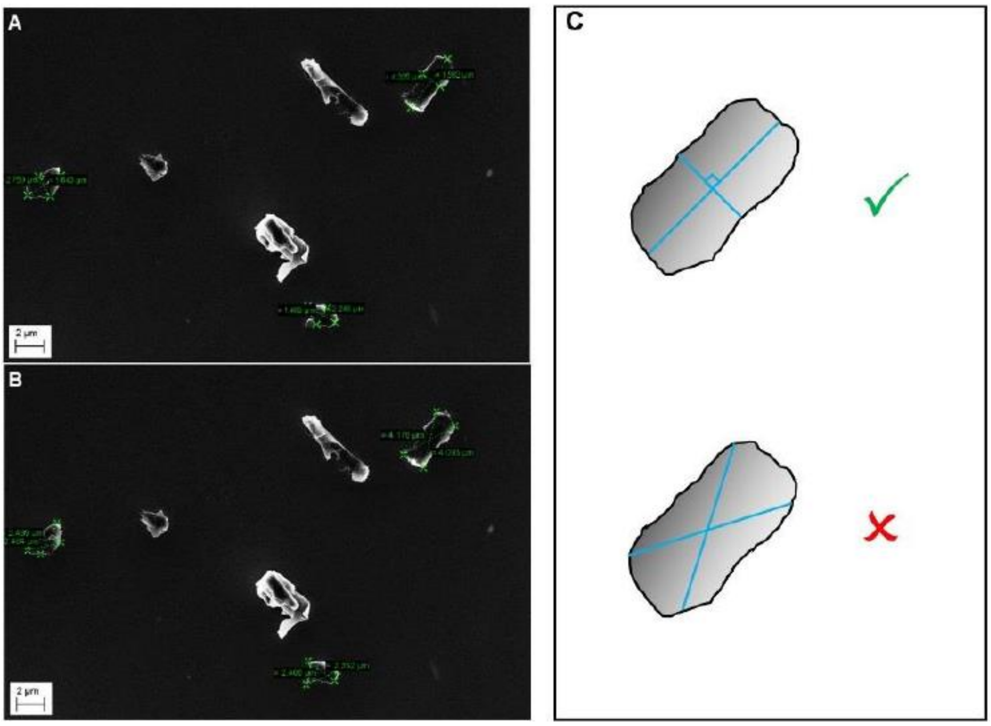

Figure 2.7. Examples of the lateral size measurements performed for an SEM image, (a) correctly, by first taking the length and then finding the width as a perpendicular bisector, and (b) incorrectly. (c) shows an enlarged schematic of the same process for clarity.[10]

2.12 Dispersibility and stability of graphene-related powders in different organic solvents

Glass samples vials fitted with screw-top PTFE lined lids of 1 mg mL^{-1} graphene-related suspensions were prepared by combining the relevant graphene-related powder (20 mg) with the solvent of investigation (20 mL). The suspensions were sonicated at 30 kHz without heating for 1 hour using a Fisherbrand F15015B ultrasonic bath. Post-sonication the samples were lined up against a white background and images were taken immediately after sonication (t = 0), 5 minutes, 10 minutes, 15 minutes, 30 minutes, 1 hour, 2 hours, 4 hours, 24 hours and 1 week.

2.12.1 Theoretical modelling of the sedimentation velocity to compare against observations

To estimate the sedimentation of the suspensions the sedimentation velocity equation given by (2.2.) using the physical parameters of the solvents given in Table 2.5, and assuming a particle density for graphene oxide and reduced graphene oxide of 2 g cm^{-3} as stacking leads to a graphite-based density.[11]

$$v = \frac{2\Delta\rho g r^2}{9\eta} \quad \textbf{(2.2.)}$$

Where Δρ is the difference in density between the particle and the liquid, g is the gravitational acceleration constant (9.81 ms^{-2}), r is the radius of the particle, and η is the dynamic viscosity of the liquid media.

Table 2.5. Physical properties of organic solvents at 25 °C used in the estimation of the sedimentation velocity modelling.[12]

Solvent	Density (g cm^{-3})	Viscosity (mPa s)
Deionised Water	0.998	0.89
Methanol	0.791	0.54
Ethanol	0.789	1.08
Isopropanol	0.785	2.07
Acetone	0.748	0.30
Methyl ethyl ketone	0.805	0.41
n-hexane	0.655	0.29
Chloroform	1.498	0.54
N, *N*-dimethylformamide	0.944	0.80
Tetrahydrofuran	0.886	0.46

2.13 Determination of GO, rGO and UPyGO aqueous suspension stability by measuring the zeta potential at different pH values.

A 0.01 mg mL^{-1} aqueous suspension was prepared by combining GO, rGO or UPyGO (10 mg) with purified water (1000 mL, 18.2 MΩ). The suspensions were initially exfoliated in 20 mL of purified water and sonicated using a Fisherbrand® FB15048 ultrasonic bath at ambient temperature for 20 minutes at 30 kHz to produce a chestnut brown (GO), black (rGO) or ashen grey (UPyGO) suspension. The exfoliated suspension was added into a 1000 mL volumetric flask and made up to the mark and inverted three times to ensure suitable mixing.

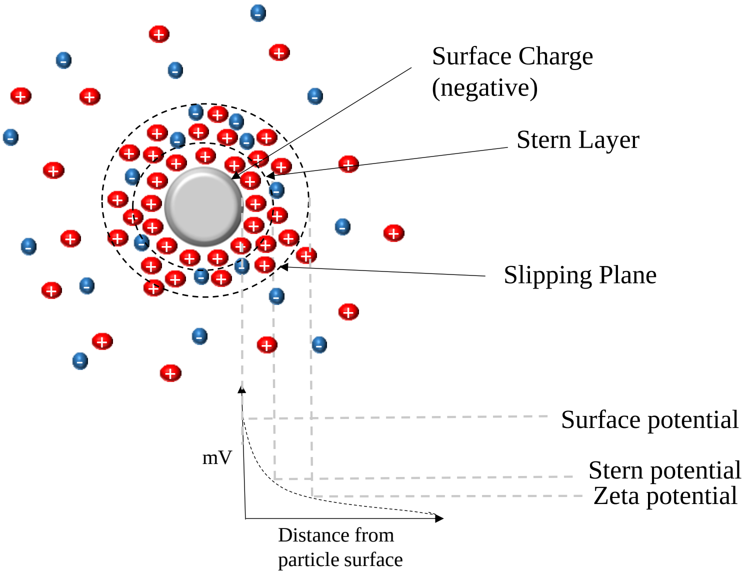

Figure 2.8. Diagram detailing the theory behind zeta potential determination

Aliquots (10 mL) of the prepared suspensions were taken in glass sample vials, and the pH was tuned between 2 and 12. The tuning of the pH was carried out using a pHenomenol pH meter fitted with a Fisherbrand® FB868793 pH probe using a three-point calibration (4, 7, 10; calibration curve = 97.5%) and aqueous solutions of 0.1 M hydrochloric acid or sodium hydroxide with magnetic stirring at 250 rpm to ensure complete mixing.

The zeta potential was run using a Malvern Nanoseries using the zeta potential programme with a dip cell and a polystyrene cuvette. Three runs were conducted for each sample and an average taken.

$$\zeta = \frac{\eta \mu_E}{\varepsilon \varepsilon_0} \tag{2.2}$$

Where η is the viscosity of the medium, μ_E is the electrophoretic mobility defined by (2.3), ε the dielectric constant and ε_0 the vacuum permittivity (8.854×10^{-12} F m^{-1})

$$\mu_E = \frac{v}{E} \tag{2.3}$$

Where ν is the drift velocity of the dispersed particle and E is the electric field strength.

2.14 Fabrication of artificial nacre

Artificial nacre in this research is defined as structures of pristine graphene oxide-based materials self-assembled by solvent deposition or vacuum filtration.

2.14.1 Solvent Deposition

Suspensions of 3 mg mL^{-1} GOBMs were prepared in either deionised water, ethanol absolute or isopropanol and sonicated as per the protocol outlined in 2.2. to generate a chestnut brown suspension. The suspension was cast into a preheated polydimethylsiloxane mould at 50 °C. The cast suspension was placed into a laboratory oven and heated at 50 °C for 12 hours with a fan setting of 20% and an exhaust flap opening of 20% to generate a thin film of pristine graphene oxide, which could be mechanically annealed from the substrate with tweezers to produce large surface area films.

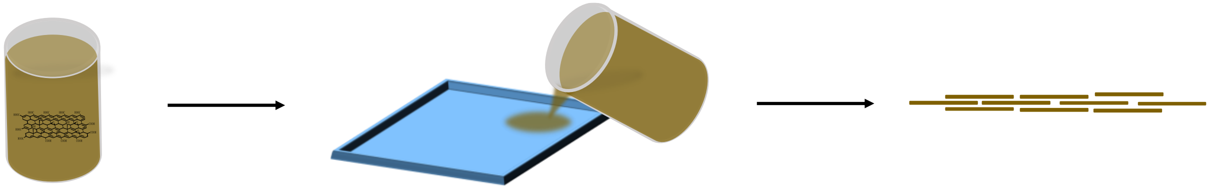

Figure 2.9. Cartoon schematic to demonstrate the preparation of graphene oxide artificial nacre by solvent deposition

2.14.2 Vacuum Filtration

Suspensions of 3 mg mL^{-1} GOBMs were prepared in either deionised water, ethanol absolute or a 1:1 v/v co-solvent of isopropanol and water or isopropanol and sonicated as per the protocol outlined in 2.2. to generate a suspension. Using a Buchner filtration arrangement, a methylcellulose filter paper (0.42 µm pore size) was placed within the funnel and wet with the solvent to ensure a good seal. The stock suspension was poured evenly over the buildings vacuum supply at a quarter turn, ensuring it remained low. The solvent was allowed to permeate the filtration leaving the GOBM to be aggregated, and dry to form the final product.

2.15 Preparation of ureidopyrimidone functionalised polyurethane matrices by in situ polymerisation

These experiments were conducted with the assistance of Mr Jacob Gordon as part of his MChem Research Project.

Easyflo120 Part A and Part B were weighed separately into polypropylene cups to create a final formulation of 1A:0.9B w/w. Differing quantities of UPyNCO (see Table 2.6) were added into Easyflo 120 Part A before Easyflo 120 Part B was combined into Part A. The combined resins were stirred by hand for 90 seconds before depositing into the mould. The mixture was left to cure for 1 h at 16 °C before post-curing at 25°C for 7 days.

Table 2.6. Loadings of UPyNCO into Easyflo120 to produce in situ polymerised UPyPU

UPy Loading (wt.%)	Mass of UPyNCO (g)
0.066	0.011
0.12	0.021
0.2	0.032
5	0.811

2.16 Preparation of complementary ureidopyrimidone functionalised graphene oxide polyurethane composites

The UPyNCO was added to the Easyflo 120 Part A and dissolved upon mixing by hand. The UPyGO powder was ground using a pestle and mortar to refine the powder before combining with Easyflo 120 Part B. The UPyGO-Part B stock suspension was sonicated using a Fisherbrand® FB15048 ultrasonic bath at ambient temperature for 30 minutes at

30 kHz to yield a black suspension. The black UPyGO-Part B suspension was divided to make the relevant loadings and combined with virgin Part B and UPyNCO-Easyflo Part A solution to form the final composite resin.

The composite resin was mixed by hand using a metal spatula for 90 seconds before being decanted into the prepared moulds detailed in 2.2.3 consecutively and left to cure at ambient conditions for 1 hour. The prepared composites were placed in a preheated laboratory oven at 25 °C and left to post-cure for 7 days. The samples were removed from the oven and prepared for differential scanning calorimetry, dynamic mechanical thermal analysis, nanoindentation, and tensile testing.

Table 2.7. The formulations used to prepare complementary ureidopyrimidone functionalised graphene oxide polyurethane composites from 10 mg mL^{-1} UPyGO-Easyflo 120 Part B stock suspension and UPyNCO

UPyGO Loading (wt.%)	Volume of UPyGO-Part B Stock (mL)	UPyNCO Loading (wt.%)	Mass of UPyNCO (mg)
0	0	0	0
0.033	0.5	0.066	11
0.066	1.0	0.12	21
0.1	1.6	0.2	32

2.17 Fourier Transform Infrared, Attenuated Total Internal Reflectance (FT-IR ATR)

Fourier transform infrared spectroscopy (FTIR) is a characterisation technique whereby the infrared beam is focused onto an analyte to cause vibrations of the chemical bonds. The versatility of sample preparation techniques and the ability to analyse in all states of matter makes FTIR a popular characterisation technique. In particular, the use of an attenuated total internal reflectance (ATR) attachment as shown in Figure 2.10 involves an infrared beam transiting through an optical crystal and the result evanescent wave interacts with the sample to cause chemical vibrations. The sampling protocol for this technique requires either a solid or liquid sample to be in contact with the optical crystal during analysis.

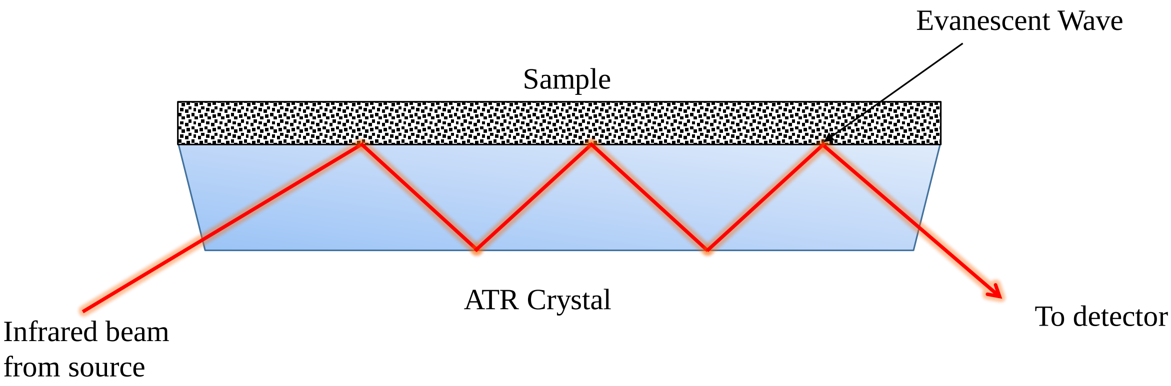

Figure 2.10. Fourier transform infrared attenuated total internal reflectance spectroscopy schematic outlining how the infrared source interacts with the sample to generate an infrared spectrum

The advantage of ATR over other sampling techniques is that it is a non-destructive technique and offers reproducible analysis, unlike other FTIR sample preparation techniques. Routinely the characterisation of GO proceeds with FTIR-ATR using either a diamond or germanium crystal. Diamond is the most used ATR crystal due to its hardwearing and broad spectral range (33 – 45000 cm^{-1}) enabling a variety of samples and hard powders to be tested without damaging the crystal. On the other hand, germanium is the more suitable crystal for rGO composites due to rGO’s high absorption in the infrared region.[13]

Through the initiation of molecular vibrations, FTIR can probe these vibrations and observe the specific chemical fingerprints within the analyte. Dependant on the functionalisation reaction pathway, observations such as the formation of a urethane linkage can be observed at c. 1700 cm^{-1}. Furthermore, transformations in chemical functionalities can be observed in FTIR either through a vibration appearing/disappearing or spectral shifts indicative of bond length changes.

The infrared analysis was conducted on a Thermo Scientific Nicolet iS5 fitted with a Pike Miracle™ diamond crystal attenuated total internal reflectance attachment. The characterisations were conducted using 6 scans, with a resolution of 4 cm^{-1}, through the 600 cm^{-1} to 4000 cm^{-1} regions. Before each analysis, a background calibration was run to remove transmissions from the environment and crystal. Analyses were also conducted using a germanium crystal at Graphitene Ltd; however, the results remained inconclusive due to the high absorbance of rGO so are not presented in this Thesis.

2.18 Thermogravimetric analysis (TGA)

Thermogravimetric analysis is an analytical technique which works by heating a sample loaded crucible on a calibrated microbalance within the instrument. The temperature is computer-controlled with a gas system flowing over the sample to assist in the controlled heating. The sample decomposes, and constituents are volatilised, resulting in a change in the loaded crucible mass. The weight loss is recorded over time and temperature range to produce the required data set for interpretation.

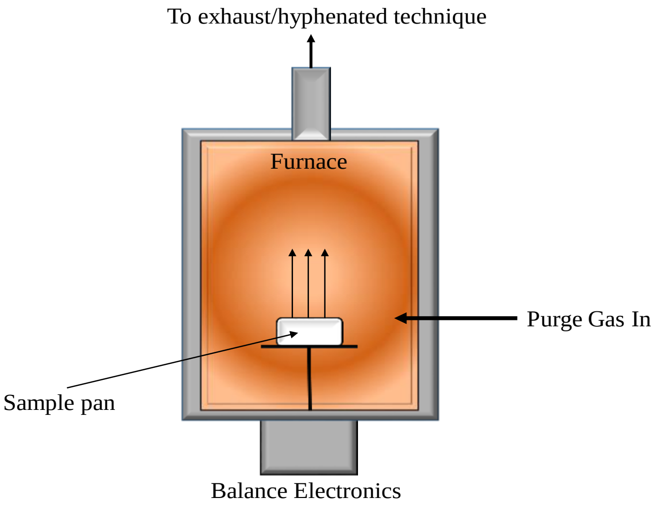

Figure 2.11. Schematic outlining the principles behind the thermogravimetric analysis technique

Thermogravimetric analysis was used to show the presence of graphene oxide within the composite matrix. Weight compositions of GO cannot be accurately determined due to the oxygenated moieties combusting at separate times throughout the analysis experiment.

The thermogravimetric analysis was undertaken on a Perkin Elmer TGA-4000, under a nitrogen atmosphere of 30 mL min^{-1} at 2.0 bar. The temperature scans were operated from 30 °C to 800 °C at a ramp rate of 10 °C min^{-1}. All experiments included a baseline subtraction, taken from a blank calibration run to account for any thermal buoyancy effects.

The collected data is exported as a .csv file and analysed using Origin 2018b software. The weight loss is calculated by substitution into

$$\boldsymbol{W_{TGA} = \left(\left(\frac{W_0 - W_B}{W_{B'}}\right) \times 100\right)_T} \qquad \textbf{(2.4)}$$

Where W_{TGA} is the analysis weight at a given temperature, T, W_0 is the unsubstracted weight; W_B is the baseline weight determined by calibration and, $W_{B'}$ is the initial unsubstracted weight at t = 0.

2.19 Differential Scanning Calorimetry

Differential scanning calorimetry (DSC) is another thermal analysis technique which measures the heat flow of a sample commonly during heating and cooling cycles. The heat flow is measured through the thermal resistance generated and detected through radially applied thermocouples. The signal observed is, therefore, the result of the difference between the heat flow of the reference pan (blank) and the analyte (sample) arranged as per Figure 2.12.

Differential Scanning Calorimetry was used to determine the thermal behaviour of the polyurethanes and composites through the observation of measured endothermic and exothermic events.

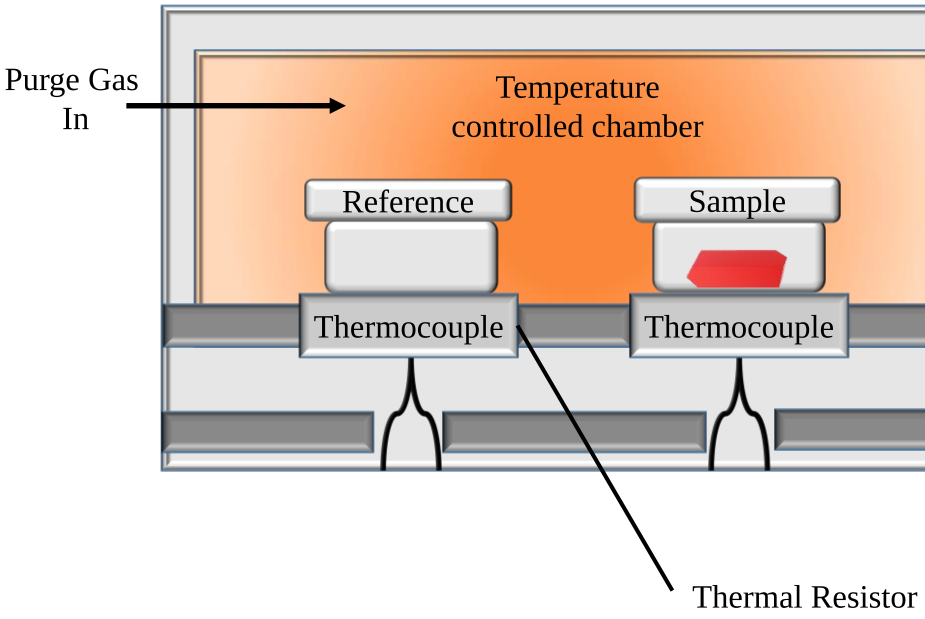

Figure 2.12. Schematic explaining the principles behind differential scanning calorimetry

All samples were conducted on a Perkin Elmer DSC4000 under a 2.0 bar, 30 mL min^{-1} nitrogen atmosphere heated between 7 °C and 220 °C at a heating and cooling rate of 10 °C min^{-1}. Calibration was conducted using an indium reference standard which was verified by the onset temperature being 156.5 ± 0.5 °C and the enthalpy measuring 28.45 ± 0.5 J g^{-1}.

Samples were prepared by weighing 3 – 4 mg products into an aluminium DSC pan using a Mettler Toledo 5-point analytical balance (d = ± 0.01 mg). Each product was run in triplicate with the sample range been prepared to ± 0.1 mg to ensure robust reproducibility.

The glass transition temperature was determined by extrapolation of the half the specific heat value from the glass transition temperature curve which the first endothermic transition in using the Perkin Elmer software.

2.20 Powder x-ray diffraction

Powder x-ray diffraction (PXRD) is a structural analysis technique that investigates the crystalline arrangement of solids.[14] The technique is based on the detection of x-rays that are diffracted from the powdered analyte, as shown by Figure 2.13. The analysis involves the source and detector transiting through defined angles along the circumference of a circle whilst the sample is spun on its axis.

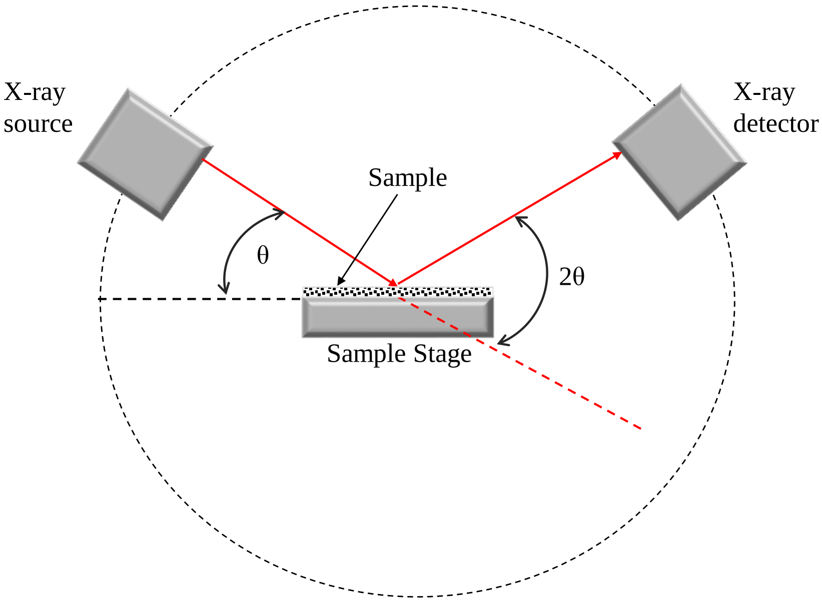

Figure 2.13. Schematic outlining the principles behind the powder x-ray diffraction technique

The diffracted x-rays are then detected usually by a scintillation detector which generates visible light pulses that are converted to intensity.

PXRD characterisation enables the comparison between GO and functionalised GO (fGO) by analysis of the (002) reflection at a 2θ around 10 ° and its corresponding d-spacing value. The inter-gallery distance (d-spacing) is calculated by rearrangement and substitution of the measured and programmed parameters into the Bragg's equation given by (2.5).

$$\boldsymbol{n\lambda = 2d\sin\theta} \tag{2.5}$$

Where n is the order of reflection (integer value), λ is the wavelength of the electrons, d is the spacing of the crystal planes, and θ is the angle of incidence. As a result of Bragg's Law, it is predicted that a decrease in 2θ which means an increase in the d-spacing, suggests steric stabilisation of the GO sheets to support the other characterisation techniques demonstrating successful functionalisation.

X-ray diffraction was achieved using a PANalytical Empyrean Series 2 with Cu Kα source (1.5406 Å) scanning through 5° to 40° fitted without a nickel filter. A nickel detector was initially trialled due to the possibility of trace manganese from the Hummer's method, which would have fluoresced under x-ray.

2.21 Scanning electron microscopy and energy dispersive spectroscopy (SEM-EDS)

Scanning electron microscopy (SEM) is a technique whereby electrons are generated and focused under vacuum through multiple electrostatic apertures until a focused beam of primary electrons collides with the sample (see Figure 2.14).

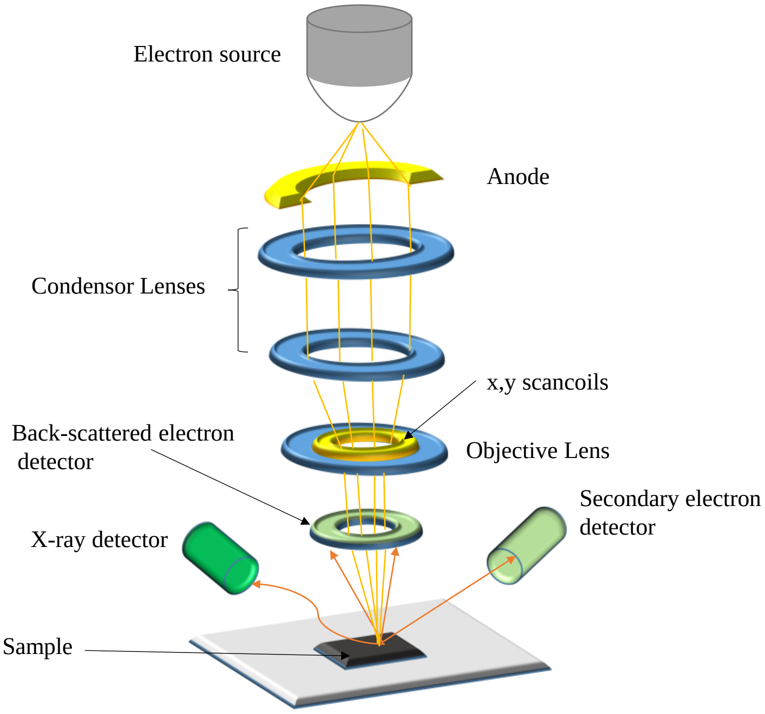

Figure 2.14. Schematic outlining the principles behind scanning electron microscopy and energy disperse x-ray spectroscopy.

Of the two main electron microscopy techniques, SEM can only observe samples magnified between 6 and 2 million times in ultra-high SEM whereas transmission electron microscopy can magnify more than 50 million times.[15] Samples which are not non-conductive materials are prepared by sputter coating with a thin layer of a conductive metal such as gold before SEM observations. For the observation of graphene-based materials, sputter coating is not required due to the conductivity of these materials.

In SEM, when the electron beam collides with the sample, the primary electrons interact to generate secondary electrons which are reflected off the sample and detected. Elastic electron interactions are reflected and detected by the backscattered electron detector (see Figure 2.14) directly above the sample and originate deeper within the sample. Backscattered electrons enable greater contrast between different atoms with atoms being brighter with increasing atomic mass.

On the other hand, inelastic collisions from the beam-sample interaction are detected by the secondary electron detector, which are lower in energy than backscattered electrons. These secondary electrons come from close to the sample surface, making this observation useful for investigating topography.[16] Modern SEM instruments also enable both detectors to be used simultaneously by mixing the ratio of backscattered electrons and secondary electrons detected to improve observations.

Another parameter that can be tuned is the energy of the electron beam, which is usually defined as acceleration voltage. At higher accelerating voltages, the focused beam spot reduces, enabling enhanced resolution observations. However, these high energy electrons also penetrate the sample's surface leading to surface observations being compromised as shown by the simulation results in Figure 2.15.

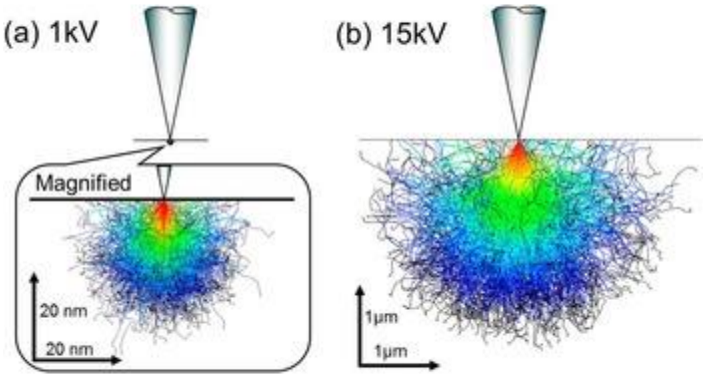

Figure 2.15. Monte Carlo simulations to illustrate the effect of primary electrons scattering in a carbon sample.[17]

Therefore, for graphene-based materials, low accelerating voltages (> 5 kV) are used for SEM observations to maintain their structure and enable high-quality observations. Different scanning electron microscopes were used throughout this research, and the details of operation are provided in the following subsections.

2.21.1 Low Magnification Microscopy

Scanning electron microscopy was conducted on a Hitachi TM4000 Plus operating at an accelerating voltage of 5, 10 or 15 kV using either a backscattered secondary electron, secondary electron, or mixed detector.

2.21.2 High Magnification Microscopy

High magnification scanning electron microscopy was conducted on a Carl Zeiss Evo-60 using a secondary electron detector. The Aperture was 20 µm with a LaB_6 filament operating are 1.96 A with a beam current of 40 µA. The working distance was 10 mm. The samples were not coated due to guidance from the Good Practice Guide,[10] however the mica substrate was gold coated with a coating thickness of 10 nm.

2.21.3 Energy dispersive spectroscopy

For energy dispersive spectroscopy the operating voltage was increased to 15 keV with a working distance of 10 mm on the Hitachi TM4000Plus. Data collection occurred on an Oxford Instruments Aztec hyphenated to the SEM instrument.

2.22 Dynamic Mechanical Thermal Analysis (DMTA)

Dynamic mechanical thermal analysis was conducted on a TA Instruments Q800 fitted with a tensile clamp attachment, as shown by Figure 2.16.

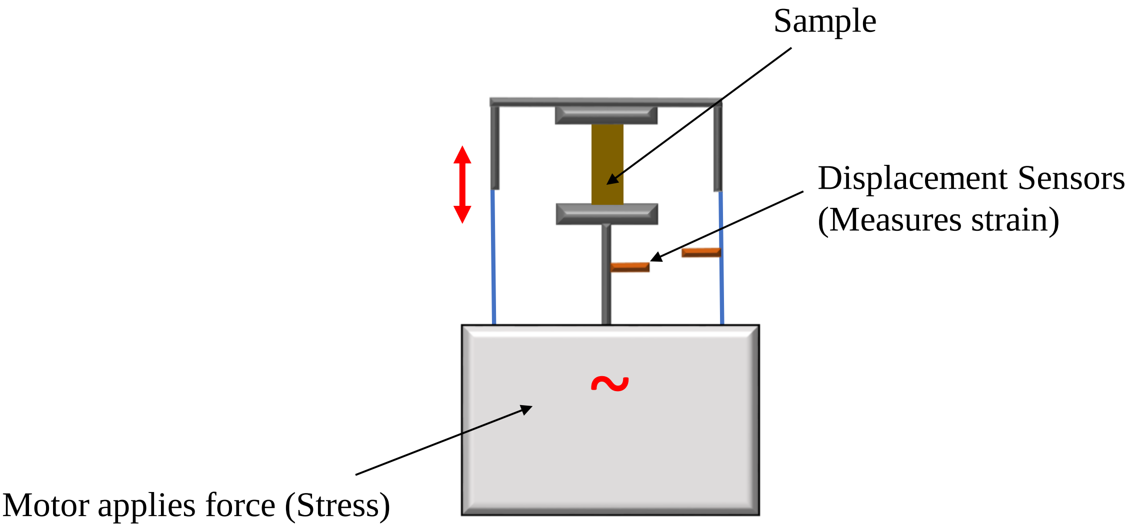

Figure 2.16. Diagram outlining the principles behind dynamic mechanical thermal analysis using a tensile clamp attachment for fibre and thin-based samples.

The calibration was conducted using the predetermined stainless-steel shim standards supplied by TA Instruments, which is conducted each time the tensile clamp is used. The test samples were cut using a sharp scalpel blade and a 3D printed jig shown in Figure 2.17 to a dimension of 30 mm long x 5 mm wide and 1 mm thick.

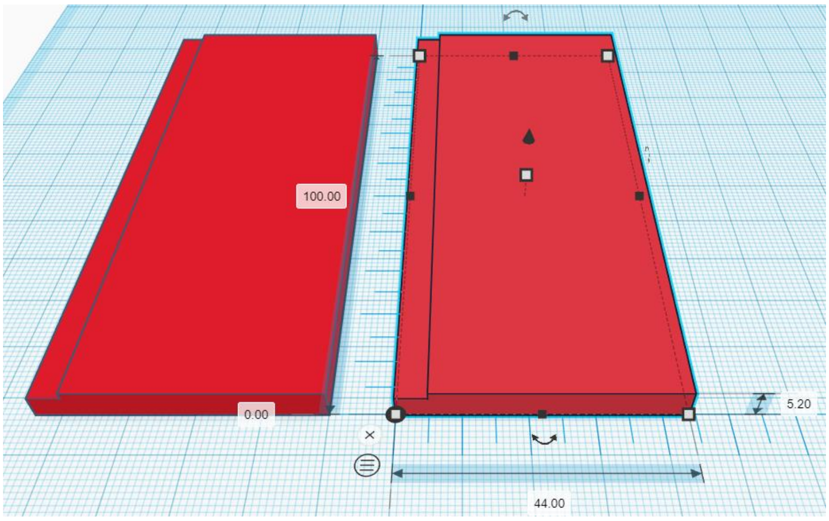

Figure 2.17. Computer-aided design for the preparation of a jig to cut DMA samples 5mm wide to ensure a consistent cross-sectional area during testing using the online design software Tinkercad.[18]

2.22.1 Dynamic moduli and glass transition temperature determination

Ten test specimens were heated between 25 °C and 180 °C at a heating rate of 10 °C min^{-1} at a single frequency of 10 Hz, which was determined by sweeping the frequency to generate a master curve. The glass transition temperature (T_g) was determined from by the relationship shown in (2.6) where the onset of the loss modulus (E’’) curve and the maxima of the tanδ peaks, are used for determination (see Figure 2.18).

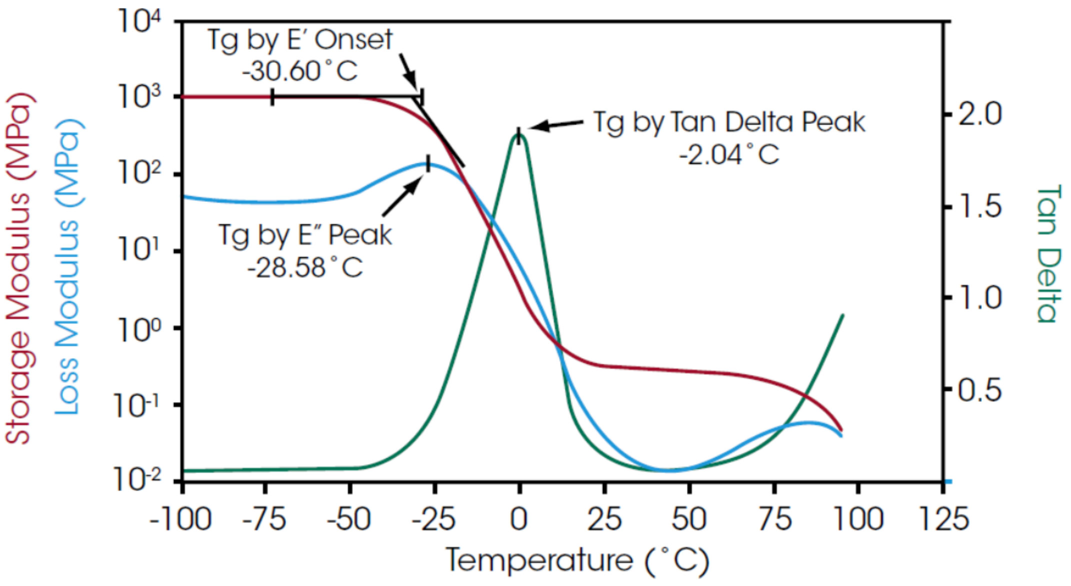

Figure 2.18. Dynamic mechanical thermograms illustrating the determination of the glass transition temperature for both techniques which will be used in this work. Image taken from.[19]

$$\boldsymbol{tan\delta_{max} = T_g = E''_{onset}} \qquad \textbf{(2.6)}$$

Due to the sensitivity of the T_g to frequency as aforementioned, it is accepted that DMTA provides a more accurate representation of the T_g as the frequency can be measured and controlled, unlike DSC.

2.22.2 Crosslink density

The crosslink density was estimated by substitution of the storage modulus at a temperature much higher than the glass transition temperature into Eqn (2.7).

$$\boldsymbol{\nu_e = \frac{E'}{3RT}} \qquad \textbf{(2.7)}$$

Where E’ is the storage modulus at 170 °C, R is the universal gas constant (8.314 J mol^{-1} K^{-1}), and T is the absolute temperature at 170 °C (443.15 K).

2.22.3 Approximating the tensile performance using the Rule of Mixtures equation

For the Rule of Mixtures equation (2.11) the volume fraction is required to predict the elastic modulus performance. Therefore, the weight percentage of graphene oxide-based material (wt.%$_{GOBM}$) of the composites was converted to a volume fraction. Initially, the volume of GO or rGO per 100 g composite was calculated by (2.8) using the assumption of a 0.65 g cm^{-3} density for the GO and 0.01 g cm^{-3} for rGO (ρ_{GOBM}) see Table 2.1 and Table 2.2. The subscript GOBM was used to signify either graphene oxide or reduced graphene oxide.

$$\boldsymbol{V_{GOBM} = \frac{wt.\%_{GOBM}}{\rho_{GOBM}}} \tag{2.8}$$

Conversion of the volume of graphene oxide-based material (V_{GOBM}) present into the volume fraction (V_f) was then calculated by substitution into **(2.9)**

$$\boldsymbol{V_f = \frac{V_{GOBM}}{V_{Total}}} \tag{2.9}$$

The total volume (V_{Total}) is determined by (2.10) which defined as the sum of the volume of graphene oxide-based material (V_{GOBM}) and volume of polyurethane matrix (V_{PU}).

$$\boldsymbol{V_{Total} = V_{GOBM} + V_{PU} = \left(\frac{wt.\%_{GOBM}}{\rho_{GOBM}}\right) + \left(\frac{100 - wt.\%_{GOBM}}{\rho_{PU}}\right)} \tag{2.10}$$

Another assumption is that the specific gravity of Easyflo120 was taken against water at 4 °C, which would mean that the specific gravity is equal to the density, leading to an assumed density (ρ_{PU}) of 1.2 g cm^{-3} for Easyflo120.[20]

Combining the results from equations (2.9) and (2.10) the elastic modulus of the composite (E_c) can be calculated by substation into equation (2.11)

$$\boldsymbol{E_c = E_f V_f + E_m(1 - V_f)} \tag{2.11}$$

Where E_f is the elastic modulus of the filler (207.6 GPa for GO,[21] and 810 GPa for rGO)[22], E_m is the elastic modulus of the matrix which was experimentally determined by the virgin Easyflo 120 tensile testing (250 MPa).

The elastic moduli for the GOBM reinforced composites were plotted as a function of filler loading alongside the experimentally obtained elastic moduli. A 5% error was added for each approximation based on a 95% confidence interval used throughout mechanical testing.

2.22.4 Tensile testing

10 test specimens measuring (l x w x h) 30 mm x 5 mm x 1 mm were analysed using a calibrated tensile test clamp. In tensile mode, the samples were heated to 30 °C at 1 °Cmin^{-1} and left to equilibrate for 5 minutes with a preload of 0.1 N. The samples were held isothermally at 30 °C and tested with a strain speed of 1% the gauge length per minute and at intervals of 0.005% until failure.

The ISO-527 elastic modulus was calculated by the stress(σ)-strain gradient using (2.12) between the strain (ε) values of 0.0005 and 0.0025 denoted as subscripts 1 and 2, respectively.

$$\boldsymbol{E_{Tensile}} = \frac{(\boldsymbol{\sigma_2} - \boldsymbol{\sigma_1})}{(\boldsymbol{\varepsilon_2} - \boldsymbol{\varepsilon_1})} \qquad \textbf{(2.12)}$$

For the polyurethane development experiments these were conducted at ambient conditions on a Mark-10 tensile testing instrument with tensile jaws, modified with Mesh-Grit to prevent jaw slippage. 10 rectangular samples with dimensions 20 mm x 5 mm x 1 mm were tested in tensile mode at a speed of 2.4 mm min^{-1} until failure. The data was computed through the version 10 Microsoft Excel macro developed by Dr Tommy Horozov. The elastic moduli (max slope and ISO-527), ultimate tensile strength, elongation at break, and toughness were averaged and compared to investigate the effect of post curing on the virgin polyurethane.

2.22.5 Tensile stiffness

The material stiffness was also evaluated using the isothermal tensile testing analysis. To determine the sample stiffness ($S_{Tensile}$), the ISO-527 gradient of a force against length plot was calculated as per (2.13).

$$\boldsymbol{S_{Tensile} = \frac{(F_2 - F_1)}{(L_2 - L_1)}} \qquad \textbf{(2.13)}$$

Where F is the applied tensile force, and L is the sample length. Subscripts 1 and 2 are defined as the ISO-527 limits of 0.0005 and 0.0025, respectively.

All measurements were averaged and validated by statistical analysis outlined in section 2.24.

2.22.6 Material performance

To assess the material performance effect of GOBM on the virgin PU, the percentage enhancement was calculated by substitution into (2.14) as follows

$$\boldsymbol{\alpha = \left(\frac{P_c - P_{PU}}{P_{PU}}\right) \times 100} \qquad \textbf{(2.14)}$$

Where α is the percentage enhancement relative to the virgin polyurethane, P_c is the observed property of the fabricated composite, and P_{PU} is the observed property of the virgin polyurethane.

2.23 Nanoindentation

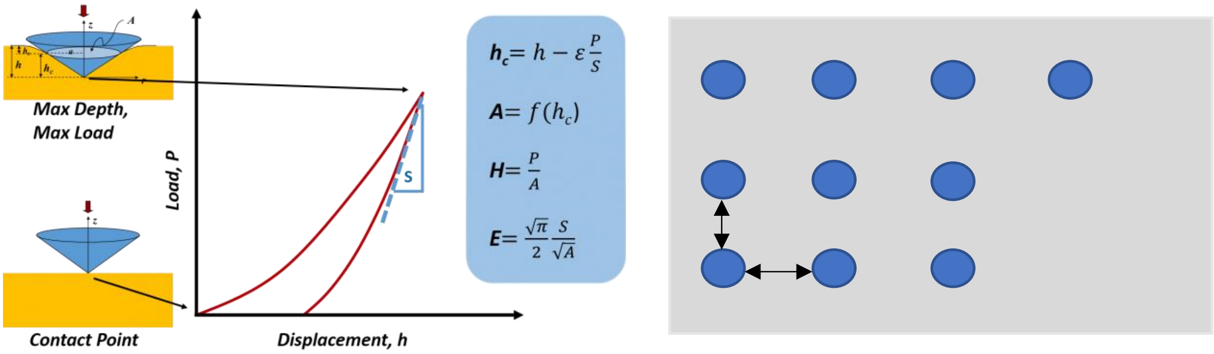

Figure 2.19. Schematic outlining the principle behind nanoindentation. Image taken from.[23]

Nanoindentation testing was conducted using an Anton Paar STeP4 connected to an NHT^3 indentor. The samples were prepared by cutting a 1 cm^2 section of the post-cured composites which were labelled in the top right-hand corner with a permanent marker so that the top surface and the bottom surface of the composites were evaluated. A Berkovich diamond tip was used to analyse 10 locations on the prepared samples which were averaged and subjected to the statistical analysis given in 2.24. to validate their significance.

Hardness, creep, indentation stiffness, indentation elastic modulus was all derived from these measurements for analysis.

2.23.1 Hardness

The hardness was calculated using the instruments software to provide both the instrumentation hardness (H_{IT})and the Vickers hardness. The instrumentation hardness was used in this study which is calculated using (2.15)

$$\boldsymbol{H_{IT}} = \left(\frac{\boldsymbol{F_{max}}}{\boldsymbol{A_P}}\right) \qquad \textbf{(2.15)}$$

Where F_{max} is the maximum indentation load and A_p is the projected contact area.

2.23.2 Creep

The indentation creep (C_{IT}) which is defined as the relative change of the indentor depth during a constant applied load. This parameter is again calculated in the instrument's software using (2.16)

$$\boldsymbol{C_{IT} = \left(\frac{h_2 - h_1}{h_2}\right) \times 100} \qquad \textbf{(2.16)}$$

Where h_2 is the indentation depth at the end of the test and h_1 is the initial depth at the beginning of the test.

2.23.3 Reduced elastic modulus

The reduced elastic modulus which is the elastic response of the material and the indentor is related to the contact stiffness of the material and can be calculated within the instrument by (2.17).

$$\boldsymbol{E_r = \frac{\sqrt{\pi}}{2\beta}\frac{S}{\sqrt{A_{p(hc)}}}} \qquad \textbf{(2.17)}$$

Where S is the contact stiffness and $A_{p(hc)}$ is the projected indentation area at contact depth h_c. β is the geometrical constant of the indenter.

The stiffness was calculated using the instrument's software through rearrangement of (2.17).

2.24 Statistical analysis of material properties data

The significance of the observed data was validated by statistical analysis. Outlier testing and analysis of variance were conducted on the surface roughness (n=10), tensile tests (n=10), DMA (n=10) and nanoindentation data (n=10).

2.24.1 Grubb's Test

If a data sample appeared erroneous from the rest of the data set, it was subjected to the Grubb's Test given in (2.18) to determine whether it was a data outlier. No more than one data point could be subjected to outlier testing within a data set.

$$\boldsymbol{G_{Test}} = \frac{|\boldsymbol{U} - \boldsymbol{\bar{x}}|}{\boldsymbol{S}} \qquad \textbf{(2.18)}$$

Where U is the suspected data outlier, $\bar{x}$ is the mean and S is the standard deviation of the data series.

For each data series, a 95% confidence interval was used for the value of $G_{Table,}$ which is given in Table 2.8, leading to rejection if $G_{Test} > G_{Table}$ was true.

Table 2.8. Critical values of G for outlier rejection[24]

Number of values	G-value (95% Confidence)
3	1.15
4	1.46
5	1.67
6	1.82
7	1.94
8	2.03
9	2.11
10	2.18

2.24.2 Analysis of variance

Single-factor analysis of variance (ANOVA) test was conducted on the analyses above (see Statistical analysis of material properties data). A single factor ANOVA test was employed due to the only expected variation in the data observations is the addition of filler into the matrix. The analysis was conducted using the data analysis wizard in Microsoft™ Excel. The programme outputs of interest from the ANOVA report (see Figure 2.20) were the P-value and F-test values used for validation.

SUMMARY

Groups	*Count*	*Sum*	*Average*	*Variance*
0GOPU	10	0.466	0.0466	1.38E-05
0.033GOPU	10	0.449	0.0449	2.19E-05
0.066GOPU	10	0.342	0.0342	0.000175
0.1GOPU	10	0.45	0.045	5.33E-05

ANOVA

Source of Variation	*SS*	*df*	*MS*	*F*	*P-value*	*F crit*
Between Groups	0.001	3	0.00032529	4.922653	0.005745	2.866266
Within Groups	0.0024	36	6.6081E-05			
					F>Fcrit	
Total	0.0034	39				

Figure 2.20. ANOVA single factor data analysis output which was used to validate all mechanical testing. (Example used is the reverse face of GOPU nanoindentation samples evaluated during this research)

Comparison of the F-value (F) with the critical F-value (F_{crit}) was used to determine whether to accept or reject the null hypothesis. For an F > Fcrit relationship, this would validate the observed trends as the null hypothesis would be rejected. The validity of the trend was further justified if the P-value < 0.005 (95% confidence) also signifying a rejection in the null hypothesis.

2.25 Chapter References

1 Polytek Development Corp, *Part A Material Safety Data Sheet*, Easton, 2010.

2 Polytek Development Corp, *Easyflo Part B Material Safety Data Sheet*, Easton, 2016.

3 Graphitene Ltd, *Product Data Sheet – Graphene Oxide Powder*, Flixborough, 2017.

4 Graphitene Ltd, *Product Data Sheet – Reduced Graphene Oxide,* Flixborough, 2017.

5 S. H. M. Söntjens, R. P. Sijbesma, M. H. P. Van Genderen and E. W. Meijer, *J. Am. Chem. Soc.*, 2000, **122**, 7487–7493.

6 F. H. Beijer, R. P. Sijbesma, H. Kooijman, A. L. Spek and E. W. Meijer, *J. Am. Chem. Soc.*, 1998, **120**, 6761–6769.

7 R. F. M. Lange, M. Van Gurp and E. W. Meijer, *J. Polym. Sci. Part A Polym. Chem.*, 1999, **37**, 3657–3670.

8 PerkinElmer Informatics, 2015.

9 X. J. Shen, X. Q. Pei, Y. Liu and S. Y. Fu, *Compos. Part B Eng.*, 2014, **57**, 120–125.

10 A. J. Pollard, K. R. Paton, C. A. Clifford, E. Legge, A. Oikonomou, S. Haigh, C. Casiraghi, L. Nguyen and D. Kelly, *Characterisation of the Structure of Graphene*, 2017.

11 Poco Graphite, *Properties and Characteristics of Graphite*, Texas, 2015.

12 S. Murov, Properties of Solvents Used in Organic Chemistry, http://murov.info/orgsolvents.htm, (accessed 20 September 2019).

13 Perkin Elmer, *Tech. Note*, 2004, 1–4.

14 S. W. N.A. Young, *Characterisation methods in Inorganic Chemistry*, Oxford University Press, Oxford, 1st edn., 2017.

15 A. Nanakoudis, SEM and TEM: what’s the difference?, https://blog.phenom-world.com/sem-tem-difference, (accessed 24 April 2020).

16 ThermoFisher Scientific, *Scanning Electron Microscopy Working Principle*, 2019.

17 Y. Hashimoto, A. Muto, E. Woods, T. Walters and D. C. Joy, *Micros. Today*, 2016, **24**, 20–25.

18 Autodesk, 2019. designed at https://www.tinkercad.com/

19 TA Instruments, *Q800 Dynamic Mechanical Analysis*, Delaware.

20 Chemical Retrieval on the Web, Polymer Properties Database, https://polymerdatabase.com/polymer classes/Polyurethane type.html, (accessed 2 October 2021).

21 J. W. Suk, R. D. Piner, J. An and R. S. Ruoff, *ACS Nano*, 2010, **4**, 6557–6564.

22 S. Wan, Y. Chen, Y. Wang, G. Li, G. Wang, L. Liu, J. Zhang, Y. Liu, Z. Xu, A. P. Tomsia, L. Jiang and Q. Cheng, *Matter*, 2019, **1**, 389–401.

23 nanoScience Instruments, Nanoindentation, https://www.nanoscience.com/techniques/nanoindentation/, (accessed 2 May 2020).

24 D. C. Harris, in *Quantitative Chemical Analysis*, W.H. Freeman and Company, New York, 8th edn., 2010, p. 83.

3. Investigating the mechanical properties of unmodified graphene oxide and unmodified rGO polyurethane composites

Graphene oxide-based materials (GOBMs) are a class of two-dimensional materials that encompass graphene oxide (GO) and reduced graphene oxide (rGO). Due to the multitude of preparatory processes to exfoliate graphite, differing degrees of oxidation are achieved which possess sheet defects,[1–3] and property variations.[4,5] Because of these considerations these berthollide fillers require characterisation before they are investigated further. This ensures the correct nomenclature,[6] batch compliance, are present to enable robust reporting of a particular graphene oxide material's properties or effect in a polymer composite.

GO which has a higher degree of oxidation than rGO possesses a greater volume of oxygenated functional groups which enables it to be more tunable with target pendant groups functionalities. rGO however forms through process treatments (heat,[7–10] chemical,[11–13] or electrochemical)[14,15] to remove some or most of the oxygenated moieties and produce a more hydrocarbon based structure which possesses greater hydrophobicity. Furthermore, the reduction treatments usually result in further sheet cleavage which produces a smaller lateral flake size also. The increase in hydrophobicity and decrease in lateral flake size is suggestive that rGO may disperse better within hydrocarbon-based polymer matrices. However, the larger specific surface area and increased functional group coverage of GO may also support desirable mechanical properties within a polymer matrix.

This chapter aims to determine by comparative studies the impact of small loadings of unmodified GO or unmodified rGO on the material properties of a commercial polyurethane matrix.

3.1. Characterisation of the commercial graphene oxide-based materials

Three graphene oxide-based materials, GO, rGO, and a new electrochemically exfoliated Graphitene product (eco-GO) were characterised to understand the structural features of these two-dimensional fillers. Eco-GO was claimed because of the electrochemical exfoliation process to produce a narrower lateral flake size distribution and fewer defects in the basal plane and sheet edges. The structure was expected to follow the Lerf-Klinowski model as it was still graphene oxide. This characterisation data would then enable their design and fabrication into a polyurethane matrix to make the final composites.

Diamond FTIR ATR was employed on the samples as powders and analysed six times to produce the spectra, as shown in Figure 3.1. The spectra for both the rGO and the eco-GO showed a weak peak at ~2116 cm^{-1}, suggesting ketene groups being present. These ketene groups are assumed to result from the thermal reduction process used to produce rGO, whereas its presence in eco-GO remains unknown. Furthermore, the FTIR reveals some carbon-oxygen vibrations in the reduced GO spectra, which implies that the rGO is present and has not sufficiently reduced to produce graphene. The high infrared absorbance of both the rGO and the eco-GO was identifiable using a diamond ATR crystal.

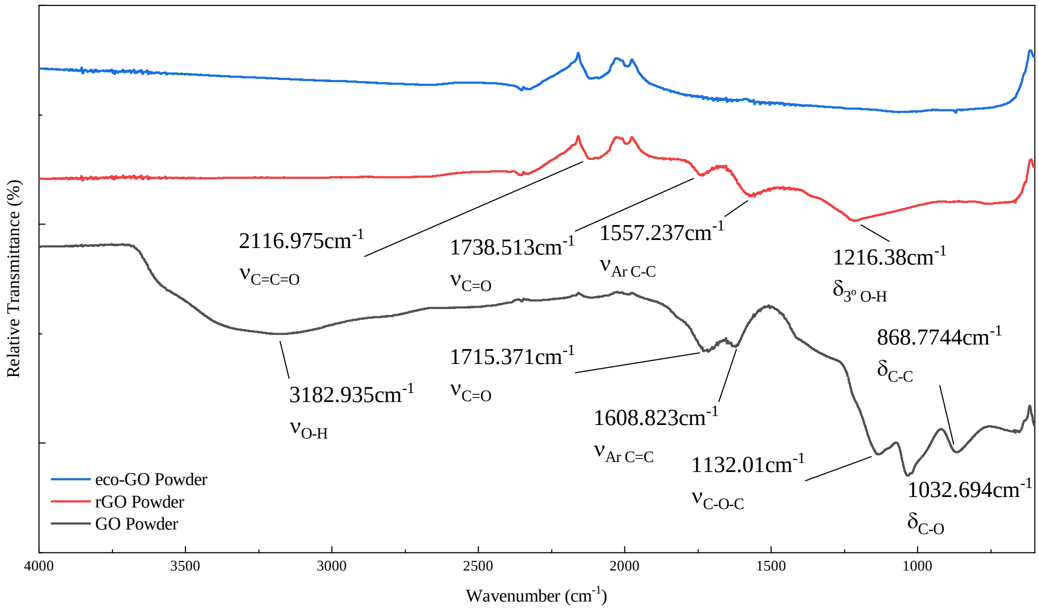

Figure 3.1. FTIR ATR of Go powder, rGO Powder, and eco GO powder

The GO FTIR ATR spectra in Figure 3.1 shows the characteristic hydrophilic oxygenated groups expected by the Lerf-Klinowski model (see Figure 3.2).

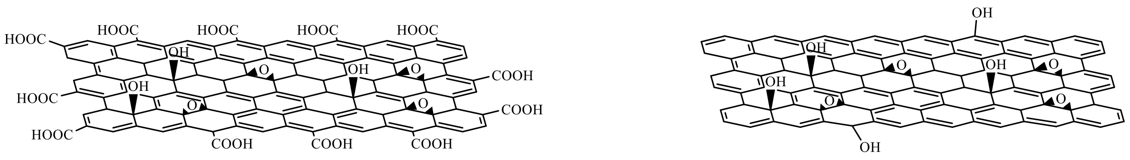

Graphene oxide

Reduced graphene oxide

Figure 3.2. Skeletal formulae for the Lerf-Klinowski model of GO and a thermally rGO sheet that results in the reduction of the carboxyl groups to hydroxyl functionalities or further reduction to the sp2 structure that makes up the basal plane (assuming no defects)

Firstly, the infrared spectrum of the parent GO was analysed and confirmed by agreement with the product datasheet and the literature reports. The broad peak at circa. 3300 cm^{-1} is attributed to the overlap of the hydroxyl groups' stretching modes, which form the many of the oxygenated groups on the sheets. The two peaks at 1611 cm^{-1} and 1688 cm^{-1} support the presence of the carbonyl component of the higher oxidised moieties (carbonyls, and carboxylic acids), and the broad 1040 cm^{-1} being the carbon-oxygen bending mode, assigned in the literature as the remaining epoxide groups.

The FTIR shows that the GO possesses epoxide groups by the C-O-C vibration at 1132 cm^{-1}, which shifts to higher wavenumbers when thermally reduced (1216 cm^{-1}) implying the epoxide group ring opens to produce a tertiary alcohol group. Also, comparison of the rGO and the GO spectra show that the thermal reduction process has diminished the carbonyl groups present in the GO as the peak increases from 1715 cm^{-1} to 1738 cm^{-1} identifying the aromatic carbon-hydrogen vibrational bending overtone.

On the other hand, the scarcity of functionality on the eco-GO with predictions required further analysis through thermogravimetric analysis (TGA) and powder x-ray diffraction (PXRD) to explain this result.

TGA analysis was conducted under an inert 2.0 bar, 30 mL min^{-1} nitrogen gas flow, which was heated at 10 °C min^{-1} between 30 °C and 800 °C to decompose the functional groups without introducing combustion reactions. Figure 3.3 shows the heating profile of GO in agreement with literature observations with the following thermal events:[16–19] drying profile (circa. 100°C); liberation of the labile oxygenated groups (e.g., carboxyl groups), (≥ 200°C ≤ 300°C); liberation of the remaining oxygenated groups (> 300°C) generally residing in the basal plane, leaving the final weight as the carbonaceous honeycomb structure. Therefore, as expected, the parent GO exhibited the weight loss events, reported within the literature. [11,20,21]

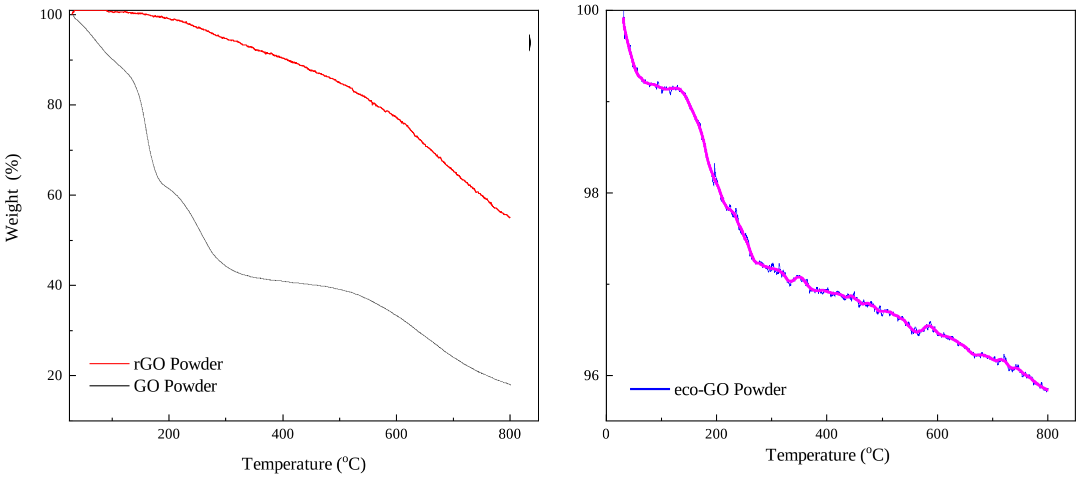

Figure 3.3. TGA trace of GO and rGO powders (left), and TGA trace of eco-GO powder with 400-point Savitsky-Golay filter (purple line) (right).

The TGA trace of the rGO in Figure 3.3 follows a single step weight loss. The thermal event here follows an expected trend due to the reduction process removing most of the oxygenated moieties, which results in the differentiation in thermal behaviour between the GO and rGO.

The significant thermal stability of the eco-GO powder between 30 ℃ and 800 ℃ contradicted all the predictions Figure 3.3. It supported that the formation of reduced defect GO through an electrochemical exfoliation technique had not been successful. Therefore, PXRD was used to investigate the crystal structure of the eco-GO powder.

All the powdered systems were characterised by powder x-ray diffraction (PXRD), to ensure the correct nomenclature is used. Furthermore it is a commonly employed comparative analytical technique to determine surface functionalisation of graphene-related materials through a change in the inter-gallery distance.[15,22–25] The need for a nickel filter was investigated in the method optimisation due to the potential for trace amounts of manganese, inherited from the chemical exfoliation manufacturing process.[26] Manganese can undergo fluorescence when irradiated with x-rays which would increase the diffraction pattern noise. However, this is not as common as iron, but it the phenomena was considered for completeness because it is essential to determine whether trace metal cations were present. The presence can be advantageous by using them as markers in graphene-polymer composites,[4] or mechanical properties enhancement by multivalent cation crosslinking.[27]

To determine whether a nickel filter was required PXRD experiments were conducted on the GO powder with and without the filter, and the scan time varied. The diffraction counts were analysed to ensure the GO diffraction peaks could be observed and the background noise minimal (see Figure 3.4).

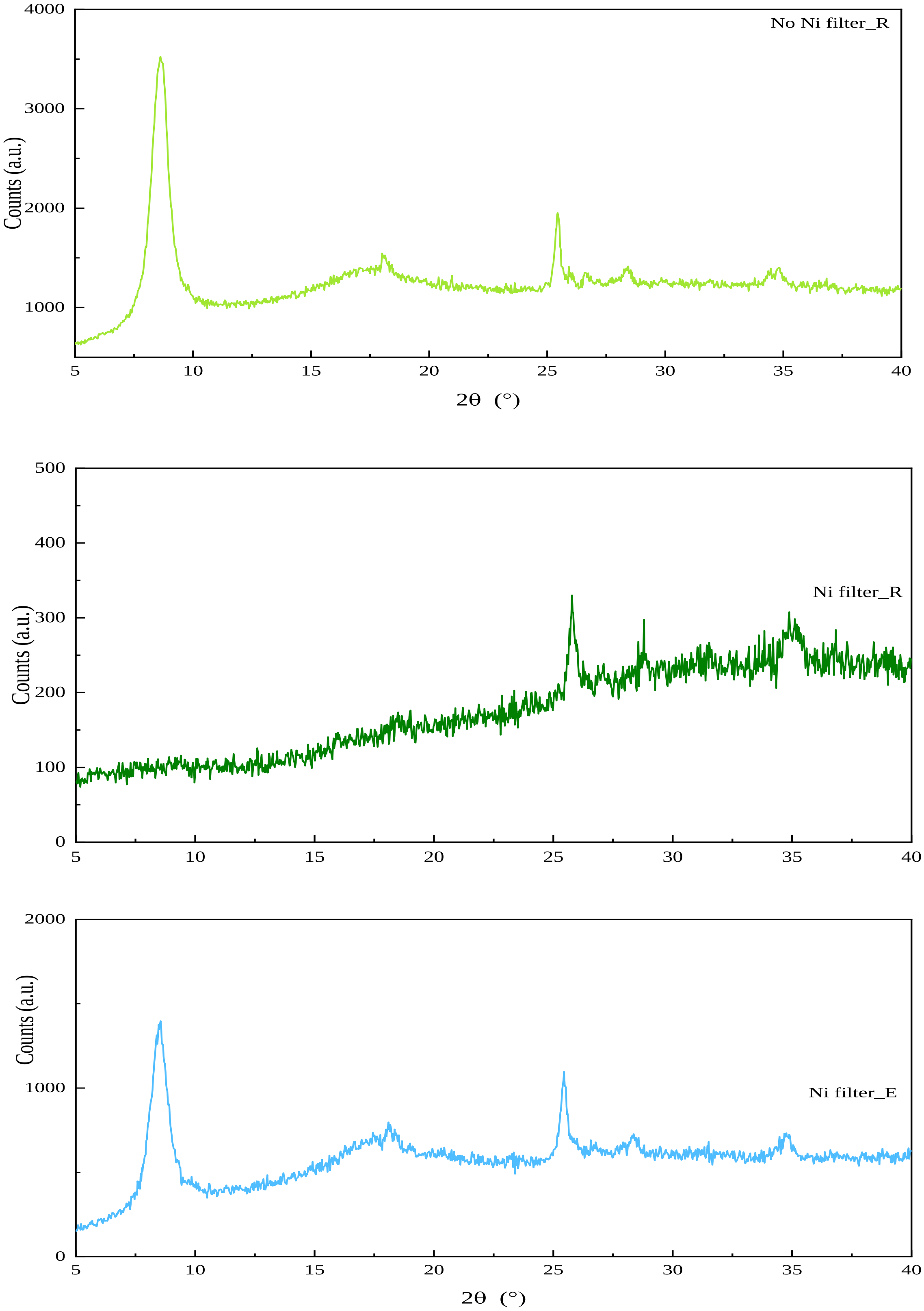

Figure 3.4. Experimental design by investigating the effect of step size change and presence of a nickel filter for the characterisation of crystallinity in GOBM powders which could be hindered by the presence of manganese cations inherited from the

modified Hummer's method. (‘R’ refers to 30-minute scan testing regime and ‘E’ denotes an extended scan regime of 2 hours).

It was found that the PXRD experiments of GO powder during the optimisation showed a nickel filter was not required. Comparison between all the trials showed no new peaks with the only variation being the relative count intensity, which was enough to prevent any peaks concealed in the background noise. The analysis using a nickel filter and a step size of 0.0260 2θ resulted in all peaks disappearing apart from the graphite 002 reflection. Therefore, the nickel filter was removed for all further PXRD experiments and carried out following the previous chapter's protocol.

Using the defined experimental parameters, GO and rGO were characterised using PXRD to determine the inter-gallery distance using the Bragg equation (see (2.5) Chapter 2). The observed diffraction patterns are summarised in Figure 3.5. The PXRD pattern for GO shows five resolvable diffraction peaks at $2\theta = 8.4°$, 18.1°, 25.4°, 28.3°, and 34.8°. The diffraction peaks are expected and satisfy the characterisation of the GO as few-layered (1-3 layers), by the presence of the 8.4° 002 peak which is present because of the oxidation. Through the oxidation process, the reagents transform the 002 sp^2 graphitic structure represented by $2\theta = 26°$ to an exfoliated berthollide exhibiting more sp^3 from the introduction of the oxygenated functionalities which leads to a characteristic peak at $2\theta = 8.4°$ for the GO. The other three peaks represent the other crystalline stacking diffractions of the different sized flakes. Therefore, the characterisation of GO by PXRD was fit for purpose in the comparative effects investigated in the next chapter.

In addition, the PXRD of rGO was carried out under the same conditions as that of the other GOBM powders. The diffraction pattern is shown in Figure 3.5 also shows resolvable peaks at $2\theta = 11.9°$ and 23.4°. The difference in the number of resolved peaks results from the reduced functionality relative to GO meaning the stacking is dominated more by Van Der Waals type interactions rather than hydrogen bonding, leading to a reduction in the inter-gallery distance (7.4 Å) at 11.9°. The other peak at 23.4° can be attributed to the more hydrophobic regions of the rGO, enabling it to possess more sp^2 character and the corresponding crystallinity analogous to graphite.

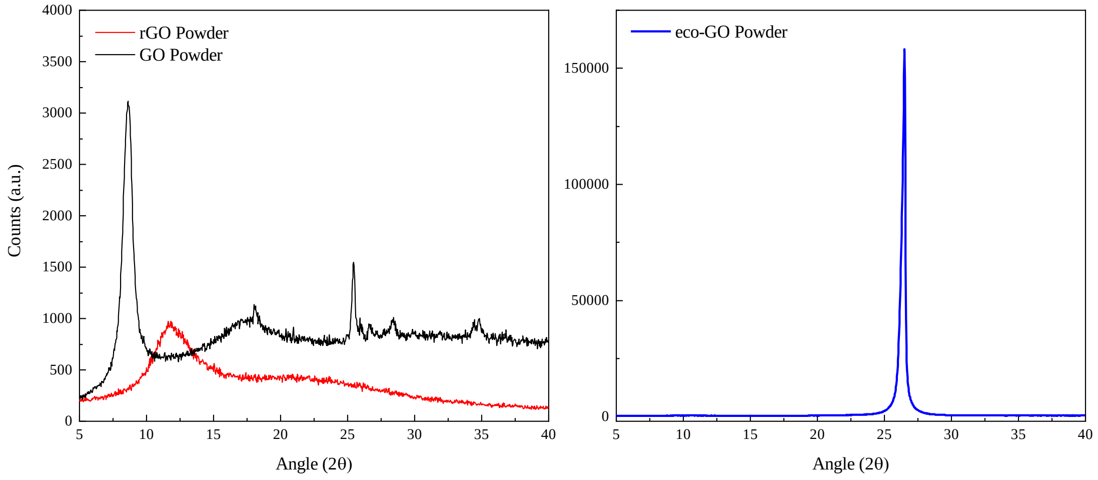

Figure 3.5. PXRD of GO and rGO powder (left), and PXRD of eco-GO powder (right).

To investigate the unexpected thermal stability of eco-GO further PXRD was conducted, and the pattern of the eco-GO shown in Figure 3.5 revealed an intense diffraction peak at 26 °, which is indicative of the 002 diffractions of graphite. As a result of no other peaks being present, this conclusively supports the proposition that the eco-GO product absorbs infrared strongly and has high thermal stability behaviour because the electrochemical exfoliation was not successful. The high purity crystalline graphite remained as a stacked sp^2 carbon allotrope.

Therefore, because of the data presented in Figure 3.1,Figure 3.3, and Figure 3.5 it was decided to conclude investigating the properties of the eco-GO product and investigate the effect of loading GO or rGO into a commercial polyurethane matrix only. The production of eco-GO was ceased commercially.

3.2. Polyurethane matrix development

Easyflo 120 was selected as a commercial polyurethane resin due to its good mechanical performance and short pot life, enabling the quick gelation, therefore, preventing phase separation of the filler and matrix through stacking.

Samples were prepared through a 1:1 v/v formulation as recommended by the manufacturer's guidelines. A 16 mL system was prepared based on the fabricated mould volume which was calculated. Mixing by volume resulted in the production of mechanically inconsistent samples, as tested by tensile testing which resulted in high standard deviation between samples. This was postulated since measuring by volume results in difficult reproducibility and molar ratios which are very important in polyaddition polymerisation systems, further development was required. To develop this, a 1:0.9 w/w formulation as recommended by the manufacturer's guidelines was tested. A 16.2 g system was prepared based on the calculation of the desired mould volume. Mixing by weight resulted in more mechanically consistent samples; however, visual defects were observed such as air bubbles, so the method required more development. The mixed resin was cast into the prepared mould and left to cure for 1 hour at ambient conditions before visual inspection. The curing time was sufficient to generate solid polymerised polyurethanes so was fixed in the method. Method development fixed the w/w formulation and curing time, and varied different parameters such a mixing speed, time, vessel, and spatula size.

Variation of the mixing vessels assessed polypropylene cups, and falcon tubes. It was found that the flat-bottomed polymeric cups were more effective in producing better-quality polyurethanes. Glass beakers were also tested however air bubble formation was present which was expected due to the hydrophilic nature of the glass surface therefore the other two tests included hydrophobic polymer vessels. These observations resulted led to the hydrophobisation of the manufactured glass plate moulds using dichlorodimethylsilane and the mould the glass plates nested into made of commercial polydimethylsiloxane which is also hydrophobic. To reduce air bubbles from the mixing technique, the spatula surface area was increased so that more surface contact could be added into the system without increasing the mixing speed. The spatula blade's surface area nearly spanned the internal diameter of the polypropylene container, meaning there was less chance for whisking errors and the spatula could collide with the trapped air bubbles. The spatula with a surface area of 4 cm^2 produced the best mixing as the larger spatula surface areas created to much drag force in the beakers leading to air bubble formations from whisking effects and the smaller spatula surface areas did not mix the resin effectively within the pot life timeframe sufficiently to prevent heterogeneous phases.

An investigation of the mixing time between 60, 75 or 90 seconds found that 90 seconds produced the most reproducible polyurethanes.

Following all the investigations it was found that the standard protocol would be a 16.2 g 1:0.9 w/w formulation mixed in a flat-bottomed polypropylene cup using a 4 cm^2 metal spatula head for 90 seconds before drop casting into hydrophobic glass plates within a silicone mould, spaced with 1 cm^3 glass spacers and compressing with a second hydrophobic glass plate which was weighed down with 250 g of mass.

To investigate whether the mixing time could be extended which could minimise the potential of air bubbles, Easyflo 95 was investigated due to its longer pot life of 5 minutes. This longer pot life enabled investigations into the introduction of a degassing step into the protocol. Therefore, virgin Easyflo 95 samples were prepared as per the standardised protocol found above and after mixing were degassed using mild vacuum for 30 seconds. However, it was found by visual inspection that the resin volume had decreased, suggesting that some of the formulated components had evaporated, which lead to inadequate sample production after repetition too. To avoid evaporating any components during degassing, the resin samples were prepared and degassed for 1 minute using the degas function on the Fisherbrand® FB15048 ultrasonic bath at ambient temperature. However, a similar observation occurred and led to inhomogeneous polyurethanes. The final degassing protocol to be trialled was to mix the resins in a 50 mL Falcon tube and centrifuge at 5000 rpm for 1 minute using a Thermo Centrifuge X7. The centrifuge samples cast and cured for 1 hour at ambient temperature were still mechanically inadequate; however, the air bubbles had reduced, but inhomogeneity still occurred, which could be resultant from phase separations during centrifugation. As a result of these investigations Easyflo 95 preparations were discontinued and Easyflo 120 was utilised in all composite fabrications.

3.1.1. Effect of post-curing on the tensile properties

Once the protocol to determine a reproducible and suitable polyurethane had been determined the effect of post-curing was evaluated. These experiments were conducted by fabrication of Easyflo 120 as a virgin polymer by curing at 16℃ and then post-curing at 25 ℃ for 7-days, 45 ℃, or 75℃ for 16 hours. The manufacturer's guidance produced two elastic moduli, one for room temperature post-curing for 7 days and the other at 75℃ for 16 hours. Both processes were investigated with another post-cure temperature at 45℃, which was just above the virgin polyurethane's glass transition temperature (T_g = 43 ± 3℃) as determined by DSC. The elastic modulus, ultimate tensile strength, elongation at break, and toughness were all calculated for comparison and shown in Figure 3.4.

For the elastic modulus, it was determined by calculating the maximum of the slope (E_{max}) and by the international standard ISO-527 (E_{ISO}) given in Chapter 2.

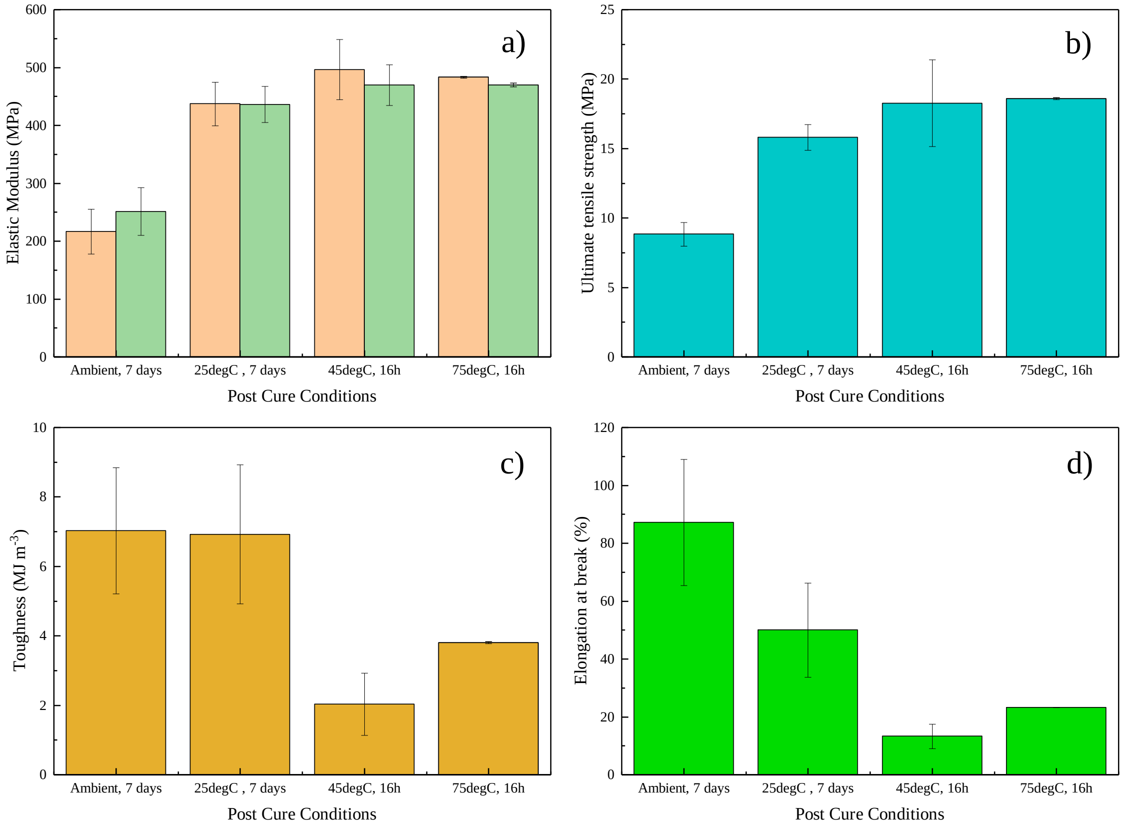

Figure 3.6. The effect of post-curing on the tensile properties of Easyflo 120 polyurethanes by variation of post-cure temperature and time. (n=10) The study investigated the effect on the a) elastic modulus, (E_{max} = orange bars, and E_{ISO} = light green), b) ultimate tensile strength, c) toughness, and d) elongation at break.

The data presented in Figure 3.4. shows an increase in the post-cure temperature resulting in an increase in the elastic modulus until 75°C, which sees a small reduction (2.6%) compared to the 45°C post-cure methodology. A similar trend is observed in the ultimate tensile strength showing that an increase in post-cure temperature increases the ultimate tensile strength. Whereas for the toughness and elongation at the break, the trends reverse and decrease as the temperature increases.

As expected, these properties which demonstrate that a higher post-cure temperature suggests stronger solid properties because of increased crosslinking in the polymer chain and the subsequent decrease in impact dissipation and elongation at break.

Therefore, it was decided due to the properties for frequent impact dissipation that a more viscous behaviour was required rather than a more cross linked stiffer material. Therefore because of the higher elongation at break and toughness at ambient temperature and 25 ˚C the standard protocol for fabrications incorporated a post-cure step of 25℃ for 7-days controlled by a programmable laboratory oven. Ambient temperature was not selected due to the fluctuation in environmental temperature and humidity throughout the study.

3.3. Fabrication of GOBM polyurethane composites

Preliminary experiments investigated the use of isopropanol, which is volatile and compatible with the filler and matrices. However, despite efforts to reduce the isopropanol in the formulation, it still resulted in plasticity effects as expected through high elongation at breaks and significantly reduced elastic moduli when it was subjected to tensile testing. Therefore, to overcome the plasticity effects stock suspensions of GOBMs were prepared directly into the polyol component (Part B) of the commercial polyurethane resin. The polyol component rather than the monomer component (Part A) was selected as the continuous phase because the blend contained a multitude of functionalities capable of hydrogen bonding. In contrast, the isocyanate in Part A could potentially react with the GO during the dispersion preparation.

To determine a suitable protocol for preparing a GO in Part B, 10 mg mL^{-1} suspensions were prepared and dispersed for 5, 15 and 30 minutes to assess their dispersibility and stability. The stability was evaluated over one month under ambient conditions and found that the some of the GO was still dispersed in Part B after one week, which was attributed to the smaller sheets from the prepared batch.

Furthermore, it was found that the longer the sonication, the better the dispersion and stability, however, all samples show good stability during the polyurethane's initial gelation time (t = 30 minutes), enabling successful *in situ* polymerisation to occur homogeneously. Because 30 minutes sonication provided the best dispersibility for the investigated suspensions, a 10 mg mL^{-1} GO in Part B stock suspension was prepared for the fabrication of the graphene oxide-based polyurethane composites (GOPU). However, for the rGO stock suspension the low bulk density which meant that large volumes of resin would be required as it formed black sols resulted when preparing a 10 mg mL^{-1} stock concentration. This black sol was not viable because no free bulk resin volume was available for the resin constituents and the rGO mobility during ultrasonication to sterically exfoliate the rGO sheets and uniformly integrate the filler into the resin. A stock suspension of 5 mg mL^{-1} was determined to be the most viable stock concentration enabling dispersion and achievable stock volumes for each weight loaded composite.

The GOBM-PU samples were cured at 16 °C for 30 minutes in the prepared mould and post cured at 25 °C for 7 days to result in white composites for the GOPU and increasing shades of grey for the rGOPU as shown in Figure 3.7.

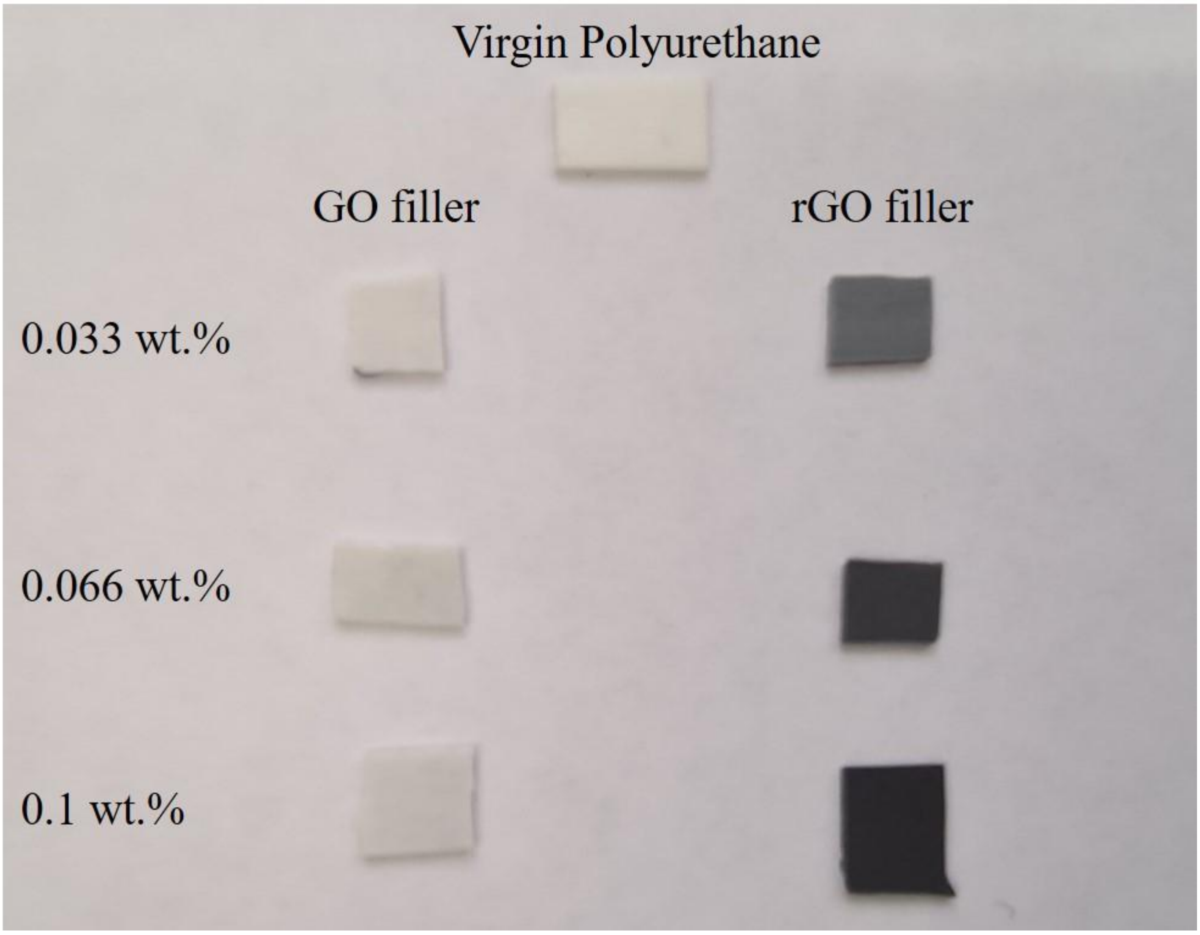

Figure 3.7. Photograph to demonstrate the variation in visual colour between the GOPU and the rGO composites. A swatch sample of the virgin polyurethane was present as a control to compare against the GOBM polymer composite swatches.

As shown by Figure 3.7 the GO does not impart any colour change to the virgin polyurethane. However, the rGO does dominate the polymer composite’s colour and it was observed that an increase in filler resulted in a darker material with 0.033 wt.%

observed as grey and 0.1 wt.% appearing black. These observations were expected due to the significantly low bulk density of the rGO (0.001 – 0.01 g cm^3).[28] This means that a greater spatial volume is required to generate the necessary weight loading of these small sheets. This leads to more pigmentation due to smaller sheets been spatially closer together within composite, unlike GO(0.5 - 0.8 g cm^3).[29] Because of the mixing of the black filler and the white matrix resulting in darker pigmentation with increasing weight loading it was deemed appropriate so no further investigations on the origin of colour where undertaken. In addition, the samples show a homogenous colour palette throughout the sample demonstrating that the filler and matrix mixed effectively. To confirm a successful polymerisation had occurred the solid composites were characterised by diamond FTIR ATR as shown in Figure 3.8 to support the successful polymerisation.

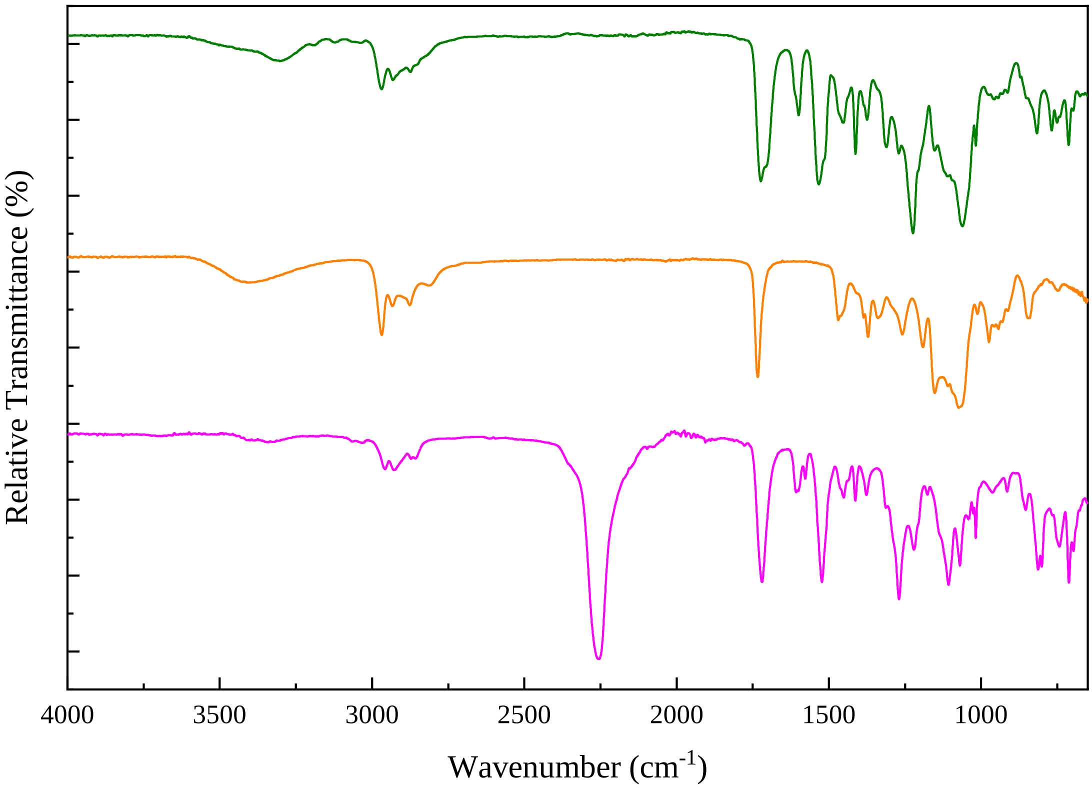

Figure 3.8. Diamond FTIR ATR showing the two-component resins, Part A (magenta), Part B (orange), and 0.033GOPU (olive green) to demonstrate the successful

polymerisation has occurred. 0.033GOPU was used to demonstrate all the polymer composites for clarity.

Figure 3.8 shows the characteristic isocyanate vibrational stretch at 2290 cm^{-1} disappeared after polymer composite formation. The isocyanate stretching mode absence, therefore, suggests that the system has polymerised as expected. To understand the effect of filler loadings within the Easyflo120 polyurethane matrix the polymer composites were analysed to evaluate their tensile properties and their impact dissipation candidacy.

3.4. Effect of filler loading on the glass transition temperature

The glass transition temperature (T_g), which is the point when a glassy polymer transitions to an amorphous rubbery like structure is an important indicator for a materials end-application and its mechanical behaviour at a given temperature.

The glass transition temperature for the unmodified GOBM polyurethane composites was determined by the differential scanning calorimetry (DSC) and dynamic mechanical thermal analysis (DMTA) techniques. To determine the effect of filler loading on the T_g using DSC the values were determined by extrapolating half the heat capacity of the T_g. The triplicate sampling for DSC was averaged and summarised in Figure 3.9.

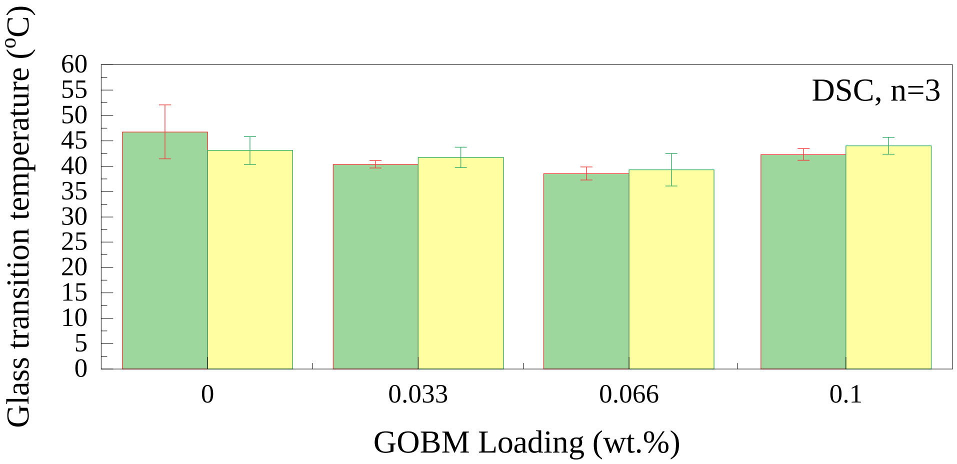

Figure 3.9. The effect of GOBM filler loading on the glass transition temperature by extrapolating half the heat capacity of the glass transition peak, for GOPU (green), rGOPU (yellow).

The average T_g determined by DSC showed no significant effect of GOBM loading on the glass transition temperature of the virgin polyurethane (T_g = 43 ± 3 °C) due to the observed changes falling well within the standard deviation range for each test set. However, it was observed that in both the GOPUB and rGOPUB that the addition of filler led to a decrease in the Tg through a minimum at 0.066 wt.% before increasing again at 0.1 wt.%.

Therefore in order to further investigate if any effect is observed DMTA was used as the frequency can be fixed, therefore negating frequency fluctuations which affect T_g.[30] The frequency was fixed at 10 Hz, based on the master curve generated during testing optimisation.

The T_g was therefore determined by DMTA by the onset of the loss modulus and by the maxima of the tanδ peak. Ten repeats were averaged, plotted (see Figure 3.10) and subjected to statistical testing by analysis of variance (ANOVA) to determine significance on the effect of GOBM filler loading.

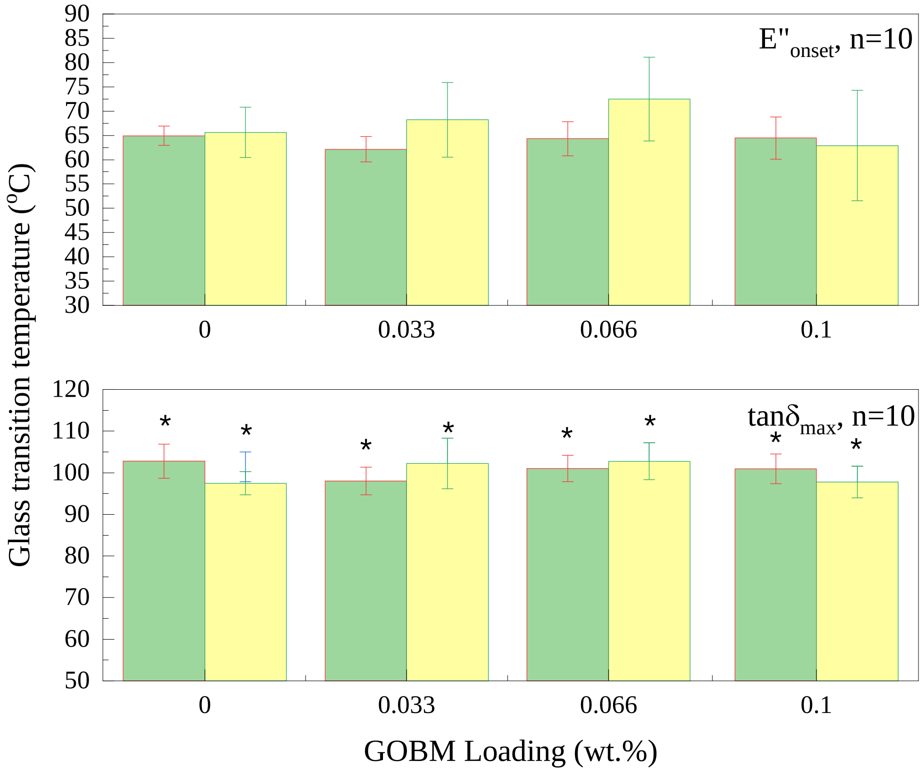

Figure 3.10 Plot to compare the effect of GO (green) and rGO (yellow) loading on the instrumented indentation elastic modulus within a polyurethane matrix at varying weight percent loadings using nanoindentation. ANOVA single factor (at 95% confidence) results, GOPU ($\tan\delta_{max}$) composites: F-value = 3.09 and p-value = 3.90 x 10^{-2} from a population of n=10. rGO PU ($\tan\delta_{max}$) composites: F-value = 17.28 and p-value = 4.07 x 10^{-7} from a population of n=10. Null hypothesis rejection denoted by an asterisk above the upper uncertainty limit.

The glass transition temperature as determined by the loss modulus onset showed a reached a maximum at 0.066 wt.% in the unmodified GOBM fillers. However, when the Tg was determined by the maximum of the impact dissipation factor, tanδ the glass transition temperature subtly rose with increasing filler loading. However, the trend decreased and was comparable with the virgin polyurethane 0.1 wt.%.

All three methodologies show that the rGO shifts the T_g to higher temperatures which was noted. This behaviour could be resultant from a few factors: enhanced thermal conductivity of the rGO which is reported,[2,31] and/or enhanced filler matrix adhesion based on hydrophobicity which creates more short-range interactions resulting in a stiffer material. Tensile analysis showed the addition of GOBM fillers did lead to a stiffer material in both cases.

3.5. Effect of filler loading on the elastic modulus

Tensile testing was conducted at a fixed isotherm of 30°C as per the protocol outlined in in the previous chapter. In addition, a theoretical elastic modulus was predicted using the Rules of mixtures. GO and rGO filled composites were theoretically calculated through substitution into equation ***(2.11)*** of the theoretical variables given in Chapter 2 to give the equations ***(3.1)*** and ***(3.2).***

$$\boldsymbol{E_{GOPU} = E_{GO} + E_{PU}(1 - V_{GO})} \tag{3.1}$$

$$\boldsymbol{E_{rGOPU} = E_{rGO} + E_{PU}(1 - V_{rGO})} \tag{3.2}$$

where E_{GOPU} refers to the theoretical elastic modulus of the specific polymer composite, E_{GO} is the theoretical elastic modulus of the filler, E_{PU} is the theoretical elastic modulus of the virgin polyurethane and V_{GO} is the volume fraction of the filler. GO subscripts denote the GO systems and rGO subscripts denote the rGO systems. The resultant theoretical tensile elastic moduli were plotted in Figure 3.11 for GO composites and Table 3.1 for rGO composites.

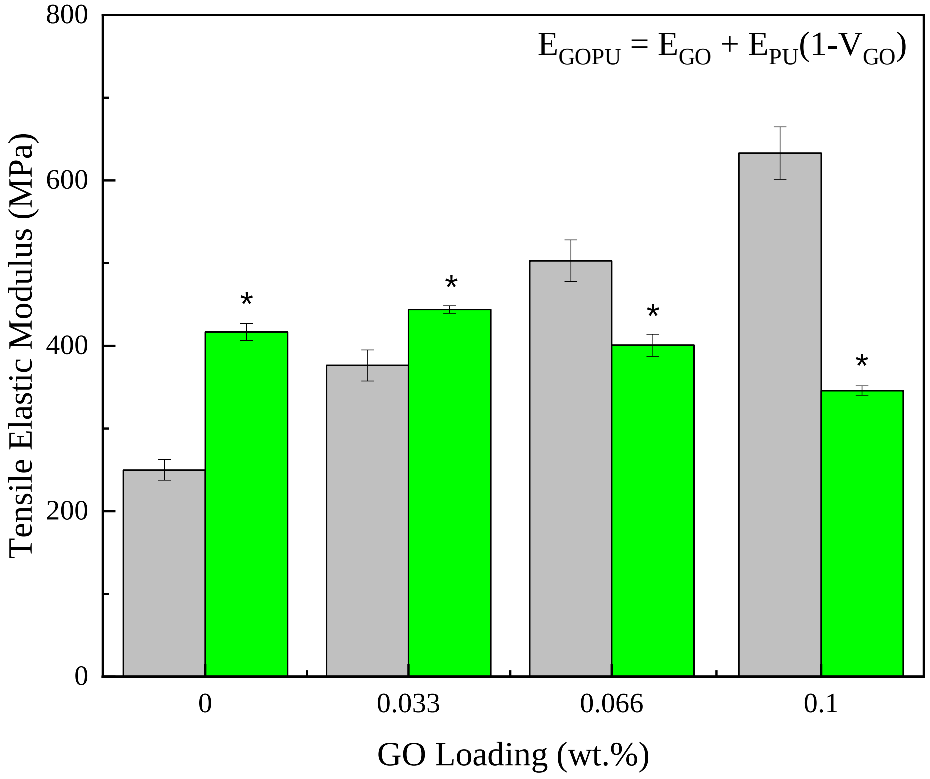

Figure 3.11. The effect of GO loading on the theoretical elastic modulus (grey) determined by the Rule of Mixtures assumptions (standard deviation set at p = 95%) for GOPU and the experimental tensile elastic modulus within a polyurethane matrix (lime green) at varying weight percent loadings using nanoindentation. ANOVA single factor (at 95% confidence) results, GOPU composites: F-value = 4.41 and p-value = 9.65 x 10^{-3} from a population of n=10. Null hypothesis rejection denoted by an asterisk above the upper uncertainty limit.

Figure 3.11 shows that the theoretical tensile elastic modulus for the virgin polyurethane was found to be higher during experimental testing. The Rule of Mixtures model for 0.033 wt.%, 0.066 wt.% and 0.1wt.% shows an -18%, 20%, and 45% model error respectively. For the 0.033 wt.% GO the greater experimental tensile modulus compared to the theoretical due to the higher experimental elastic modulus of the polyurethane matrix. Unlike the 0.066 wt.% and 0.1 wt.% which underperformed against the calculated Rule of Mixtures tensile modulus it shows that the 0.033 wt.% GO composite agrees with the assumptions specified in the model (uniform distribution and good filler matrix adhesion). The underperformance of the 0.066 wt.% and 0.1 wt.% suggests that under tensile conditions the assumptions are not fully observed with it suggested that at 01 wt.% aggregation of the sheets could be occurring.

The rGO composites were calculated and experimentally determined and tabulated in Table 3.1 due to the high theoretical elastic moduli which were not in the same order of magnitude as experimental tensile testing.

Table 3.1. Tensile elastic modulus data of rGOPU composites calculated using the Rule of Mixtures and tested experimentally at 30˚C

rGO Loading (wt.%)	E_{rGOPU} (GPa)	$E_{Experimental}$ (GPa)
0	0.25 ± 0.01	0.42 ± 0.01
0.033	32 ± 2	0.38 ± 0.02
0.066	64 ± 3	0.41 ± 0.03
0.1	97 ± 5	0.40 ± 0.03

The theoretical elastic modulus calculated by the rule of mixtures model for rGO shows significant predicted enhancements. For rGO they are even more significant than GO with a monotonic increase in tensile elastic modulus of 13 – 15 GPa for every 0.033 wt.% increase. However, these trends were not observed experimentally. This significant discrepancy in the model and experimental values shows that the assumptions made in the rule of mixtures model are not reflected in the fabricated composites. These deviations from the model are expected by the model's limitations which makes assumptions such as unidirectional alignment of the filler and optimal filler-matrix adhesion.[31]

The indentation elastic modulus was also measured and analysed using nanoindentation to determine the elastic response under compressive forces as a comparison to the tensile investigations. The data was averaged and plotted as a function of the GOBM filler loading in Figure 3.12.

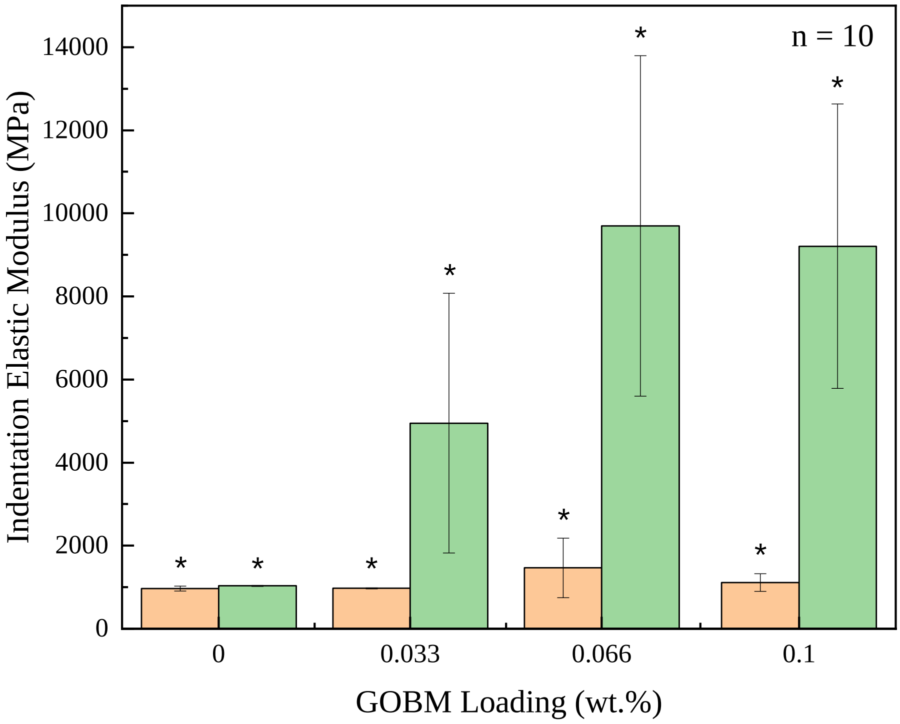

Figure 3.12. Plot to compare the effect of GO (orange) and rGO (green) loading on the instrumented indentation elastic modulus within a polyurethane matrix at varying weight percent loadings using nanoindentation. ANOVA single factor (at 95% confidence) results, GOPU composites: F-value = 3.83 and p-value = 1.81×10^{-2} from a population of n=10. rGO PU composites: F-value = 17.28 and p-value = 4.07×10^{-7} from a population of n=10. Null hypothesis rejection denoted by an asterisk above the upper uncertainty limit.

Figure 3.12 shows that addition of GO to the polyurethane does not lead to a significant elastic response under indentation conditions. An observable enhancement of 51% is observed at 0.066 wt.% but decreases again after reaching a maxima indentation elastic modulus at 0.066 wt.%. However, at 0.1 wt.% the elastic modulus enhancement remains 15% higher compared to the virgin polyurethane. For the rGO filled composites a similar trend is observed however significant enhancements are observed for 0.033 wt.% (380%), 0.066 wt.% (840%), and 0.1 wt.% (792%). The significance of the indentation enhancement is attributed to the smaller lateral flake size of the rGO not restricting the composite molecular mobility as much as the GO during elastic response under compression.

Comparison with the theoretical rule of mixtures elastic modulus assumptions shows both systems align better with indentation elastic modulus than the tensile elastic modulus. This closer representation suggests that when the material is under compressive loads the elastic response suggests that the sheets have a more unidirectional structure, and the filler matrix adhesion increases which could be expected as the applied load compresses the sheets closer to the matrix giving greater adhesion contact.

3.6. Effect of filler loading on the tensile viscoelastic properties

Dynamic mechanical analysis was conducted on a TA Instruments Q800 setup in dynamic testing mode at 10 Hz, heating at 10 °C min^{-1} between 25°C and 180 °C. The analysis was conducted on the fabricated GOBM polyurethane composites to investigate the viscoelastic response to tensile load. This study investigated the effect of filler loading on the impact dissipation factor, tanδ, which relates the system's elastic and viscous components together the data was averaged and presented in Figure 3.13.

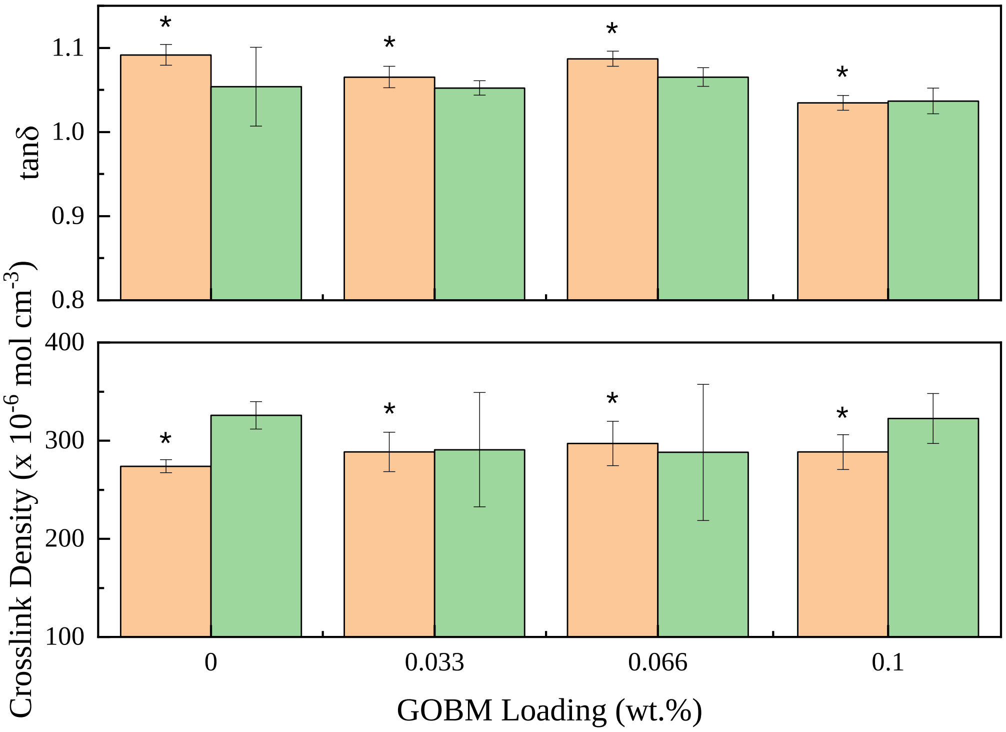

Figure 3.13. Plot to compare the effect of GO (orange) and rGO (green) loading on the instrumented indentation elastic modulus within a polyurethane matrix at varying weight percent loadings using nanoindentation. ANOVA single factor (at 95% confidence) results, GOPU (tanδ) composites: F-value = 57.4 and p-value = 8.59 x 10^{-14} from a population of n=10. GOPU (crosslink density) composites: F-value = 3.06 and p-value = 4.10 x 10^{-2} from a population of n=10. rGO PU (tanδ) composites: F-value = 1.90 and p-value = 0.149 from a population of n=10. rGO PU (crosslink density) composites: F-value = 1.73 and p-value = 0.179 from a population of n=10. Null hypothesis rejection denoted by an asterisk above the upper uncertainty limit.

Figure 3.13 showed a decrease in the tanδ with the addition of 0.033 wt.% GO but increased at 0.066 wt.% then decreased again at 0.1 wt.%. As expected the tanδ was highest for the virgin polyurethane showing that this system possessed greater molecular mobility of the polymer chains, and with the addition of a filler to the system this reduced as the filler interacted with the polymer matrix.[32,33] To further determine the data's significance, single-factor analysis of variance (ANOVA) was computed across the whole sample population. The computed F-value from this analysis was much greater than the critical F-value, therefore rejecting the null hypothesis and concluding that there was significance that the addition of GO reduced the polymer chain mobility in the composites. Furthermore, the P-value was significantly less than the 95% confidence interval, further supporting the data. The impact dissipation factor decreases, which is expected, suggesting the GO filler forms a network at higher loadings. This results in the reduction of viscous flow to produce a more elastic response and less energy dissipation.[34]

The crosslink density shows a subtly but consistent trend with the tanδ which suggests that at 170 ℃ the elastic component decreases at 0.1 wt.% which could be resultant from either microphase aggregation during tension or reduced covalent cross links in the polymer matrix.

3.7. Effect of filler loading on the material stiffness

A Berkovich tipped nanoindentation was made at 10 sites within a 15 µm^2 area to evaluate the mechanical performance. The indentation stiffness was calculated from the instrumentation before it was averaged and plotted as a function of the GOBM loading (see Figure 3.14) with statistical testing using single-factor ANOVA to determine significance.

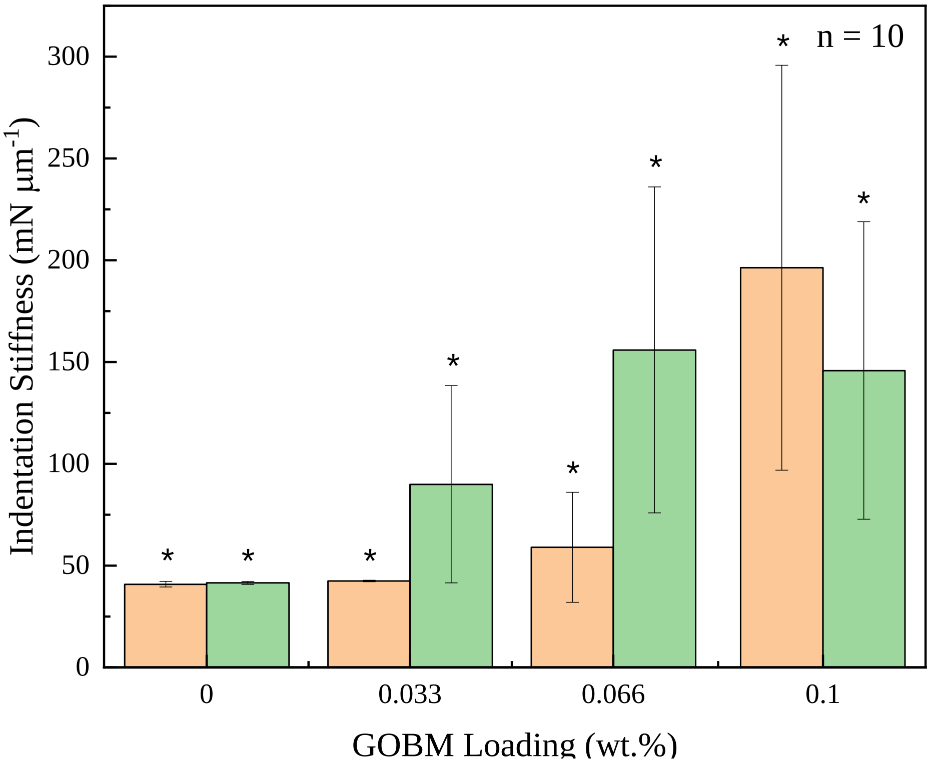

Figure 3.14. Plot to compare the effect of GO (orange) and rGO (green) loading on the indentation hardness within a polyurethane matrix at varying weight percent loadings using nanoindentation. ANOVA single factor (at 95% confidence) results, GOPU composites: F-value = 21.1 and p-value = 4.58 x 10^{-8} from a population of n=10. rGOPU composites: F-value = 9.61 and p-value = 8.42 x 10^{-5} from a population of n=10. Null hypothesis rejection denoted by an asterisk above the upper uncertainty limit.

Figure 3.14 shows that the addition of unmodified GOBM fillers leads to an increase in the indentation stiffness. In the rGO polyurethane composites the addition of rGO continues to increase before the stiffness begins to decrease again at 0.1 wt.%. For GO filled composites the stiffness continues to increase throughout the whole weight loading range. The increase in the indentation stiffness is postulated to arise from the enhanced filler matrix adhesion of the sp^2 carbon honeycomb basal plane with the polymer backbone.[31] The difference in GO and rGO is attributed due to the larger surface area and lateral flake size (see data sheet,[28,29] and Chapter 4) meaning greater relative crystallinity characteristics from the filler.

3.8. Effect of filler loading on the hardness and creep

The material hardness which is the ability to resist plastic deformation. The analysis was conducted using nanoindentation fitted with a Berkovich tip. The hardness measurements were calculated by the instruments software to produce the instrumentation hardness (H_{IT}) which was averaged and plotted in Figure 3.15.

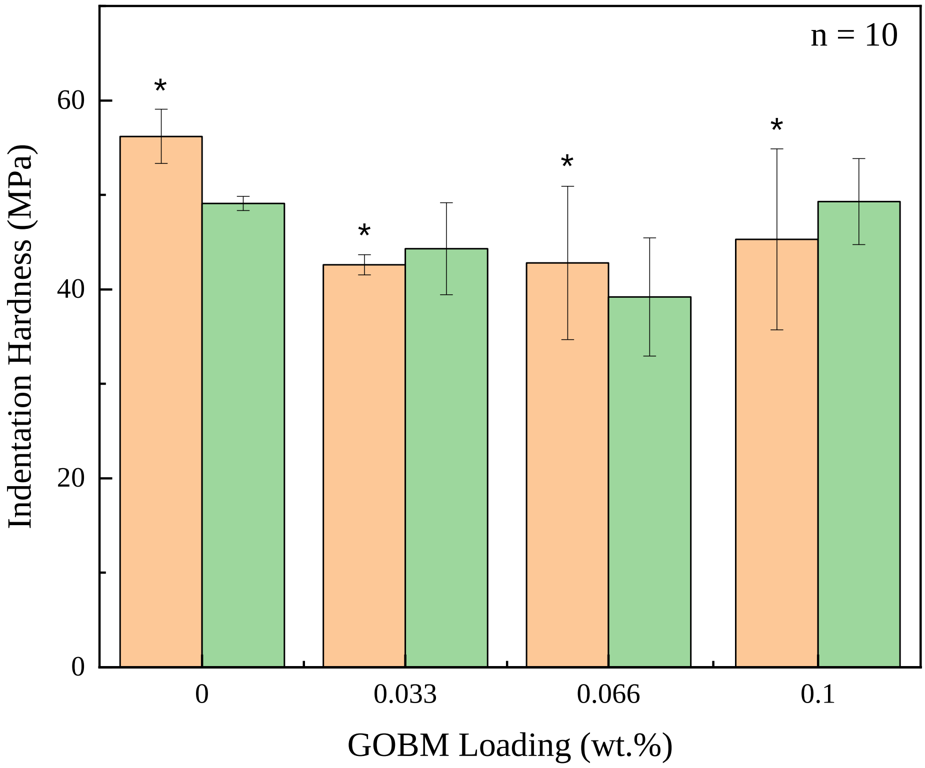

Figure 3.15. Plot to compare the effect of GO (orange) and rGO (green) loading on the indentation hardness within a polyurethane matrix at varying weight percent loadings

using nanoindentation. ANOVA single factor (at 95% confidence) results, GOPU composites: F-value = 42.1 and p-value = 7.45×10^{-12} from a population of n=10. rGOPU composites: F-value = 1.94 and p-value = 0.14 from a population of n=10 Null hypothesis rejection denoted by an asterisk above the upper uncertainty limit.

For the GO-based polyurethane composites the addition of GO results in a decrease in the indentation hardness initially at 0.033 wt.% and then gradually increases again as more GO is added. For the rGO composites the negative trend was extended to 0.066 wt.% instead. Statistical analysis using ANOVA demonstrated that the GO-based composites were statistically significant at 95% confidence. The rGO composites did not meet the statistical threshold like the GO composites including their repeats. The decrease in indentation hardness of the polymer composites indicates that the GO and rGO could be imparting too much crystallinity and creating a more brittle material with an increase in plastic stress response when cross referenced with the indentation stiffness trends (see Figure 3.14).

The indentation creep was investigated to characterise the composites under constant load. The creep was measured using nanoindentation, averaged and summarised in Figure 3.16.

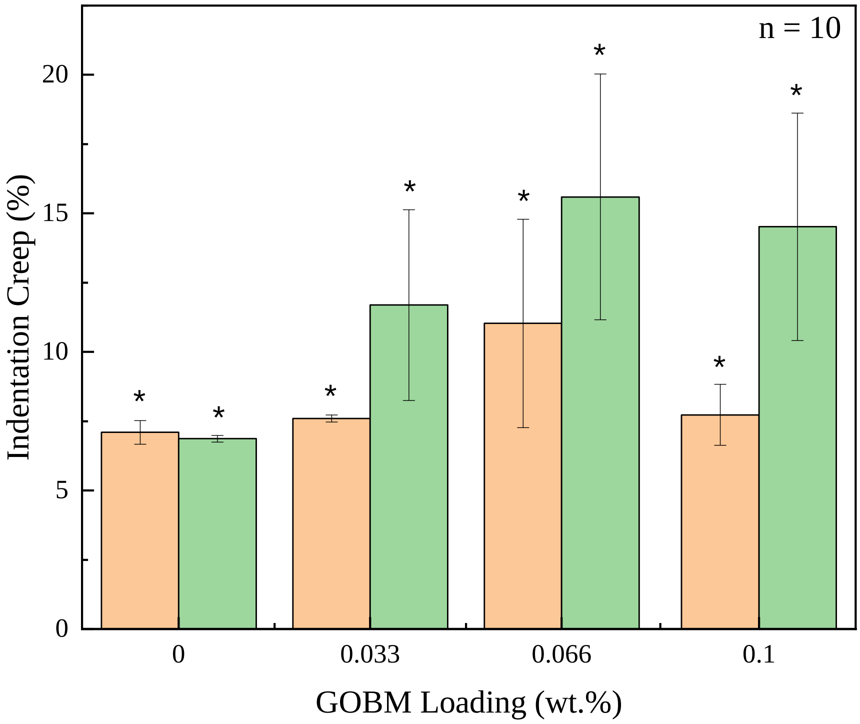

Figure 3.16. Plot to compare the effect of GO (orange) and rGO (green) loading on the indentation stiffness within a polyurethane matrix at varying weight percent loadings using nanoindentation. ANOVA single factor (at 95% confidence) results, GOPU composites: F-value = 9.59 and p-value = 1.24 x 10^{-4} from a population of n=10. rGO PU composites: F-value = 12.6 and p-value = 9.04 x 10^{-6} from a population of n=10. Null hypothesis rejection denoted by an asterisk above the upper uncertainty limit.

In both cases the addition of a GOBM filler increases the indentation creep of the polymer composite in which rises to a maximum creep at 0.066 wt.%. The addition of more filler at 0.1 wt.% results in a decrease in the creep. Comparison of both the GO and rGO found that rGO possessed a more significant creep enhancement than the GO.

The creep enhancement is expected due to the large specific surface areas of the fillers restricting polymer chain motion which would occur under an applied load and favour disentanglement rather than chain rupture. The rGO is significantly larger that the GO because the bulk density means a larger number of flakes are present within the matrix which raises the probability of polymer chain mobility further. The observed creep behaviour is expected due to the fillers compacting under load and imparting crystallinity into the matrix or creating stacking of rGO sheets that are in proximity.

3.9. Chapter conclusion

Three different GOBMs have been characterized by using infrared spectroscopy, thermogravimetric analysis, and powder x-ray diffraction. It was found that eco-GO, a new commercial product, had not successfully exfoliated by the presence of the strong graphite diffraction pattern. Because of this GO and rGO were continued into the fabrication of commercial polyurethane composites by an *in situ* polymerisation approach. The unmodified GO and rGO were prepared in 10 mg mL^{-1} and 5 mg mL^{-1} suspensions in Part B of the two-component resin and cast at 16 °C for 1 hour before post-curing at 25 °C for 7-days. The mechanical performance was evaluated by isothermal tensile testing, dynamic mechanical thermal analysis, and nanoindentation.

The glass transition temperature was compared by three different methods: differential scanning calorimetry, the tanδ maximum, and the onset of the loss modulus curve. As a result of the natural frequency fluctuations, the data by differential scanning calorimetry was found to be not as robust. The fluctuation potential was overcome by fixing the frequency at 10 Hz using dynamic mechanical analysis.

It was found that the rGO imparted significant stiffness into the matrix during the nanoindentation investigations which saw a peak stiffness at 0.066 wt.% with an enhancement of 840% compared to the virgin polyurethane. The GO also behaved similarly, however the enhancement was not as significant. In both cases the effect of GOBM filler did decrease the indentation hardness to below 0.1 wt.% with the GO been comparable to the virgin polyurethane.

The composites were also subjected to tensile testing regimes which confirmed the increased crystallinity assumptions with the tensile stiffness increasing with filler loading. The tensile elastic modulus showed no significant enhancement which could be attributed to the virgin polyurethanes high elastic modulus leading to no significant enhancement. Comparing the elastic modulus with the theoretical elastic modulus, calculated by the rule of mixtures showed that the indentation elastic modulus was more representative to the model's assumptions.

The objectives of this chapter were achieved by the selection of suitable graphene oxide-based fillers and investigating the effect of preparing *in situ* polymerised composites by variation of the loaded stock which have different stabilities and comparing the performance to the impact dissipation brief design brief.

Finally, it was found that the addition of GO or rGO does not impart the relevant properties for the rain erosion protection candidates due to their addition increasing the indentation stiffness and therefore reduced flexibility to resist frequent liquid impingement impacts.

Chapter references

1 K. Krishnamoorthy, M. Veerapandian, K. Yun and S. J. Kim, *Carbon N. Y.*, 2013, **53**, 38–49.

2 C. Botas, P. Álvarez, P. Blanco, M. Granda, C. Blanco, R. Santamaría, L. J. Romasanta, R. Verdejo, M. A. López-Manchado and R. Menéndez, *Carbon N. Y.*, 2013, **65**, 156–164.

3 P. T. Araujo, M. Terrones and M. S. Dresselhaus, *Mater. Today*, 2012, **15**, 98–109.

4 B. Brennan, S. J. Spencer, N. A. Belsey, T. Faris, H. Cronin, S. R. Silva, T. Sainsbury, I. S. Gilmore, Z. Stoeva and A. J. Pollard, *Appl. Surf. Sci.*, 2017, **403**, 403–412.

5 A. J. Pollard, K. R. Paton, C. A. Clifford, E. Legge, A. Oikonomou, S. Haigh, C. Casiraghi, L. Nguyen and D. Kelly, *Characterisation of the Structure of Graphene*, 2017.

6 A. Bianco, H. M. Cheng, T. Enoki, Y. Gogotsi, R. H. Hurt, T. Kyotani, M. Monthioux, C. R. Park, J. M. D. Tascon and J. Zhang, *Carbon N. Y.*, 2013, **65**, 1–6.

7 I. Sengupta, S. Chakraborty and M. Talukdar, *J. Mater. Res.*, , DOI:10.1557/jmr.2018.338.

8 D. Zheng, G. Tang, H. Zhang, Z. Yu, F. Yavari, N. Koratkar, S. Lim and M. Lee, *Compos. Sci. Technol.*, 2012, **72**, 284–289.

9 W. Chen, L. Yan and P. R. Bangal, *Carbon N. Y.*, 2009, **48**, 1146–1152.

10 H. Liu, Nottingham, 2014.

11 D. R. Dreyer, S. Park, C. W. Bielawski and S. Ruoff, Rodney, *Chem. Soc. Rev.*, 2010, **39**, 228–240.

12 J. Guerrero-Contreras and F. Caballero-Briones, *Mater. Chem. Phys.*, 2015, **153**, 209–220.

13 S. Stankovich, D. A. Dikin, R. D. Piner, K. A. Kohlhaas, A. Kleinhammes, Y. Jia, Y. Wu, S. T. Nguyen and S. Ruoff, Rodney, *Carbon N. Y.*, 2007, **45**, 1558–1565.

14 L. Dong, J. Yang, M. Chhowalla and K. P. Loh, *Chem. Soc. Rev.*, 2017, **46**, 7306–7316.

15 F. H. Baldovino, A. T. Quitain, N. P. Dugos, S. A. Roces, M. Koinuma, M. Yuasa and T. Kida, *RSC Adv.*, 2016, **6**, 113924–113932.

16 S. Stankovich, D. A. Dikin, R. D. Piner, K. A. Kohlhaas, A. Kleinhammes, Y. Jia,

Y. Wu, S. B. T. Nguyen and R. S. Ruoff, *Carbon N. Y.*, 2007, **45**, 1558–1565.

17 D. A. Dikin, S. Stankovich, E. J. Zimney, R. D. Piner, G. H. B. Dommett, G. Evmenenko, S. T. Nguyen and R. S. Ruoff, *Nature*, 2007, **448**, 457–460.

18 J. Mao, Z. Bao, R. M. Stoltenberg, Z. Liu, H. A. Becerril and Y. Chen, *ACS Nano*, 2008, **2**, 463–470.

19 J. I. Paredes, A. Marti, J. M. D. Tasco and A. Martı, *Langmuir*, 2008, **24**, 10560–10564.

20 A. Lerf, H. He, M. Forster and J. Klinowski, *J. Phys. Chem. B*, 1998, **102**, 4477–4482.

21 H. He, J. Klinowski, M. Forster and A. Lerf, *Chem. Phys. Lett.*, 1998, **287**, 98–101.

22 J. Liang, Y. Huang, L. Zhang, Y. Wang, Y. Ma, T. Cuo and Y. Chen, *Adv. Funct. Mater.*, 2009, **19**, 2297–2302.

23 F. Ren, G. Zhu, P. Ren, Y. Wang and X. Cui, *Appl. Surf. Sci.*, 2014, **316**, 549–557.

24 Y. Li, D. Pan, S. Chen, Q. Wang, G. Pan and T. Wang, *Mater. Des.*, 2013, **47**, 850–856.

25 A. Navaee and A. Salimi, *RSC Adv.*, 2015, **5**, 59874–59880.

26 R. Ye, J. Dong, L. Wang, R. Mendoza-Cruz, Y. Li, P. F. An, M. J. Yacamán, B. I. Yakobson, D. Chen and J. M. Tour, *Carbon N. Y.*, 2018, **132**, 623–631.

27 C. N. Yeh, K. Raidongia, J. Shao, Q. H. Yang and J. Huang, *Nat. Chem.*, 2015, **7**, 166–170.

28 Graphitene Ltd, *Product Data Sheet – RGO*, Flixborough, 2017.

29 Graphitene Ltd, *Product Data Sheet – Graphene Oxide Powder*, Flixborough,

2017.

30 Mettler-Toledo AG, *The frequency dependence of the glass transition*, Switzerland, 2009, vol. 1.

31 D. G. Papageorgiou, I. A. Kinloch and R. J. Young, *Prog. Mater. Sci.*, 2017, **90**, 75–127.

32 S. S. Chee, M. Jawaid, M. Thariq and B. Hameed, *Bioresources*, 2017, **12**, 7118–7132.

33 M. Jacob, B. Francis, K. T. Varughese and S. Thomas, *Macromol. Mater. Eng.*, 2006, **291**, 1119–1126.

34 J. Chen, Z. xing Zhang, W. bin Huang, J. le Li, J. hui Yang, Y. Wang, Z. wan Zhou and J. hong Zhang, *Mater. Des.*, 2015, **69**, 105–113.

4. Preparation and characterisation of a novel covalently functionalised graphene oxide with ureidopyrimidone

Here, we exploit the idea of creating a complementary functionalised filler and matrix which, when combined, should afford enhanced filler matrix interfacial adhesion. Such improvements in the interfacial adhesion according to the rule of mixtures should result in improved polymer composites.

Taking inspiration from nature, there are several mechanical enhancing strategies different organisms employ, such as hydrogen bonding,[1,2] metal-ligand interactions,[3,4] and disulfide metathesis.[5,6] Spider silk takes its strength from complementary hydrogen bonding arrays which could provide a robust route to enhance filler matrix interfacial adhesion. The supramolecular research field currently utilise quadruple hydrogen bonding arrays such as ureidopyrimidone (UPy). Because of the quadruple intramolecular bonding capability, it affords greater potential than monofunctionalised groups within a composite system and would sterically stabilise the filler preventing aggregation. Furthermore, by functionalisation with a bulky aromatic motif it enables greater pre-emptive stress performance as more interactions are favourable as the arrays shear under force.

In this chapter, we investigate the covalent functionalisation of graphene oxide with the quadruple hydrogen bonding motif ureidopyrimidone to make UPyGO.

This facile synthesis method which produces UPyGO differs from the work by Wang *et al*.[7] by an absence of polydopamine pretreatment. The synthesis is characterised by FTIR ATR, elemental combustion analysis, and energy dispersive spectroscopy to demonstrate successful functionalisation. In addition, the literature does not report to comparative investigations on thermal stability, effect on inter-gallery distance, lateral flake size distribution, suspension stability and self-assembly, against other graphene oxide based materials. The findings in this chapter aims to support a greater understanding of this novel filler which will support the polymer composite fabrications discussed in Chapter 5.

4.1. Grafting UPy functionality at GO

The isocyanate terminated ureidopyrimidone (UPyNCO) required for successful functionalisation onto the graphene oxide sheet can only be derived by synthesis of 1,6-diisocyanatohexane and the primary amine of the ureidopyrimidine ring. Due to the establishment of ureidopyrimidone in the self-healing and self-assembly supramolecular polymer fields the methodology is widely reported which was used for these preparations.

The synthesis of the isocyanate-terminated ureidopyrimidone done as per the literature preparation and agreed with the reported characterisation.[8] Preliminary test reactions to functionalise graphene oxide with the isocyanate-terminated ureidopyrimidone monomer (UPyNCO) were conducted to optimise the ratio of UPyNCO to GO. Microscale reactions of UPyNCO and GO ranging from 66 – 98 wt.% of UPyNCO were performed in *N, N*-dimethylformamide owing to its suitability for both reagents and assumed solvation properties, unlike other solvents. The test reactions were monitored by FTIR ATR every hour by drying aliquots to observe the disappearance of the isocyanate stretch at 2285.7 cm^{-1} confirming successful functionalisation with the graphene oxide.[9,10] It was found that after 2 hours at 80 °C in *N, N*-dimethylformamide with magnetic stirring was sufficient to functionalise the graphene oxide. It is apparent from above 85 wt.% that saturation of UPyNCO occurred by the observation of an off-white suspension, postulated as UPy dimerisation. The functionalisation was not optimised further as it was found that 79 wt.% UPyNCO was suitable for scaling and investigation.

Comparison between the parent graphene oxide and UPyNCO monomer was used to support the characterisation the ureidopyrimidone functionalised graphene oxide (UPyGO). Most notably the disappearance of the isocyanate stretch at 2290 cm^{-1} from the UPyGO spectrum in Figure 4.1.

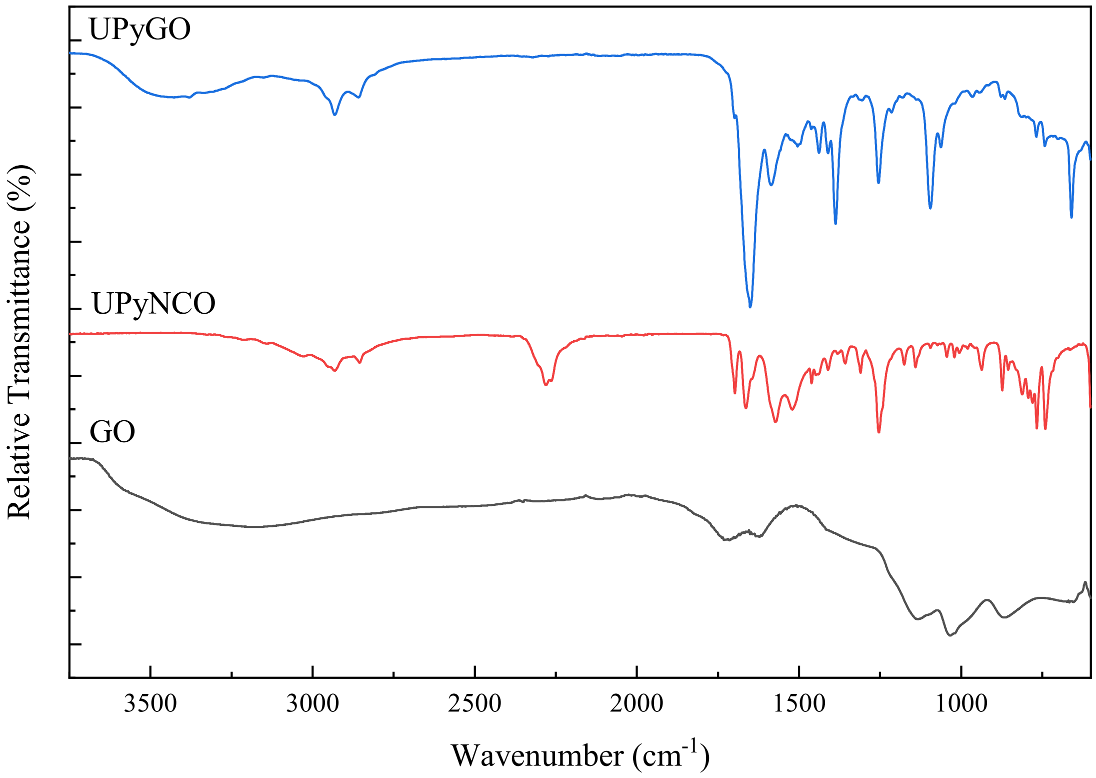

Figure 4.1. Diamond FTIR ATR of the graphene oxide powder (black), UPyNCO (blue) and UPyGO (red) showing the loss of the isocyanate peak at 2200 cm^{-1} in the UPyGO spectra, supporting successful modification.

Comparison between the parent graphene oxide and UPyNCO monomer was used to support the characterisation the ureidopyrimidone functionalised graphene oxide (UPyGO). Most notably the disappearance of the isocyanate stretch at 2290 cm^{-1} from the UPyGO spectrum in Figure 4.1. This disappearance confirms the successful functionalisation of the isocyanate terminus of the UPyNCO with the graphene oxide[7,11] In addition, the UPyNCO and UPyGO the vibrations suggest the stronger keto DDAA array has formed by the presence of the vibrations at c.3200 cm^{-1} and c.3150 cm^{-1} assigned to the hydrogen-bonded secondary amine stretches.[12] This is further supported by the absence of the enol hydroxyl found in the DADA hydrogen bond array at 2500 cm^{-1}.[12] The appearance of alkyl stretches around 2900 cm^{-1} also supports the addition of the hexyl chain on the UPy motif. In agreement with previous studies, which suggest the reaction occurs through the alcohol groups on the surface of the graphene oxide and the isocyanate terminus to produce the urethane.[13] Therefore, it is assumed that the basal plane has reactive alcohol functionalities present; otherwise, the mild reaction conditions would lead to unsuccessful reactions.

The characterisation of the parent graphene oxide, which is reported in the previous chapter (see Chapter 3) shows a broad C-O at 1041 cm^{-1}. Also, within the same vibrational region, the UPyGO spectrum shows a sharp shoulder vibration at 1093 cm^{-1}.

One possible explanation for these vibrations could be that the carbon-oxygen bond length decreases because of the alcohol becoming part of the urethane functionality. Therefore, to test this, preliminary molecular dynamics calculations were conducted using Chem3D software. A pyrene ring was used as a simulate the graphene oxide sheet to ease computational demands. The functionalities were constructed on the central carbon atom and the energy-optimised using an MM2 force field calculation before the bond lengths were calculated and the basal plane carbon-oxygen recorded (Figure 4.2).

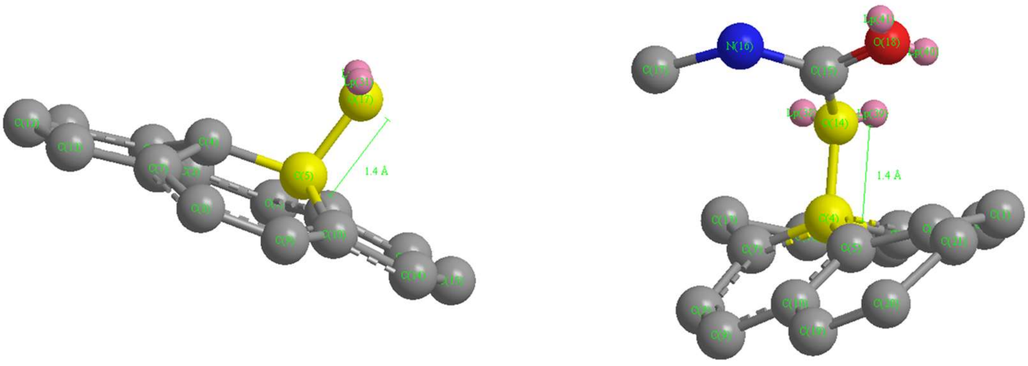

C(5)-O(17) 1.428 Å

C(4)-O(14) 1.425 Å

Figure 4.2. Theoretical bond length calculations using molecular dynamics to determine whether a change in the basal plane carbon-oxygen bond has changed during the transformation from a hydroxyl (left) to part of the urethane group (right), which could correspond to the 1041 cm^{-1} and 1093 cm^{-1} C-O vibrations observed in the GO and UPyGO spectra respectively. A pyrene structure was used to simulate the graphene structure (hydrogen atoms are hidden to aid clarity).

The molecular dynamics calculations show that the basal plane carbon-oxygen bond length decreases from 1.428 Å to 1.425 Å because of urethanisation. However, the difference in bond lengths is negligible; therefore, it would not result in a shift to higher wavenumbers.

Another hypothesis for the new peak sharp peak at 1093 cm^{-1} is the functionalisation process has resulted in the formation of primary (C-O stretch 1050 – 1085 cm^{-1}) or secondary alcohols (C-O stretch 1087 – 1127 cm^{-1}) too. Both reduction products are possible due to the multitude of oxygenated groups decorated across the sheet edges (carboxylic acids, carbonyls) and in the basal plane (epoxides). For the reduction of carboxylic acids and aldehydic carbonyls would result in primary alcohols; ketonic carbonyls would produce secondary alcohols, and if ring epoxide opening occurred, tertiary alcohols would result.

As a result of the carboxyl groups residing along the sheet edges in graphene oxide, they can undergo dissociation when placed in aqueous media.[14] Therefore, a comparative study on the natural pH of different suspension concentrations was carried out due to alcohols not dissociating as readily due to their higher pKa relative to carboxylic acids.

The analysis involved preparing aqueous suspensions at concentrations up to 4 mg mL^{-1} of UPyGO GO and rGO, and recording their natural pH at each concentration, as shown in Figure 4.3.

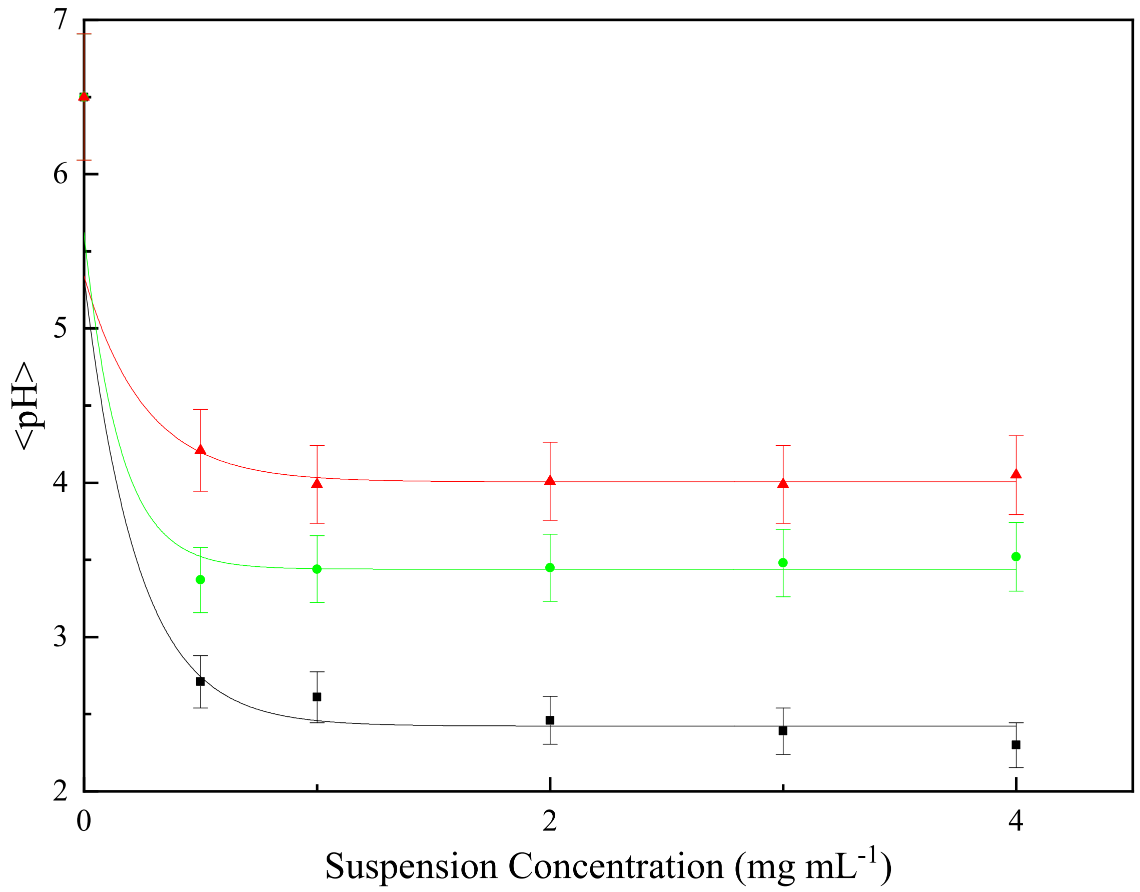

Figure 4.3. Plot for the effect of concentration on the natural pH (n =3) of aqueous suspensions of GO (black squares), rGO (light green circles) and UPyGO (red triangles)

As expected, the graphene oxide exhibits the higher acidity in comparison to reduced graphene oxide because of the increased carboxylic acid content present on the graphene oxide. As expected, the UPyGO displayed a lower degree of acidic groups due to its natural pH remaining above pH 4, which plateaued after a concentration of 2 mg mL^{-1}. This could be the result of carboxylic acid reduction, which is observed by the 1093 cm^{-1} FTIR peak of the dry powder, therefore, supporting the hypothesis. It is believed that the UPy functionality also possesses a higher pH due to the tautomerisation of the donor donor acceptor acceptor (DDAA) keto form and the acceptor donor acceptor donor (ADAD) enol form as shown in Figure 4.4.

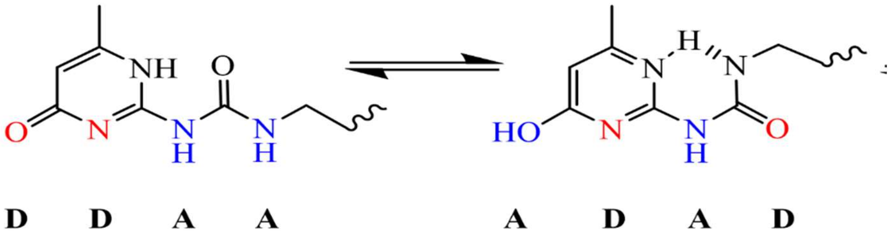

Figure 4.4. Tautomerisation between the keto form and enol form (red signifies acceptor groups and blue signifies donor groups)

Due to the heterogeneity of graphene oxide, further investigations were not carried out as the FTIR characterisation supported proof of successful functionalisation. Repeats of the reaction also produced the same spectra, demonstrating a reproducible method.

To further support the success of the reaction, carbon, hydrogen, and nitrogen combustion elemental analysis (CHN), and energy dispersive spectroscopy (EDS) were conducted.

4.2. Identification of nitrogen to confirm the UPy functionalisation using electron dispersive spectroscopy (EDS)

Electron dispersive spectroscopy (EDS) was carried out to investigate the carbon, oxygen, nitrogen content and if trace metal were present from the chemical exfoliation. The analysis was conducted on multiple random locations (see Chapter 2) with the mean elemental composition presented in Figure 4.6.

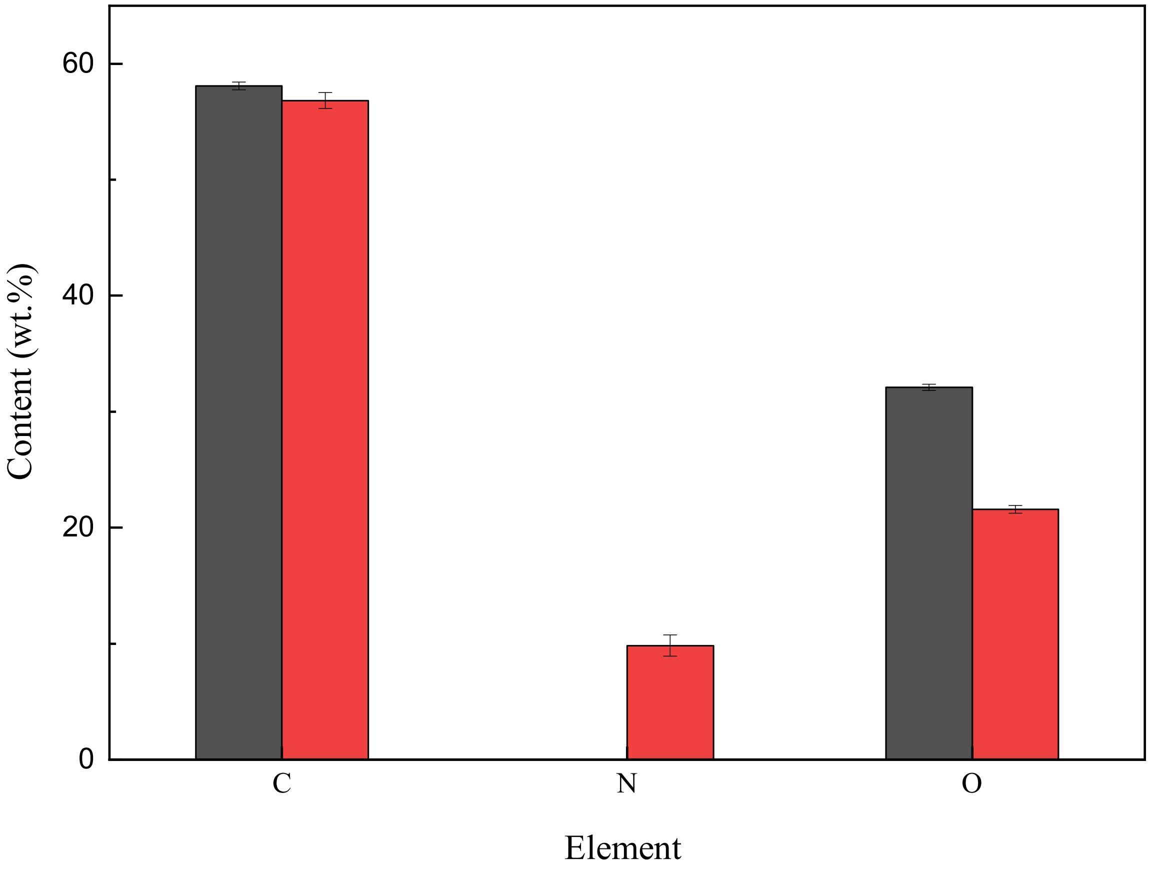

Figure 4.5. Average (n=3) elemental composition of 0.1 mg mL^{-1} aqueous graphene oxide (dark grey) and UPyGO (red) suspensions drop cast onto cleaned glass substrates.

Figure 4.6 supports the successful functionalisation by the appearance of nitrogen in the elemental spectra of UPyGO compared to the parent graphene oxide. Also, it was observed that the oxygen composition in the UPyGO system is suggesting partial reduction based on the C:O ratio estimated and tabulated in Table 4.1

Table 4.1. Carbon and oxygen compositional analysis for GO and UPyGO determined by EDS

Sample	Carbon content (wt.%)	Oxygen content (wt.%)	C:O ratio
GO	58.1 ± 0.3	32.1 ± 0.3	1.81 ± 0.02
UPyGO	56.8 ± 0.7	21.6 ± 0.3	2.63 ± 0.05

The increase in the estimated C:O ratio tabulated in Table 4.1. for UPyGO suggests that the functionalisation of UPy with GO causes a relative reduction in oxygen content as expected due to the addition of the nitrogen from the UPy structure diversifying the overall elemental composition. To define the UPyGO as per the standardised nomenclature, x-ray photoelectron spectroscopy (XPS) could be used.[15] Since the XPS was not available, the estimated C:O is found to be suitable for the current studies.

On the other hand, the analysis did show the presence of silicon and multivalent cations which were expected from their origin in the glass substrate and consequently disregarded from Figure 4.5. Unlike multivalent cations,[16] silicon does not present any implications for mechanical enhancement, unlike electronic applications.[17].

4.3. Determination of the reproducibility and nitrogen presence to confirm UPyGO functionalisation by CHN Elemental Combustion Analysis

Elemental combustion analysis was conducted on the parent graphene oxide and three separate fresh batches of UPyGO and pre-dried in a vacuum oven to minimise the presence of adsorbed water on the functionalised sheets. The carbon, hydrogen and nitrogen elemental composition were measured, and the oxygen content calculated as the non-assigned percentage content for all samples and presented in Figure 4.6.

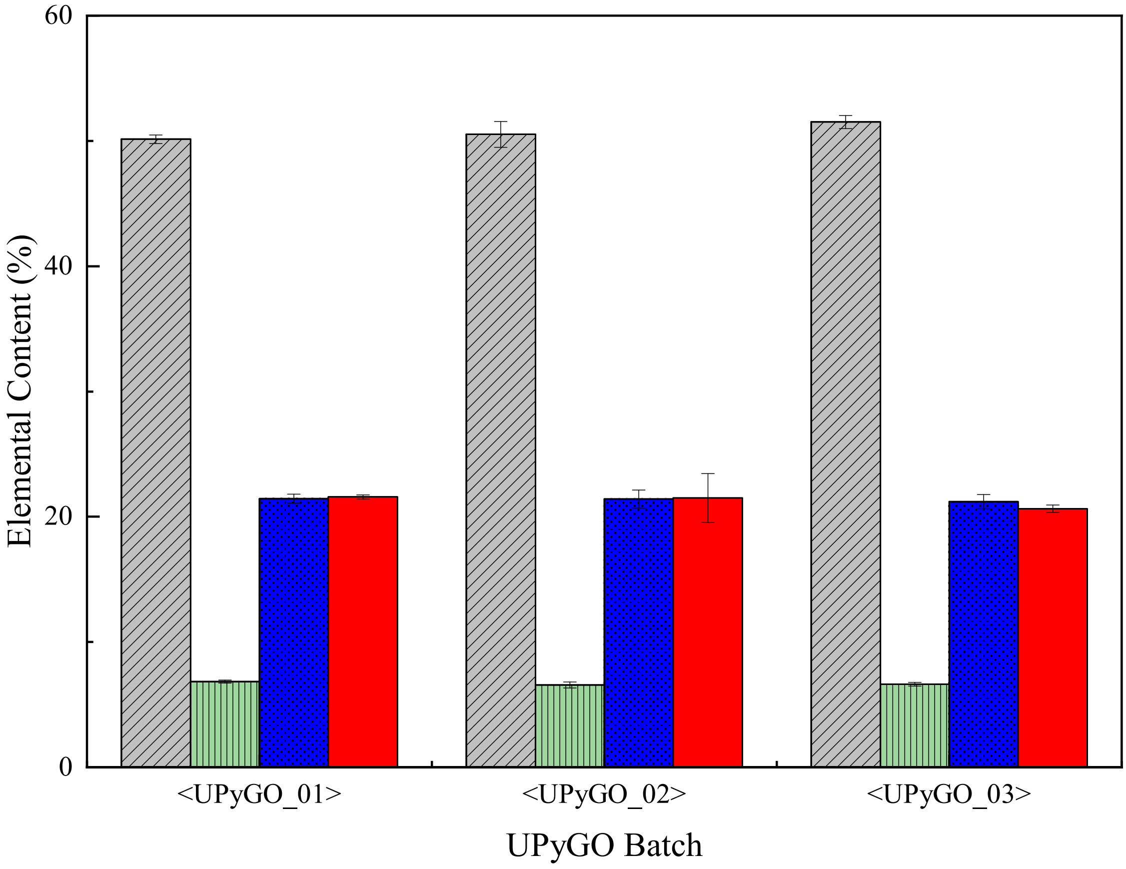

Figure 4.6. Average elemental content (atomic %) of (n=3) carbon (black, diagonal lines), hydrogen (green vertical lines) and nitrogen (blue dot fill), and oxygen (red solid fill) in three independently prepared batches of UPyGO.

shows the presence of nitrogen in each UPyGO batch supports the ability to reproduce the UPyGO filler under these conditions successfully.[18,19] Though, a difference in nitrogen composition was observed between the EDS and elemental combustion analysis; it is considered the result of EDS being a non-destructive surface technique. Therefore, the electron beam or detector may not have captured all the nitrogenated groups in the UPyGO, unlike elemental combustion analysis which is a destructive technique providing a more accurate result. However, the calculated oxygen content in CHN analysis (21.4 ± 0.5%) agreed with experimental EDS analysis (see Table 4.1).

Because of the berthollide nature of graphene oxide, the reproducibility of the UPyGO was further supported by the estimation of the degree of functionalisation using equation (4.1).

$$\boldsymbol{f^{o}} = \left(\frac{[\boldsymbol{N_{UPy}}]}{[\boldsymbol{C_{GO}}]}\right) \times \mathbf{100} \qquad \mathbf{(4.1)}$$

Where: f^{o} is the degree of functionalisation; [N_{UPy}] is the concentration of ureidopyrimidone, which is determined by the nitrogen content and [C_{GO}] is the carbon content (34.55%) in the parent graphene oxide.

To determine [N_{UPy}] the total nitrogen composition was taken and divided by the number of nitrogen atoms to correspond with the assumption of a monofunctionalisation on each basal plane (2 grafting per sheet), and the mean nitrogen content was from a single functionalised sheet. As a result of the UPy motif and the urethane linkage between the graphene oxide and UPy, five nitrogen atoms per grafting was expected.

Through a division of 10 to the mean nitrogen content to determine [N_{UPy}] and substitution into Eqn (4.1) it resulted in the mean degree of functionalisation (n = 3) to be estimated as 6.20 ± 0.04%.

The small standard deviations observed within the elemental composition data presented in Figure 4.6 and from the mean degree of functionalisation estimations support a reproducible process to covalently functionalise graphene oxide with ureidopyrimidone.

Therefore, because of the characterisation demonstrating successful functionalisation, and batch to batch reproducibility, the thermal stability, crystallinity, and flake size distribution were compared against the parent graphene oxide.

4.4. Thermogravimetric analysis

Thermogravimetric analysis under a nitrogen flow gas was carried out to investigate the effect of heat and characteristics of the powdered samples, which are presented in Figure 4.7.

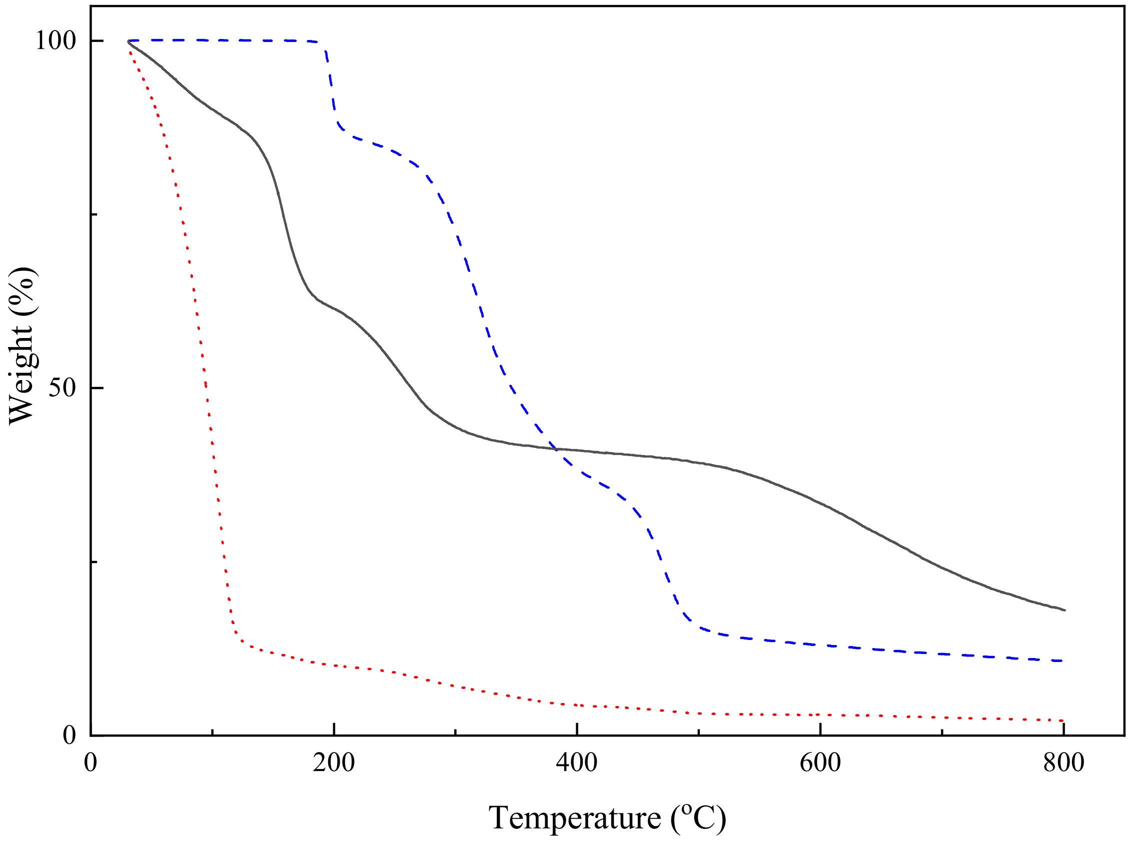

Figure 4.7. TGA analysis of graphene oxide powder (solid black line), UPyGO (red dotted line) and UPyNCO (blue dashed line) under a 2.0 bar, 30 ml min^{-1} nitrogen atmosphere at a ramp rate of 10 °Cmin^{-1} between 30 °C and 800 °C. All runs were run with baseline correction from an empty crucible to account for thermal buoyancy.

The UPyNCO and GO powder were also subjected to TGA analysis to investigate any effects which could be attributed to the UPy dimer behaviour or graphene oxide. The blue trace presented in Figure 4.7. shows no drying profile demonstrating the UPyNCO is dry with no adsorbed water in the UPy region, suggesting that all UPy monomers are engaged in dimerisation. The first weight loss is observed at 200 °C through a steep profile. The steepness of the gradient is attributed to the melting of the UPyNCO through the disengagement of hydrogen bonding, which agrees with the melting point analysis run post-synthesis and literature.[8] The melting behaviour can be observed using TGA due to the increase in vapour pressure or a rapid decomposition of the melt. [20] As a result of the high reactivity of the isocyanate terminus, thermal conditions could result in the decomposition of the isocyanate functionality.[21] Due to the inert atmosphere generated from the nitrogen purge gas and no observable mass gain, decomposition rather than reactivity remains the most plausible interpretation. Furthermore, the remaining two weight loss profiles are ascribed to volatile melting behaviour.

In comparison, the weight loss profile of the UPyGO showed unexpected behaviour during the 10 °C min^{-1} TGA experiment. A rapid weight loss event occurs from the beginning of the temperature scan (30 °C) up to approximately 115 °C. The extremity of the weight loss cannot be attributed to adsorbed solvents on the surface which would appear as a gentle profile,[22] similar to the drying profile of the graphene oxide (56 – 145 °C) trace.[23] Therefore, it is postulated that this thermal event is resultant from the production of liberated gas that causes expansion events in the crucible, leading to rapid weight loss. [24] Such outputs of gas could be resultant from the UPy dimer network disengaging and releasing trapped moisture.

Furthermore, in both the GO and UPyGO thermal curves, the next weight loss (187-312°C) is attributed to the decomposition of the remaining oxygenated moieties on the GO and UPyGO basal plane and sheet edges and any DDAA dimers dissociating.[25,26] Also, the UPyGO displays significantly poorer thermal stability in comparison to the GO powder.

As a result of TGA curves being kinetic in nature, with samples not having specific fingerprints, unlike techniques such as FTIR, repeats where conducted. All repeats produced the same TGA curves profiles; therefore, to determine the origin of the steep weight loss of the UPyGO in Figure 4.7. further analysis was conducted at a slower ramp rate of 1 °C min^{-1} in the area of interest (30 – 300 °C) given by Figure 4.8.

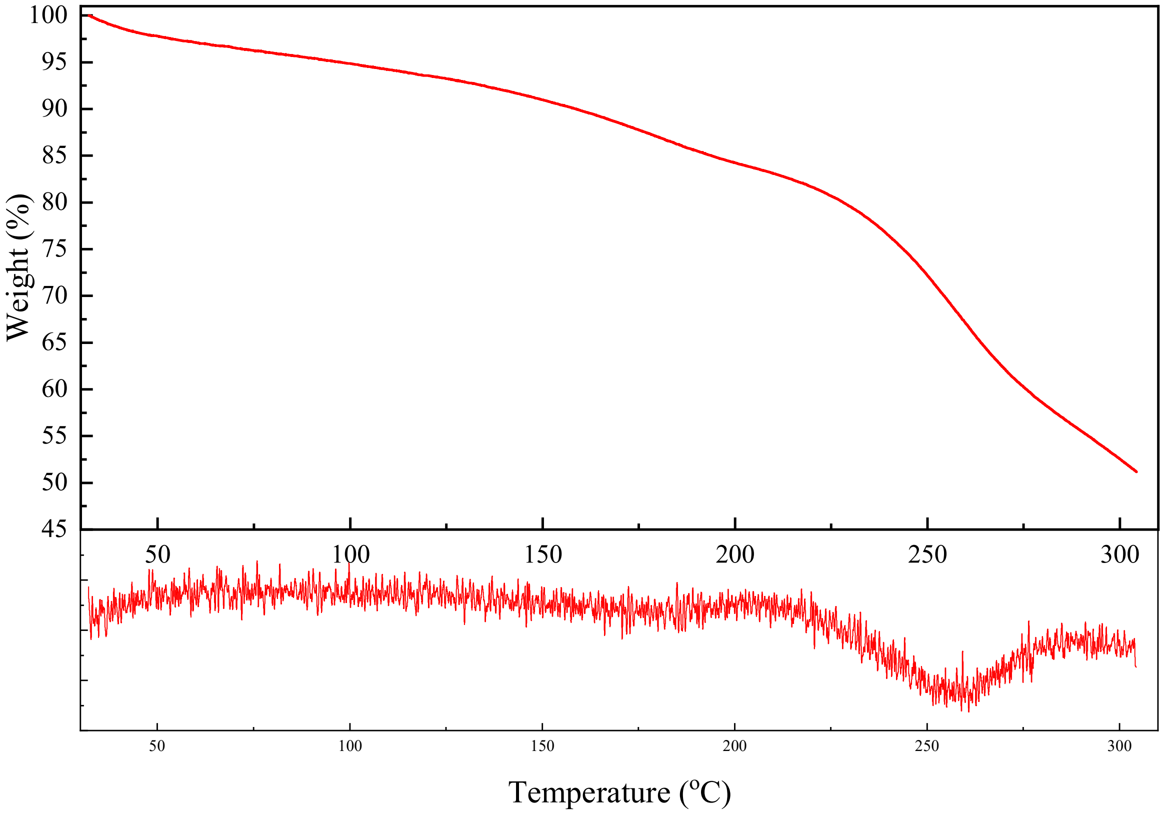

Figure 4.8. TGA (top) of UPyGO run under a 2.0 bar, 30 ml min^{-1} nitrogen atmosphere at the reduced ramp rate of 1°C min^{-1}between 30 °C and 300 °C, the calculated first derivative curve (DTG, below) was smoothed with a Savitsky-Golay (50 points) to minimise signal to noise and emphasise the weight loss events.

Figure 4.8. shows no initial catastrophic weight loss curve, as observed in Figure 4.7. at the slower heating cycle, which is supported by the first derivative curve of the weight loss profile. The first derivative curve shows no visible drying event, suggesting a dry material. However, the TGA curve shows a gentle weight loss which coincides with the disconnection of the hydrogen bonds that make up the DDAA quadruple hydrogen bonding array leading to a thermally exfoliated monomeric UPyGO system.[26] Therefore, by inspection of both the standard heating regime of 10 °C min^{-1} and the reduced rate of

1 °C min^{-1}, it demonstrates that the most suitable explanation remains of thermal expansion of the UPyGO within the TGA instrument as discussed previously.[24]

4.5. The effect of UPy on the inter-gallery distance of graphene oxide

Powder x-ray diffraction (PXRD) was employed to investigate any changes in inter-gallery distance that would occur because of UPy functionalisation. It is predicted that because of basal plane functionalisation, it would exfoliate the graphene oxide leading to an increase in the inter-gallery distance for the UPyGO for the GO 002 plane (c. 2θ = 8.5). The PXRD patterns were analysed using the software which computes the Bragg equation (see Chapter 2) to determine the inter-gallery distance of the 002 plane, which corresponds to graphene oxide crystallite.[27,28]

Table 4.2. Crystallographic data for the 002 plane between the parent graphene oxide and UPyGO

Sample	2θ (°)	Inter-gallery distance (Å)
Graphene oxide powder pc92p	8.491	10.40539
UPyGO_01	5.864	15.05946
UPyGO_02	6.723	15.20041
UPyGO_03	5.703	16.63919

Table 4.2. shows the average difference in the inter-gallery distance of the UPyGO has increased by 5.23 Å compared to the parent graphene oxide suggesting exfoliation has occurred because of the UPyNCO functionalisation.

However, the extent of exfoliation does not conform with the length of the UPy functionality measured using molecular dynamics to be 16.9 Å which would have suggested a vertical exfoliation structure. Therefore it is postulated that the variance in the expected inter-gallery distance revealed in the 002 plane is the result of random orientations adopted by self-assembly of the dimer formation producing a heterogenous crystallite[10,14] making a true representation of the Scherrer equation challenging.

The heterogeneity of the UPyGO can be observed by comparison with the parent graphene oxide powder (Figure 4.9) which reveals that the functionalisation process creates a structure with no long-range atomic order by the appearance of the very broad graphite 002 plane at 2θ = 23.4°. This assumption is supported by scanning electron micrographs of the UPyGO, which show an irregular self-assembled structure (see Figure 4.11).

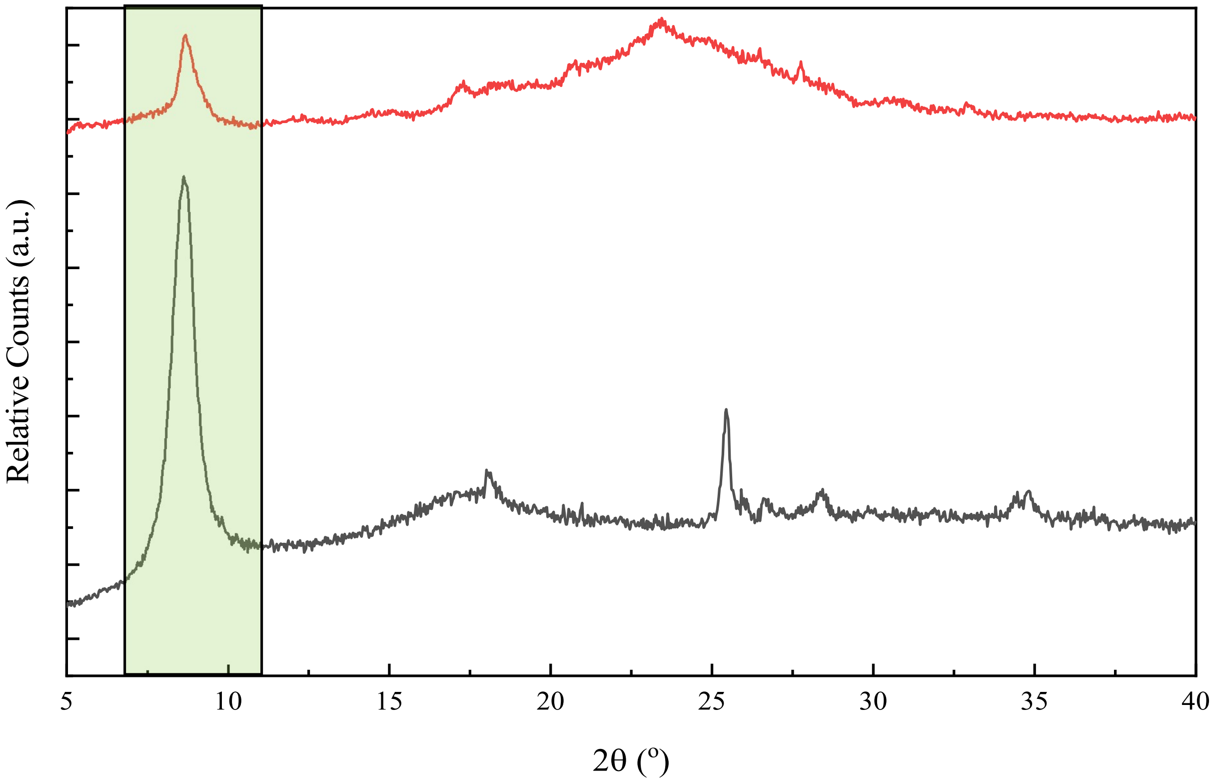

Figure 4.9. PXRD of graphene oxide powder (bottom, black) and UPyGO powder (top, red) using a Kα source without the need for a nickel filter as per the optimised methodology described in Chapter 3. The 002 plane (highlighted green) is of interest due to this corresponding to the single-layered graphene oxide.[27,28]

Furthermore, comparison of the PXRD pattern of UPyNCO (Figure 4.10) reveals a material with a higher degree of symmetry to relative to both the parent GO and the UPyGO as expected from its unidirectional self-assembly leading to regular crystallites.

The broad range at 2θ = 23.4 ° at UPyGO overlays with the UPyNCO crystallite planes (see inset Figure 4.10) which suggests that similar crystallite planes are present in both UPyGO and UPyNCO.

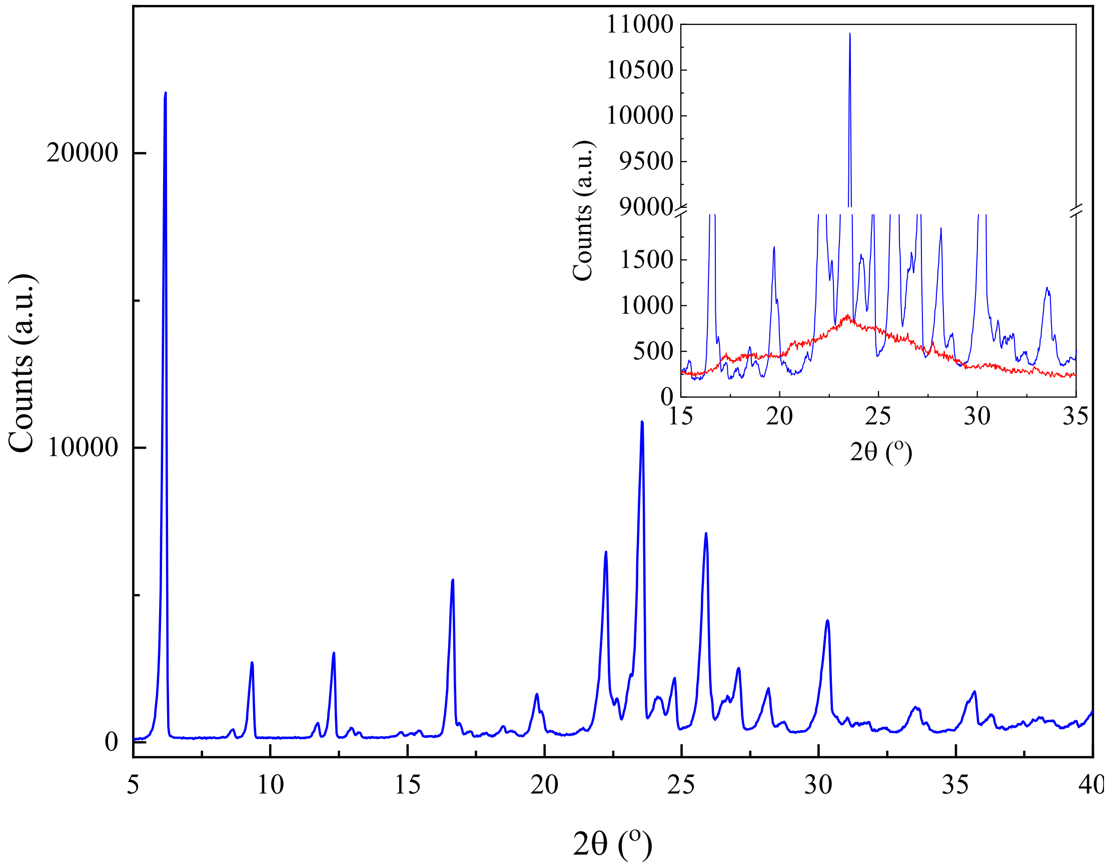

Figure 4.10. PXRD of the UPyNCO reagent (blue pattern) showing a higher degree of symmetry from the multiple reflection planes with which mirrors the broad reflection plane observed in UPyGO between 2θ = 15 – 35 ° (inset, UPyGO pattern) A line break is inserted between 2000 and 9000 counts to emphasise the UPyGO pattern.

As shown by Figure 4.11, the scanning electron micrograph of aqueous deposited UPyGO forms a disordered aggregate structure on the surface of the glass unlike the lamellar-like structure of the parent graphene oxide shown in Figure 4.12. The high level of random aggregation is resultant from the spontaneous dimerisation. This is because the dominant aggregation mechanism for UPyGO is now through the self-assembly of the quadruple hydrogen bonding arrays of the UPy which also sterically inhibits the basal plane stacking behaviour observed in the unmodified parent graphene oxide.

It was observed as presented in Figure 4.11. that the UPyGO a significantly different surface morphology to that of the parent graphene oxide. As expected, the graphene oxide showed islands and holes coverage of the substrate as determined by the standardisation protocol.[29] The surface coverage did show a large volume of monolayer graphene oxide as determined by the high transmittance of light through the sheets determined by optical microscopy prior to SEM.[30] Also, 100% of the material is not present as graphene oxide with some aggregates of potentially few-layered graphene oxide, shown by the large graphitic structure inset in Figure 4.12a.

On the other hand, the higher absorbance observed by the ureidopyrimidone functionalised graphene oxide was expected as the ureidopyrimidone dimers induce a structured self-assembly formation by the stable dimerisation of the free monomers as the polarity decreases with the evaporation of polar solvents such as water.[31] Therefore requiring further development to produce a suitable drop cast sample for flake size distribution.

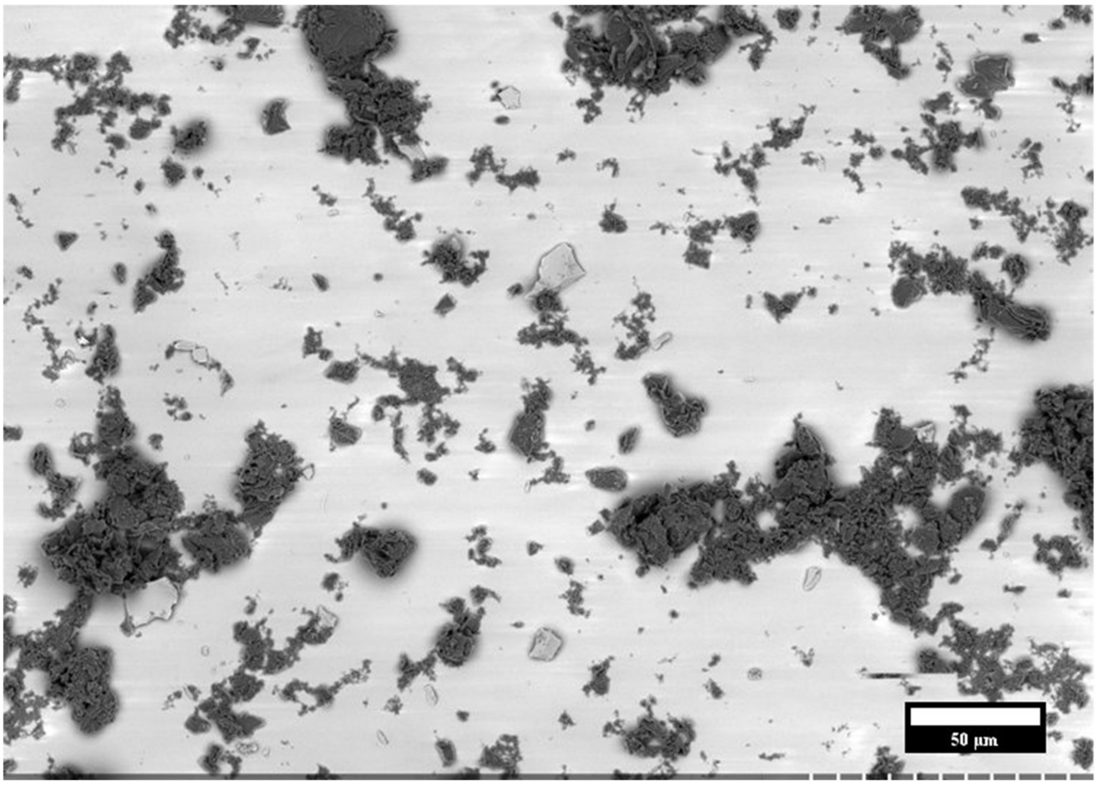

Figure 4.11. Scanning electron micrograph of aqueous drop cast UPyGO on a cleaned glass substrate, magnification 300 x, scale bar 50 µm.

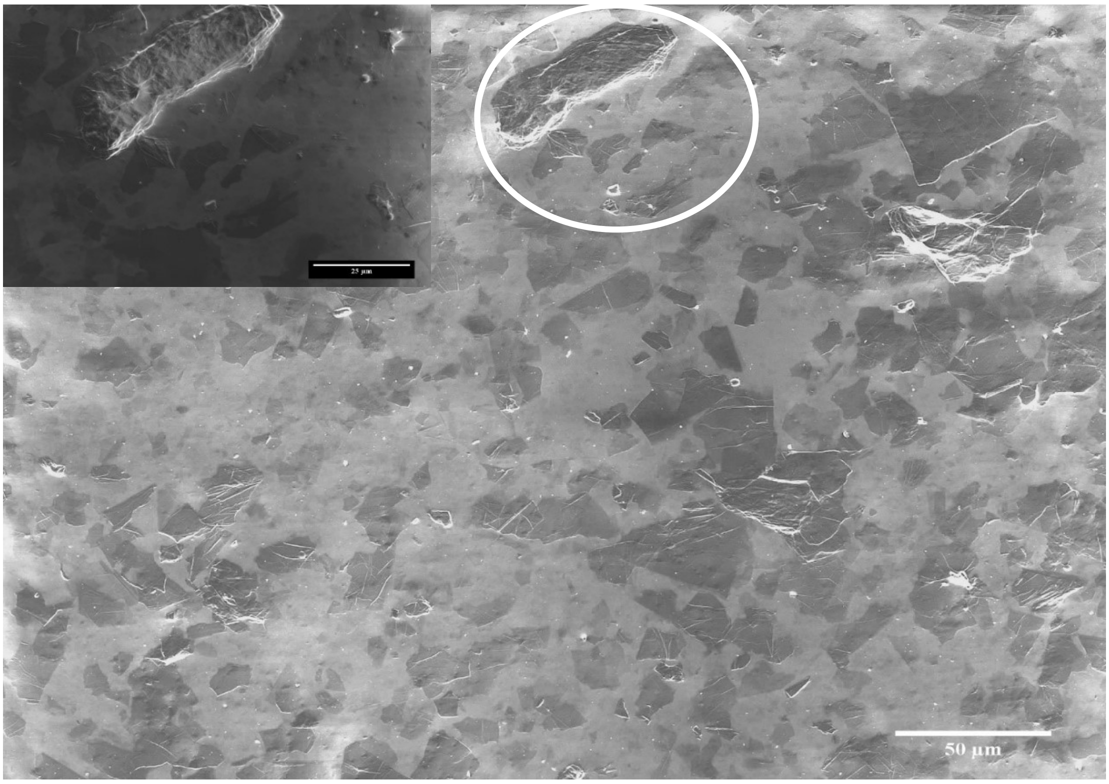

Figure 4.12. Scanning electron micrograph of aqueous drop cast GO on a cleaned glass substrate, magnification 300 x, scale bar 50 µm. White ellipse used to highlight the inset area. (Inset: 1000 x magnification, scale bar 25 µm) showing the expected wrinkled morphology.

4.6. The effect of functionalisation on the lateral flake size distribution of GO and UPyGO flakes

Aqueous 0.1 mg mL^{-1} GO, rGO and UPyGO suspensions were made by ultrasonic dispersion and drop cast on pre-heated freshly cleaved mica substrates to evaporate off the purified water. The samples were quality checked by optical microscopy before size distribution measurements by SEM.

The samples were scanned using an acceleration voltage of 10 keV with a secondary electron detection method. Two hundred flakes were observed with the lateral sizes of these flakes measured using imaging software and presented into histograms using 20 bins for comparison between GO, and UPyGO (Figure 4.13).

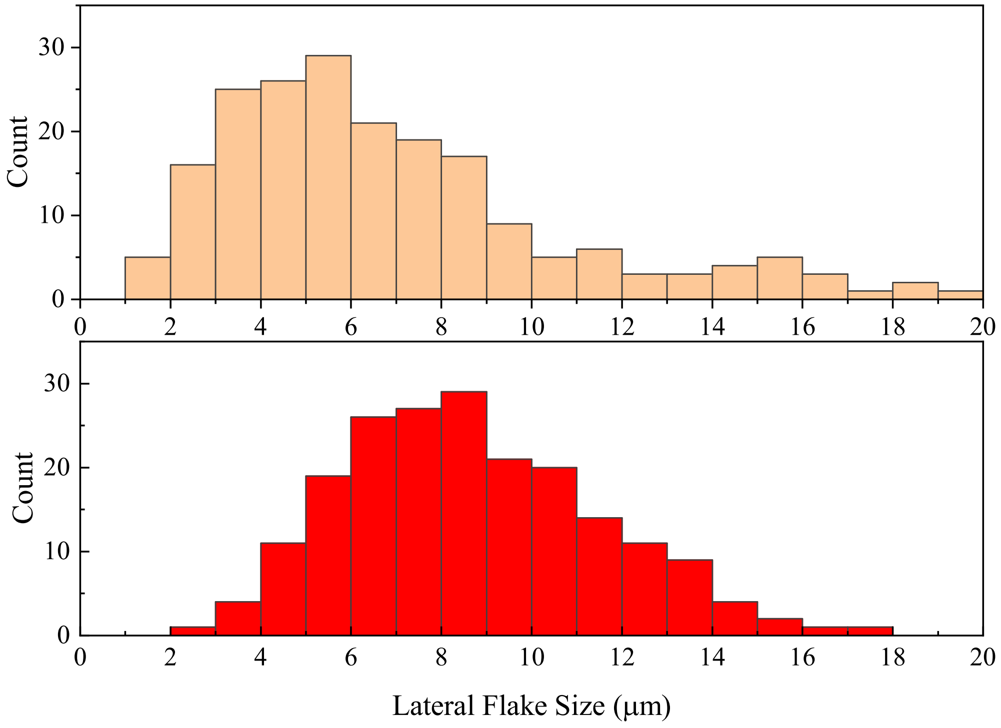

Figure 4.13. Histogram (n=200) of the range of lateral flake sizes of parent GO (orange, top) and UPyGO (red, bottom) drop cast onto freshly cleaved mica, determined through SEM measurements

The size distribution of the GO flakes resulted in an asymmetric right hand skewed broad distribution with the greatest frequency of flakes possessing a lateral size of between 5 and 6 µm. The lateral size range for GO flakes agreed with the technical data sheet provided by Graphitene Ltd.[32] Comparison of the lateral flake size distribution of UPyGO revealed that it possessed a narrower and more symmetric distribution than the GO system.

For UPyGO flakes, it was observed that the most frequent lateral flake size was residing between 8 and 9 µm. Furthermore, the distribution showed that for the synthesis of UPyGO, it produced larger lateral sized flakes that also fell within the graphene oxide lateral size range. The predisposition for larger flakes is expected due to the assumption that the larger parent graphene oxide flakes possess greater oxidation and reactivity, leading to a greater density of addressable groups that could react with the UPyNCO.[33–

[35] Another factor towards this observation is that during centrifugation, the larger functionalised flakes collide and aggregate and are collected in the product pellet whilst the smaller unfunctionalised flakes are removed with the supernatant.[36]

The smaller size distribution of the rGO flakes required a Carl Zeiss Evo-60 scanning electron microscope to provide further resolution for the measurements. Due to the LaB_6 filament, the freshly cleaved mica did not provide sufficient resistance on the surface leading to low image quality. Therefore, fresh mica substrates were sputter-coated with gold to create a conductive surface on the substrate before flake deposition to overcome this. To this, a fresh aqueous suspension of rGO flakes was drop cast onto the surface. The introduction of substrate conductivity was overcome, and 200 flakes were observed and measured in the same manner as the GO and UPyGO flakes. The size distribution was again plotted as a histogram (see Figure 4.14)

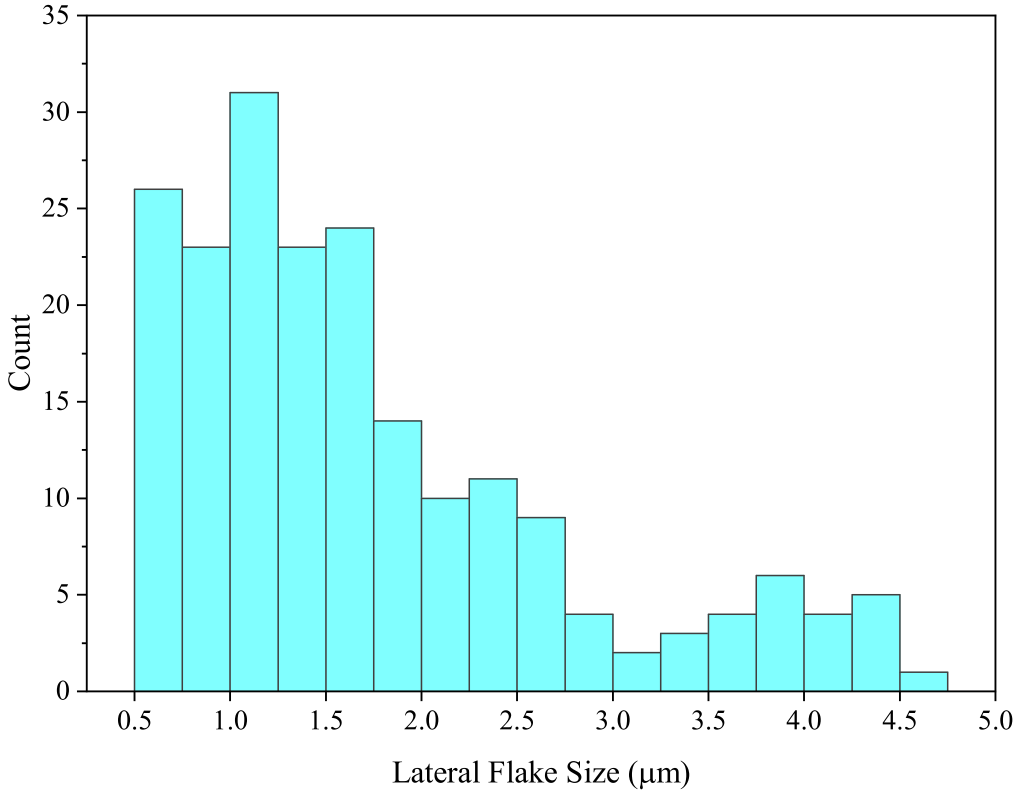

Figure 4.14. Histogram (n=200) of the range of lateral flake sizes of rGO drop cast onto a gold treated mica surface, determined through SEM measurements.

The size distribution of the rGO flakes resulted in an asymmetric right hand skewed narrow distribution with the greatest frequency of flakes possessing a lateral size of between 1 and 1.25 µm. The lateral size range for rGO flakes agreed with the technical data sheet provided by Graphitene Ltd.[37]

4.7. Dispersion of GO, rGO and UPyGO in different solvents

The stability and compatibility of GOBMs in different solvents is an area of interest within the wider field due to the variance in these materials (flake size, degree of functionalisation) it necessitates those compatible solvents need to be investigated to differentiate these systems by their physical properties. However there are only a few dedicated papers,[38–40] that seek to investigate their systems dispersibility in different solvents, therefore it is vital to determine their dispersion behaviour in different organic solvents. To investigate the dispersion behaviour of the parent graphene oxide (see Figure 4.15), UPyGO (see Figure 4.17), which was also compared against reduced graphene oxide (see Figure 4.16), 1 mg mL^{-1} suspensions were prepared. The suspensions were dispersed by ultrasonication as described in Chapter 2 for 1 hour. The dispersion and stability of the suspensions were then observed over a period of a week taking photographs immediately after sonication, 5 10, 15, 30 minutes, 1, 2, 4, 24 hours, and 1 week.

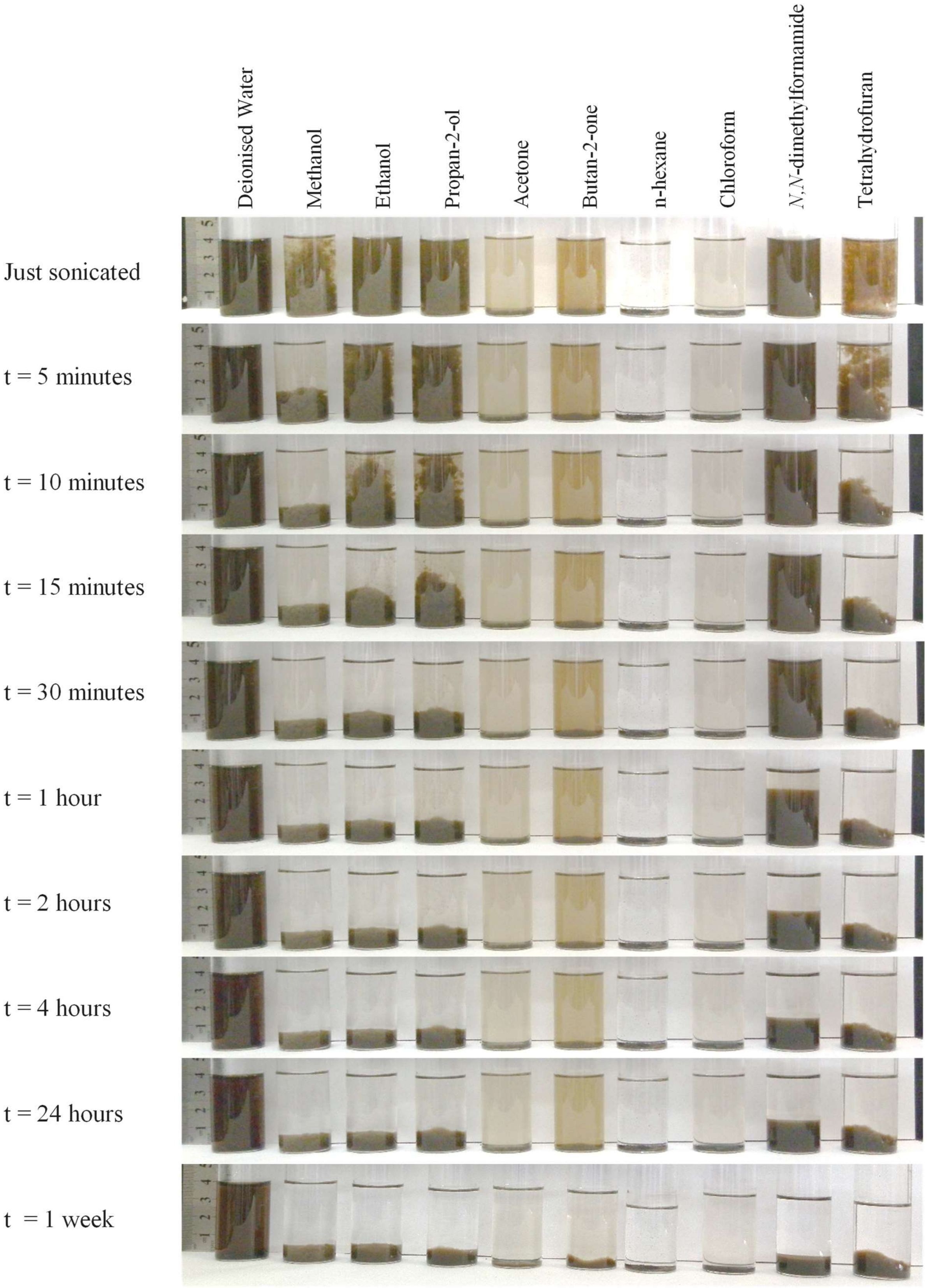

Figure 4.15. Dispersibility study of 1.0 mgmL^{-1} suspensions of graphene oxide in 10 different solvents to assess the stability and compatibility of different solvent systems towards solvent deposition fabrication

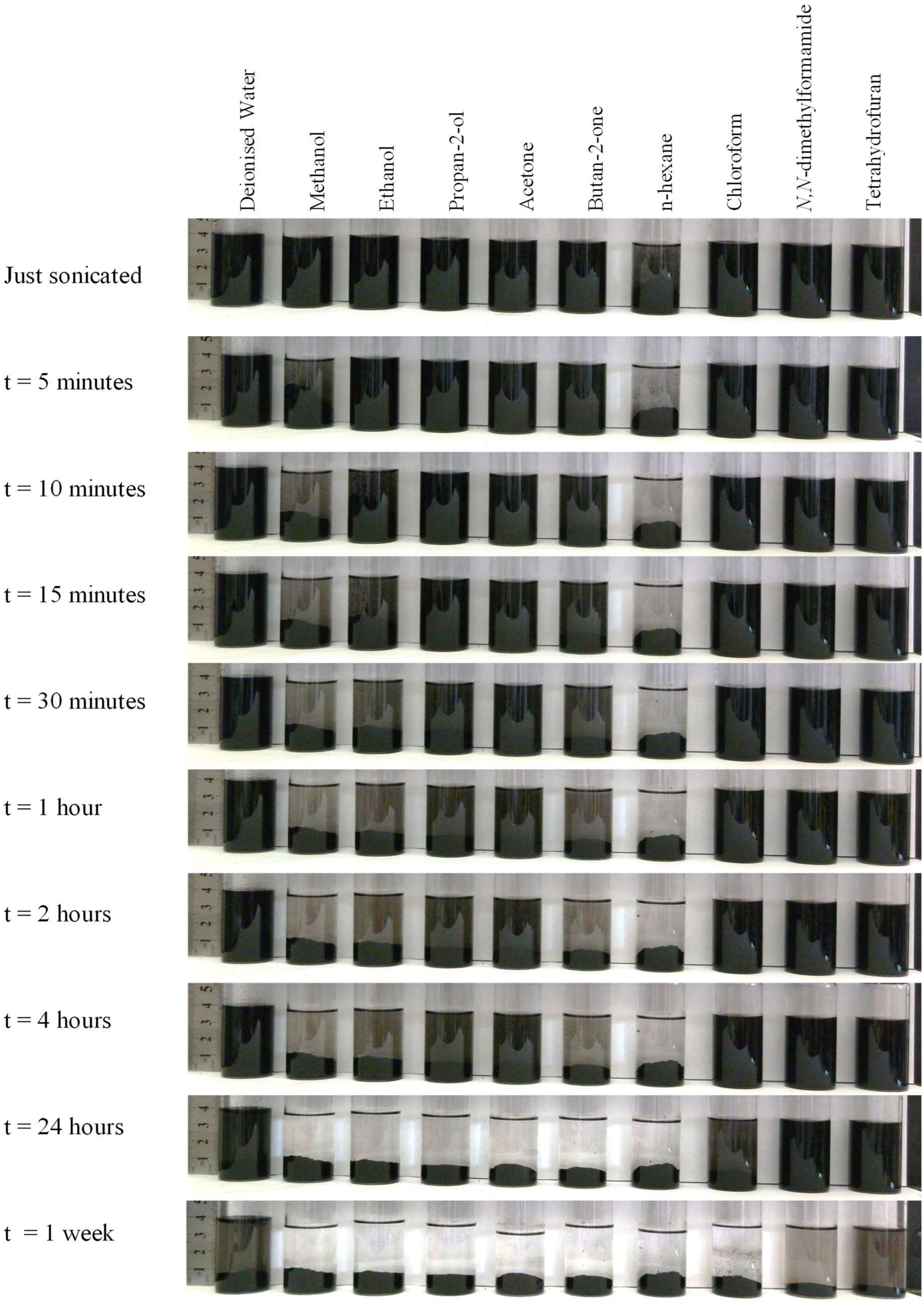

Figure 4.16. Dispersibility study of 1.0 mgmL^{-1} suspensions of reduced graphene oxide in 10 different solvents to assess the stability and compatibility of different solvent systems towards solvent deposition fabrication. The photographs were corrected to visualise small changes in the black suspensions.

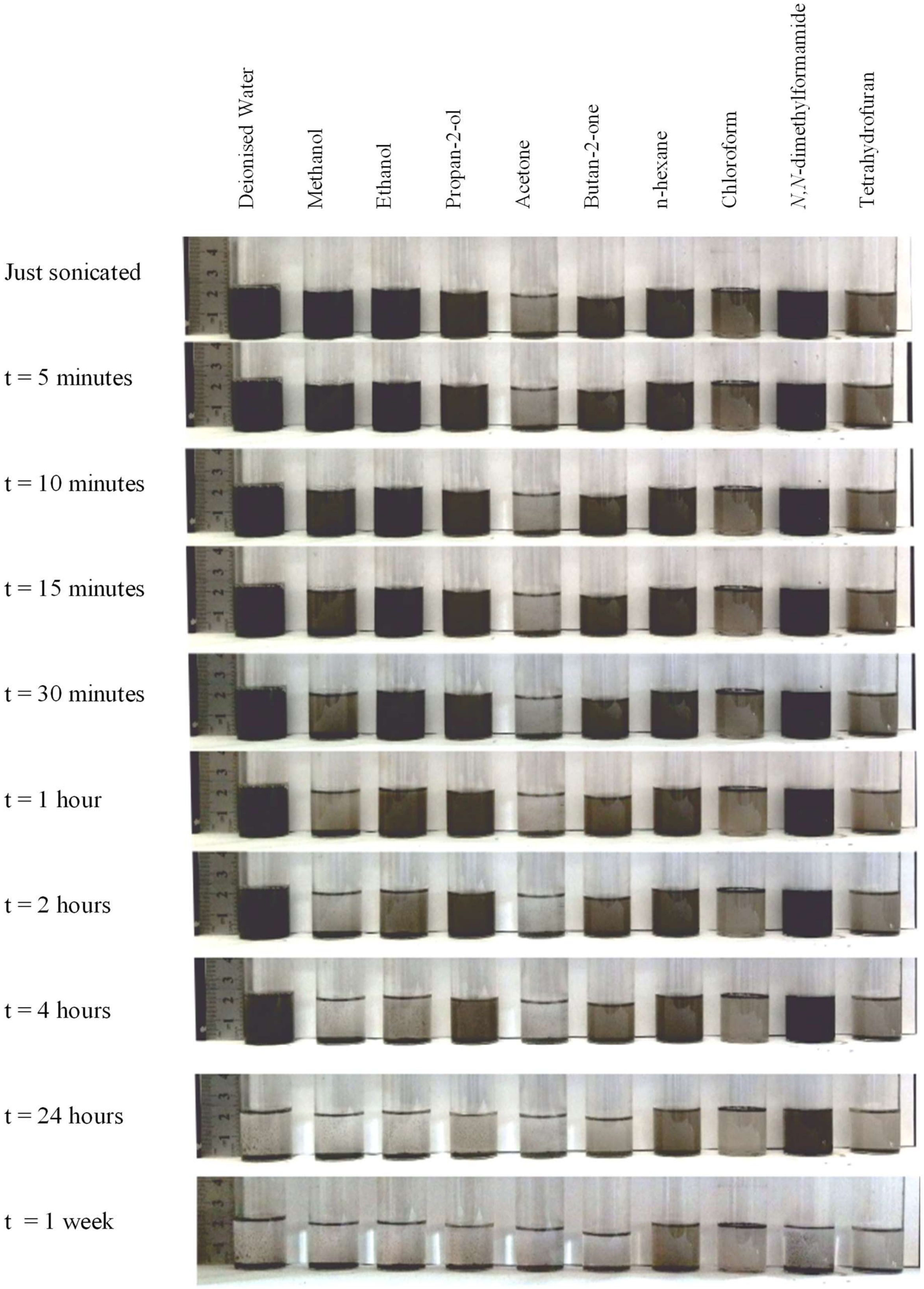

Figure 4.17. Dispersibility study of 1.0 $mgmL^{-1}$ suspensions of UPyGO in 10 different solvents to assess the stability and compatibility of different solvent systems towards solvent deposition fabrication.

The effects of density difference between that of the particles and the surrounding liquid and the liquid viscosity on the sedimentation could be roughly estimated by considering the terminal velocity, *v*, of a single particle suspended in the liquid. A simple analytical expression for *v* in the case of a non-spherical particle is not available. Usually, *v* is expressed by the drag coefficient, which is a complex empirically determined function of the Reynolds number and the particle sphericity - a parameter depending on the particle shape.[41] For this reason, we use the well-known Stokes formula for the terminal velocity of a spherical particle (eq. 4.1) to roughly estimate the effect of density and viscosity on the sedimentation of GO, rGO and UPyGO suspensions in different solvents. This is done by comparing the terminal velocity in a solvent, *v*, to that in water, v_w, using eq. 4.2 obtained from eq.4.1, assuming that the particle size in both cases is the same.

$$\boldsymbol{v = \frac{2\Delta\rho g r^2}{9\eta}} \qquad \textbf{(4.1)}$$

Where $\Delta\rho$ is the difference in density between the particle and the liquid, g is the gravitational acceleration constant (9.81 m s^{-2}), *r* is the radius of the particle, and η is the dynamic viscosity of the liquid media.

$$\boldsymbol{\frac{v}{v_w} = \frac{(\rho_p - \rho_l)\eta_w}{(\rho_p - \rho_w)\eta_l}} \qquad \textbf{(4.2)}$$

The results are shown in Table 4.1.

Table 4.1 Physical properties of solvents at 25 °C used in the estimation of the drag coefficient.[42]

Solvent	Density (g cm^{-3})	Viscosity (mPa s)	v/v_w
Deionised Water	0.998	0.89	1.00
Methanol	0.791	0.54	1.99
Ethanol	0.789	1.08	1.00
Isopropanol	0.785	2.07	0.52
Acetone	0.748	0.30	3.71
Butan-2-one	0.805	0.41	2.59
n-hexane	0.655	0.29	4.12
Chloroform	1.498	0.54	0.83
N,N-dimethylformamide	0.944	0.80	1.17
Tetrahydrofuran	0.886	0.46	2.15

The sedimentation velocity model explains reasonably well the observations of the alcohol systems in all three GOBMs series. As shown by the relative sedimentation velocity (v/v_W), methanol possesses the highest value of 1.99 in the alcohol series and isopropanol being the lowest (0.52). As such, for the alcohol series, the difference in the solvent viscosity and density does dominate the sedimentation behaviour for all GOBMs. For the ketone series again, the relative sedimentation velocity can be used to explain the destabilisation effects of GO and UPyGO; however, this model disagrees for the rGO suspensions.

The sedimentation velocity model estimates that n-hexane should lead to the quickest sedimentation ($v/v_W = 4.12$), which is found for the GO and rGO suspensions. On the other hand, for UPyGO n-hexane shows remarkable stability for a week, stabilising the UPyGO better than all the other solvents. Since this disagrees with the sedimentation velocity, it is postulated that the n-hexane chains form Van der Waal’s interactions with the hexane backbone of the UPy motif, preventing stacking through hydrogen bonding.

Furthermore, water, *N, N*-dimethylformamide, and tetrahydrofuran don’t follow the sedimentation velocity model leading to the support that the stabilisation of GOBMs is not describable by solely sedimentation velocity but combine with their wetting ability on the functional groups present.

The stability for the reduced graphene oxide suspensions followed a similar trend to the graphene oxide for the aqueous and alcohol series. However, for the ketones, the butan-2-one destabilised faster than the acetone. Furthermore, the reduced graphene oxide showed greater stability to *n*-hexane than the GO as expected due to the increase in hydrophilicity. Interestingly the chloroform, *N, N*-dimethylformamide and tetrahydrofuran displayed stability like aqueous conditions.

It is postulated that the observed behaviour in the GO and rGO systems is resultant from the ability to wet intercalate between the sheets via short-range interactions such as hydrogen bonding, therefore limiting the predictions by the relative sedimentation velocity due to the assumption that the Stoke's equation relates to a single particle rather than aggregates. Huang *et al.* proposed a combinational effect which overcomes the limitations to the Stokes law assumptions.[43] It is assumed that the GOBMs do not comply with such as a frictional drag being equal regardless of particle orientation as a result of their spherical geometry assumptions. They propose that due to the ability for solvent molecules to intercalate between the graphene oxide sheets, which produce solvation layers that can reduce the density of the GO sheets by increasing the inter-gallery distance, as shown in Figure 4.18.

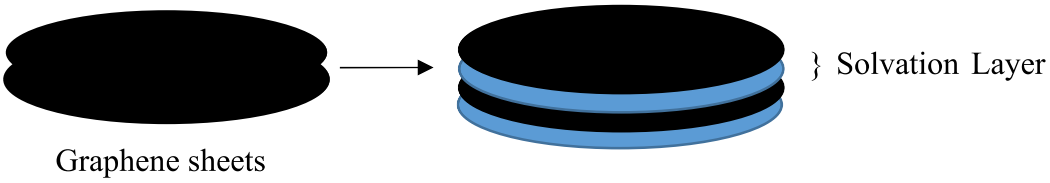

Figure 4.18. Reducing the GO sheet density by solvent exfoliation from solvent intercalation.

As such, the relationship between sedimentation velocity and intercalated sheet density becomes a distinguishing factor for the stability of the system as successful intercalation becomes a prerequisite for this model.

In contrast, the UPyGO suspensions behaved differently to both the GO and rGO—the UPyGO sediment in aqueous conditions after 24 hours. The alcohol and ketone series again showed a linear trend like graphene oxide with an increase in chain length resulting in greater suspension stability. Interestingly, the *n*-hexane remained stable for over a week with stability like that of *N, N*-dimethylformamide.

Therefore, this model can explain the solvent variances such as n-hexane which possesses some stability in UPyGO. As a result of the hydrocarbon structure of n-hexane, which is also mirrored in the hexyl chain of the UPy pendant, the dominant intramolecular interactions are Van der Waals which therefore can aid intercalation of n-hexane.

Finally, the tetrahydrofuran and the chloroform exhibited similar stabilities, however, as shown in Figure 4.19, the UPyGO destabilises by floatation in chloroform, suggestive that the UPyGO aggregates possess a lower density than the chloroform (1.498 g cm^{-3}) unlike the reduced graphene oxide and the graphene oxide which both sedimented.

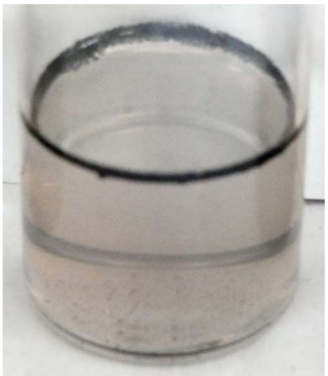

Figure 4.19. 1.0 mg mL^{-1} UPyGO in chloroform showing flotation rather than sedimentation as observed in all the systems investigated.

One explanation for the unexpected creaming in chloroform is that the air trapped within the aggregates could result in buoyancy effects overcoming the sedimentation forces due to gravity. However, the most plausible suggestion is that the UPyGO has some adsorbed water which was released into the chloroform during ultrasonication. The solubilised water within chloroform then supported aggregation formation of UPyGO with the aggregates possessing a lower density than the solvent and therefore resulting in creaming. To fully understand this behaviour, further testing would be required; however, for the purposes of this Thesis, no further investigations are necessary.

Hence by the ability to reduce the density of the sheets further by tuning the intercalation potential, facilitates any unexpected observations in the stability and stability. Studies on the electrophoretic mobility and zeta potential were carried out in aqueous conditions at different pH values to understand the electrostatic stability behaviour of the GOBMs further.

4.8. Zeta Potential

The stability of pH tuned 0.01 mg mL^{-1} aqueous suspensions of graphene oxide, reduced graphene oxide and UPyGO were analysed by measuring the electrophoretic mobility and the zeta potential. The pH was tuned using 0.1 M aqueous solutions of hydrochloric acid and sodium hydroxide as outlined by in the Experimental Chapter. The samples were analysed and averaged (n = 3) and plotted in Figure 4.20.

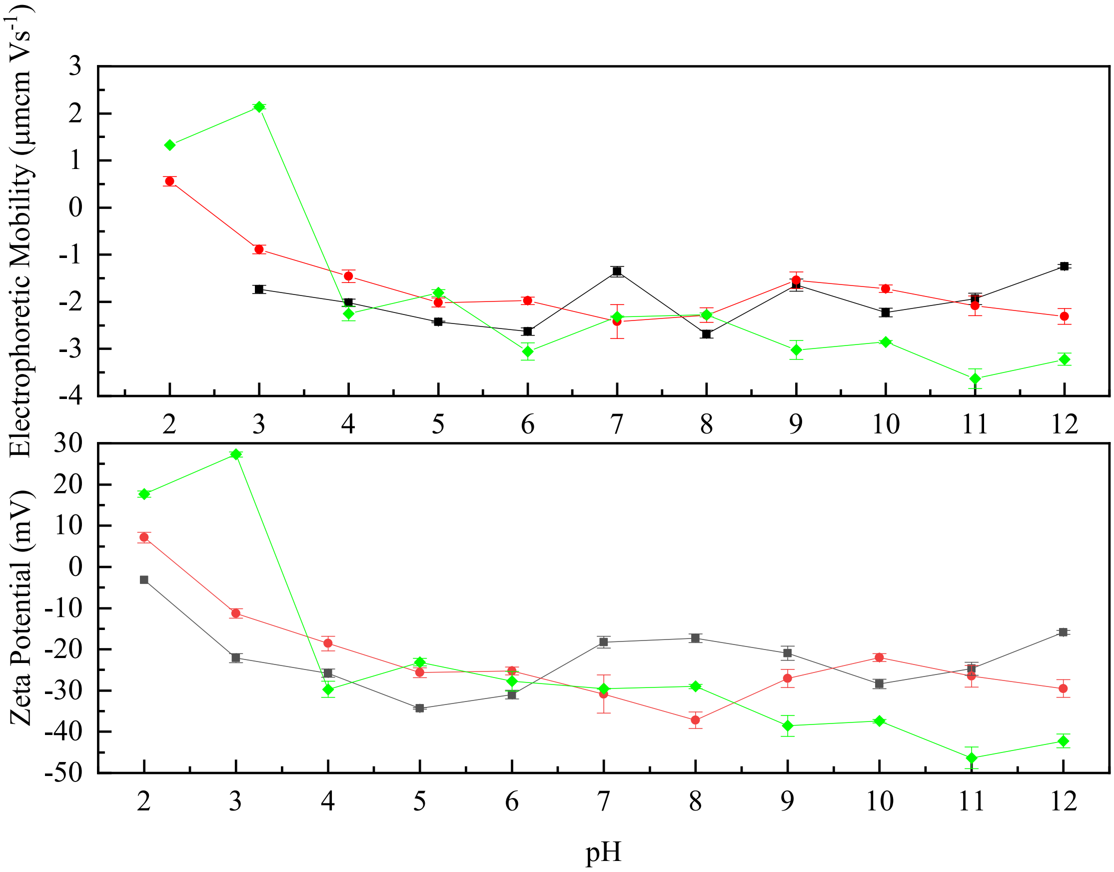

Figure 4.20. Mean electrophoretic mobility and zeta potential (n=3) of 0.01 mg mL^{-1} aqueous graphene oxide (black squares), reduced graphene oxide (red circles), and UPyGO (light green triangles) suspensions after tuning the pH.

Figure 4.20 shows that the electrophoretic mobility and the zeta potential follow complementary trends as expected. Therefore the three-dimensional electric double layer assumptions of zeta potential do not hinder meaningful interpretations of these two-dimensional lamellar-like GOBMs.[14] Triplicate analysis reveals that all three systems vary in their stability in different pH environments.

As predicted, graphene oxide remains at its most unstable at low pH, which is postulated because of the zeta potential is nearly zero. Therefore, this means that electrostatic repulsion considerations are not the dominant mechanism leading to non-DVLO forces causing Van der Waal's attractions and destabilising the system through aggregated stacking due to the multitude of oxygenated moieties present in graphene oxide. An increase in instability was also observed at high pH, which is postulated as the sodium cations stabilise the negative charges formed from dissociated carboxylate groups to form sodium carboxylate salts. The resultant salts, therefore initiate charge screening mechanisms leading to the system aggregating

The relative stability at pH 5 is the result of the water molecules hydrating the sheets leading to functionality group dissociations leaving a negative surface charge on the GO, causing electrostatic repulsion effects to be the dominant stabilising factor. The isoelectric point which is determined by the zeta potential at zero could not be observed for graphene oxide, but at pH 2 the zeta potential was approaching zero which suggests the isoelectric point will be at pH 1 or even lower.

A similar initial trend is observed with rGO; however, its relative charge possesses more positive character than GO which agrees with expectation due to the decrease of dissociable groups during reduction as followed by TGA (see Chapter 3). It was found that rGO is most stable at pH 8 where a presence of any remaining carboxylate ions would lead to electrostatic repulsion between the sheets. Also, the isoelectric point again was at higher pH than GO which was observed between pH 2 and 3.

A general trend for UPyGO showed that the higher the pH, the greater the stability of dispersed UPyGO. The zeta potential for UPyGO shows incipient instability at pH = 2 and 6, which is observed by the magnitude being below 30 mV. Above pH 4, it is evident from the positive values that a positive surface charge is generated, which is resultant from the protonation of the amine functionalities on the UPy pendant. Also, the isoelectric point for UPyGO is estimated to reside between pH 3 and 4 which could explain the incipient instability in that region because of non-DVLO forces dominating to aggregate the system through Van der Waal's attractions. The instability between these pH ranges is postulated to be the result of the UPy groups self-assembling via dimerisation and the protonation of the carboxyl groups being screened. The stability improves in basic conditions as a result of the enol deprotonating into the enolate, leading to an inability to form the stronger DDAA UPy dimer as shown by Figure 4.21.[44]

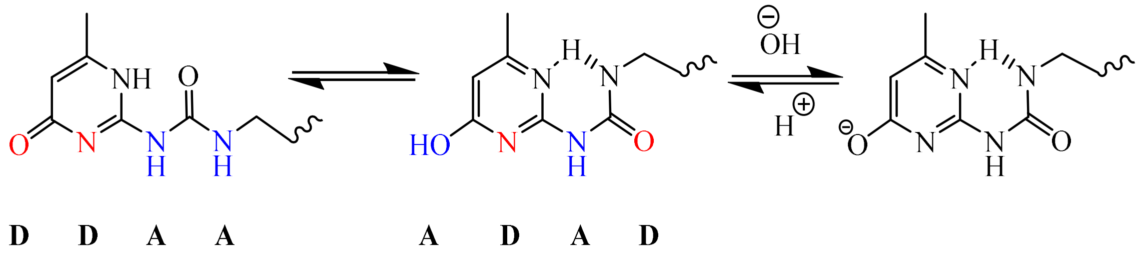

Figure 4.21. Tautomerisation of keto form to enol and consequent deprotonation to form the enolate (red signifies acceptor groups and blue signifies donor groups)

Therefore, as the pH decreases to 11 and 12, which possesses good UPyGO stability is evident from an increase in the enolate present.

4.9. Fabrication of artificial nacre by solvent evaporation of UPyGO suspensions

Self-assembled systems were prepared and investigated to understand the influence of UPy functionalisation on the stacking and mechanical properties of pristine systems. These self-assembled systems are bioinspired to nacre, a lamellated structure of hexagonally arranged aragonite.[45] Because the only other reference to UPyGO was published by Wang *et al.* in 2018,[7] which reported the preparation of UPyGO by fabrication of a nacre-based structure.. Whilst not central to the aims of this thesis the work in this section was conducted to recreate a similar pristine structure for comparison.

Various methods of preparation were investigated to produce GOBM variants of artificial nacre such as vacuum assistance, solvent evaporation, and substrate variation. All methods investigated required the preparation of GOBM-based suspensions to exfoliate the sheets before self-assembly. The only successful preparation of artificial nacre was the evaporation of aqueous GO suspensions, which was determined by observation of visual films, SEM, and mechanical testing. The rGO and UPyGO films did not produce artificial nacre by any of the methods investigated.

First, the initial suspensions were optimised to achieve high quality exfoliated suspensions. The suspension concentration, solvent and volume required were all investigated as part of the optimisation. The solvent selected for the studies were initially deionised water, ethanol, and isopropanol, which were identified as suitable solvents in the stability in different organic solvents study (see section 4.7). The concentrations required and volume of suspension were calculated as per the experimental procedure given (see Chapter 2).

Vacuum-assisted deposition and solvent evaporation deposition techniques were employed to fabricate the artificial nacre and hopefully produce a generic fabrication methodology for the three GOBM systems. However, it was found that vacuum filtration did not produce reproducible and high-quality artificial nacre (see Table 4.3) which was postulated due to the force of the reduced pressure causing accelerated aggregation leading to irregular and enforced stacking.

The mechanical properties were investigated to provide a comparative test for the variation in fabrication method and solvent system, with a 30 µm thickness film. This was because it was found that the GO films in aqueous conditions which acted as the control system provided the most homogenous and continuous film suitable for tensile testing. All films were described and summarised in Table 4.3, based on the following definitions:

- Elastic modulus (E) – The system subjected to tensile testing and provided a returnable data output
- Weak – Yields immediately under force, so could not obtain returnable data outputs
- Aggregate cake – An inhomogeneous system that collapses when force was applied to anneal from the substrate
- Brittle – Mechanically brittle so cannot be prepared for tensile testing

Table 4.3. Mechanical observations of the resultant products of 30 µm thickness GO, rGO or UPyGO artificial nacre systems prepared by variation of solvent system or process.

Fabrication method	Solvent	Solute		
		GO	rGO	UPyGO
Solvent Evaporation	Deionised Water	E= 17 ± 7 MPa	Brittle	Brittle
	Ethanol	Weak	Brittle	Brittle
	Isopropanol	Aggregate cake	Brittle	Brittle
	1:1 v/v Deionised Water: Isopropanol	-	Brittle	Brittle
	Dimethyl carbonate	-	Brittle	Brittle
Vacuum Filtration	Deionised Water	Aggregate cake	Aggregate cake	Brittle
	Ethanol	Aggregate cake	Aggregate cake	Aggregate cake
	Isopropanol	Aggregate cake	Aggregate cake	Aggregate cake
	1:1 v/v Deionised Water: Isopropanol	-	Aggregate cake	Aggregate cake
	Dimethyl carbonate	-	Aggregate cake	Brittle

4.11.1 *Graphene oxide*

The most efficient method to produce graphene oxide artificial nacre was by dispersing few-layered graphene oxide in either deionised water or ethanol to a suspension concentration of 11.8 mg mL^{-1} and evaporating the solvent at 50 °C. It was found that isopropanol dispersed the graphene oxide; however, it did not produce a high-quality nacre film with irregular graphitic clusters observed in the films.

These observations shown in agree with expectations as it is assumed that the volatility of isopropanol is higher than both ethanol and deionised water. This difference, therefore, postulates that the presence of undesirable graphitic clusters is due to uncontrolled self-assembly mechanisms caused by faster solvent evaporation inhibiting steady and controlled lamellated stacking. As a result of this being attributed to the solvents physical properties, preparation in isopropanol was abandoned as deionised water and ethanol were suitable solvents for fabrication.

The structural arrangement, morphology and tensile properties of the graphene oxide artificial nacre investigated using 30 µm thick fabricated films. The structural arrangement was investigated by using scanning electron microscopy using electron energies (5 kV) to observe the surface morphology and inner structure, as shown in Figure 4.22.

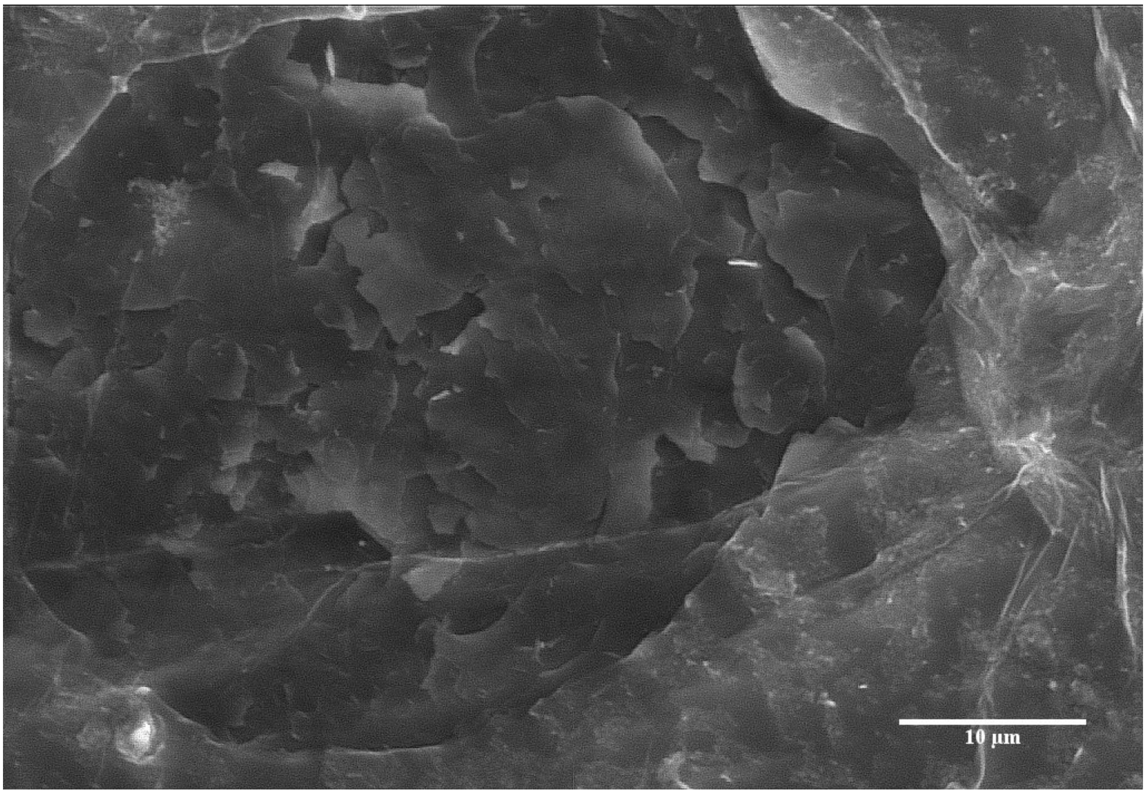

Figure 4.22. Scanning electron micrograph of GO artificial nacre produced by aqueous solvent deposition. (Conditions: 5 kV back-scattered detector, x 4000 magnification) The micrograph shows the expected wrinkled surface morphology, and the basal plane stacking arrangement of the graphene oxide sheets in the hole created by gentle annealing of the top layer using the electron beam.

The electron micrograph (Figure 4.22) shows a well-reported wrinkled surface morphology for graphene oxide nacre.[24,46,47] Through electron beam annealing of the surface, it was found that the inner lamellated graphene oxide structure could be observed, confirming that self-assembled stacking of graphene oxide to graphite oxide nacre was successful. From the observations, it appears that the graphene oxide has self-assembled predominantly by stacking along the basal plane, which agrees with predictions due to the presence of a larger surface area and concentration of functionalities compared to the sheet edges. Observations of the films fabricated in ethanol produced similar observations.

4.11.2 *Reduced graphene oxide*

To produce comparable films of using reduced graphene oxide, both vacuum-assisted and solvent evaporation techniques were investigated. The same selection of solvents was investigated for dispersion with a mixed solvent of 1:1 v/v deionised water and isopropanol proving the most suitable solvent. The mixed solvent proved the most successful owing to the addition of isopropanol to the water as with graphene oxide, it was found that solvent evaporation produced large continuous systems and vacuum-assistance produce poor quality systems as shown by Figure 4.23.

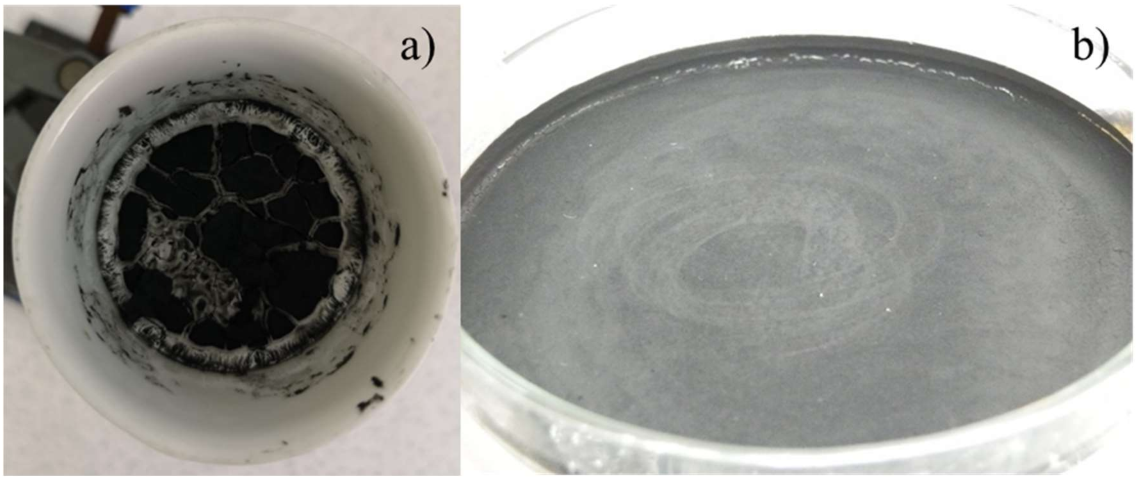

Figure 4.23. Fabrication of reduced graphene oxide artificial nacre from a 1:1 v/v deionised water: isopropanol co-solvent by a) vacuum assistance and b) solvent evaporation.

Comparison between vacuum-assistance and solvent evaporation shows that the use of applied force through reduced pressure produces a discontinuous system that resembles a riverbed. In contrast, solvent evaporation produces a continuous solid deposit across the whole of the container. Neither technique nor any of the solvent systems investigated could be optimised to produce a smooth continuous micrometre thick film. The observations in Figure 4.23a show that the rapid removal of the solvent through vacuum filtration apparatus caused rapid aggregation with discontinuity resulting from aggregates not being in close enough proximity to form effective short-range interactions, producing larger aggregate formations. Furthermore, this ‘caking’ phenomenon is more profound in rGO compared with GO due to the reduction process removing many of the functional groups which can engage in hydrogen bonding.

This reduced concentration of functional groups further supports the observations that the concentration of short-range interactions is reduced, also resulting in continuous powdered deposits rather than continuous films. The lack of functionality and the powered nature of the investigated reduced graphite oxide nacre led to tensile testing being dismissed and comparative testing being conducted between graphite oxide nacre and UPyGO nacre only.

4.11.3 *UPyGO artificial nacre*

Following the same preparation of artificial nacre reported by Wang *et al.*[7] aqueous suspensions of UPyGO were cast onto a cellulose acetate filter membrane under vacuum. Unfortunately, the fabrication of artificial nacre by vacuum filtration was not achieved, as shown in Figure 4.24.

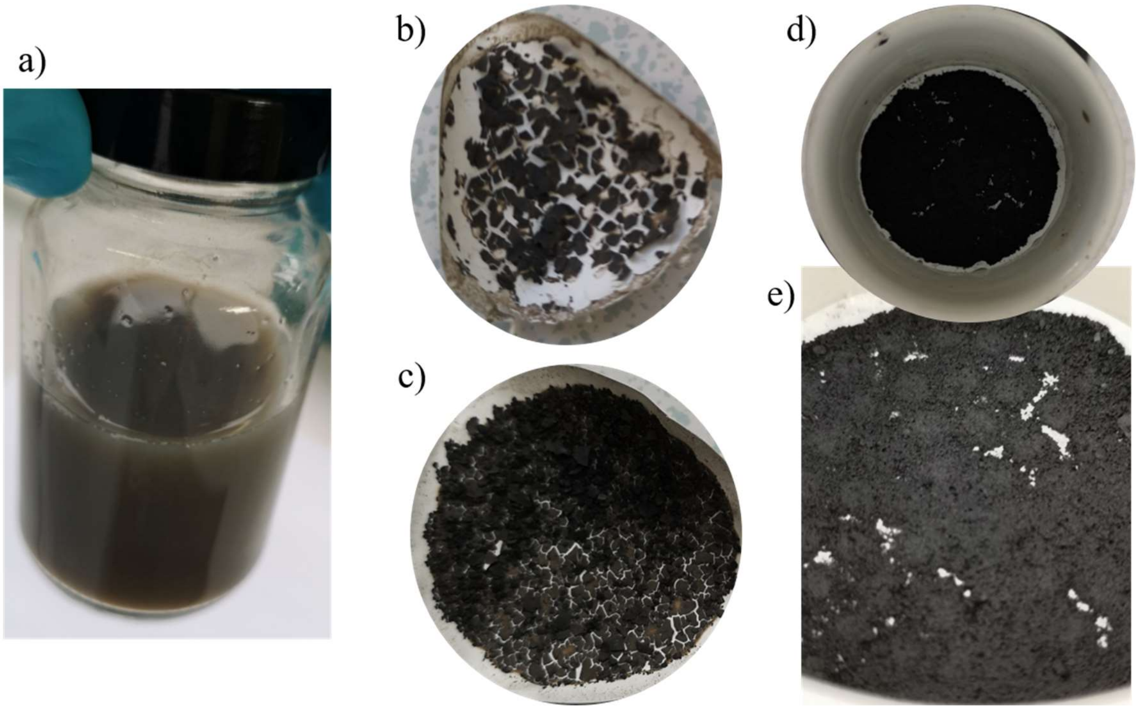

Figure 4.24. Fabrication of UPyGO nacre by vacuum filtration, which did not produce a continuous film a) Aqueous suspension after sonication b) UPyGO with reduced vacuum filtration time (30 mins) followed by a gentle heating cycle of 30 °C for 2 hours to dry the material, c) UPyGO with a reduced vacuum time and allowed to air-dry overnight, d) Wet UPyGO immediately after 30 minutes of vacuum filtration showing a discontinuous film and e) close up of image ‘’d’ showing the production of an aggregate’ cake’ by the rough surface morphology.

As observed in Figure 4.24, the UPyGO forms a cracked film, analogous to a dried riverbed. This behaviour suggests that the rapid dehydration of the UPyGO results in significant shrinkage of the UPyGO film, leading to channel cracks forming when the film strain is overcome.

However, the pre-emptive stress properties reported by UPy previously,[48] cannot sustain a continuous film due to the rapid removal of the water preventing close enough contact for all the UPy groups to self-assemble into a large film. On the other hand, Wang *et al.* show images of the UPyPDG GO as a continuous film displaying actuator-based properties. Current comparison of the fabrication technique suggests that the differences could be attributed to a more sensitive vacuum system or the polydopamine enhancing the fabrication by vacuum filtration.

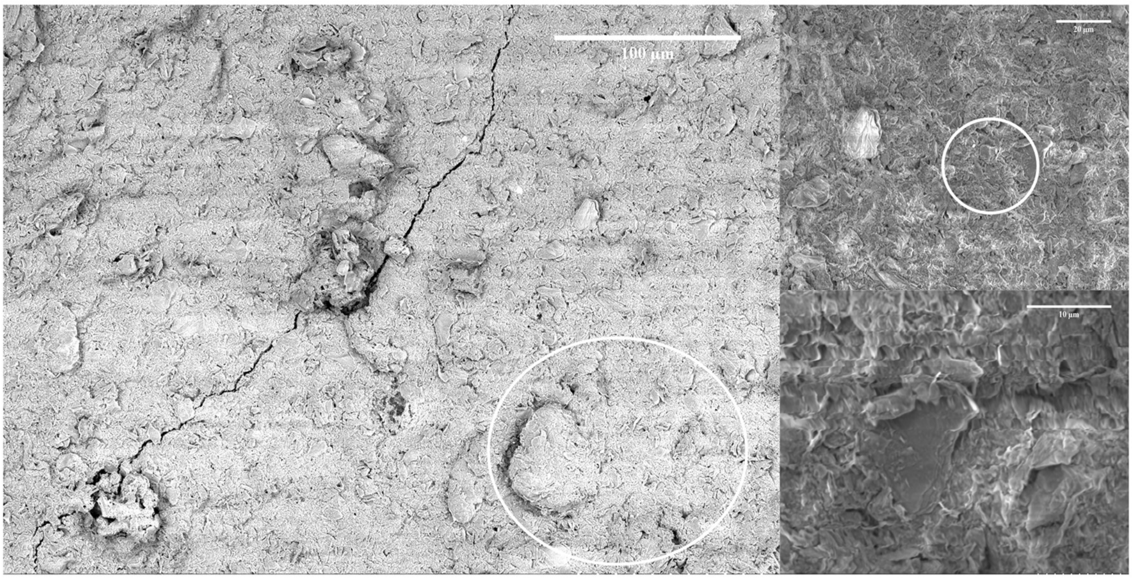

Figure 4.25. UPyGO aqueous films

To test this hypothesis, the dispersion of a UPyGO into a polar apolar solvent capable of evaporation at mild temperatures (> 80 °C) would be required.

Dimethyl carbonate (DMC) was selected because of its polar aprotic characteristics, which are advantageous for the dispersion of UPyGO as determined by its relative stability in *N, N*-dimethylformamide (previous work). Furthermore, the similarity in physical properties to water (b.p. 90 °C STP) enables it to be a good comparison solvent and easier to evaporate than *N, N*-dimethylformamide (b.p. 151 °C STP). In addition, if suitable dimethyl carbonate is exempt from the volatile organic compounds in the United States and regarded as a green reagent due to its biodegradability, rendering it desirable for industrial application.

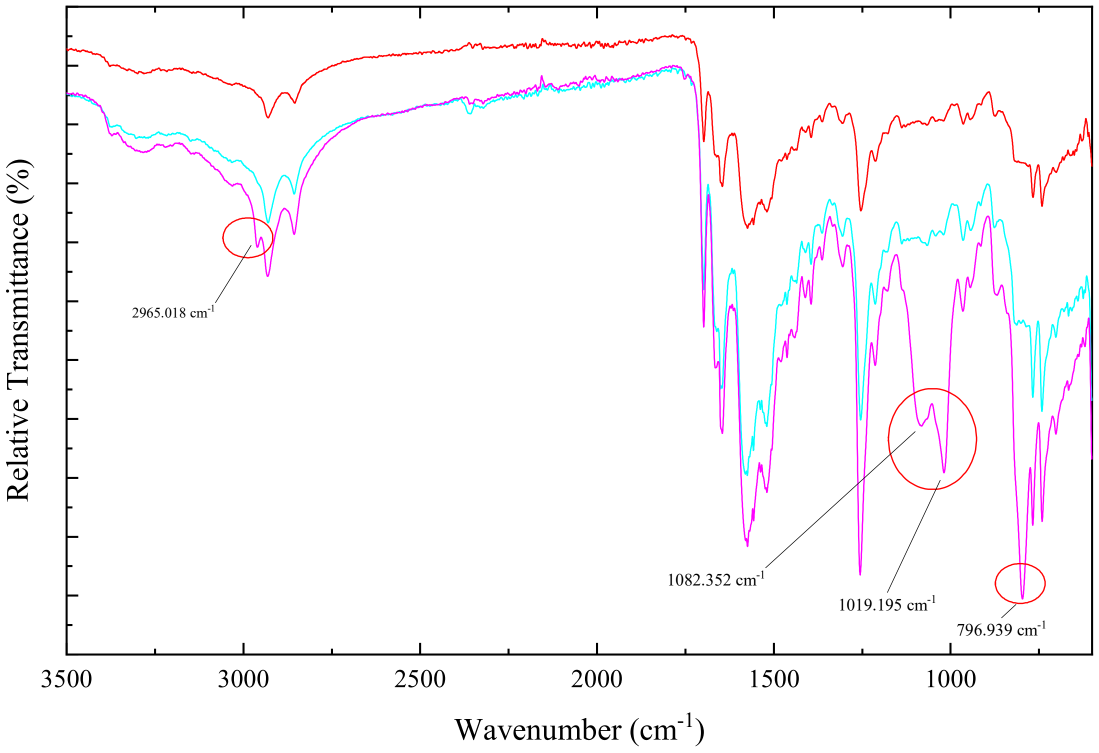

Figure 4.26. Diamond transmittance FTIR ATR to investigate whether the dimethyl carbonate has interacted with the UPyGO. The original UPyGO powder (red), UPyGO($_{aq}$) (sky blue), and UPyGO($_{DMC}$) (magenta).

However, the fabrication of UPyGO in DMC unexpectedly did not produce a thin film like the aqueous samples and instead produced an aggregate cake. Comparison between the two suspensions showed that the dimethyl carbonate completely evaporated overnight whereas the aqueous sample took approximately 60 hours. The difference is expected due to DMC's higher vapour pressure (18 mmHg at 21.1 °C) than water (~17.5 mmHg at 20 °C).

To investigate why such a stark difference in post-fabrication was observed the two samples and the parent UPyGO were analysed by diamond FTIR ATR to determine whether any the DMC has interacted with the UPyGO (Figure 4.26)

Figure 4.26 shows that the aqueous cast UPyGO and the parent UPyGO show no differences in the molecular vibrations suggesting that the water solvates the UPyGO. Interestingly, the UPyGO powder residue cast from the dimethyl carbonate shows four additional vibrations at 2965 cm^{-1}, 1082 cm^{-1}, 1019 cm^{-1} and 796 cm^{-1}. The 2965 cm^{-1} is consistent with the vibrational stretch of carbon-hydrogen. The two peaks at 1082 cm^{-1} and 1019 cm^{-1} are consistent with the strong transmittance of the carbon-oxygen bending and the strong 796 cm^{-1}. Despite the esterification of carboxylic acids with dimethyl carbonate requiring high temperature or pressure in basic conditions,[49] the broad doublet band suggests an ester functionality.

To test the plausibility of the dimethyl carbonate engaged in some short-ranged interaction with the UPyGO, a sample of the cast film was heated to the boiling point of dimethyl carbonate (90 °C STP) for 3 hours with 20% fan and flap setting to exhaust any residual DMC. No visual differences were observed between the samples before or after heating. The post-dried sample (UPyGO Dried) was then analysed by diamond FTIR ATR to observe whether the mystery vibrations disappeared to confirm the hypothesis.

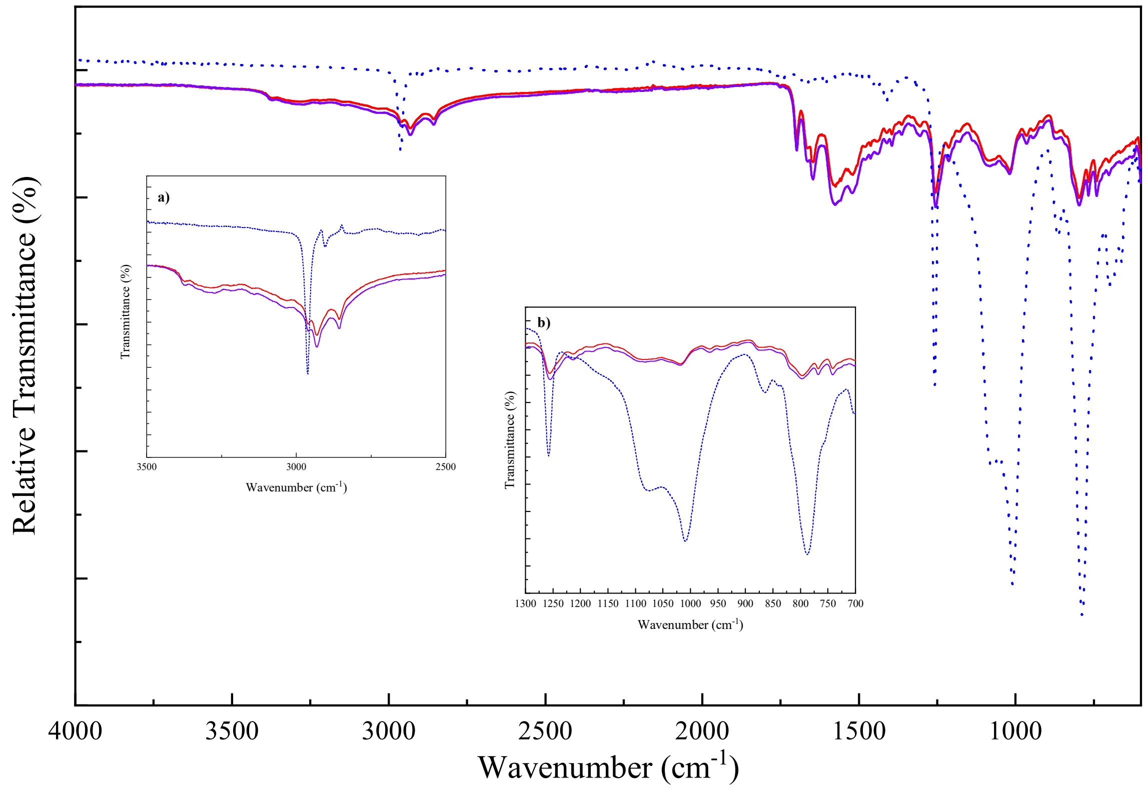

Figure 4.27. Diamond FTIR to test the hypotheses of the mystery peak appearances from the UPyGO cast by DMC. Insets a) the shoulder vibration in the alkyl stretching region c. 2900 cm^{-1} appears to be resultant from the methyl groups present in the PDMS mould substrate shown by the overlay. Inset b) the unexpected peak at c. 1250 cm^{-1} is assigned again to the PDMS mould as it is absent in the UPyGO aqueous castings and the parent powder.

However, as Figure 4.27 shows the unassigned peaks remain and therefore the plausibility of short-range dimethyl carbonate being responsible is not the origin of these peaks, suggesting that the dimethyl carbonate completely evaporates during casting.

4.10. Chapter conclusion

In this chapter, we have presented the successful covalent functionalisation of graphene oxide (GO) with the quadruple hydrogen bonding monomer, ureidopyrimidone. This novel filler which differs from the work of Wang *et al.*[7] due to the absence of polydopamine in the fabrication is extensively characterised and the physical properties compared against the parent graphene oxide and reduced graphene oxide.

To conclude, this chapter investigated the comparison between the graphene oxide powder batch pc92p supplied gratuitously by Graphitene Ltd with the functionalised ureidopyrimidone graphene oxide produced by the formation of a carbamate ester directly onto the basal plane. The two variants were characterised by diamond FTIR ATR, TGA, PXRD and the elemental analysis determined by EDS and CHN combustion analysis, respectively.

The FTIR ATR showed the successful functionalisation by the disappearance of the isocyanate stretching mode at 2297 cm^{-1} and the appearance of vibrational modes indicating a urethane functionality. TGA was employed under a nitrogen atmosphere to investigate the physical properties of the two powders with the parent graphene oxide conforming to the literature and the UPyGO displaying thermal behaviour postulated to thermal expansion. Powder x-ray diffraction method was optimised and run on the powdered materials. As expected, the graphene oxide agreed with the literature, and upon functionalisation, the powder pattern showed the loss of long-range order and an increase in the inter-gallery distance.

The elemental analysis confirmed the presence of nitrogen the UPyGO system to support the successful functionalisation. Elemental combustion analysis was further employed to calculate a mean degree of functionalisation of 6.20 ± 0.04% for three different fresh batches of the UPyGO to demonstrate the reproducibility of the reaction.

The effect of functionalisation on the lateral flake size distribution was also investigated by scanning electron microscopy, which showed that the UPyGO possessed a more symmetric and narrower distribution which was postulated to be the result of centrifugation removing smaller flakes and increased oxidation of larger flakes enabling greater reactivity towards UPyNCO.

Also, comparisons of graphene oxide, reduced graphene oxide and UPyGO in terms of stability in 10 different solvents and different pH environments using zeta potential were carried out. The results showed a significant difference between the parent graphene oxide and the UPyGO further supporting successful functionalisation.

Finally, different strategies were employed to produce artificial nacres of GO, rGO and UPyGO either by vacuum assistance or solvent deposition. The 30 µm thick artificial nacre was subjected to tensile testing, which found GO to be the only system that could be tested whilst the rGO, and UPyGO nacre could not be tested due to their brittleness.

Chapter References

1 S. Keten and M. J. Buehler, *Nano Lett.*, 2008, **8**, 743–748.

2 G. Li, H. Meng and J. Hu, *J. R. Soc. Interface*, 2012, **9**, 3279–3287.

3 W. Weng, J. Benjamin Beck, A. M. Jamieson and S. J. Rowan, *J. Am. Chem. Soc.*, 2006, **128**, 11663–11672.

4 D. Zhong, Q. Yang, L. Guo, S. Dou, L. Jiang and K. Liu, *Nanoscale*, 2013, **5**, 5758–5764.

5 Y. Xu and D. Chen, *Mater. Chem. Phys.*, 2017, **195**, 40–48.

6 J. Canadell, H. Goossens and B. Klumperman, *Macromolecules*, 2011, **44**, 2536–2541.

7 Y. Wang, T. Li, S. Zhang, H. Zhang, M. Du, Y. Xie, M. Chen, W. Dong and W. Ming, *ACS Nano*, 2018, **12**, 6228–6235.

8 B. J. B. Folmer, R. P. Sijbesma, R. M. Versteegen, J. A. J. Van der Rijt and E. W. Meijer, *Adv. Mater*, 2000, **12**, 874–878.

9 Y. Li, D. Pan, S. Chen, Q. Wang, G. Pan and T. Wang, *Mater. Des.*, 2013, **47**, 850–856.

10 F. Ren, G. Zhu, P. Ren, Y. Wang and X. Cui, *Appl. Surf. Sci.*, 2014, **316**, 549–557.

11 S. Stankovich, R. D. Piner, S. T. Nguyen and R. S. Ruoff, 2006, **44**, 3342–3347.

12 F. H. Beijer, R. P. Sijbesma, H. Kooijman, A. L. Spek and E. W. Meijer, *J. Am. Chem. Soc.*, 1998, **120**, 6761–6769.

13 S. Stankovich, R. D. Piner, S. B. T. Nguyen and R. S. Ruoff, *Carbon N. Y.*, 2006, **44**, 3342–3347.

14 K. Krishnamoorthy, M. Veerapandian, K. Yun and S. J. Kim, *Carbon N. Y.*, 2013, **53**, 38–49.

15 VAMAS, *Chemical composition of G/GO flakes: Elemental analysis and Oxygen content using X-ray photoelectron spectroscopy (XPS)*, 2017.

16 C. N. Yeh, K. Raidongia, J. Shao, Q. H. Yang and J. Huang, *Nat. Chem.*, 2015, **7**, 166–170.

17 R. Jalili, D. Esrafilzadeh, S. H. Aboutalebi, Y. M. Sabri, A. E. Kandjani, S. K. Bhargava, E. Della Gaspera, T. R. Gengenbach, A. Walker, Y. Chao, C. Wang, H.

Alimadadi, D. R. G. Mitchell, D. L. Officer, D. R. MacFarlane and G. G. Wallace, *Nat. Commun.*, 2018, **9**, 1–13.

18 F. H. Baldovino, A. T. Quitain, N. P. Dugos, S. A. Roces, M. Koinuma, M. Yuasa and T. Kida, *RSC Adv.*, 2016, **6**, 113924–113932.

19 A. Faghani, I. S. Donskyi, M. Fardin Gholami, B. Ziem, A. Lippitz, W. E. S. Unger, C. Böttcher, J. P. Rabe, R. Haag and M. Adeli, *Angew. Chemie - Int. Ed.*, 2017, **56**, 2675–2679.

20 Mettler-Toledo AG, in *Thermal Analysis in Practice*, ed. M. Wagner, Schwerzenbach, 2013, p. 158.

21 J. H. Saunders, *Rubber Chem. Technol.*, 1959, **32**, 337–345.

22 Mettler-Toledo AG, in *Thermal Analysis in Practice*, ed. M. Wagner, Schwerzenbach, 2013, p. 157.

23 K. Josepovits, Y. Sanakis, D. Petridis and I. De, 2006, 2740–2749.

24 D. A. Dikin, S. Stankovich, E. J. Zimney, R. D. Piner, G. H. B. Dommett, G. Evmenenko, S. T. Nguyen and R. S. Ruoff, *Nature*, 2007, **448**, 457–460.

25 H. Tang, G. J. Ehlert, Y. Lin and H. A. Sodano, *Nano Lett.*, 2012, **12**, 84–90.

26 G. Armstrong and M. Buggy, *Mater. Sci. Eng. C*, 2001, **18**, 45–49.

27 J. Guerrero-Contreras and F. Caballero-Briones, *Mater. Chem. Phys.*, 2015, **153**, 209–220.

28 L. Stobinski, B. Lesiak, A. Malolepszy, M. Mazurkiewicz, B. Mierzwa, J. Zemek, P. Jiricek and I. Bieloshapka, *J. Electron Spectros. Relat. Phenomena*, 2014, **195**, 145–154.

29 A. J. Pollard, K. R. Paton, C. A. Clifford, E. Legge, A. Oikonomou, S. Haigh, C.

Casiraghi, L. Nguyen and D. Kelly, *Characterisation of the Structure of Graphene*, 2017.

30 H. Liu, Nottingham, 2014.

31 S. H. M. Söntjens, R. P. Sijbesma, M. H. P. Van Genderen and E. W. Meijer, *J. Am. Chem. Soc.*, 2000, **122**, 7487–7493.

32 Graphitene Ltd, *Product Data Sheet – Graphene Oxide Powder*, Flixborough, 2017.

33 L. Dong, J. Yang, M. Chhowalla and K. P. Loh, *Chem. Soc. Rev.*, 2017, **46**, 7306–7316.

34 R. Sharma, J. H. Baik, C. J. Perera and M. S. Strano, *Nano Lett.*, 2010, **10**, 398–405.

35 S. Eigler and A. Hirsch, *Angew. Chemie - Int. Ed.*, 2014, **53**, 7720–7738.

36 J. J. Huang and Y. J. Yuan, *Phys. Chem. Chem. Phys.*, 2016, **18**, 12312–12322.

37 Graphitene Ltd, *Product Data Sheet – Reduced Graphene Oxide*, Flixborough, 2017.

38 D. Konios, M. M. Stylianakis, E. Stratakis and E. Kymakis, *J. Colloid Interface Sci.*, 2014, **430**, 108–112.

39 J. I. Paredes, A. Marti, J. M. D. Tasco and A. Martı, *Langmuir*, 2008, **24**, 10560–10564.

40 S. Wang, Y. Zhang, N. Abidi and L. Cabrales, *Langmuir*, 2009, **25**, 11078–11081.

41 A. Haider and O. Levenspiel, *Powder Technol.*, 1989, **58**, 63–70.

42 S. Murov, Properties of Solvents Used in Organic Chemistry, http://murov.info/orgsolvents.htm, (accessed 20 September 2019).

43 J.-J. Huang and Y. J. Yuan, *Phys. Chem. Chem. Phys.*, 2016, **18**, 12312–12322.

44 M. M. C. Bastings, S. Koudstaal, R. E. Kieltyka, Y. Nakano, A. C. H. Pape, D. A. M. Feyen, F. J. van Slochteren, P. A. Doevendans, J. P. G. Sluijter, E. W. Meijer, S. A. J. Chamuleau and P. Y. W. Dankers, *Adv. Healthc. Mater.*, 2014, **3**, 70–78.

45 J. Wang, Q. Cheng and Z. Tang, *Chem. Soc. Rev.*, 2012, **41**, 1111–1129.

46 Y. Lu, T. Wang, Z. Tian and Q. Ye, *Int. J. Electrochem. Sci.*, 2017, **12**, 8944–8952.

47 X. J. Shen, X. Q. Pei, Y. Liu and S. Y. Fu, *Compos. Part B Eng.*, 2014, **57**, 120–125.

48 J. L. Wietor, A. Dimopoulos, L. E. Govaert, R. A. T. M. Van Benthem, G. De With and R. P. Sijbesma, *Macromolecules*, 2009, **42**, 6640–6646.

49 M. G. Gallego and M. A. Sierra, in *Organic Reaction Mechanisms: 40 Solved Cases*, Springer Berlin Heidelberg, Berlin, Heidelberg, 2004, pp. 131–137.

5. Investigating the mechanical properties of complementary ureidopyrimidone dimerised graphene oxide polyurethane composites

By taking inspiration from nature, many different novel materials have been developed over the last few decades.[1–4] In particular the chemistry residing around spider silk, which is known for its lightweight yet high strength properties, are owing to the hydrogen bonds aligned between the β-sheet crystals.[5]

Hydrogen bonding arrays such as the AADD array attributed by UPy enables the formation of high binding energies.[6] Over the last 2 decades work has been undertaken to utilise these units to deliver more stable products. The incorporation of UPy into polymeric systems is achieved by 2 different strategies: telechelic units or side group attachment on the polymer backbone.[7]

This successful incorporation of UPy into the backbone enables the ability to produce enhanced mechanical properties in addition to autonomous self-healing by exploitation of the strong dimerisation constant and the structures of self-healing groups residing in the hard segments.

In 2009, Wietor *et al.* published results on incorporating UPy into polyurethane-polyester co-polymer matrices and measured the mechanical properties as a function of UPy percentage concentration.[8] The work found that the presence of UPy within the polymer relaxed stresses occurred during the preparation of coatings, such as film shrinkage during curing. They concluded that the autonomous pre-emptive self-healing, which their present work is currently trying to understand the healing mechanism in greater depth. Furthermore, Faghihnejad *et al.* demonstrated that the presence of UPy within a matrix can "*dramatically enhance the polymer adhesion*" due to the quadruple hydrogen bonding formed at the contact interface, which consequently leads to enhanced chain interpenetration and dimer formation across the interface.[9]

Published in June 2017, a patent for the preparation of supramolecular polymers containing quadruple hydrogen bonding groups by using UPy by Janssen *et al.* from the Eindhoven group, which is well known for its work on quadruple hydrogen bonding in supramolecular polymers.[10] The work furthermore claims the use of liquid-based reagents, thus making the need for dissolving solid reagents in organic solvents "*obsolete*".[10]

Nevertheless, the diversity of UPy as a self-healing strategy is seen in both organic and aqueous environments, as reported by Lin and Li in 2014 using PUR hydrogels.[11] Their work saw the addition of UPy groups into a hydrophilic structure using acrylate functional groups in a PUR/PA co-polymer, which provides the potential for developing aqueous-based solvent systems in next-generation coatings.

In this Chapter, we report the successful functionalisation of Easyflo120 polyurethane with UPyNCO to produce a UPy-modified polyurethane through an *in situ* polymerisation approach favoured by industry. The modified polyurethane is then further expanded by combination with the UPyGO, made in Chapter 4 to create a complementary dimerised UPyPU-UPyGO polyurethane composite. An *in situ* polymerisation approach is utilised again for comparison with previous works in this Thesis.

5.1. **Fabrication of UPy-Easyflo 120 by *in situ* polymerisation**

To produce the complementary polyurethane bearing the UPy functionality, 0, 0.066, 0.12, 0.2 and 5 wt.% loadings of UPyNCO were prepared as stock suspensions in either Easyflo 120 Part B or Part A and dispersed by ultrasonication for 15 minutes.

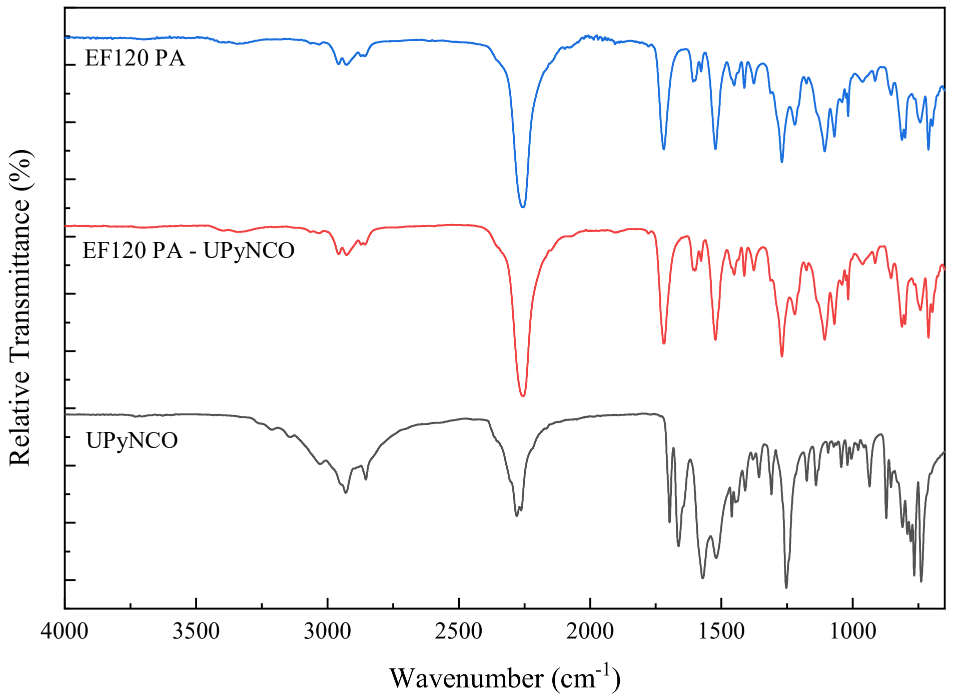

Figure 5.1. Diamond FTIR ATR demonstrating that the UPyNCO (black spectra) does not react with the Easyflo 120 Part A resin (red spectra) under ultrasonication conditions (blue spectra)

No reactivity was observed in the stock suspensions prepared in Part A as expected due to the isocyanate stretch at 2297 cm^{-1} and no new vibrational modes observed when compared against the virgin Easyflo 120 Part A resin.

However, the room temperature reactivity of the two-component Easyflo120 suggests that the Quadrol™ is a tertiary amine that acts as a crosslinker but can also be an organocatalyst in the polymerisation of polyurethanes too.[12–14] Therefore to investigate whether any reaction occurs in the preparation of the stock suspension, Easyflo 120 Part B and UPyNCO were combined together and dispersed by ultrasonication in the same manner as the Part A stock suspension was prepared and characterised by FTIR ATR (see Figure 5.2).

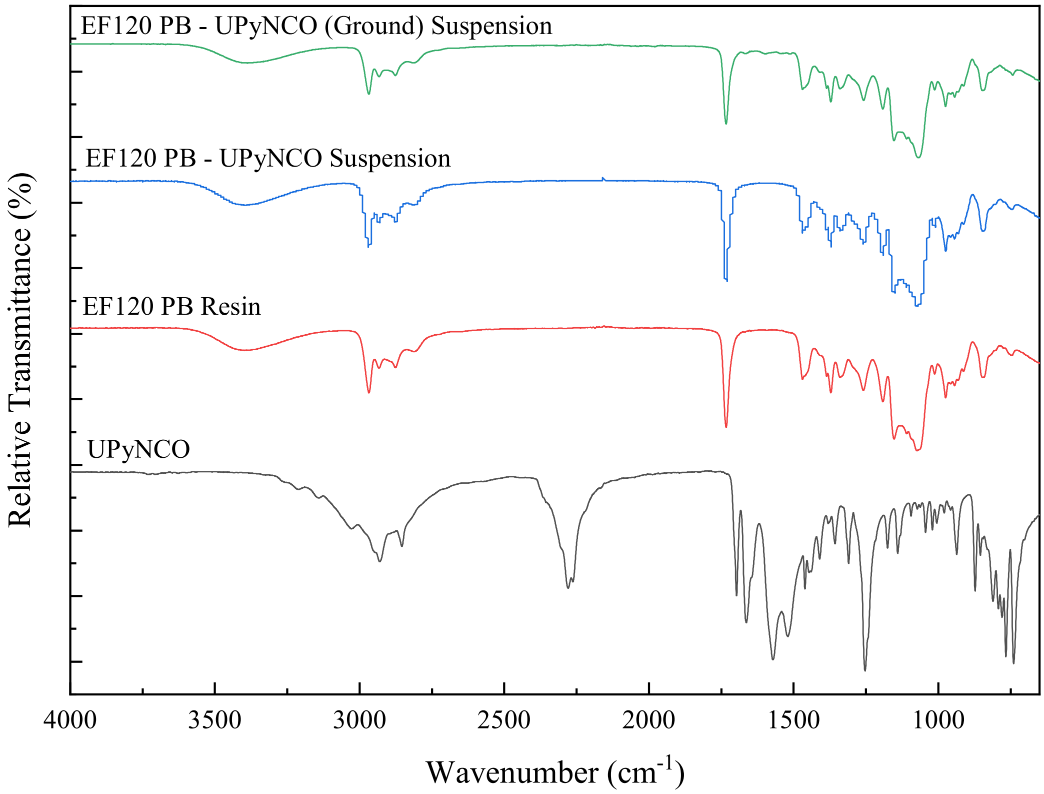

Figure 5.2. Diamond FTIR ATR demonstrating that the UPyNCO (black spectra) does not react with the Easyflo120 Part B (red spectra) under ultrasonication conditions (blue spectra) even if the UPyNCO is ground before addition (green spectra)

Comparison of the spectra in Figure 5.2 show no variation in the vibrational modes between the suspension and the virgin Easyflo 120 Part B resin. The broad peaks in all the resin and suspension samples at c.3400 cm^{-1} denotes intermolecular hydrogen bonding between hydroxyl groups which is expected by the appearance of viscous samples in EF120 PB Resin, EF120PB – UPyNCO Suspension, and EF120PB – UPyNCO (Ground) Suspension. The sharp peaks at c.1720 cm^{-1} originate from the carbonyl groups on the phthalate esters which make up 30-50% of the Part B resin. No other peaks or peak shifts are present in this region for the suspension samples which would only be present if the isocyanate terminus reacted to form a carbamate ester. The disappearance of the 2297 cm^{-1} was determined as a concentration factor and therefore masked by the virgin resin. For completeness, the assumption of increased surface area and reactivity was evaluated and the UPyNCO was ground using a mortar and pestle and a fresh stock suspension was prepared under the same conditions. The FTIR ATR analysis shows no specific reactivity between the UPyNCO and the resins before combination which suggests that the components from both resins are required to generate successful polymerisation. The absence of reactivity in the separate components is expected because of the composition of the two resins. Part A possesses the isocyanate functionalities from the 4,4’ methylene diphenyl diisocyanate (MDI) which is solvated in esters of aliphatic acids. The solid MDI would not react with the isocyanate terminus of the UPyNCO, and it is also expected that the esters of aliphatic esters would solvate rather the UPyNCO also, therefore no reaction expected. Part B possesses viscous polyols (alkyl polyol blends and Quadrol™) no reactivity is expected from the known structure of the phthalate esters so reactivity would be challenging. Also, the hydroxyl groups would favour engagement in intermolecular hydrogen bonding with the incorporation of UPyNCO into the mixture adding further hydrogen bonding potential and less availability for successful reaction from isocyanate terminus to a carbamate ester linkage. The hydroxyl intermolecular hydrogen bonding is observed in Figure 5.2.

Therefore, an in-situ polymerisation approach was conducted due to the only variable being the UPyNCO, a white crystalline powder, analogous to 4,4'-diphenyl-dimethyl diisocyanate suspended in alkyl ester. The in-situ polymerisation was conducted as per Chapter 2 to reveal the final fabricated functionalised white polymers UPyPU.

The UPyPU polyurethanes were cut into small test samples and placed onto the diamond ATR crystal window for analysis by FTIR ATR as a function of the UPyNCO loading and compared in Figure 5.3.

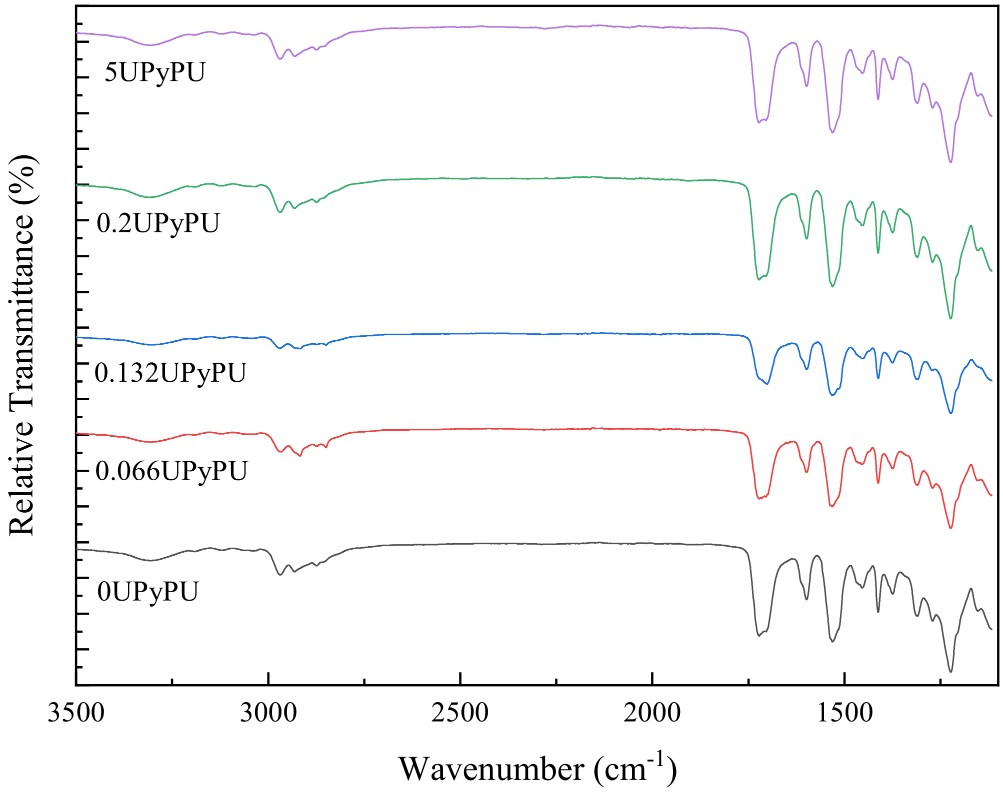

Figure 5.3. Diamond FTIR ATR of the in-situ polymerisation UPy-functionalised Easyflo 120 polyurethane composites as a function of the UPyNCO loading as a weight percentage.

The diamond FTIR ATR shows no observed isocyanate stretching mode, suggesting that the 4,4'-diphenylmethylenediisocyanate (MDI) present in Part A and the UPyNCO have fully reacted or are not detectable. Figure 5.3. confirm that the broad vibration observed in each spectrum at 1723 cm^{-1} supports the formation of a urethane bond and successful polymerisation of isocyanates and the polyols. However, establishing a more reliable technique for confirming UPyNCO functionalisation requires analysis by differential scanning calorimetry (DSC) and dynamic mechanical thermal analysis (DMTA) to quantify factors such as an increase in glass transition temperature (T_g) and crosslink density. Such factors would suggest increased crystallinity caused by the UPy dimerisation within the polymer architecture and therefore afford a more three-dimensional thermosetting polyurethane.

In a comparative manner to the polyurethanes and GOBM polyurethane composites, DSC analysis was conducted in triplicate. The triplicate analysis was averaged and subjected to the standard deviation of the sample set and summarised in Figure 5.4.

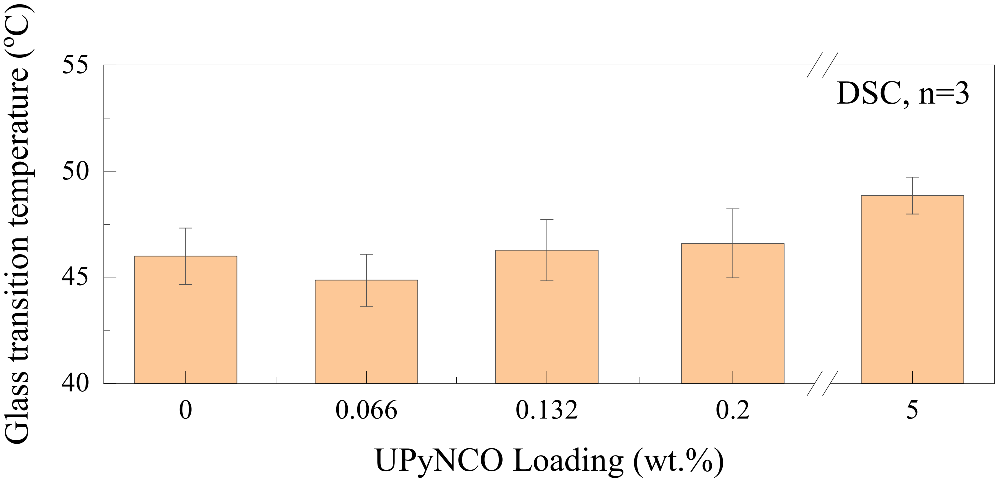

Figure 5.4. The effect of UPyNCO loading on the T_g as determined by DSC analysis

The DSC data in Figure 5.4 shows a progressive increase in the T_g with the addition of UPyNCO. The data shows a 6% increase in the T_g at 5 wt.% when comparing against the virgin polyurethane. The relationship between the addition of UPyNCO and the increase in the T_g would suggest the polymerisation was successful and afforded a more crystalline polyurethane as expected, with UPyNCO dimer matrix functionality increasing the crystallinity. This investigation provided enough characterisation for the development which therefore resulted in the impact dissipation and crosslink density been considered next.

Tanδ, the ratio between the storage modulus and the loss modulus, measures a materials' ability to dissipate energy during an applied load. The tanδ peak (Figure 5.5) as determined by the instrument's software, and the crosslink density, ν_e (Figure 5.5) calculated using Equation **(5.1)**

$$\nu_e = \frac{E'}{3RT} \tag{5.1}$$

Where E' is the storage modulus at 170 °C, R is the universal gas constant (8.314 J mol^{-1} K^{-1}), and T is the absolute temperature at 170 °C (443.15 K).

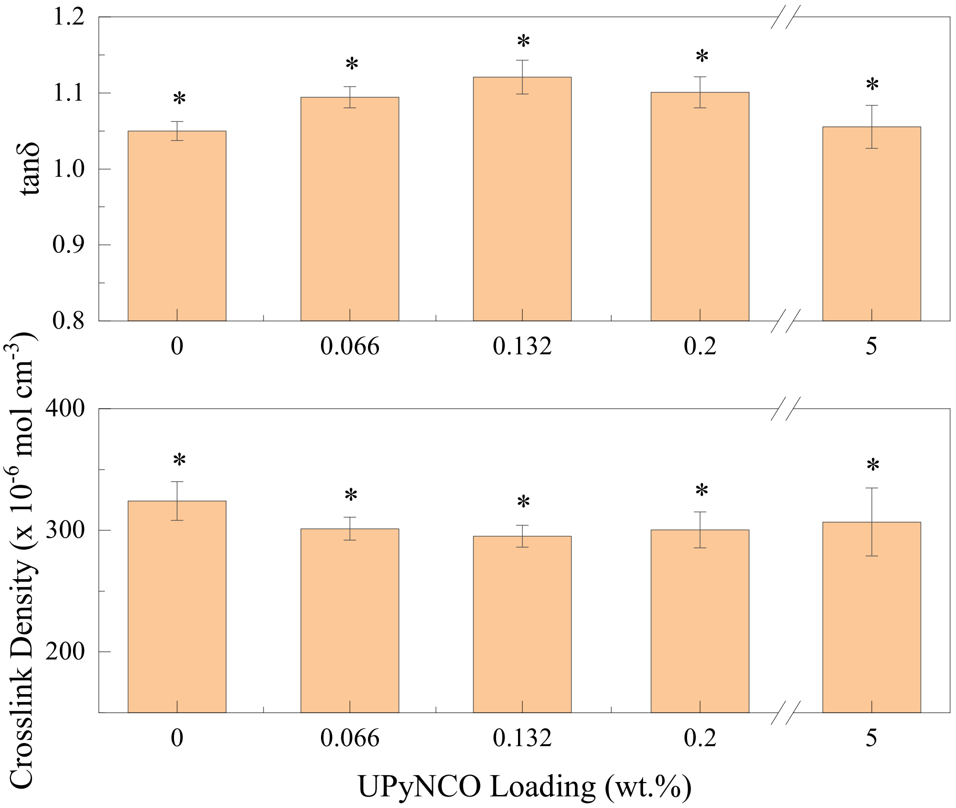

Figure 5.5. The effect of UPyNCO loading on the impact dissipation factor, tanδ, measured at the maximum of the peak (top); and the calculated crosslink density is taken at T=170 °C (bottom). Asterisk denotes statistical significance (p=0.05) through Analysis of Variance (ANOVA) testing.

Figure 5.5 shows a bell-shaped trend for the effect of UPyNCO loading on the impact dissipation factor. This trend suggests that the addition of UPyNCO assists the modified polyurethane to dissipate the applied tensile load indicative of pre-emptive stress enhancement.[8] However, as observed in other works, UPyNCO can saturate the system and diminish the material performance of a UPy-modified polymer due to imparting crystallinity and tensile stiffness, which leads to a decrease in the storage modulus performance.[8]

This reduction in elastic modulus is demonstrated by reducing the calculated crosslink density, which shows that the UPy units are not observed at the calculated temperature range (170 °C). This suggests that the UPy functionalisation competes with the covalent polymer chain crosslinks within the system, leading to a reduction in calculated crosslink density, but an observed increase in the T_g and before the postulated UPyNCO saturation point an ability to dissipate energy more effectively under applied load.

Through the creation of UPyPU, this work is extended to develop and investigate the effect of incorporating the UPyGO filler created as described in Chapter 4 into the matrix through complementary dimerisation. The following sections within this Chapter outline the developments and investigations and the comparative difference between unmodified and complementary dimerised UPyGO-UPyPU composites.

5.2. Fabrication of complementary UPyPU-UPyGO composites

The UPyNCO was added to the Easyflo Part A and dissolved upon mixing by hand. The solubility of the UPyNCO within the Easyflo 120 Part A was expected and resultant from the suspected ethyl acetate solvent formulated into Part A to solubilise the solid 4,4’-methylene diphenyl diisocyanate also.

The UPyGO fabricated as per Chapter 2 was dispersed in Easyflo 120 Part B via sonication. The sonication of the virgin UPyGO resulted in poor dispersion, and the larger aggregates sedimented in the Easyflo 120 Part B (see Figure 5.6). To create a homogenous UPyGO in Easyflo 120 Part B suspension, the virgin UPyGO before addition to Part B was ground. The effect of grinding on the dispersibility of the UPyGO results from the considerations in the Stokes Law equation, where the reduction in particle radius possesses a squared relationship with the sedimentation velocity.[15] The ground UPyGO dispersed in Easyflo 120 via sonication to prepare the UPyGO stock suspension.

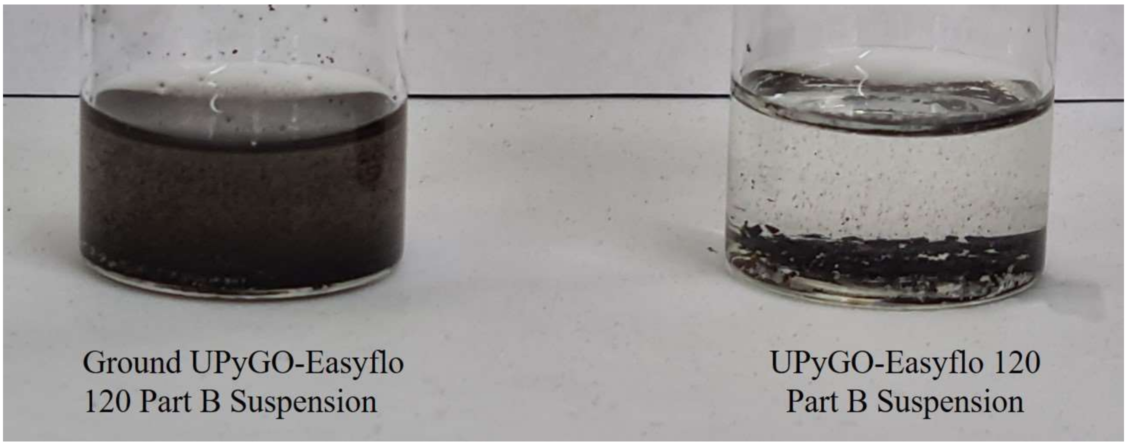

Figure 5.6. The effect of mortar and pestle grinding of UPyGO on its dispersibility in Easyflo 120 resin.

The prepared UPyGO stock suspension, Easyflo 120 Part A/UPyNCO solution and virgin Easyflo 120 Part B were combined. The composite fabrication followed the same procedure as the unmodified GOBM polyurethane composites to produce a white polymer composite.

Differential scanning calorimetry determined the T_g; nanoindentation for the hardness, creep, indentation elastic modulus, and indentation stiffness; dynamic mechanical thermal analysis for tensile storage modulus, tensile loss modulus, tanδ, crosslink density, and refine the T_g; and isothermal tensile testing to determine the elastic modulus, and tensile stiffness.

5.3. Effect of UPyGO filler loading on the UPyGO-UPyPU composite T_g

Both DSC and DMA determined the T_g to investigate the effect of UPyGO loading on the modified UPy-PU matrix earlier in this Chapter. DSC analysis and DMA were conducted in triplicate and n=10, respectively. The data sets were treated similarly to the unmodified graphene-oxide-based material composites (Chapter 3) and the UPyPU samples. The standard deviation was calculated for all the data sets as part of the uncertainty analysis.

The DSC samples were conducted under the standard parameters (see Chapter 2) within this research and averaged. The averaged data is presented in Figure 5.7.

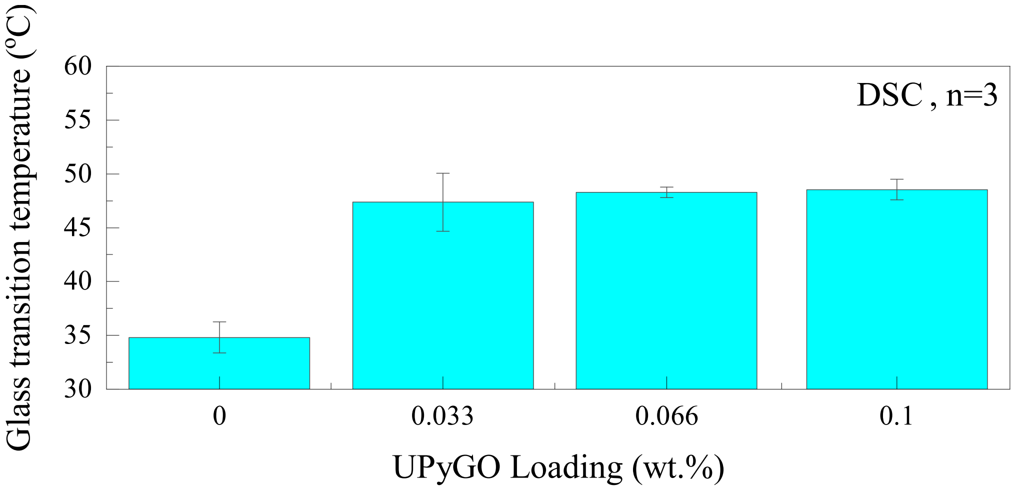

Figure 5.7 The effect of UPyGO loading on the T_g of the UPyGO-UPyPU composite measured by DSC analysis through the extrapolation of half the specific heat method.

The effect of UPyGO-UPyPU weight loading on the T_g determined by DSC shows a significant increase in the T_g in the presence of filler and modification. The creation of the UPyGO-UPyPU polyurethane composite increased the T_g by 36% (47.8°C), 39% (48.3°C), and 39% (48.5°C) for 0.033 wt.%, 0.066 wt.% and 0.1 wt.% respectively, compared to the virgin polyurethane. Such observations suggest that the π-π stacking and rigidity from the aromatic rings in the graphene oxide basal plane and the UPy heteroaromatic end group require additional thermal energy to transition from a glassy state to an amorphous rubber state hence the observation in the increase in T_g.[16,17]

However, the T_g can be influenced by frequency variations, which limits the precision of these studies, so DMA studies using a fixed frequency mitigate these limitations. To maintain uniformity with the unmodified and UPyPU systems the T_g was compared using the loss modulus onset (E''_{onset}) and the maxima of the tanδ peak ($\tan\delta_{max}$). The samples were measured and analysed before single factor ANOVA was performed to determine significance. The averaged samples were plotted as a function of UPyGO loading and presented below in Figure 5.8.

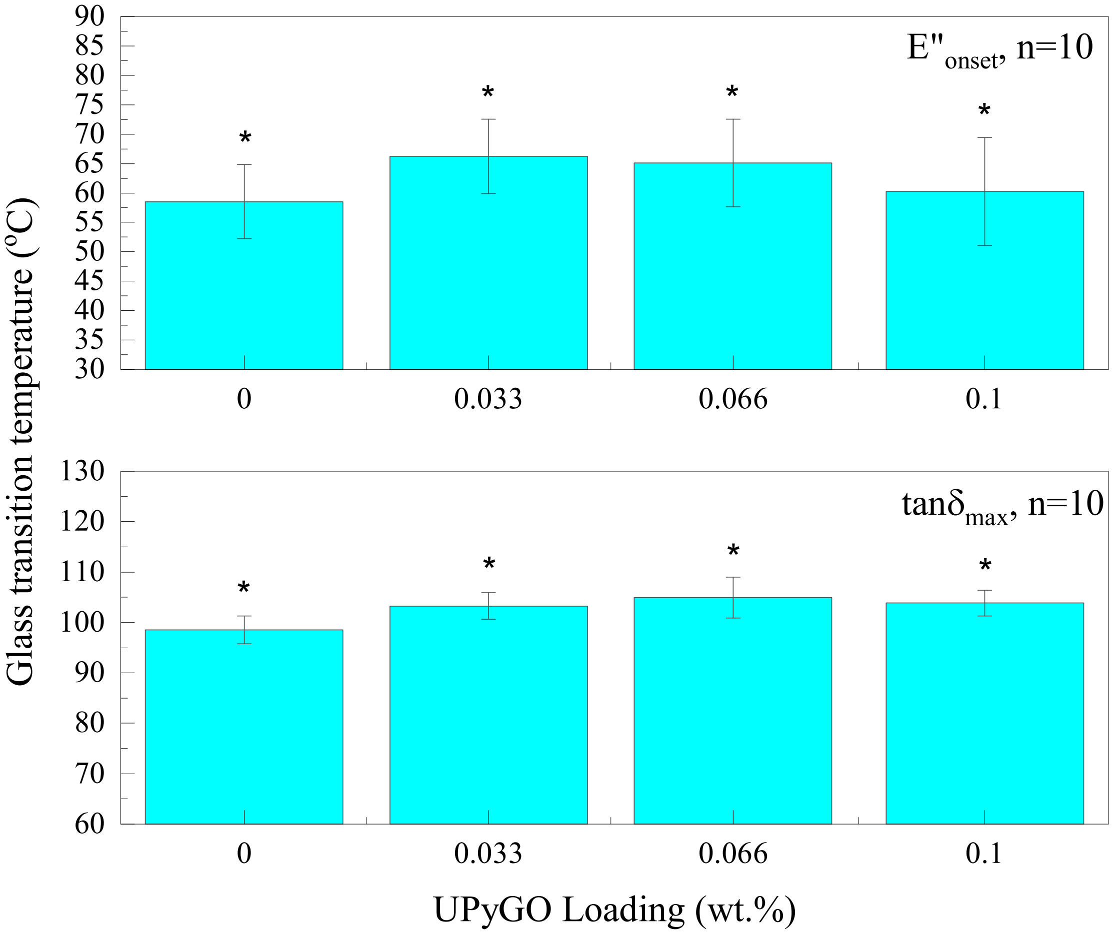

Figure 5.8 The effect of UPyGO loading on the T_g within a polyurethane matrix at varying weight percent loadings using dynamic mechanical thermal analysis at a fixed frequency of 10 Hz. E" onset statistical results: ANOVA single factor (at 95% confidence) results, F-value = 3.24 and p-value = 3.99×10^{-2} from a population of n=10. Tanδ max statistical results: ANOVA single factor (at 95% confidence) results, F-value = 8.29 and p-value = 2.84×10^{-4} from a population of n=10. Null hypothesis rejection denoted by an asterisk above the upper uncertainty limit.

The effect of UPyGO on the T_g determined by loss modulus onset shows that the addition of UPyGO filler increases the T_g. A 13% increase in the T_g as determined by loss modulus onset was observed in 0.033 wt.%. It was found that the enhancement reduced with further UPyGO loading with an 11% and 5% enhancement observed for 0.066 wt.% and 0.1 wt.%, respectively.

In comparison, the effect on the T_g was also determined by the maxima of the tanδ peak. As observed in the loss modulus onset analysis, the effect of UPyGO again increases the T_g; however, the observed effect is not as significant. In contrast to the loss modulus treatment, the tanδ imparts a smoother increase on the T_g with the addition of UPyGO, leading to a 5%, 6%, and 5% increase at 0.033 wt.%, 0.066 wt.% and 0.1 wt.% respectively.

The observed increase in the T_g suggests that the introduction of UPyGO contributes to an increase in chain stiffness which could be resultant from the steric bulking on the graphene oxide surface by the UPy. These steric effects are further evidenced by the minimal effect unmodified GOBM species have on the T_g (see Chapter 3). To draw further significance from these studies, single-factor ANOVA was conducted and led to the rejection of the null hypothesis in both analyses (see Figure 5.8).

5.4. Effect of UPyGO filler loading on the tensile viscoelastic behaviour of UPyGO-UPyPU composites

Dynamic mechanical thermal analysis was employed the investigate the impact dissipation properties of the UPyGO-UPyPU.

It was found that below the T_g (E''_{onset}) that the addition of UPyGO resulted in a reduced loss modulus in all cases compared to the virgin polyurethane. This observation suggests that in a glassy state the UPyGO polyurethane composites cannot dissipate tensile stresses as effectively as the virgin polyurethane. However, above the T_g the UPyGO polymer composites maintain performance with the loss moduli decreasing slower than the virgin polyurethane. This is because upon reaching the T_g the virgin polyurethane exhibits more reduction in molecular friction leading to the inability to dissipate heat as effectively. For the UPyGO composites the T_g is higher and due to the increased intermolecular interactions from dimerisation and graphene oxide aromaticity it presents a higher probability for molecular frictions above the T_g and therefore greater loss modulus performance.

No effect on the weight loading was observed for loss moduli with all samples performing within the consecutive uncertainty limits. To further elucidate the effect of UPyGO on the modified UPyPU matrix the energy dissipation factor, tanδ and the calculated crosslink density were plotted in Figure 5.9.

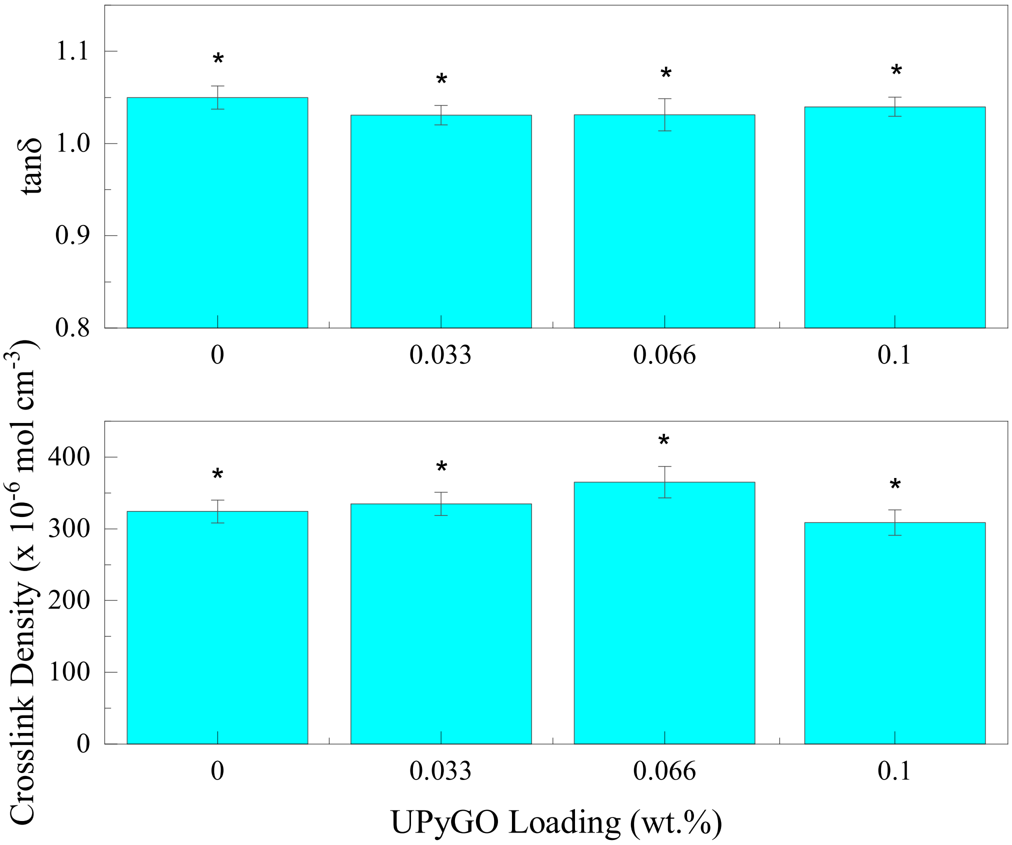

Figure 5.9 The effect of UPyGO loading on the impact dissipation factor, tanδ, measured at the peak maximum (top), and the calculated crosslink density taken from the tensile storage modulus at T=170 °C (bottom) using dynamic mechanical thermal analysis at a fixed frequency of 10 Hz. Tanδ statistical results: ANOVA single factor (at 95% confidence) results, F-value = 4.40 and p-value = 1.03×10^{-2} from a population of n=10. Calculated crosslink density statistical results: ANOVA single factor (at 95%

confidence) results, F-value = 15.1 and p-value = 2.70 x 10^{-6} from a population of n=10. Null hypothesis rejection denoted by an asterisk above the upper uncertainty limit.

Figure 5.9 showed that the increase in UPyGO led to a decrease in tanδ with observed reductions of 2%, 2% and 1% for 0.033 wt.%, 0.066 wt.% and 0.1 wt.% compared against the virgin polyurethane. This result shows that the ratio between dissipated energy and the stored energy is lower than the desired brief specifications. This observation is postulated to result from the steric bulking in the matrix from the UPyGO, which has imparted the increase in chain stiffness and therefore reduced the system's viscous capabilities, leading to a reduced energy dissipation performance observation.

The crosslink density analysis shows that the addition of UPyGO increases the calculated crosslink density through to a maximum at 0.066 wt.% (13% increase) before it reduces to a minimum at 0.1 wt.% (-5%) compared against the virgin polyurethane.

5.5. **Effect of UPyGO filler loading on the elastic modulus of UPyGO-UPyPU composites**

The elastic modulus was studied under isothermal conditions to investigate any effects of UPyGO loading on the elastic modulus. The elastic modulus was conducted using the same sample dimensions and a controlled environment on a TA Q800 DMA instrument. The instrument computed the elastic modulus, which was averaged over the repeats, subjected to standard deviation of the sample population, and statistically validated, which is presented in Figure 5.10.

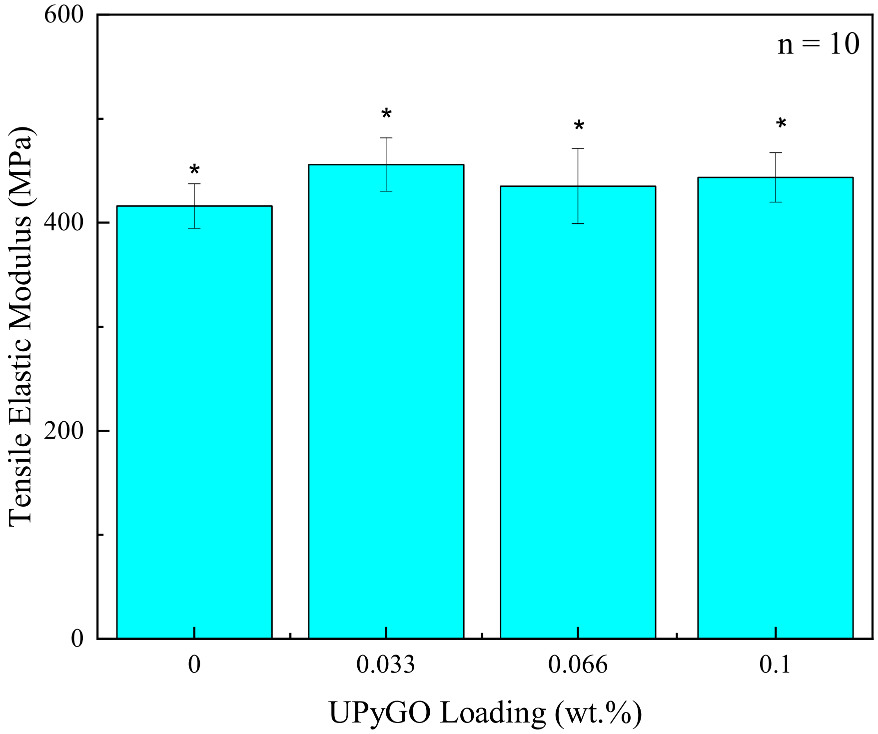

Figure 5.10. The effect of UPyGO loading on the tensile elastic modulus measured isothermally (T=30 °C) within a polyurethane matrix at varying weight percent loadings using nanoindentation. ANOVA single factor (at 95% confidence) results, F-value = 3.74 and p-value = 0.0193 from a population of n=10. Null hypothesis rejection denoted by an asterisk above the upper uncertainty limit.

It is postulated that the tensile elastic modulus decreases as UPyGO loading increases because as the applied axial load it increases the intermolecular distance between the short-range interactions. The UPy modification within the matrix is expected to compete with polymerisation of the co-polymers leading to a reduced three-dimensional polymeric architecture. This reduction in covalent bonds leads to UPy dimerisation being a key polymer adhesion component, imparting polymeric elasticity. However, the UPy dimer units connect via a donor-donor-acceptor-acceptor (DDAA) quadruple hydrogen bonding array which can be disturbed under applied loads leading to a loss of dimerisation (see Figure 5.11).

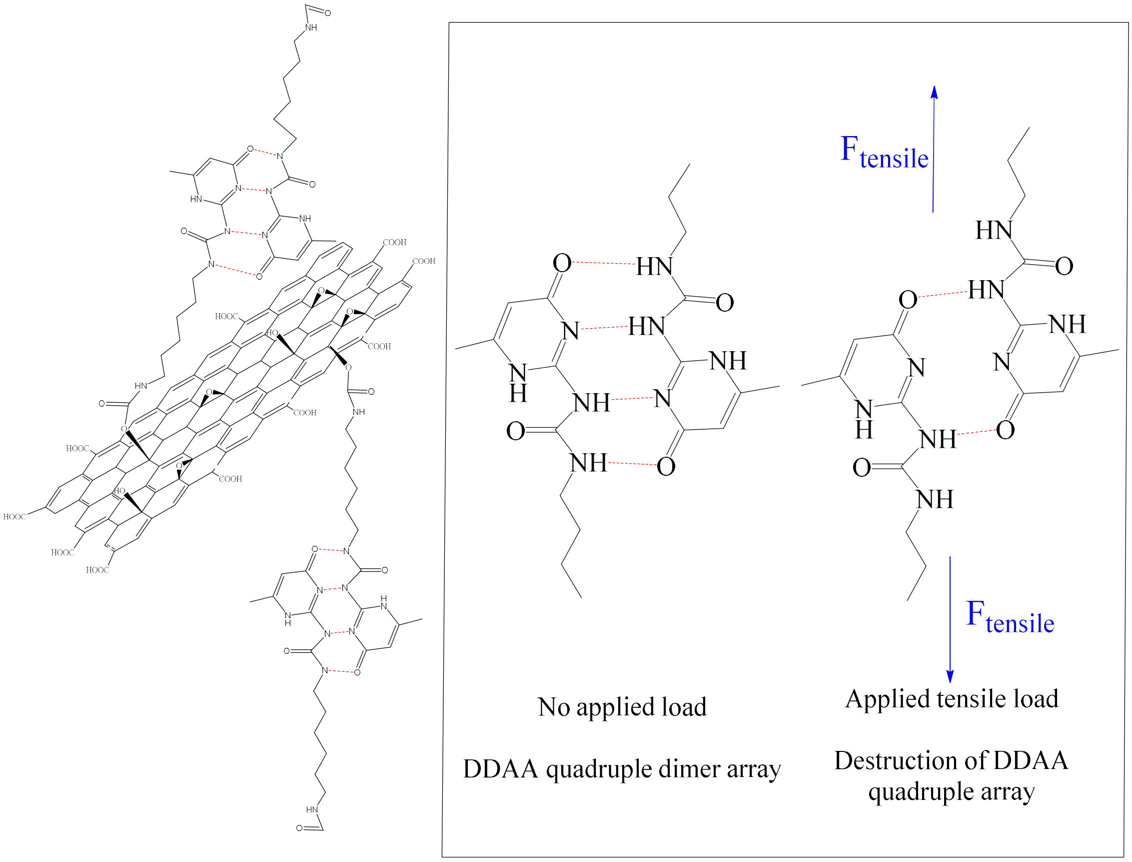

Figure 5.11. Illustration of the UPyGO filler dimerised to UPy units within the matrix and the effect of applied load shearing the DDAA array (see box) with eventual loss of all hydrogen bonding interactions with a complementary UPy monomer as the applied load increases further.

Hydrogen bonding is a reversible short-range interaction the shearing potential of dimer under applied tensile loads will result in architectural failure within the polymer composite architecture because of the reduction in bond strength with increasing interatomic distance.[18]

The indentation elastic modulus was also measured and calculated using the nanoindentation instrumentation. The instrument computed the indentation elastic modulus, which was averaged over the repeats, subjected to standard deviation of the sample population, and statistically validated and presented in Figure 5.12.

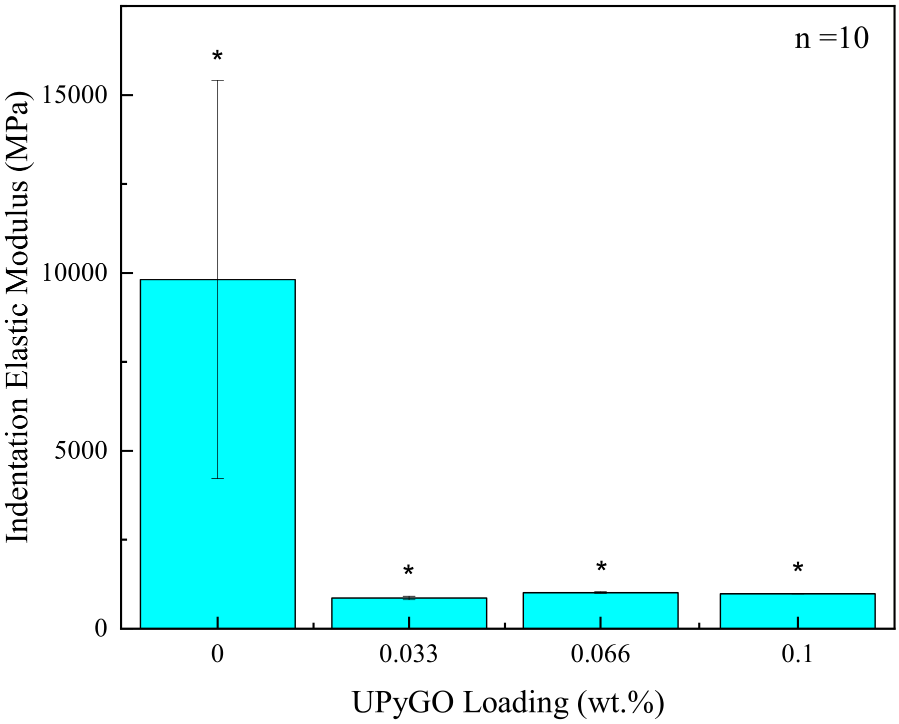

Figure 5.12. The effect of UPyGO loading on the indentation elastic modulus within a polyurethane matrix at varying weight percent loadings using nanoindentation. ANOVA single factor (at 95% confidence) results, F-value = 22.6 and p-value = 2.14 x 10^{-8} from a population of n=10. Null hypothesis rejection denoted by an asterisk above the upper uncertainty limit.

Figure 5.12 shows an opposite trend to the tensile modulus, with the addition of UPyGO, leads to significant reductions in the indentation elastic modulus. The significant reduction in the indentation elastic modulus shows addition of UPyGO reduces the stiffness of the polyurethane composite. It is postulated that the steric bulking of the UPy dimerisation adds flexibility to the composite structure providing a less rigid structure under compression.

5.6. Effect of UPyGO filler loading on the material stiffness

Stiffness is how a material resists deformation in response to an applied force. The effect of UPyGO loading on the indentation stiffness was investigated by using a nanoindenter fitted with a Berkovich tip. Repeats were averaged, and uncertainty determined by the standard deviation and plotted in Figure 5.13.

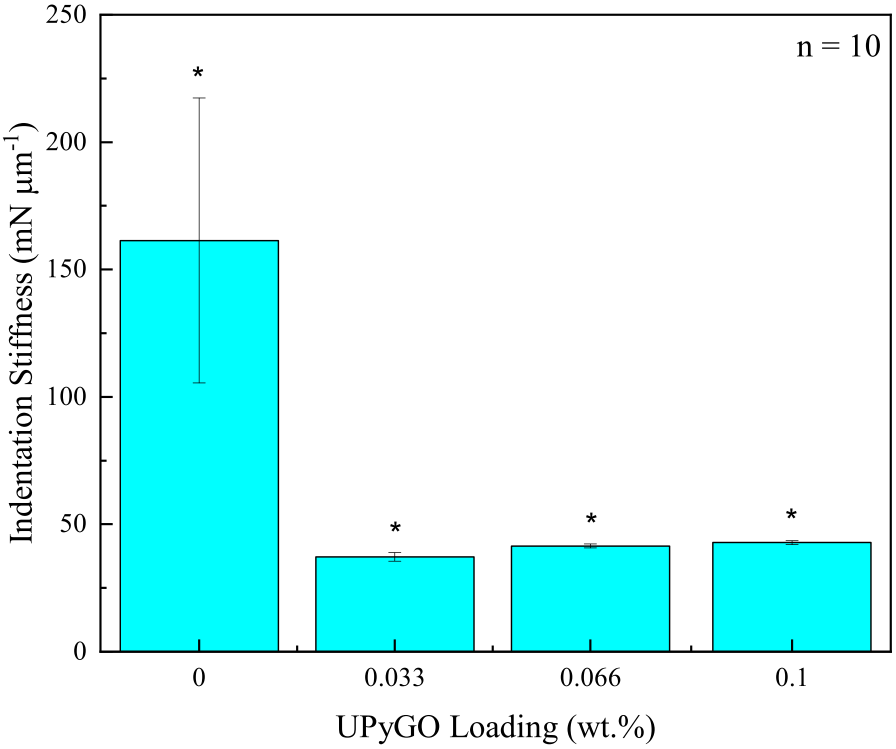

Figure 5.13. The effect of UPyGO loading on the indentation stiffness within a polyurethane matrix at varying weight percent loadings using nanoindentation. ANOVA single factor (at 95% confidence) results, F-value = 42.1 and p-value = 7.32×10^{-12} from a population of n=10. Null hypothesis rejection denoted by an asterisk above the upper uncertainty limit.

Figure 5.13 shows a significant effect on the indentation stiffness with the addition of UPyGO. The stiffness in the virgin material decreases significantly in the presence of UPyGO. The addition of UPyGO leads to a subtle increase in the indentation stiffness is also observed with increasing UPyGO weight loading. The observations suggest that addition of UPyGO imparts elasticity to the polymer composite structure. This elasticity is assumed to originate from the complementary UPy dimer units which possess a greater degree of elasticity compared to the covalent bonds in the polymer chain crosslinks. Furthermore the indentation reduction properties are desirable for impact dissipation performance and suggest that these UPy units support pre-emptive stress within the polymer matrix too.[8]

The tensile stiffness was also investigated to the indentation stiffness to investigate the difference in applied loads and the stiffness response. The tensile measurements were determined instrumentally using the TA Q800 DMA analyser, and the tensile stiffness was calculated by the gradient of force against length between the ISO-527 boundaries (0.0005 and 0.0025). The calculated tensile stiffness values were averaged, error analysis taken by computing the standard deviation, and plotted in Figure 5.14.

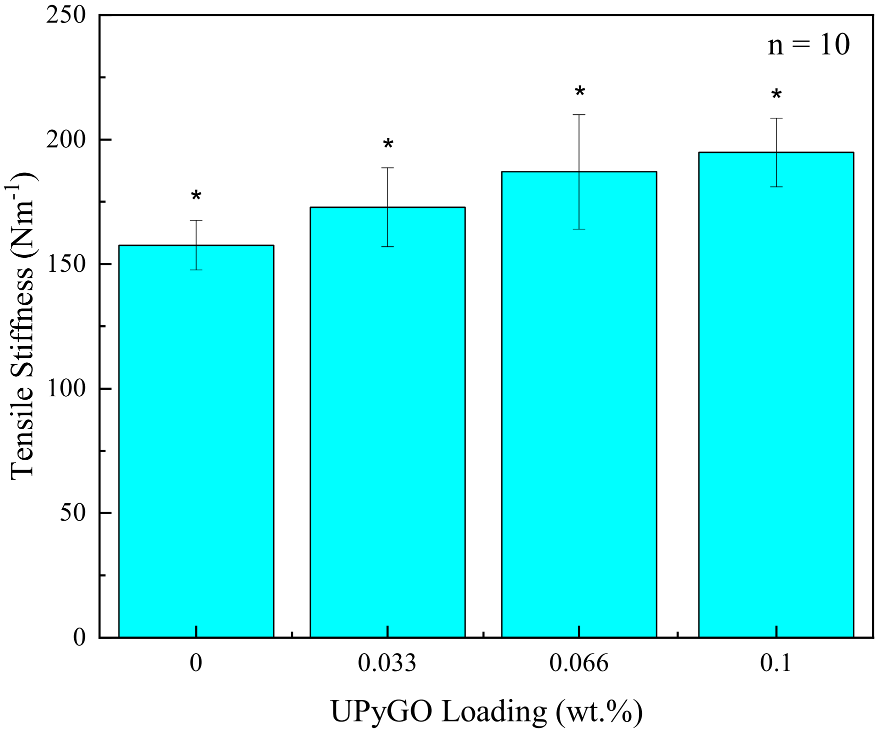

Figure 5.14 The effect of UPyGO loading on the tensile stiffness measured isothermally (T=30 °C) within a polyurethane matrix at varying weight percent loadings using nanoindentation. ANOVA single factor (at

95% confidence) results, F-value = 10.1 and p-value = 5.72 x 10^{-5} from a population of n=10. Null hypothesis rejection denoted by an asterisk above the upper uncertainty limit.

The monotonic increase in tensile stiffness with UPyGO loading suggests that the UPy dimers and the graphene basal plane again provide additional aromaticity to the polymer matrix. This is therefore observed as the applied tensile load increases within the elastic region molecular functionalities the steric bulking effects which are observed in the T_g increase are again observed here.

5.7. **Effect of UPyGO filler loading on the hardness and creep**

The material hardness was determined by nanoindentation testing using a pyramid shaped Berkovich tip. The sample was indented, and the hardness through the Oliver and Pharr method was calculated using the instrument's software. The repeats were averaged and subjected to standard deviation uncertainty analysis and presented in Figure 5.15.

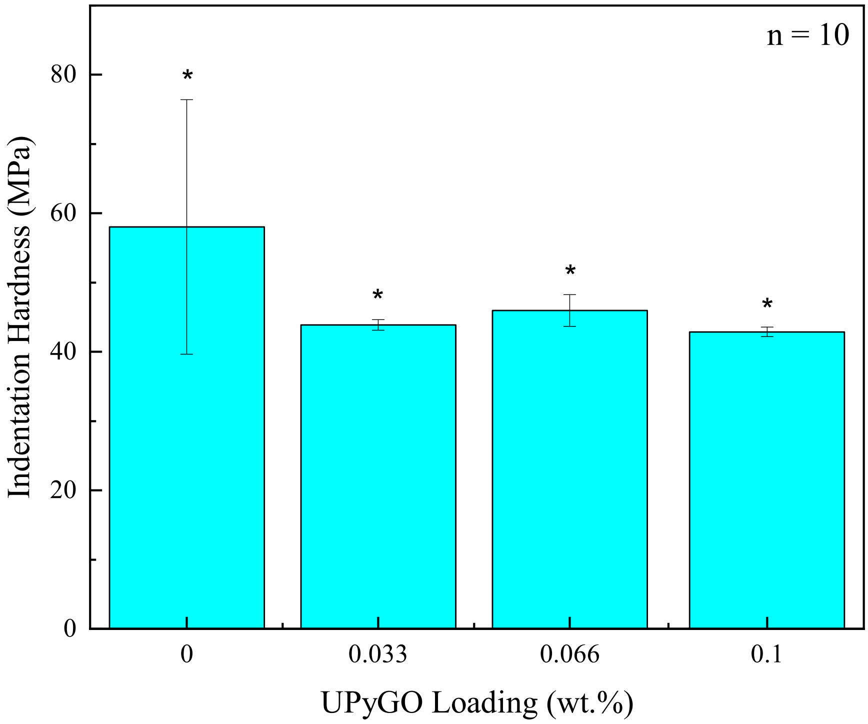

Figure 5.15. The effect of UPyGO loading on the indentation hardness within a polyurethane matrix at varying weight percent loadings using nanoindentation. ANOVA single factor (at 95% confidence) results,

F-value = 5.13 and p-value = 4.67 x 10^{-3} from a population of n=10. Null hypothesis rejection denoted by an asterisk above the upper uncertainty limit.

Figure 5.15 shows a reduction in the hardness with increasing UPyGO loading, which is desirable for impact dissipation properties.[22] The reduction in hardness is postulated to result from the complementary dimerisation of the filler and matrix, creating a less rigid three-dimensional structure through a reduction in covalent crosslinks. The UPyGO, therefore, are less resistant to plastic deformation, but these UPy units could be sacrificially failing at a micro-level. Such a strategy is employed in bone, enabling weaker sacrificial bonds to break to protect the overall structural integrity of the system through preserving the main structure.[4,23,24] Due to the intermolecular bonding nature of the quadruple hydrogen bonding that UPy utilises in dimerisation, these effects could be investigated to determine if intrinsic self-healing could be achieved in these UPyGO composites at certain conditions as seen in the UPy supramolecular literature.[11,19,25] However, such studies are beyond the scope of this research and therefore not investigated further.

Another consideration is Creep, a material's ability to resist plastic deformation under constant load. This again was measured using the nanoindenter was calculated using the instrument's software by substituting the indentation depth values into Equation **(5.2)**.

$$\boldsymbol{C_{IT} = \left(\frac{h_2 - h_1}{h_1}\right) \times 100} \qquad \textbf{(5.2)}$$

Where h_2 is the indentation depth at the start of the test and h_1 is the indentation depth at the end of the test. The repeats were averaged and subjected to standard deviation and ANOVA validation and presented in Figure 5.16.

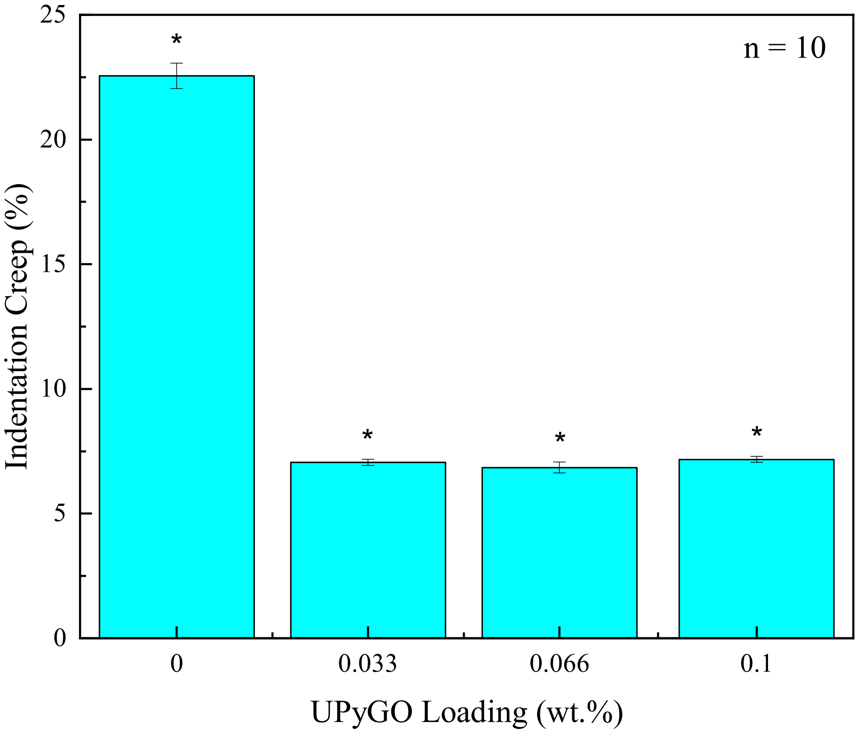

Figure 5.16. The effect of UPyGO loading on the indentation creep within a polyurethane matrix at varying weight percent loadings using nanoindentation. Validation by ANOVA single factor (at 95% confidence), F-value = 6445 and p-value = 3.41×10^{-49} from a population of n=10. Null hypothesis rejection denoted by an asterisk above the upper uncertainty limit.

The data presented in Figure 5.16 shows a comparative trend with the data observed for the indentation stiffness (see Figure 5.13) with significant creep resistance with the addition of UPyGO. The addition of UPyGO leads to a reduction in the order of 70% for all the investigated composite weight loadings. This behaviour is expected due to the increase in aromatic rings within the composite from both the graphene oxide basal plane and the UPy units, which result in an decrease in creep resistance.[17]

5.8. Evaluating the candidacy of unmodified GOBM composites and UPy-functionalised GO composites on enhancing the impact dissipation performance of Easyflo 120 polyurethane.

For a material to possess candidate properties for impact dissipation, the following material characteristics are desirable: a reduced indentation stiffness and material hardness, and the surface roughness should not increase.[22]

A change in the surface roughness was not investigated in this work owing to a uniform preparation technique throughout which would impart negligible effects on the macro surface morphology.[26] In this work, curing between two hydrophobic glass plates created a consistent surface to contain the bulk during polymerisation with a physically controlled sample thickness.

It was also found that the mechanical performance of the UPyGO-UPyPU composites resulted in smaller standard deviations between samples compared to the unmodified GOBMs from Chapter 3. Through statistical analysis (ANOVA) the null hypotheses were rejected leading to the suggestion that the complementary UPyGO-UPyPU could impart self-assembly properties. This could therefore support more control during polymerisation within the composite leading to reduced fabrication stresses, similar to the work reported by Wietor *et al.* in 2009.[8]

The reduction in material hardness is desirable according to studies that showed softer materials perform better and a reduced mass loss during erosion testing.[27,28] Therefore, Table 5.1 summarises the material hardness to evaluate the effect of the different GOBM fillers.

Table 5.1. Comparison in material hardness of GOBM composites against the virgin polyurethanes from nanoindentation testing (p = 0.05)

	GO Filled	rGO Filled	UPyGO Filled
0.033 wt.%	-7.1 ± 0.4%	-10 ± 0.5%	-24.3 ± 0.4%
0.066 wt.%	-3.9 ± 0.2%	-6.1 ± 0.3%	-21 ± 1%
0.1 wt.%	-6.9 ± 0.3%	0.41 ± 0.02%	-26.1 ± 0.4%

A reduction in the indentation stiffness is desirable because it correlates to an expected reduction in the indentation storage modulus.[22] A reduction in indentation storage modulus also assists in the material's impact dissipation through a reduction in the acoustic impedance and the speed of sound through the material. Therefore, Table 5.2 summarises the material stiffness as determined by nanoindentation to evaluate the effect of the different GOBM fillers on the candidacy of rain erosion applications.

Table 5.2. Comparison in indentation stiffness of GOBM composites against the virgin polyurethanes from nanoindentation testing (p = 0.05)

	GO Filled	rGO Filled	UPyGO Filled
0.033 wt.%	0.2 ± 0.01%	54 ± 3%	-77 ± 4%
0.066 wt.%	-0.96 ± 0.05%	76 ± 4%	-74 ± 1%
0.1 wt.%	-0.24 ± 0.01%	63 ± 3%	-73 ± 4%

Table 5.2 shows that the addition of UPyGO to the modified polymer composite brings about a reduction in the indentation stiffness in the region of 77% - 74% for all the UPyGO composites. In contrast, for the unmodified GO and rGO composites, an increase in material stiffness was identified. The reduction in the material stiffness from

nanoindentation compression seeks to support desirable properties for the impact dissipation applications. This comparison of the indentation stiffness suggests that the unmodified GO and rGO fillers imparted crystallinity into the system from their aromatic basal planes, but the rGO filled composites became significantly stiffer, which is postulated due to the greater hydrophobic properties compared to GO, leading to greater filler-matrix adhesion.

In summary it was found that the UPyGO-UPyPU polymer composites possessed the most desirable indented material properties for the candidacy of impact dissipation applications. To evaluate the tensile candidacy of the different polyurethane composites the energy dissipation factor, tanδ, and the tensile elastic modulus were compared.

Under certain conditions, research has shown that functionalisation with UPy imparts intrinsic self-healing properties.[11,19,20] In addition the assumed shearing and progressive loss of the array provides sacrificial bonds that yield like bone structures.[4] If some of the array remains intact or enough chain mobility is inputted through an external stimulus such as heat it could lead to self-healing of the DDAA if the UPy monomers are within close enough proximity,[20,21] offering another avenue of investigation beyond this work.

5.9. Chapter conclusion

This Chapter reported the development of UPy-functionalised polyurethanes through an *in situ* polymerisation approach. The work further expanded by combining UPyGO made in Chapter 4 with the UPy-polyurethane to generate a UPyGO-UPy-polyurethane composite.

The addition of UPyNCO did not impact the room temperature polymerisation of the Easyflo120 and through an absence of an isocyanate vibrational stretch using FTIR ATR spectroscopy. To further confirm the successful modification, the UPy-polyurethane was subjected to DSC analysis which showed a positive trend with the T_g increasing with increasing UPyNCO weight loading, suggesting an increase in crystallinity resultant from the UPy units. As observed with previous works, the UPyNCO loading can lead to negative material performance, which was observed with a bell-shaped trend in the impact dissipation factor, tanδ.

The work then progressed to investigate the effect of UPyGO been loaded into the UPy-modified polyurethane through an *in-situ* polymerisation technique. It was found that the addition of UPyGO did not enhance the mechanical properties when tension forces were applied, suggesting that the UPyGO units and UPy-modifications imparted stiffness into the material, which prevents chain mobility from dissipating mechanical energy when a load is applied.

However, when the UPyGO-UPy-polyurethane composites are subjected to nanoindentation testing, these composites performed desirably according to the evaluated specifications suggesting potential for rain erosion applications.

Finally, as a function of the filler type GO, rGO and UPyGO composites were compared using the tensile storage modulus, tanδ, hardness and compressive stiffness to assess their candidacy for rain erosion and tensive applications.

On the other hand, the work found that for rain erosion properties, modification with UPyGO and UPy in the polymer resulted in significant reduction of hardness (24-26%) and stiffness (73-77%) suggesting that the addition of UPyGO could be a candidate for further rain erosion testing.

5.10. Chapter references

1 B. Pokroy, A. K. Epstein, M. C. M. Persson-Gulda and J. Aizenberg, *Adv. Mater.*, 2009, **21**, 463–469.

2 J. Huang, Z. Tang, Z. Yang and B. Guo, *Macromol. Rapid Commun.*, 2016, **37**, 1040–1045.

3 X. Qi, D. Zhang, Z. Ma, W. Cao, Y. Hou, J. Zhu, Y. Gan and M. Yang, *ACS Nano*, 2018, **12**, 1062–1073.

4 G. E. Fantner, T. Hassenkam, J. H. Kindt, J. C. Weaver, H. Birkedal, L. Pechenik, J. A. Cutroni, G. A. G. Cidade, G. D. Stucky, D. E. Morse and P. K. Hansma, *Nat. Mater.*, 2005, **4**, 612–616.

5 S. Keten, Z. Xu, B. Ihle and M. J. Buehler, *Nat. Mater.*, 2010, **9**, 359–367.

6 F. H. Beijer, R. P. Sijbesma, H. Kooijman, A. L. Spek and E. W. Meijer, *J. Am. Chem. Soc.*, 1998, **120**, 6761–6769.

7 R. F. M. Lange, M. Van Gurp and E. W. Meijer, *J. Polym. Sci. Part A Polym. Chem.*, 1999, **37**, 3657–3670.

8 J. L. Wietor, A. Dimopoulos, L. E. Govaert, R. A. T. M. Van Benthem, G. De With and R. P. Sijbesma, *Macromolecules*, 2009, **42**, 6640–6646.

9 A. Faghihnejad, K. E. Feldman, J. Yu, M. V. Tirrell, J. N. Israelachvili, C. J. Hawker, E. J. Kramer and H. Zeng, *Adv. Funct. Mater.*, 2014, **24**, 2322–2333.

10 Nederlandsch Octrooibureau, EP2450394B1., 2017, 1–17.

11 Y. Lin and G. Li, *J. Mater. Chem. B*, 2014, **2**, 6878–6885.

12 H. Sardon, A. Pascual, D. Mecerreyes, D. Taton, H. Cramail and J. L. Hedrick, *Macromolecules*, 2015, **48**, 3153–3165.

13 M. Muuronen, P. Deglmann and Ž. Tomović, *J. Org. Chem.*, 2019, **84**, 8202–8209.

14 R. Van Maris, Y. Tamano, H. Yoshimura and K. M. Gay, *J. Cell. Plast.*, 2005, **41**, 305–322.

15 E. Gregersen, *Br. Online Encycl.*, 2021, 2–3.

16 G. Widmann, R. Riesen, J. Schawe, M. Schubnell and M. Wagner, in *Thermal Analysis in Practice*, ed. M. Wagner, Mettler Toldeo AG, Schwerzenbach, 2009, pp. 225–245.

17 M. A. Meyers and K. K. Chawla, *Mechanical Behavior of Materials*, Cambridge University Press, 1st edn., 1999.

18 P. Atkins and J. de Paula, in *Atkins' Physical Chemistry*, Oxford University Press, Oxford, 10th edn., 2014, p. 399.

19 E. Schlangen and C. Joseph, *Self-Healing Materials: Fundamentals, Design Strategies, and Applications*, Wiley-VCH, Weinheim, 2009.

20 J. Cui and A. del Campo, *Chem. Commun.*, 2012, **48**, 9302.

21 M. Wei, M. Zhan, D. Yu, H. Xie, M. He, K. Yang and Y. Wang, *ACS Appl. Mater. Interfaces*, 2015, **7**, 2585–2596.

22 A. O. Carroll, M. Hardiman, E. F. Tobin and T. M. Young, *Wear*, 2018, **412–413**, 38–48.

23 G. E. Fantner, E. Oroudjev, G. Schitter, L. S. Golde, P. Thurner, M. M. Finch, P. Turner, T. Gutsmann, D. E. Morse, H. Hansma and P. K. Hansma, *Biophys. J.*, 2006, **90**, 1411–1418.

24 T. T. T. Myllymäki, L. Lemetti, Nonappa and O. Ikkala, *ACS Macro Lett.*, , DOI:10.1021/acsmacrolett.7b00011.

25 M. M. C. Bastings, S. Koudstaal, R. E. Kieltyka, Y. Nakano, A. C. H. Pape, D. A. M. Feyen, F. J. van Slochteren, P. A. Doevendans, J. P. G. Sluijter, E. W. Meijer, S. A. J. Chamuleau and P. Y. W. Dankers, *Adv. Healthc. Mater.*, 2014, **3**, 70–78.

26 H. R. Allcock, in *Introduction to Materials Chemistry*, John Wiley & Sons, Inc, New Jersey, 2008, pp. 355–371.

27 F. P. Bowden and J. H. Brunton, *Proc. R. Soc. A*, 1961, **263**, 433–450.

28 N. E. Wahl and J. L. Beal, *A Study of the Rain Erosion of Plastics and metals*, New York, 1951.

6. Summary of Conclusions and Future Work

6.1. Summary of Conclusions

This Thesis investigated the impact dissipation and tensile candidacy of unmodified graphene oxide and reduced graphene oxide and also a ureidopyrimidone modified graphene oxide filler.

In conclusion from the literature review identified the potential for ureidopyrimidone (UPy) as a potential modification to graphene oxide inspired by sacrificial bonds found in bone, and its reported intrinsic self-assembly and healing properties in supramolecular polymer chemistry.

Chapter 3 reported the characterisation of commercially supplied graphene oxide-based materials, gratuitously supplied by Graphitene Ltd as part of the research partnership. The characterisation study which provided a basis for quality control identified that the electrochemically exfoliated graphene oxide (eco-GO) was not successful and was removed from further studies. Easyflo polyurethane resins were investigated due to their room temperature curing which was selected to mirror similar conditions to that of current offshore wind turbine manufacture which this was the basis for the wider GreenPort Growth programme research cluster.

The investigations in Chapter 3 found that the addition of unmodified GOBM fillers led to an increase in the indentation stiffness which is not desirable for impact dissipation applications. The reduced graphene oxide imparted an 840% increase in the stiffness at 0.066 wt.%. The graphene oxide still enhanced the material stiffness but was not as significant. Under tensile conditions the addition of filler lead to an increase in the stiffness as was observed in an increase in the glass transition temperature with filler loading. This chapter concluded that the addition of unmodified GOBMs did not meet the candidacy requirements identified in the literature and design brief, so a bioinspired filler modification was investigated to investigate the quadruple hydrogen bonding dimer motif, ureidopyrimidone.

Chapter 4 reported the novel functionalisation synthesis of graphene oxide with the quadruple hydrogen bonding monomer, ureidopyrimidone (UPy). This synthesis was conducted without the use of polydopamine which is used in the only other report of UPyGO from Wang *et al.* in 2018. The UPyGO is extensively characterised and physical properties comparisons are conducted against the parent graphene oxide and also reduced graphene oxide to further extend the understanding of these systems, which is not reported within the literature.

Elemental analysis confirmed the successful functionalisation through the presence of nitrogen which was also validated in elemental combustion analysis and provided a calculated degree of functionalisation of 6.20 ± 0.04%. Multiple batches were synthesised and compared and demonstrated reproducibility.

The physical properties further confirmed variance to the parent graphene oxide and the its stability in different solvents demonstrated different suspension behaviour. Pristine films were attempted via vacuum filtration and solution casting to test the mechanical properties however the reduced graphene oxide and UPyGO were too brittle for examination.

Chapter 5 reported the successful functionalisation by in situ polymerisation of UPy to the Easyflo120 polyurethane. The UPy-functionalised polyurethane was combined with the synthesed novel UPyGO filler from Chapter 4 and its impact dissipation candidacy investigated in addition to its tensile performance. The addition of UPyGO found that the addition of UPyGO decreased the indentation stiffness and hardness significantly which was validated by statistical means to reject a null hypothesis. It was concluded that the steric bulking on the UPy units enhanced the composites flexibility enabling a more viscous response to impact. Under tensile conditions the addition of UPyGO led to a monotonic increase in the tensile stiffness and an enhancement in the elastic modulus.

It was found that the UPyGO composites possessed the most desirable properties for impact dissipation candidacy compared to the unmodified GOBMs with a reduction observed in both the indentation hardness and stiffness, which are key requirements from the work by O'Carroll *et al.* in 2018. Under tensile conditions the modified UPyGO polyurethane composite was also found to possess the best material properties which were postulated due to greater filler matrix adhesion within the polymer chains.

Therefore, the objectives of this Thesis were achieved which demonstrated that modification with UPy onto graphene oxide enhances the indentation (compressive) and tensile properties desirably for each application and identifies a potential candidate for rain erosion applications that is synthesised through a facile route.

This ability to covalently surface functionalise the graphene oxide with a motif able to spontaneously dimerise enables the exploitation of properties such as; intrinsic self-healing, pre-emptive stress relaxation, or a strategy to incorporate fillers into incompatible matrices by dynamic crosslinking. Therefore, these exploitations introduce new avenues of applications into high-profile technologies such as smart coatings, enhanced mechanical reinforcement, next-generation composites and self-healing polymer composites.

6.2. Future Work

To further extend the scope of this research into a greater understanding of the potential these GOBM polyurethane composites have towards minimising liquid droplet impingement would see these formulations tested by simulated weathering techniques. The polyurethane matrices used in this formulation are suspected to be chemically catalysed by the tertiary amine crosslinker (Quadrol™) because there are no ultraviolet or thermal treatment requirements for successful polymerisation. However, due to the aromaticity of the diphenyl rings in the methylene diisocyanate, these formulations could be susceptible to ultraviolet degradation. Therefore, humidity and ultraviolet degradation testing would be essential assays to determine application feasibility.

In conjunction with determining the environmental susceptibility of the composites, the mechanical performance of the composite coatings through rain erosion testing is essential. Following the work published by O'Carroll *et al.*[1], the whirling-arm rain erosion test rig provides a realistic investigation of the rain erosion dissipation properties. Therefore, casting onto pure epoxy or aluminium substrates for rain erosion testing also enables further studies on the how the application protocol affects the surface roughness, adhesion properties, flexural and fracture toughness to complement the rain erosion test data.

Another measurable parameter, which is utilised primarily in aviation studies is the damage threshold velocity (V_{DT}), which can also be determined from rain erosion testing.[2] The V_{DT} is defined by the "*lowest velocity which theoretically could cause damage in the target material"*.[3] This is further described by Evans *et al.* with a theoretical expression for the (V_{DT}) as shown in ((6.1).[4]

$$V_{DT} \approx 1.41 \left(\frac{K_{ic}^2 c_R}{\rho_w^2 c_w^2 d_w} \right)^{1/3} \qquad \textbf{\textit{(6.1.)}}$$

Where K^2_{ic} the fracture toughness of the target material; c_R the Raleigh wave velocity (***6.2***)of the target material, ρ_w the density of water; c_w the compressional wave speed in water, and d_w is the diameter of the water droplets. The Raleigh wave velocity is given by (1.3),[5] with ν being the Poisson's ratio; ρ - the density and E - Young's modulus.

$$c_R = \left(\frac{0.862+1.14\nu}{1+\nu} \right) \left(\frac{E}{2(1+\nu)\rho} \right) \qquad \textbf{\textit{(6.2.)}}$$

Eqs (6.1 and (6.2.)enable predictive estimations into the V_{DT} of rain erosion upon the blade surface, which provides a comparative measure for coating performance.[3] From inspection of (6.1.), it is apparent that an increased fracture toughness increases the theoretical damage threshold velocity, enabling a more resilient surface towards water impingement.

Once an accurate measurement of Poisson's ratio for the materials can be determined experimentally, it enables the Raleigh Wave also to be calculated as per ((***6.2***). Through variation of the rain droplet diameter between 0.5 mm and 3 mm a range for the V_{DT} can be plotted as a function of the rain droplet diameter as shown by Figure 6.1.

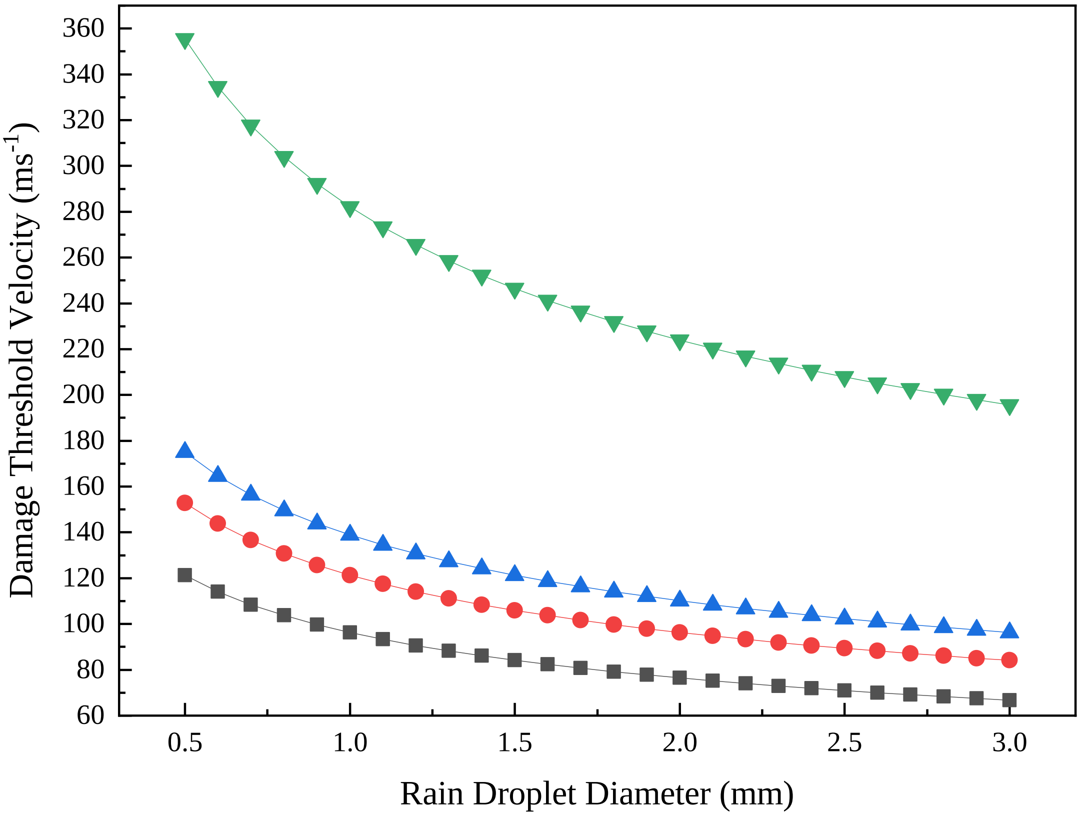

Figure 6.1. Theoretical damage threshold velocity for pure epoxy with a fracture toughness of 0.5 MPa m$^{-0.5}$ (black squares), 1 MPa m$^{-0.5}$ (red circles), 1.5 MPa m$^{-0.5}$ (blue triangles), and 35 wt.% glass-filled epoxy (green triangles) as a function of the rain droplet diameter. The physical parameters for the pure epoxy are from the review by Keegan et al.,[6] and the fracture toughness from Betelie et al. .[7]

Through a comparative study, the damage threshold velocity could be investigated and compared against current reinforcements such as glass fibre reinforced epoxy (see Figure

6.1) to gauge performance against existing technologies. The ability to create complementary dimerisation also enables variation of the polymer matrix utilising the extensive supramolecular modifications using UPy.[8–10] If these areas of future study are considered, it allows active development that underpins the design of the next generation protective coatings.

6.3. Chapter References

1 A. O. Carroll, M. Hardiman, E. F. Tobin and T. M. Young, *Wear*, 2018, **412–413**, 38–48.

2 O. Gohardani, *Prog. Aerosp. Sci.*, 2011, 47, 280–303.

3 E. A. Valaker, S. Armada and S. Wilson, *Droplet erosion protection coatings for offshore wind turbine blades*, Elsevier B.V., 2015, vol. 80.

4 A. G. Evans, *Impact damage in brittle materials in the plastic response regime Report No SC5023*, 1977, vol. 73.

5 J. . Achenbach, *Wave Propagation in Elastic Solids*, North Holland, Amsterdam, 1st edn., 1984.

6 M. H. Keegan, D. H. Nash and M. M. Stack, *J. Phys. D. Appl. Phys.*, 2013, **46**, 383001.

7 A. A. Betelie, Y. T. Megera, D. T. Redda and A. Sinclair, *AIMS Mater. Sci.*, 2018, **5**, 93–104.

8 C. Dooley and D. Taylor, *Fatigue Fract. Eng. Mater. Struct.*, 2017, **40**, 655–669.

9 A. W. Bosman, R. P. Sijbesma and E. W. Meijer, *Mater. Today*, 2004, **7**, 34–39.

10 Y. Yang and M. W. Urban, *Chem. Soc. Rev.*, 2013, **42**, 7446.